Travail de Fin d'Etudes : Modelling of drying phenomena in concrete with recycled aggregates

Auteur : Fanara, Arthur
Promoteur(s) : Courard, Luc
Faculté : Faculté des Sciences appliquées
Diplôme : Master en ingénieur civil des constructions, à finalité spécialisée en "civil engineering"
Année académique : 2019-2020
URI/URL : http://hdl.handle.net/2268.2/9028

Travail de fin d'études réalisé en vue de l'obtention du grade de master "Ingénieur Civil des constructions, à finalité"

MODELLING OF DRYING PHENOMENA IN CONCRETE WITH RECYCLED AGGREGATES

—

Modélisation des phénomènes de séchage dans les bétons à base de granulats recyclés

Arthur FANARA

ANNÉE ACADÉMIQUE 2019-2020

UNIVERSITÉ DE LIÈGE - FACULTÉ DES SCIENCES APPLIQUÉES

JURY:

Mr. Luc COURARD (ULiège)
Mr. Frédéric COLLIN (ULiège)
Mr. Julien HUBERT (ULiège)
Mrs. Angélique LÉONARD (ULiège)
Mr. Frédéric MICHEL (ULiège)
Mr. Sébastien REMOND (PolyTech Orléans)

Remerciements

Je voudrais tout d'abord remercier mon promoteur Mr. Courard, ainsi que mon co-promoteur Mr. Collin, pour leur confiance et leur disponibilité tout au long de ce travail de fin d'étude. Leurs conseils m'auront été précieux tout au long de cette épreuve, de l'expérimentation à la modélisation. Merci pour les longues heures que vous m'avez allouées, elles m'auront permis d'y voir plus clair et de mieux progresser.

Je remercie également Julien Hubert pour sa disponibilité et sa grande patience. Son expérience dans le sujet abordé a permis de me débloquer à de nombreuses reprises et ainsi atteindre mes objectifs. Merci pour les nombreuses heures qui m'auront été consacrées.
Il m'est aussi important de remercier Frédéric Michel, responsable du Laboratoire des Matériaux de Construction, pour son aide tout au long de mon expérimentation, ses conseils m'ayant aidé à analyser et interpréter les résultats obtenus. Merci aussi car c'était toujours un plaisir de discuter et d'en apprendre toujours plus.

Je tiens également à remercier les différents membres des différents laboratoires pour leur aide et leurs conseils qui m'ont permis de mener à bien l'expérimentation de ce travail. Merci à Amaury, Monique, Fabienne et Véronique du Laboratoire des Matériaux de Construction, merci à Pierre du Laboratoire de Géomécanique et pour finir, merci à Thierry de la Halle de Génie Chimique.

Merci aussi à mes collègues de bureau: Adèle, Louis et Marine, pour votre bonne humeur et votre enthousiasme tout au long de ce travail. Les pauses cafés n'auraient pas été les mêmes sans vous.

Je remercie d'avance les membres de mon jury, Mme. Léonard et Mr. Remond, pour leur intérêt porté à ce travail et le temps consacré à sa lecture.

Enfin, je remercie mes proches et ma famille pour leur soutien tout au long de mes études. Merci à mes parents d'avoir toujours cru en moi, et merci à Laura pour ta présence à mes côtés durant ces huit dernières années et ton précieux soutien dans tous mes projets.

Arthur.

Abstract

Concrete is the most used building material in the construction industry, with a production estimated to be about 1 billion tons/year in the European Union. Natural aggregate (NA) is one of the main ingredients of concrete, whose production reached about 2.8 billion tons in Europe in 2017. It is today evident that natural aggregates and sand are becoming a scarce resource and their availability becomes therefore an important challenge.
Furthermore, environmental concerns regarding the construction industry have risen, particularly regarding CO_2 emissions and waste production from construction and demolition activities (C&D Waste).

That's why the construction industry needs to develop and implement processes able to incorporate recycled products into its building materials. Recycled Concrete Aggregates (RCA) produced from crushed C&DW as a replacement of natural aggregates is one of those solutions which has made it a thoroughly studied field.
RCA consist of coarse particles containing natural aggregates as well as residual cement paste which impairs negatively their properties compared to NA. Indeed, the use of RCA inside concrete increases the porosity and may therefore reduce its durability. The focus of this master thesis is to analyse the influence of RCA on transfer properties (water retention curves, permeability and porosity) and drying behaviour of concrete. Indeed, a better knowledge of those properties will help to determine the effect of RCA on the durability of concrete as water and vapour transfers are the necessary condition to observe degradation processes like carbonation, chloride ion diffusion or alkali-aggregate reaction.

A numerical model for drying phenomena of concrete samples with recycled aggregates is developed in this thesis. To support this modelling, an experimental programme with sorption and desorption tests as well as porosity and permeability determination, is implemented.
To better study the influence of the RCA alone, several concrete mixes are studied: a reference composition with natural aggregates and the same composition with RCA (same granulometric curve), a mix with natural aggregates but another cement type and, finally, a mortar without any aggregates. The three concrete compositions have the same paste content and type as it highlights the influence of the change of aggregates/cement type.
The modelling is performed with a nonlinear finite element software developed at the University of Liège (called Lagamine). It follows the theory of nonlinear finite elements modelling of flows in porous media and consists of a coupled thermo-hydraulic study of the material.
An application is also carried out in the form of an exterior parking lot's column subjected to real outdoor conditions: at constant and variable temperature, the relative humidity will vary between 40% and 95%, with multiple cycles of 6 months.

Results show that, as predicted, concrete made from Recycled Concrete Aggregates (RCA) is more porous than its Natural Aggregates (NA)-based counterpart. Its water absorption and intrinsic permeability are also superior than for regular concrete. In terms of water retention properties, both concretes are similar, with no significant differences.
The first indicator of durability measured in this thesis is the resistance to carbonation, which showed that concrete made from RCA is more prone to carbonation than concrete with NA.

Nota Bene: this master thesis has been performed during the COVID-19 period when lockdown was applied from March 19th to May 31st, 2020.
Keywords: Concrete, Recycled Concrete Aggregates, Nonlinear Finite Element Modelling, Drying Phenomena, Water Retention Curve, Convective Drying, Transfer Properties, Durability.

Résumé

Le béton est le matériau de construction le plus utilisé dans l'industrie du bâtiment, avec une production estimée à environ 1 milliard de tonnes/an dans l'Union européenne. Les granulats naturels sont l'un des principaux ingrédients du béton, dont la production a atteint environ 2,8 milliards de tonnes en Europe en 2017. Il est aujourd'hui évident que les granulats naturels et le sable deviennent une ressource rare et leur disponibilité devient donc un défi important.
En outre, les préoccupations environnementales concernant l'industrie de la construction ont augmentées, notamment en ce qui concerne les émissions de CO_2 et la production de déchets provenant des activités de construction et de démolition (déchets C&D).

C'est pourquoi l'industrie de la construction doit développer et mettre en œuvre des processus capables d'incorporer des produits recyclés dans ses matériaux de construction. Les granulats de béton recyclés produits à partir de déchets C&D broyés en remplacement des granulats naturels sont l'une de ces solutions qui en ont fait un domaine soigneusement étudié.
Les granulats de béton recyclés sont constitués de particules grossières contenant des agrégats naturels ainsi que des résidus de pâte de ciment qui modifient négativement leurs propriétés par rapport aux granulats naturels. En effet, l'utilisation de ces granulats recyclés à l'intérieur du béton augmente sa porosité et peut donc réduire sa durabilité. L'objectif de ce travail de fin d'étude est d'analyser l'influence des granulats recyclés sur les propriétés de transfert (courbes de rétention d'eau, perméabilité et porosité) et le comportement au séchage du béton. En effet, une meilleure connaissance de ces propriétés permettra de déterminer l'effet de ceux-ci sur la durabilité du béton car les transferts d'eau et de vapeur sont la condition nécessaire pour observer des processus de dégradation comme la carbonatation, la diffusion d'ions chlorure ou la réaction alkali-agrégats.

Un modèle numérique pour les phénomènes de séchage d'échantillons de béton avec des agrégats recyclés est développé dans ce travail. Pour soutenir cette modélisation, un programme expérimental comprenant des tests de sorption et de désorption ainsi que la détermination de la porosité et de la perméabilité, est mis en œuvre.
Pour mieux étudier l'influence des granulats recyclés seule, plusieurs mélanges de béton sont étudiés : une composition de référence avec des granulats naturels et la même composition avec les recyclés (même courbe granulométrique), un mélange avec des granulats naturels mais un autre type de ciment et, enfin, un mortier sans aucun granulat. Les trois compositions de béton ont la même teneur en pâte et le même type de pâte car elles mettent en évidence l'influence du changement de type de granulats/ciment.
La modélisation est réalisée à l'aide d'un logiciel d'éléments finis non linéaires développé à l'Université de Liège (appelé Lagamine). Il suit la théorie de la modélisation par éléments finis non linéaires des écoulements dans les milieux poreux et consiste en une étude thermo-hydraulique couplée du matériau.
Une application est également réalisée sous la forme d'une colonne de parking extérieur soumise à des conditions extérieures réelles : à température constante et variable, l'humidité relative variera entre 40 et 95%, avec de multiples cycles de 6 mois.

Nota Bene: ce travail de fin d'étude a été réalisé durant la période de COVID-19 pendant laquelle le confinement a été mis en place du 19 Mars au 31 Mai 2020.
Mots-clés: Béton, Granulats de Béton Recyclé, Modélisation par Éléments Finis Non Linéaires, Phénomènes de Séchage, Courbe de Rétention d'Eau, Séchage Convectif, Propriétés de Transfert, Durabilité.

Contents

List of Figures

List of Tables

Glossary

Constants

D_a^w	Coefficient of diffusion of dissolved air inside liquid water	2 10^{-9} m^2/s
g	Gravitational acceleration	9.81 m/s^2
L	Water evaporation latent heat	2500 kJ/kg
M	Molar mass of water	18.016 g/mol
M_{gas}	Molar mass of the gas	[g/mol]
p_{atm}	Atmospheric pressure	101325 Pa
R	Universal constant of perfect gases	8.3143 $\mathrm{J}.\mathrm{mol}/\mathrm{K}$

Concrete: a Porous Media

η	Volume fraction (Theory of mixture)	-
ρ_i	Density of the phase i	[kg/m^3]
σ_{ij}	Surface tension between the phases i and j	[N/m]
θ	Contact angle	[$^\circ$]
e	Void ratio	-
h	Degree of hydration	day
m	Mass	[kg]
n	Porosity	-
p_c	Capillary pressure	[Pa]
p_g	Gas pressure	[Pa]
p_l	Liquid pressure	[Pa]
r_c	Capillary radius	[m]
s	Suction	[Pa]
S_r	Degree of saturation of the porous medium	-
V	Total volume of the porous medium	[m^3]
V_g	Volume of the gas phase	[m^3]
V_l	Volume of the liquid phase	[m^3]
V_s	Volume of the solid phase	[m^3]

V_v	Pore volume	[m^3]
V_{cp}	Volume of the capillary pores	[m^3]
w/c	Water-to-cement ratio	-

Drying Processes

α_{vG}	Van Genuchten formulation's model parameter (Air-entry pressure)	[Pa]
h_c	Capillary pressure head	[m]
m_{vG}	Van Genuchten formulation's model parameter	-
n_{vG}	Van Genuchten formulation's model parameter	-
p_a	Air pressure	[Pa]
p_v	Partial water vapour pressure	[Pa]
p_v^0	Saturating (Equilibrium) water vapour pressure	[Pa]
p_w	Water pressure	[Pa]
q	Drying rate	[$\mathrm{kg/m^2.s}$]
RH	Relative Humidity	-
$S(w)$	External drying surface	[m^2]
$S_{r,w}$	Water saturation	-
S_{res}	Water residual saturation	-
S_{sat}	Maximum water saturation	-
T	Temperature	[K]
T_0	Temperature at the boundary of the sample	[K]
T_{air}	Temperature of the drying air	[K]
T_{db}	Dry bulb temperature (ambient air temperature)	[K]
T_{wb}	Wet bulb temperature	[K]
w	Gravimetric water content	-

State of the Art

D_h	Diffusion coefficient	[m^2/s]
h	Pore relative humidity	-
h_s	Self-desiccation function	-
w	Moisture content	-

Modelling of Convective Drying

α	Coefficient of thermal dilatation	$[\mathrm{m}/^{\circ}\mathrm{C.m}]$
α	Mass transfer coefficient	$[\mathrm{m/s}]$
α_s	Thermal expansion coefficient of the solid grain	$[\mathrm{m}/^{\circ}\mathrm{C.m}]$
$\bar{f}$	Heat flux from the boundary of the sample to the drying air	$[\mathrm{J/m^2.s}]$
$\bar{q}$	Vapour flow from the sample to its surroundings	$[\mathrm{m/s}]$
β	Heat transfer coefficient	$[\mathrm{W/m^2.K}]$
$\dot{E}^{l\rightarrow g}_{H_2O}$	Term of exchange from the liquid phase to the gaseous phase	$[\mathrm{kg/m^3}]$
Γ	Border of the volume Ω	-
Γ_i	Thermal conductivity of the constituent/phase i	$[\mathrm{W/m.K}]$
μ	Dynamic viscosity of the fluid	$[\mathrm{kg/m.s}]$
Ω	Volume of porous medium studied	-
ρ^g_a	Density of the dry air	$[\mathrm{kg/m^3}]$
ρ^w_a	Density of the dissolved air	$[\mathrm{kg/m^3}]$
ρ^g_w	Density of the water vapour	$[\mathrm{kg/m^3}]$
$\rho_{s,0}$	Solid grain density at the reference temperature T_0	$[\mathrm{kg/m^3}]$
$\rho_{v,air}$	Vapour density of the drying air	$[\mathrm{kg/m^3}]$
$\rho_{v,surf}$	Vapour density of the external surface of the sample	$[\mathrm{kg/m^3}]$
$\rho^g_{w,0}$	Density of saturating water vapour	$[\mathrm{kg/m^3}]$
τ	Tortuosity	-
$\underline{\underline{K}}$	Hydraulic conductivity	$[\mathrm{m/s}]$
$\underline{f}$	Mass flow	$[\mathrm{kg/s}]$
$\underline{i}_{a,d}$	Diffusion of dissolved water inside liquid water	$[\mathrm{kg/m^2.s}]$
$\underline{i}_{a,g}$	Diffusion of the gaseous mix	$[\mathrm{kg/m^2.s}]$
$\underline{i}_{w,g}$	Diffusive flow of vapour	$[\mathrm{kg/m^2.s}]$
$\underline{q}$	Mean velocity of the phase	$[\mathrm{m/s}]$
ξ	Fluid compressibility	$[\mathrm{Pa}]$
c_p	Storage coefficient	$[\mathrm{kg/m^3}]$
$c_{p,i}$	Specific heat of the constituent i	$[\mathrm{J/kg.K}]$
D^v_a	Diffusion coefficient of the dry air inside the water vapour	$[\mathrm{m^2/s}]$
H_a	Henry's constant for air	-

k	Intrinsic permeability of the porous medium	$[\mathrm{m}^2]$
K_l^a	Constant from the Henry's law	-
k_r^w	Water relative permeability	$[\mathrm{m}^2]$
p_i	Pressure of the phase i	$[\mathrm{Pa}]$
Q	Fluid flow rate	$[\mathrm{m}^3/\mathrm{s}]$
Q	Term of production/consumption of heat	$[\mathrm{J}/\mathrm{m}^3.\mathrm{s}]$
q	Specific fluid flow rate	$[\mathrm{m}^2/\mathrm{s}]$
S	Storage term	$[\mathrm{kg}/\mathrm{m}^3]$
S_T	Enthalpy of the system	$[\mathrm{J}/\mathrm{m}^3]$
T_{surf}	Temperature of the surface of the sample	$[\mathrm{K}]$
v	Fluid flow rate per unit area or Darcy's velocity	$[\mathrm{m}/\mathrm{s}]$
V_T	Heat flux	$[\mathrm{J}/\mathrm{m}^2.\mathrm{s}]$
X^g	Gas mass fraction	-
x_l^a	Molar fraction of dissolved air	-
z	Water level (height)	$[\mathrm{m}]$

Experimental Approach

A	Cross-sectional area of the sample	$[\mathrm{m}^2]$
H	Height of the sample	$[\mathrm{m}]$
i	Hydraulic gradient	-
$K(10^{\circ}\mathrm{C})$	Saturated water conductivity at $10^{\circ}\mathrm{C}$ (reference for water tables)	$[\mathrm{m}/\mathrm{s}]$
K_{sat}	Saturated water conductivity	$[\mathrm{m}/\mathrm{s}]$
P_{int}	Internal pressure	$[\mathrm{bar}]$
Q	Discharge	$[\mathrm{m}^3/\mathrm{s}]$

Part I

LITERATURE REVIEW

1 General Introduction

Contents

1.1 Introduction

Concrete is the most used building material in the construction industry, with a production estimated to be about 1 billion tons/year in the European Union [Eurostat, 2014].

Natural Aggregates (NA) are one of the main ingredients of concrete, whose production reached about 2.8 billion tons in Europe in 2017 [UEPG, 2018]. Within this frame, natural aggregates may become a scarce resource and its availability becomes therefore an important question.

Furthermore, environmental concerns regarding the construction industry have risen, particularly related to CO_2 emissions and waste production from the construction and demolition sector (C&D Waste). For example, C&D waste account for about 25-30% of all waste generated in the EU [European Commission, 2019], that is 374 million tons in 2016 (excluding excavated soil) [European Environment Agency, 2020].

That's why the construction industry needs to develop and implement processes able to incorporate recycled products into its building materials. Recycled Concrete Aggregates (RCA) produced from crushed C&DW as a replacement of natural aggregates is one of those solutions which has made it a thoroughly studied field.
RCA consist of coarse particles containing natural aggregates as well as residual adherent cement paste which usually impairs negatively their properties compared to NA.

This recycling process has the potential to, at first, decrease the amount of C&DW to be landfilled and, on the other hand, preserve natural aggregates resources.

At the moment, RCA are only used in basic engineering applications and usually downcycled. Indeed, the poor knowledge of this material creates doubts about its durability and resistance. Therefore, the market (demand) is insufficient to meet the deposits (offer) and the recycling process is then poorly developed. The apprehension to use RCA in construction is comprehensible: it is a new building material which still needs to prove its capabilities and to do so, models and experimentations are required. Moreover, the durability is essential in construction as most of the new buildings are expected to last at least a century.

Therefore, the use of a building material of poorer quality, whose durability is not well known at this stage, may be frightening.
Indeed, the main obstacle to using RCA in concrete is regulation: recycled materials are new on the market and are therefore rarely used, which leads to a lack of specification. And this lack of specification prevents the use of this material, forming a loop [Courard, 2018].

Hence the scope of this thesis is to study properties of concrete with recycled concrete aggregates, and more specifically the drying phenomena happening in this porous media.
Indeed, water is the root of all evils when speaking of concrete durability, and many degradation processes require water or humidity to take place. Modelling the drying processes, first, allows a better understanding of the water migration processes inside the porosity of concrete and may give, on the other hand, an indication of the durability of concrete.

Drying (and moistening) of concrete is a complex phenomenon that requires experimental devices as well as modelling: temperature and relative humidity of the environment play an important role in this phenomenon, but also the porous structure in terms of shape and pore diameter [Ollivier & Torrenti, 2008].
Those phenomena and the influence of the parameters are essential and must be understood to explain major durability issues as the properties and performance of concrete are inextricably related to its moisture history [Parrott, 1988]. Furthermore, the presence of liquid water in the pores of the concrete plays an important role in the transfer possibilities because it favours the penetration of ionic species whereas it opposes the penetration of gases [Ollivier & Torrenti, 2008].
Indeed, carbonation and chloride attacks are the two most important causes of degradation in concrete and they both require the penetration of ionic species: carbonation requires CO_2 for the formation of carbonic acid, which is an intermediate stage in the carbonation of portlandite, while the chloride attacks require O_2 for the formation of rust. The understanding and predictability of the durability of concrete therefore rely on the understanding of those drying and wetting cycles.

1.2 Information about Recycled Concrete Aggregates

Recycled concrete aggregates are produced through crushing of concrete that was obtained by demolition of old concrete structures. Various fragmentation techniques are available [Salomao, 2019]:

- Impact crusher with horizontal or vertical axis;
- Jaw crusher;
- Cone crusher.

They all have their advantages and drawbacks, more specifically in terms of aggregates' size and morphology, production of fines and energy consumption [Salomao, 2019].

RCA are embedded in a hardened, porous and cracked cement matrix, which has a higher water absorption capacity than natural aggregates [Hussain et al., 2000]. This is mainly due to the traditional fragmentation techniques used, which work by grinding and are therefore not selective.

New techniques are developed based on the minimisation of intra-granular breaks to produce mono-mineral particles with a particle size distribution close to that of natural aggregates, namely [Salomao, 2019]:

- Grinding;
- Micro-wave treatment;
- Heating treatment;
- Electro-dynamic fragmentation;
- High performance sonic pulses.

These new techniques have the potential to release the natural aggregates from the hardened cement paste, resulting in better quality RCA, but are unfortunately not industrially viable at the moment.

Various internal parameters impact the amount of residual cement paste in RCA, among which are the initial paste content and the properties of this cement paste, as well as the mechanical quality of the transition zone (ITZ) at the interface between the initial aggregates and the cement paste [Belin et al., 2014]. The crushing process and considered particle size of the RCA are considered external parameters [Belin et al., 2014].
Moreover, chemical compatibility issues between the new paste and the residual one into RCA may appear, as the presence of sulphate, for example [Belin et al., 2014].

The main property of interest regarding RCA, with respect to this thesis, is their water absorption. Water absorption ranges from 3 to 12%, which is significantly higher than the values obtained for NA, ranging from 0.5 to 2.0% [Belin et al., 2014]. A general rule obtained from experimental data is that when cement paste content increases, water absorption increases too [de Juan & Gutiérrez, 2009]. Therefore, the greater the RCA content in concrete, the bigger the water absorption and water porosity [Gómez-Soberón, 2002], which in parallel decreases the durability of said concrete [Guo et al., 2018].
Water absorption is correlated with morphological and mechanical properties of aggregates [Deodonne, 2015]. Indeed, the negative effects of RCA are more obvious for fine aggregates than for coarse aggregates [Guo et al., 2018], mainly because recycled fine aggregates are composed of more cement paste than coarse ones in which there is a part of old NA. In addition to this, larger aggregates have a smaller specific surface area and therefore adsorb less water during mixing, which results in a smaller W/C ratio required for the workability and therefore smaller porosity and water absorption.

However, it has been proven that the bigger the aggregate is, the greater gas permeability is. This is due to two possible reasons: the tortuosity of the flow path inside concrete decreases with the increase of the size, and the possibility of bleeding (creation of an Interfacial Transition Zone) decreases with the size of RCA used [Guo et al., 2018].

1.3 About circular economy

Today's economy is described as a linear take-make-consume-dispose economic model, based on the assumption that natural resources are indefinitely available. However, we all

know it is not the case and that we are reaching boundaries. Therefore, a new economic model was developed: the circular economy aims to be restorative in nature, maintaining the utility (and value) of the materials for as long as possible. A comparison of both economic models is shown at the Figure 1.1.
Circular economy thus decreases the need for new virgin materials and energy, hence *"reducing environmental pressures linked to resource extraction, emissions and waste management"* [European Environment Agency, 2020].

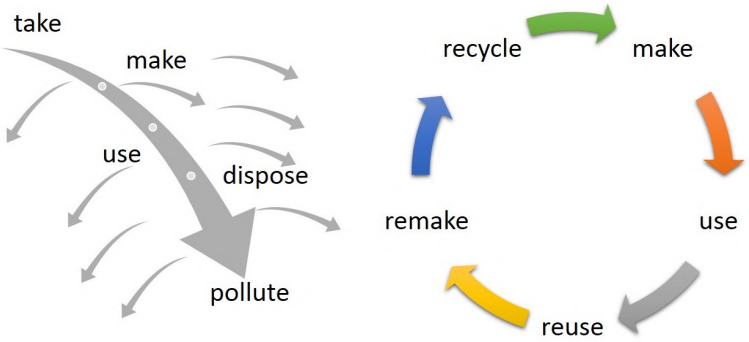

Figure 1.1: Linear versus Circular economy [Wikipedia, 2020a]

In order to achieve a circular economic model, recycling must take place. Recycling is part of the waste treatment strategy called 3R [Courard, 2018]:

1. Reduce: reduction of waste production (the best waste is the one that has not been produced);
2. Reuse: give a new use to a used product (same use);
3. Recycle: treat waste by recycling (different uses).

The awareness of limits is what promotes recycling. It is the essence of the circular economy: we live in a limited world, with limited:

- Energy;
- Raw materials;
- Land use (space);
- Adaptability of nature: the environment is able to regenerate waste but very slowly, leading to saturation of the environment.

In order to better promote a circular economy, policymakers must intervene and facilitate the uptake of circular economy actions, in our case to improve C&DW management. The European Environment Agency (EEA) gave generic examples to better illustrate the policies available, among which [European Environment Agency, 2020]:

- Introduce "green taxes" to help secondary materials be competitively priced;
- Standardisation of the treatment and production of secondary raw material, at a national or even EU scale;
- Research and development of technological solutions focusing on developing a circular economy.

1.4 Objectives

The scientific question this master thesis tries to answer is the following: "Is the use of recycled concrete aggregates inside concrete affecting its durability?" The answer to this question will be found through a better understanding of the material. Indeed, an extensive experimental programme will be conducted. Then, modelling of the various transport and drying phenomena inside concrete will be performed to promote the use of RCA in concrete, allowing the prediction of a possible loss of durability of concrete produced with recycled concrete aggregates. Indeed, as the state of the art will cover later in this thesis, there is little research done in the field of modelling the drying phenomena happening in concrete made from RCA.

The modelling will be performed in a nonlinear finite elements software developed at the University of Liège (called Lagamine). It follows the theory of nonlinear finite elements modelling of flows in porous media and consists of a coupled thermo-hydraulic study of the material.

As for any good modelling program, it will be supported by the experimentation conducted in this master thesis: sorption and desorption experiments as well as a porosity and water permeability determination, will be implemented. Therefore, the results but also the various parameters required for the modelling will be linked to experiments done in the laboratory.

To better study the influence of the RCA, several concrete mixes will be studied: a reference composition with natural aggregates and the same composition with RCA (same granulometric curve), a mix with natural aggregates but another cement type and, finally, a mortar without any aggregates. The three concrete compositions have the same paste content and type as it highlights the influence of the change of aggregates/cement type.

1.5 Outlines of this thesis

This master thesis is divided into three major parts, starting with a literature review followed by an experimental campaign and some numerical modelling and ending with results analysis.

The literature review starts with the theory of concrete. The composition of this construction material is introduced, from the chemistry of cement and the reactions happening during the hardening of concrete, to the different types of aggregates. Then, the porous structure of this material is examined, from the different pores systems to the parameters influencing the porosity. Finally, this chapter ends by laying down the theory of the porous media that can be applied to concrete to model complex drying phenomena.

Once the fundamentals of concrete and its porous system are introduced, the drying processes can be examined. First, several drying processes used experimentally are discussed and then, we focus on the particular case of drying that is convective drying and the drying kinetics tied to it. The drying rate is defined and the Krischer curve is addressed through the three distinct periods that define convective drying: the preheating period, the constant rate period and finally, the falling rate period.

The end of this chapter marks the transition from the literature review to the modelling and experimentation part. To start with, the modelling of water transfer in concrete is introduced. This chapter starts by laying down the state of the art concerning several models of moisture migration as well as their possible application to concrete made from recycled concrete aggregates. Then, the actual model used in this thesis and the equations that govern it are discussed. The thermal and hydraulic equilibrium are also expressed as well as the coupling between them and, finally, the boundary layer model will be introduced.

Following the explanation of the model, the experimental approach of this thesis is laid down. This chapter starts with the composition of our test concretes and mortars, and then the explanations of the various experiments conducted are presented. Those consist of vapour control drying and convective drying experiments, as well as tests to determine the water permeability, porosity, water absorption among other key modelling parameters of concrete.

The final part of this thesis is the analysis of the results obtained from the experimentations as well as from several simulations. Indeed, the multiple experiments conducted are analysed to determine the values of key parameters used in our model. Then, the modelling starts with a sensibility analysis on those parameters. After that, a validation of the model is undertaken based on the convective drying's results obtained. Finally, an application will be proposed, consisting of a column subjected to real external conditions in terms of relative humidity and temperature cycles.

This thesis ends with a discussion of the results between the concrete made from natural aggregates and the one made from recycled concrete aggregates, leading to a conclusion and a vision of the work still to be done in order to further improve this research.

2 | Concrete: a Porous Media

Contents

2.1 Introduction

This master thesis investigates properties of concrete which is a complex building material. To better understand these properties, this chapter will cover the theory of this material. To start with, the composition of concrete is laid down, from the chemistry of cement and the reactions happening during the hardening of concrete, to the different types of aggregates.

Once the various constituents of concrete have been thoroughly studied, the porous structure of this material will be explained. Indeed, concrete is a multiphasic material which also contains a liquid phase composed of a mixture of air and water vapour [Ollivier & Torrenti, 2008]. This liquid phase therefore creates a complex porous structure which is worth to be examined. From the different pores systems to the parameters influencing the porosity, one will learn the complexity of the porous media that is concrete.

Finally, as the goal of this thesis is to model complex drying phenomena happening inside concrete, the theory of the porous media will be laid down to better understand the concepts behind it. The theory of mixture will be introduced first, followed by the concepts of capillarity and then suction. To finish with, the water retention curves and their analogue, the sorption isotherms, will be described and their use in this thesis will be justified.

2.2 Composition of concrete

Concrete is a building material whose primary constituents are water and cement (the two forming mortar) as well as sand and aggregates that increase its resistance. For one cubic metre of concrete, a standard composition is [Courard, 2018]:

- 1300 kg of aggregates (50% by volume);
- 650 kg of sand (25% by volume);
- 325 kg of cement (10% by volume);
- 170 kg of water (15% by volume);

resulting in a density of 2400 $\mathrm{kg/m^3}$.

Concrete is a multiphasic material whose internal structure is heterogeneous, consisting of coarse aggregates embedded in a mortar matrix itself made of fine aggregates, hydrated and unhydrated cement and finally the pore system [Winslow et al., 1994][Kumar & Bhattacharjee, 2003]. Concerning the pore system, the one that is present in the mortar matrix of concrete is different from the one found in plain mortar whose proportions of the relevant ingredients are identical. This is due to the Interfacial Transition Zone (ITZ), that is the transition zone between the aggregates and the cement paste [Kumar & Bhattacharjee, 2003]. Furthermore, it has been shown through mercury intrusion porosimetry that the paste in concrete contains larger pores with a higher degree of connection than plain cement paste [Winslow et al., 1994].

2.2.1 Constituents of concrete

2.2.1.1 Cement

Cement is a binder, i.e. it ensures cohesion between inert elements. It consists of a fine powder with hydraulic properties: it hardens in the presence of water (whether it is underwater or in the air) to form a water-insoluble substance [Courard, 2017]. Hydraulicity is the ability of a product to set and harden in the presence of water with the formation of stable compounds.

The main components of the Portland cement (Table 2.1), which is the basis for most cement, are tricalcium and dicalcium silicates ($\mathrm{C_3S}$ and $\mathrm{C_2S}$), as well as the aluminate and ferroaluminate of calcium ($\mathrm{C_3A}$ and $\mathrm{C_4AF}$ respectively) [Courard, 2017] [Bertolini et al., 2004].
In the chemistry of concrete and cement, abbreviations are used: S ($\mathrm{SiO_2}$), A ($\mathrm{Al_2O_3}$), F ($\mathrm{Fe_2O_3}$), H ($\mathrm{H_2O}$), $\bar{\mathrm{S}}$ ($\mathrm{SO_3}$) and C (CaO).

As mentioned previously, the compounds of Portland cement react with water to form hydrated products of very low solubility.
The first components to react are aluminates, which are responsible for the solidification of the cement paste: the hydration of $\mathrm{C_3A}$ and $\mathrm{C_4AF}$ creates, in presence of gypsum, hydrated sulfoaluminates of calcium.
The development of strength that follows solidification, called hardening of the cement paste, is governed by the hydration of silicates $\mathrm{C_2S}$ and $\mathrm{C_3S}$ that gives rise to calcium silicate hydrates forming a rigid gel indicated as CSH [Powers, 1958][Bertolini et al., 2004]:

$$\mathrm{C_3S + 6H \rightarrow C_3S_2H_3 + 3Ca(OH)_2}$$
$$\mathrm{2C_2S + 4H \rightarrow C_3S_2H_3 + Ca(OH)_2}$$

Name	Chemical formula	Abbreviations	Percentage by mass
Before clinkerization process			
Calcium oxide (Quicklime)	CaO	C	65%
Silicon dioxide (Silicate)	SiO_2	S	20%
Alumina	Al_2O_3	A	10%
Iron trioxide	Fe_2O_3	F	5%
After clinkerization process			
Tricalcium silicate	$3CaO.SiO_2$	C_3S	60%
Dicalcium silicate	$2CaO.SiO_2$	C_2S	20%
Tricalcium aluminate	$3CaO.Al_2O_3$	C_3A	10%
Tetracalcium ferroaluminate	$4CaO.Al_2O_3.Fe_2O_3$	C_4AF	8%
Gypsum	$CaSO_4.H_2O$	$C\bar{S}$	2%

Table 2.1: Main constituents of the Portland cement [Bertolini et al., 2004][Courard, 2017]

CSH is composed of extremely small gel particles with a high surface area, giving considerable strength to the cement paste, but it also consists of interstices between those particles, called gel pores. It represents approximately 50-60% of the volume of the completely hydrated cement paste. A model describing its structure is shown at the Figure 2.1.
Hydration of the calcium silicates may also produce hexagonal crystals of calcium hydroxide $Ca(OH)_2$ called Portlandite, which occupy 20 to 25% of the volume of solids. However, they do not contribute to the strength of the cement paste [Bertolini et al., 2004].

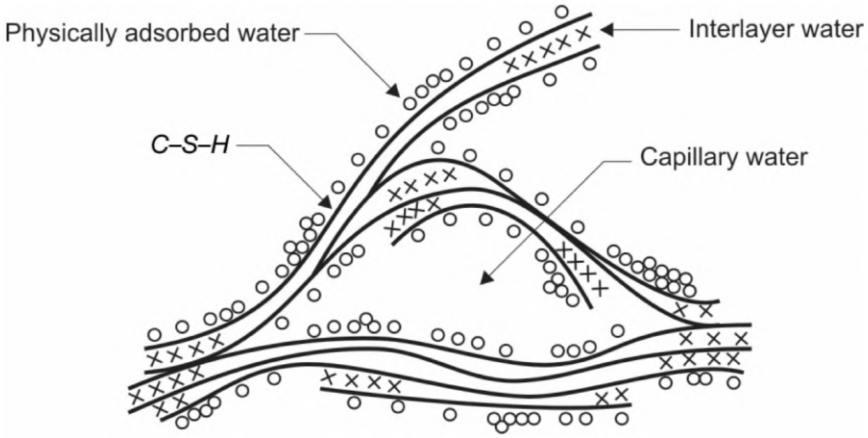

Figure 2.1: Feldman–Sereda model for C–S–H [Bertolini et al., 2004]

Besides Portland clinker, cement may also contain blast furnace slag, fly ashes, calcined shale and other by-products.

There exist several types of cement on the market (see Figure 2.2). In Europe, we use mainly four types of cement based on their composition:

- CEM I: "pure" Portland cement;
- CEM II: Portland cement with either blast furnace slag (S), fly ashes (V), limestone (L) or a mix of those (M);
- CEM III: blast furnace cement (S);
- CEM V: compound cement.

Besides being referred to with their composition, we also precise the amount of substitution material the cement possesses. For example, a CEM III A will have between 36% and 65% (in mass) of blast furnace slag.
Finally, the cement types are divided in three categories of resistance, depending on the grain fineness: 32.5, 42.5 or 52.5 MPa after 28 days of curing.

Aside from those cements, there also exist special cement such as Low Alkali (LA) cement, High Sulphate Resisting (HSR) cement, ... but those won't be presented here as they are not considered for this research.

CLASSIFICATION ET COMPOSITION DES PRINCIPAUX CIMENTS DE LA NORME EN 197-1

Types	Différentes désignations		Constituants principaux en %							
			Clinker K	Laitier de haut fourneau S	Fumée de silice D	Pouzzolane P ou Q	Cendres volantes V ou W	Schiste calciné T	Calcaire L ou LL	Constituants secondaire
CEM I	Ciment Portland	CEM I	95-100	-	-	-	-	-	-	0-5
CEM II	Ciment Portland au laitier	CEM II/A-S	80-94	-	-	-	-	-	-	0-5
		CEM II/B-S	65-79	-	-	-	-	-	-	0-5
	Ciment Portland fumée de silice	CEM II/A-D	90-94	-	6-10	-	-	-	-	0-5
	Ciment Portland à la pouzzolane	CEM II/A-P	80-94	-	-	6-20	-	-	-	0-5
		CEM II/B-P	65-79	-	-	21-35	-	-	-	0-5
		CEM II/A-Q	80-94	-	-	6-20	-	-	-	0-5
		CEM II/B-Q	65-79	-	-	21-35	-	-	-	0-5
	Ciment Portland aux cendres volantes	CEM II/A-V	80-94	-	-	-	6-20	-	-	0-5
		CEM II/B-V	65-79	-	-	-	21-35	-	-	0-5
		CEM II/A-W	80-94	-	-	-	6-20	-	-	0-5
		CEM II/B-W	65-79	-	-	-	21-35	-	-	0-5
	Ciment Portland au schiste calciné	CEM II/A-T	80-94	-	-	-	-	6-20	-	0-5
		CEM II/B-T	65-79	-	-	-	-	21-35	-	0-5
	Ciment Portland au calcaire	CEM II/A-L	80-94	-	-	-	-	-	6-20	0-5
		CEM II/B-L	65-79	-	-	-	-	-	21-35	0-5
		CEM II/A-LL	80-94	-	-	-	-	-	6-20	0-5
		CEM II/B-LL	65-79	-	-	-	-	-	21-35	0-5
	Ciment Portland composé	CEM II/A-M	80-94	6-20						0-5
		CEM II/B-M	65-79	21-35						0-5
CEM III	Ciment de haut fourneau	CEM III/A	35-64	36-65	-	-	-	-	-	0-5
		CEM III/B	20-34	66-90	-	-	-	-	-	0-5
		CEM III/C	5-19	81-95	-	-	-	-	-	0-5
CEM IV	Ciment pouzzolanique	CEM IV/A	65-89	-	11-35			-	-	0-5
		CEM IV/B	45-64	-	36-55			-	-	0-5
CEM V	Ciment composé	CEM V/A	40-64	18-30	-	18-30	-	-	-	0-5
		CEM V/B	20-38	31-50	-	31-50	-	-	-	0-5

Figure 2.2: Definition of the cement types according to the standard EN 197-1 [Courard, 2018]

2.2.1.2 Water

The use of water in concrete is necessary for the hydration reaction of the cement particles. However, we cannot use any type of water as waste water or sea water contain suspended matter and dissolved salts that will bind to the cement grains and slow the reaction. Therefore, the water must be of good quality (see standard NBN EN 1008), and will often be tap water.

2.2.1.3 Aggregates

An aggregate is a building material which is inert with its environment. It is possible to distinguish several types of aggregates, as it has already been mentioned [Courard, 2018]:

- Natural aggregate: of mineral origin and that has only undergone a mechanical treatment (crushing, sieving, etc.);
- Artificial or industrial aggregate: of mineral origin and resulting from an industrial process such as a heat treatment (e.g. industrial residues);
- Recycled aggregate: originates from the treatment and transformation of inorganic materials that have already been used in construction.

Aggregates are classified according to their size, D being the biggest diameter of the grain [Courard, 2018]:

- Filler: $D \leq 0.063$mm;
- Sand: $D \leq 4$mm;
- Big aggregate: $D \geq 4$mm;
- Gravel: $D \geq 6.3$mm.

Finally, depending on their origin, they may be considered as rolled aggregates or crushed aggregates, the latter being harder to process. Indeed, the angular shape of the aggregate increases its resistance to movement resulting in a poorer workability.

When using aggregates, the most important property is the granulometry as the composition of concrete relies highly on this characteristic. As a matter of fact, a concrete of better quality is a concrete with fewer pores, and therefore using a continuous granulometry increases the compactness of the concrete mix, decreasing its porosity. A granulometry is said to be continuous when every size of grain, in between the lower and upper limits, is represented equally.

2.3 Porous structure of concrete

Concrete is a multiphasic material: the aggregates, hydrates and unhydrated parts of the cement constitute the solid phase. The liquid phase consists of the interstitial solution while the gas phase is a mixture of air and water vapour [Ollivier & Torrenti, 2008]. It is shown schematically at the Figure 2.3.

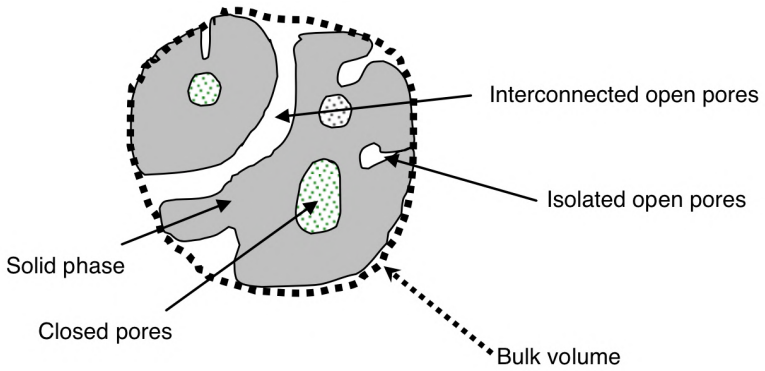

Figure 2.3: Schematic description of concrete: a porous material (translated from [Ollivier & Torrenti, 2008])

As it has been presented in the Section 2.2.1 related to the constituents of concrete, the grains of cement react with water. The quantity of water chemically fixed by cement accounts for approximately 25% of the cement mass used in the composition, depending on the cement type and hydration degree of the constituting grains. This water then undergoes a morphological transformation which reduces its volume by 25%, resulting in small pores scattered all around the cement mass, called "gel" pores [Courard, 2017].

2.3.1 Types of pores in concrete

Concrete has various types of pores: open porosity which is linked to the surface and closed porosity which isn't. Only the open porosity may be filled with water coming from the environment [Courard, 2018].

The various types of pores mentioned here above are, from the smallest to the coarsest one [Apers & de Schutter, 2018]:

- "Gel" pores due to the hydration reaction of the cement grain, the volume of the product being smaller than the volume of the reagents;
- Capillary pores from excess water not required by the hydration reaction;
- Pores due to internal (endogenous) shrinkage which are of a size relatively similar to capillary pores. These are important in the freeze-thaw resistance of concrete;
- Pores of the aggregates which have less influence on the transport mechanisms as they are often discontinuous;
- Internal micro-cracks due to shrinkage, creep, freezing, and so on which are often located in the interfacial transition zone. As those are tortuous and rarely interconnected, they do not play an important role in the transport mechanisms;
- Volume due to occluded air or entrained air;
- External cracks due to a restrained shrinkage, overloading ... .

Regarding the durability of concrete, capillary pores are the most important ones. Indeed, capillary pores filled with excess water (that is less connected to cement grains), are bigger

than the pores resulting from the hydration process, hence their greater role in the degradation of concrete.

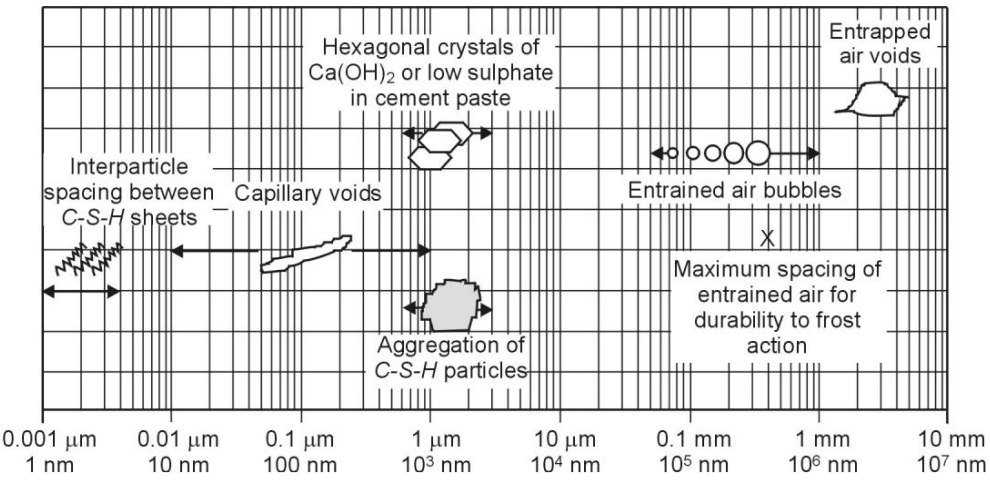

Figure 2.4: Distribution of pores according to size [Bertolini et al., 2004]

The accessible pores can potentially be filled with water. Indeed, water is present in the hydrated cement paste under various forms, classified from the easiest to the hardest form to remove [Bertolini et al., 2004]:

- Capillary water: the water contained in the capillary pores accounts for the major part of the water in concrete. According to the Jurin law, as those pores are the biggest, the water they contain is the least energy-consuming to remove.
- Adsorbed water: once the capillary water has been removed from the concrete, some water still remains adsorbed to the inner surface in the form of a very thin layer of adsorbed water. This thin layer of water can be removed if the external humidity drops below 30%, and requires more energy as the contact forces are greater the closer you are to the surface of the solid.
- Interlayer water: the CSH layers also retain water in between them, which can only be removed if the relative humidity drops below 11%.

In addition to these forms, which are removable from the concrete without reaching extreme temperature, there also exists water chemically bonded to cement and concrete constituents [Zingg, 2013].

Under equilibrium conditions and in the absence of wetting, the water content of a concrete exposed to the atmosphere is related to the relative humidity (RH) of its environment (as it will be covered in depth in the Section 2.4.2). Therefore, as the RH increases, more and more water fills the capillary pores: water is first adsorbed on their surface then condensates and fills up the pores, starting from the smallest to the largest [Bertolini et al., 2004].
The Figure 2.5 represents the capillary pores as spherical cavities connected by small capillary cylinders, whose dimensions are considered statistically distributed. Only open porosity is represented as water cannot reach closed porosity. This diagram shows that pores whose diameter is below a specific value are filled with water while others are partially filled with air and adsorbed water [Bertolini et al., 2004].

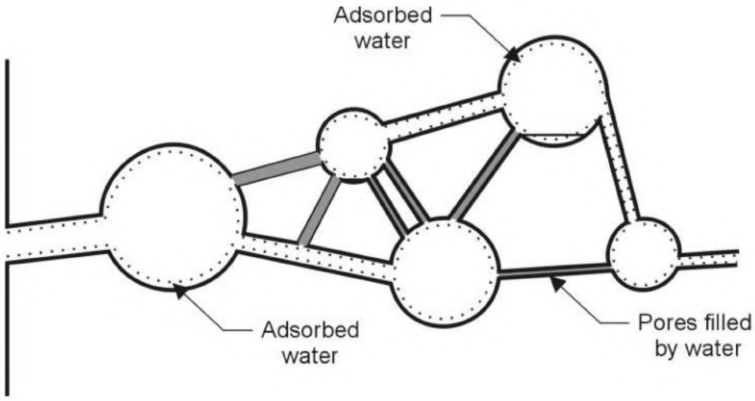

Figure 2.5: Representation of water present in capillary pores in concrete in equilibrium with a non-saturated atmosphere [Bertolini et al., 2004]

2.3.2 Transport phenomena

The three main types of transport mechanisms in concrete are permeation, diffusion and capillary adsorption, that are to be explained thereafter. Permeation and capillary absorption involve mechanical forces (gravity, pressure potential, etc.) while diffusion requires chemical forces (osmosis, difference in concentration, etc.) [Courard, 2018].

Permeability is a measure of the ability of a fluid to penetrate and migrate inside a porous system. The main condition to have permeation is the presence of voids and pores. However, those must be connected into open porosity [Apers & de Schutter, 2018].

Diffusion is due to a difference of relative humidity between two points of the medium or between the concrete and the environment. This difference in relative humidity and temperature results in a pressure difference, forcing water vapour into the pores until the properties of the air inside and outside the solid are equal in terms of temperature and relative humidity. Once the water vapour enters the pores, it transforms into liquid water by condensation and adsorption at the capillary surfaces [Apers & de Schutter, 2018].

Another transport phenomena discussed before is capillary adsorption: when a pore is in contact with a water surface, adsorption causes the formation of a meniscus rising up the walls of the pore [Apers & de Schutter, 2018]. The suction force resulting from this meniscus formation is inversely proportional to the pore diameter, but the speed at which the water rises is proportional to the square of the diameter.

Transport phenomena are influenced by [Courard, 2018]:

- Connectivity of porosity: the larger the porosity, the greater the connectivity is, increasing the permeability through opening of pores. Moreover, if the water-to-cement ratio is higher than 0.7, connectivity is impossible to avoid.
- Pore constrictivity: constrictivity is a parameter that qualitatively reflects the cross-sectional variation that pores offer to flow [Ollivier & Torrenti, 2008]. Low constrictivity means that there may be fewer pores but, at equal porosity, those pores will be of

higher volume. As in hydraulic theory, there will be less pressure drop in a large capillary than in multiple fine capillaries. Therefore, a low constrictivity (large capillaries) leads to a higher permeability.

- Porosity: the larger it is, the greater the permeability is. However, only the open porosity allows transport phenomena. Moreover, the pores must be of a diameter at least equal to the size of the molecules of water, that is approximately 0.3 nm [Apers & de Schutter, 2018].

- Tortuosity: the more tortuous the capillaries are, the longer they will be for the same separation distance between the start and the end. This again leads to higher pressure drops. Therefore, a low tortuosity leads to a high permeability. In addition, the faster the water evaporates when the concrete sets, the straighter the capillaries will be.

2.3.3 Parameters influencing the porosity

The first parameter that comes to mind while speaking of porosity in concrete is the water-to-cement ratio. Indeed, it is due to the capillary pores whose creation is promoted by excess water not required for the hydration process. The bigger the W/C ratio is, the more porosity there will be as more water will evaporate during curing of concrete, as it is expressed in the Figure 2.6. Moreover, a greater W/C ratio increases connectivity of the pores, resulting in a more open porosity [Courard, 2018][Apers & de Schutter, 2018]. However, it has been shown that for a capillary porosity of less than approximately 18%, the communication between capillary pores decreases, therefore decreasing the permeability [Ollivier & Torrenti, 2008].

Hydration conditions (during the cure) are also important to limit permeability. Indeed, a sufficient cure time with high RH limits evaporation and therefore the creation of capillaries (Figure 2.7) [Courard, 2018]. Indeed, it is as essential to ensure adequate curing as to specify a low water-to-cement ratio [Dhir et al., 1989]. Moreover, the greater the curing period is and the smaller the porosity. While the cement cures, it absorbs water and creates gel pores which are of a smaller diameter than capillary pores [Apers & de Schutter, 2018], therefore closing the porosity with CSH [Bertolini et al., 2004].

In conclusion, the volume of the capillary pores (V_{cp}) in the cement paste may be linked to the quantity of water used through the water-to-cement ratio (w/c) as well as to the degree of hydration (h), particularly according to the following formula [Bertolini et al., 2004]:

$$V_{cp} = \left(\frac{w}{c} - 0.36\ h\right) \tag{2.1}$$

In our case, as we are considering concrete and not only cement paste, there are other parameters related to the presence of aggregates and the creation of the ITZ. However, the two parameters expressed above still remain the main ones.

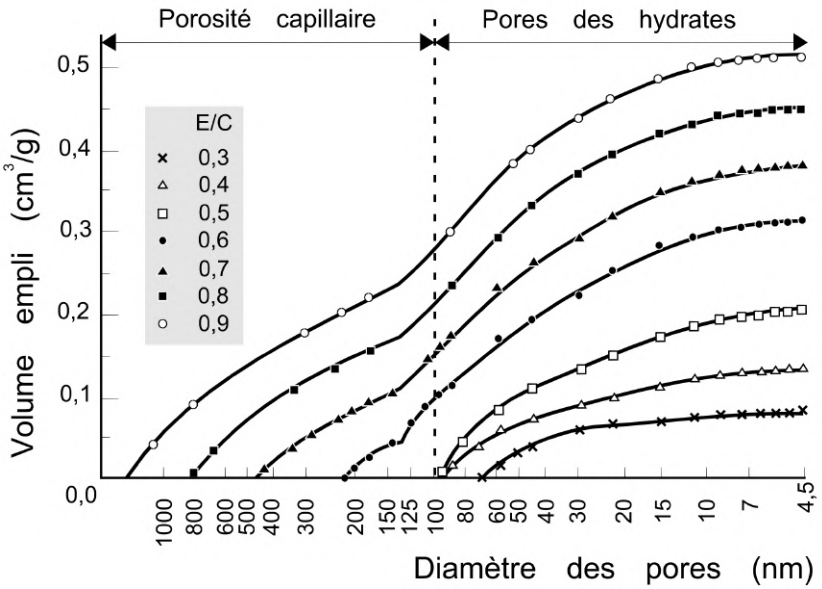

Figure 2.6: Influence of the W/C ratio on the porosimetric evolution of 28 day-old Portland cement pastes [Ollivier & Torrenti, 2008][Courard & Michel, 2014]

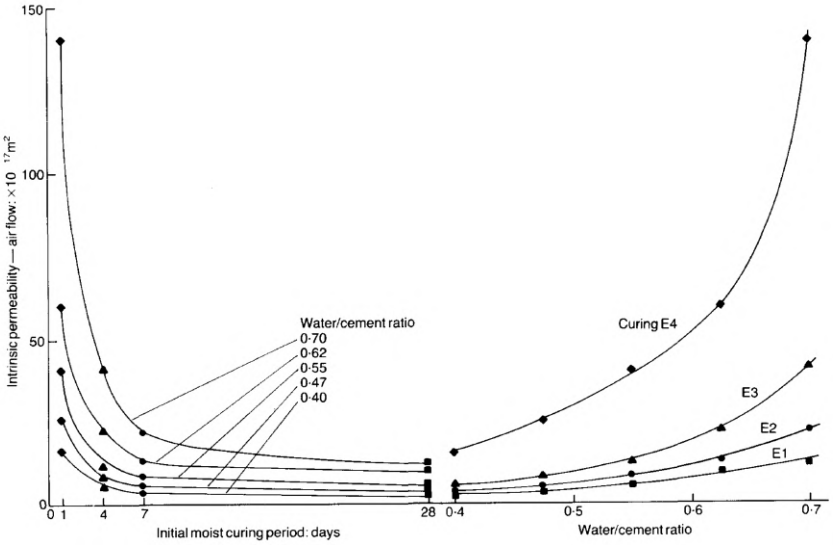

Figure 2.7: Effect of initial moist curing period and water/cement ratio on intrinsic permeability of concrete [Dhir et al., 1989][Courard & Michel, 2014]

As far as aggregates are concerned, research has proven that the larger they are, the greater the permeability will be (Figure 2.8). Indeed, the cement paste forms a zone known as the Interfacial Transition Zone (ITZ) around the aggregates. The closer you are to the contact area between the cement and the aggregate and the more hydration will be restricted by the presence of the aggregate [Courard, 2018]. The width of this zone, which is therefore highly permeable, may be estimated to be in the range of 10 to 100μm which is the same order of magnitude as the size of a grain of cement [Bentur & Odler, 1996].

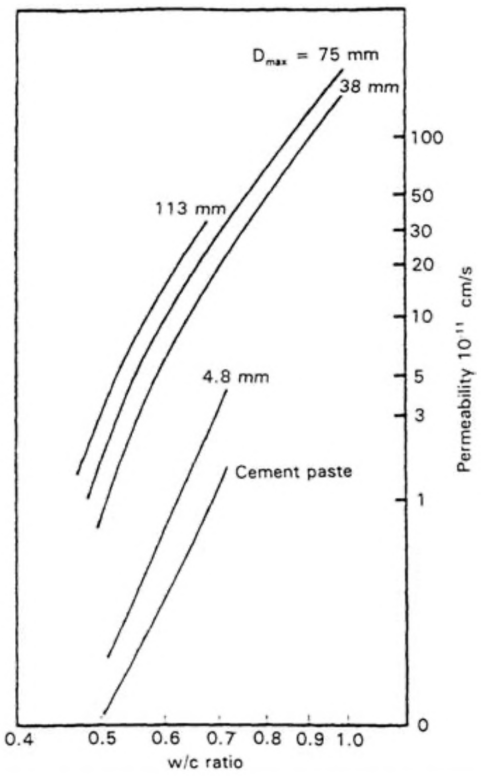

Figure 2.8: Influence of water/cement ratio and maximum aggregate size on concrete permeability [Ollivier & Massat, 1996][Courard & Michel, 2014]

The formation of the ITZ is mainly due to the formation of water-filled spaces around the aggregates of the fresh mix, i.e. the water distribution is non-uniform around the aggregates where the W/C ratio peaks locally. The non-uniform distribution may be caused by bleeding, in addition to a wall effect preventing effective filling of the space adjacent to the aggregate with cement grains of a bigger diameter than $10\mu\mathrm{m}$. This results in a zone around the aggregates which is less filled by products of the hydration reactions, generating what one can call a "hydrate malformation". This malformation, at the porosity level in the ITZ, results in a greater tendency to develop larger crystals like CH and ettringite as the pores are larger, compared to the bulk paste [Hussain et al., 2000][Mehta & Monteiro, 1988][Bentur & Odler, 1996].
An example of what the ITZ of an aggregate may look like is depicted at the Figure 2.9.

Applied to the RCA, this theory is even more significant as the transition zone of the original concrete is found in the cement matrix surrounding the recycled aggregates. Therefore, once those substitute aggregates are introduced in the cement paste to make a new concrete mix, this cement gangue further weakens the new transition zone. It has been shown that the difference in weakness between the ITZ in the reference concrete versus the one with RCA increases as the difference in porosity between the NA and RCA increases [Hussain et al., 2000].

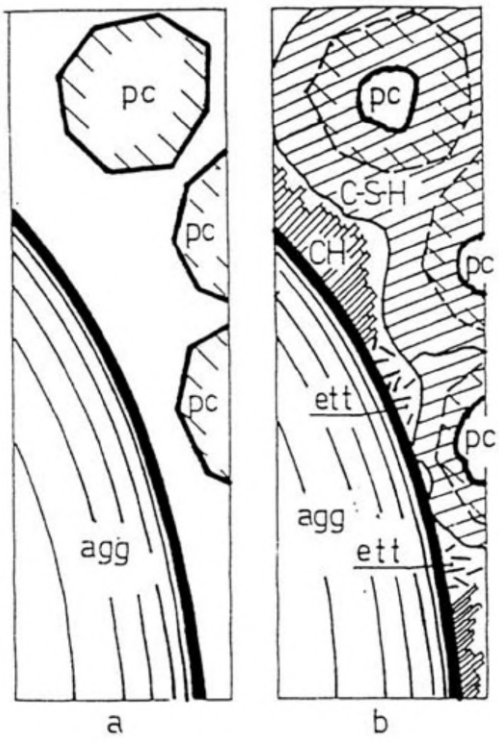

Figure 2.9: Schematic description of the mode and nature of formation of the ITZ around aggregates in a cementitious mix, before (a) and after (b) hydration of the cement particles. Before, the fresh concrete exhibits a water-filled space due to bleeding, while after the ITZ is partially filled with CH and CSH [Bentur & Odler, 1996]

2.4 Theory of the porous media

Concrete is a porous medium, that is to say it contains pores. What is called the "solid phase" is the matrix or skeletal part of the material, composed of the aggregates, sand and cement. The volume in between the solid grains forms the pores.

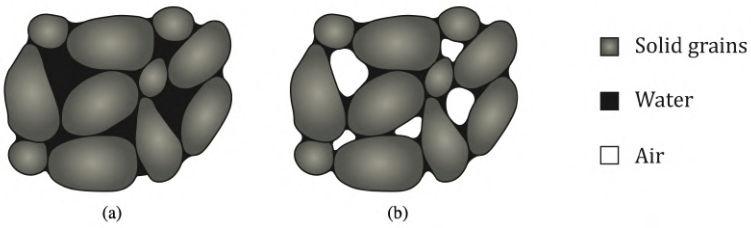

Figure 2.10: Saturated (a) and unsaturated (b) porous medium [Hubert, 2018]

A porous medium is often characterised by its porosity n, defined as the ratio of the pore volume (V_v) to the total volume of the medium (V) [Verruijt & Baars, 2007]. Another characteristic of the porous media is the void ratio (e), defined as the ratio of the pore volume to the solid volume (V_s):

$$n = \frac{V_v}{V} \quad \text{and} \quad e = \frac{V_v}{V_s} \tag{2.2}$$

A porous medium may be defined as "saturated" or "unsaturated" (Figure 2.10). In a saturated porous medium, the pores are filled by only one fluid, whereas in an unsaturated

porous medium, the porosity is filled by two fluids. Those fluids form different phases: a liquid phase (wetting fluid) and a gas phase (non-wetting fluid) [Hubert, 2018].
In concrete, the gas phase is traditionally dry air and water vapour while the liquid phase is composed of water and dissolved air [Collin & de Ville de Goyet, 2019].

Another important property of a porous medium is its degree of saturation (S_r) defined as the portion of the porosity occupied by each fluid phase, specifically regarding unsaturated medium:

$$S_{r,l} = \frac{V_l}{V_v} \quad \text{and} \quad S_{r,g} = \frac{V_g}{V_v} \tag{2.3}$$

where V_l and V_g are the volume of the liquid phase and the gas phase respectively, and V_v is the pore volume.

One approach to describe this complex system in a simplified manner is to build an idealised homogeneous continuum [Dieudonné, 2016]. Among many theories, one draws our attention: the theory of mixtures. In the theory of mixtures, the porous medium is studied at the macroscopic scale and is seen as a mixture of various incompressible phases constituting every point of the idealised system, hence, each point (in space) is occupied by a finite number of particles simultaneously, one for each constituent of the mixture [Concha, 2014].

However, the balance equations are expressed for each constituent separately [Bowen, 1980]. Within this frame, the mixture is defined as a superposition of continuous media, where each follows its own movement while respecting restrictions due to the interactions between components [Concha, 2014]. All phases are assumed to occupy the same region of space simultaneously as the overlapping of different interpenetrable continua (Figure 2.11), allowing the use of the methods of continuum mechanics [Hubert, 2018]. Therefore, each phase obeys the laws of conservation of momentum and mass, accounting for the exchange of mass and momentum between components [Concha, 2014].

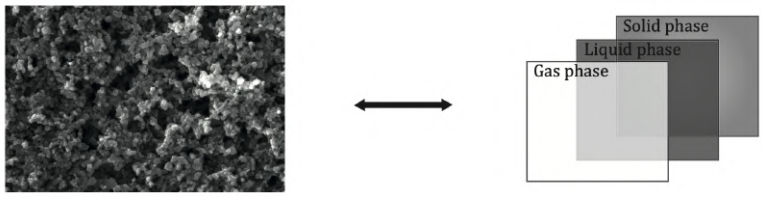

Figure 2.11: Definition of equivalent continua [Hubert, 2018]

In order to apply methods of continuum mechanics, the definition of volume fractions must be established to create homogenised continua [Hubert, 2018]:

$$\eta_i = \frac{V_i}{V} \quad \text{where} \quad \sum_i \eta_i = 1 \tag{2.4}$$

where V_i is the volume of the phase i.

The following volume fractions can be defined:

$$\eta_s = 1 - n \tag{2.5}$$
$$\eta_l = S_{r,l}\, n \tag{2.6}$$
$$\eta_g = S_{r,g}\, n = (1 - S_{r,l})\, n \tag{2.7}$$

where s, l and g correspond respectively to the solid, liquid and gas phase.

The density (ρ_i) of a given phase i is defined as:

$$\rho_i = \frac{m_i}{V_i} \tag{2.8}$$

with m_i the mass of said phase.

It was decided to use the approach of mixture theories as it allows the description of deformation of the porous medium as well as of fluid flows, heat transfer and coupled phenomena [Hubert, 2018].

2.4.1 Capillarity

Surface tensions are forces which result of the difference in intermolecular forces between different particles. For example, two immiscible fluids in contact will develop such forces between the particles at the interface and those in the fluid (Figure 2.12) [Hubert, 2018].

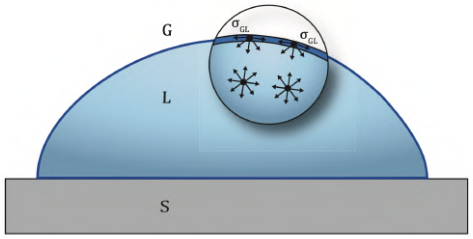

Figure 2.12: Molecular forces on a particle of water ([Collin, 2003] from [Hubert, 2018])

Those forces result from a lack of equilibrium: particles within the fluid are at equilibrium while those in the interface are not. It induces surface tensions (σ_{GL}) to restore the force equilibrium, where G is the gas phase and L is the liquid phase.

If we now add a perfectly plane solid phase S in contact with both fluids L and G (Figure 2.13), there are surface tensions σ_{SL}, σ_{GL} and σ_{SG} at the interfaces. This equilibrium is formulated with Young-Dupré's formula [Dupré & Dupré, 1869]:

$$\sigma_{SG} = \sigma_{SL} + \sigma_{GL} \cos\theta \tag{2.9}$$

where the product $\sigma_{GL} \cos\theta$ is defined as the adhesion tension and expresses which of the two fluids is more likely to wet the solid, in other words, to adhere to it and to have a tendency to spread over it [Bear & Verruijt, 1987].

The parameter θ is defined as the contact angle, that is the angle between the interface of the two fluids and the solid surface. It depends on the fluids-solid surface affinity, and it is the most widely used technique to characterise the hydrophobicity and overall surface properties of solids [Courard et al., 2011]. The higher the contact angle, the more hydrophobic the solid surface. The condition to ensure contact is:

$$\cos\theta = \frac{\sigma_{SG} - \sigma_{SL}}{\sigma_{GL}} < 1 \longrightarrow \theta < \frac{\pi}{2} \tag{2.10}$$

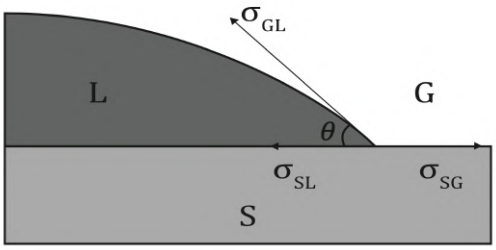

Figure 2.13: Surface tension ([Collin, 2003] from [Hubert, 2018])

There is contact if the contact angle is lower than 90°; therefore the fluid is called a wetting fluid. On the contrary, when $\theta > 90°$, the fluid is said to be a non-wetting fluid.

The capillary effect, shown in the experiment of the Figure 2.14, is caused by the surface tensions explained above. In this experiment, a capillary tube of radius r_c is immersed into a few centimetres of water and the water level rises into the tube up to a certain height, noted h_c and called the capillary pressure head. The Jurin law is able to predict this level by expressing the vertical equilibrium [Bear & Verruijt, 1987][Collin & de Ville de Goyet, 2019]:

$$h_c = \frac{p_c}{\rho_l \, g} \quad \text{with} \quad p_c = p_g - p_l = \frac{2 \, \sigma_{GL} \, \cos\theta}{r_c} \tag{2.11}$$

where p_c, p_g and p_l are the capillary pressure, gas pressure and liquid pressure respectively. One can also see the liquid density ρ_l and the gravitational acceleration g.
The smaller the radius of the capillary tube is, the higher level the water will reach as the capillary effect increases.

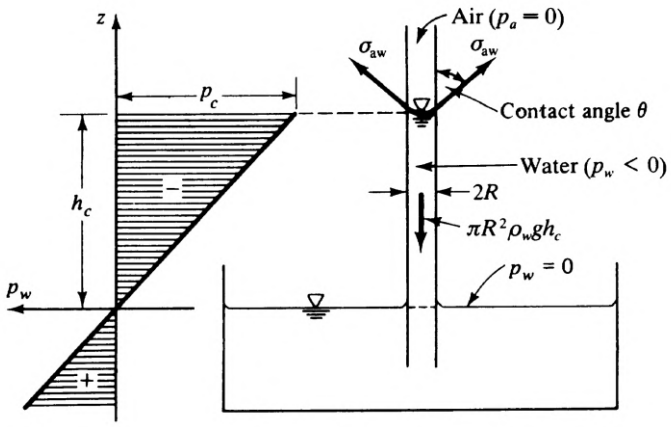

Figure 2.14: Experimental configuration [Bear & Verruijt, 1987]

This concept may be applied to unsaturated porous medium with two fluids, where the pores act like capillaries [Delage, 1987]. The capillary pressure is linked to the relative quantity of each fluid in the pore volume, i.e. with the saturation degree of the liquid phase [Hubert, 2018].

2.4.2 Concept of suction

Suction is the development of capillary menisci within the porous structure, causing a negative value of the water pressure [Delage, 1987]. The capillary pressure is a function of the

capillaries' radius, hence, as the porous material is drying, smaller and smaller capillaries are affected.

Indeed, the value of the atmospheric pressure, by convention, is assumed to be nil. Therefore, Equation 2.11 expresses that the capillary pressure is negative, and the suction increases as the capillary radius decreases.
In other words, as pores have various dimensions, they will not empty at the same suction. Therefore, the larger pores (large channels of entry) will empty for low suctions while those with narrow channels of entry will empty at higher suctions as they support interfaces of a larger curvature [Bear & Verruijt, 1987].

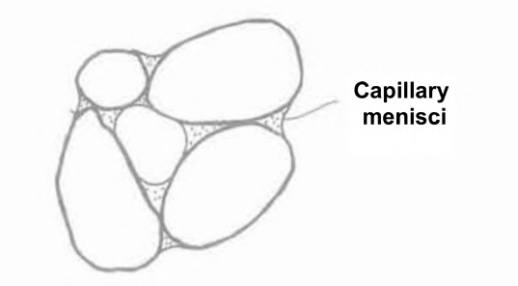

Figure 2.15: Suction phenomenon in granular structure,
showing capillary menisci [Delage, 1987]

The total suction was defined by the Jurin law in the Equation 2.11:

$$s = p_c = p_g - p_l \tag{2.12}$$

where, as a reminder, p_g and p_l are the gas and liquid pressure respectively. The total suction is related to the quantity of water stored in a porous medium through the water retention curves [Hubert, 2018]. The quantity of water may be expressed in terms of water content or saturation degree, but the latter is preferred as it already appears in the mass balance equation.

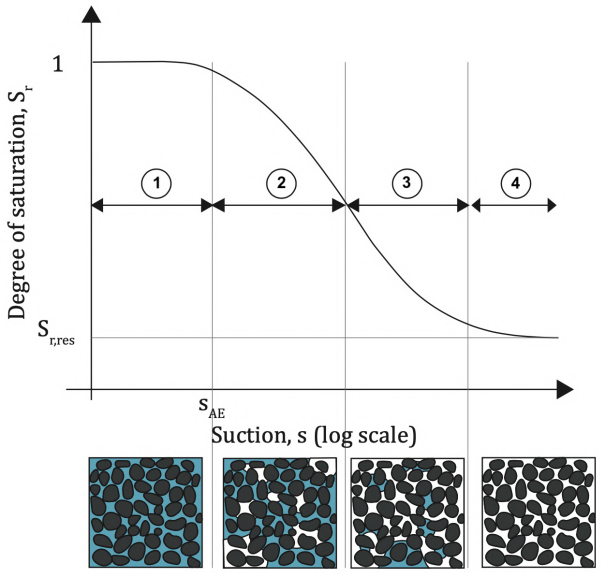

Figure 2.16: Typical water retention curve (from [Hubert, 2018])

The shape of the water retention curve depends significantly on the grain size distribution [Pap et al., 2018]. A generic water retention curve is shown at the Figure 2.16, where four domains are depicted [Hubert, 2018]:

1. If the suction is lower than the air-entry pressure, then the medium is almost if not completely saturated as no air can enter the pores and therefore no water is pushed outside. This section is almost horizontal, and is called the boundary effect zone due to the exchange happening between the surface of the sample and the environment [Pap et al., 2018][Fredlund et al., 2011];
2. Once this air-entry pressure is reached, the curve enters a funicular state where the liquid phase is continuous and the gas phase is composed of isolated bubbles. The water content is therefore largely reduced while the air content is increasing. This region is the first half of what some authors call the transition zone [Pap et al., 2018][Fredlund et al., 2011];
3. After the funicular state, neither the gas nor the liquid phase is continuous: that is the pendular state, where the liquid phase forms bonds in between the granular skeleton;
4. Finally, the last domain observed consists of a residual state where the saturation is said equal to the residual saturation degree, noted $S_{r,res}$, corresponding to the quantity of water that may never be extracted from the medium without extreme heating.

Some porous medium display a water retention curve whose shape does not fit the unimodal characteristic shown in Figure 2.16 but a rather bimodal or multimodal shape, as it can be the case for concrete (Figure 2.17). This is due to the porosity of the medium which does not feature only one pores series but also larger (macropores) and smaller pores (capillary pores) [Pap et al., 2018].
For such a porous medium, one would be able to see a plateau in the middle of the water retention curve due to the change from one pores series to another. As the water is quickly removed out of the opened macropores of the concrete for low suction, due to the gravity-driven flow, concrete's water retention curve may display one curve change for very low suction corresponding to the end of emptying of the macropores and beginning of the drying of the capillary pores.

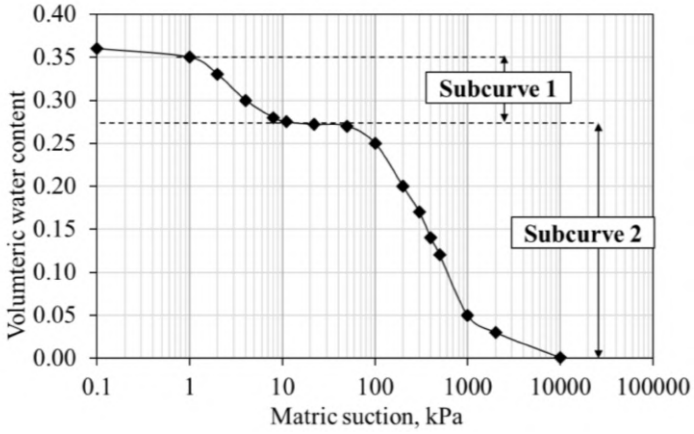

Figure 2.17: Bimodal characteristic of concrete [Pap et al., 2018]

Whether the surface is upon rewetting or during drainage, the water retention curve may exhibit different paths [Collin & de Ville de Goyet, 2019]. This phenomenon is called hysteresis and is due to two phenomena [Bear & Verruijt, 1987]:

1. the first one is called ink-bottle effect and is due to water re-entering narrow channels, requiring a local increase of suction;

2. the second effect is referred to as the raindrop effect which is simply an expression of the difference in the value of the contact angle between an advancing and receding interface.

Finally, entrapped air is also a factor causing hysteresis as liquid is required to push the air out of the porous material before rewetting.
This phenomenon is shown in the Figure 2.18 for a coarse material. The retention curve is expressed in terms of the capillary pressure head h_c instead of the suction s but the behaviour is identical. One can also see that the relationship between the two variables of the retention curve, that is the capillary pressure head and the saturation, depends on the wetting-drying history of the sample [Bear & Verruijt, 1987].

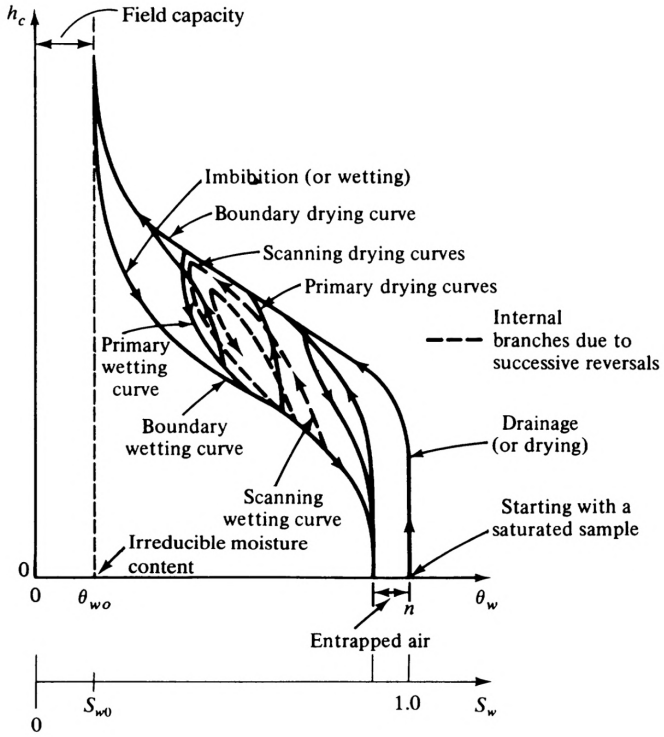

Figure 2.18: Hysteresis in the retention curve for a coarse material [Bear & Verruijt, 1987]

The water retention curve of a granular material may be determined by fitting an empirical formulation onto multiple experimental points obtained by the following analytical formulation, called the Kelvin law:

$$s = \frac{\rho_w \, R \, T}{M} \, \ln(RH) \tag{2.13}$$

where s is the suction and RH the relative humidity. The most famous empirical formulation is the one suggested by Van Genuchten [Van Genuchten, 1980]:

$$S_{r,w} = S_{res} + (S_{sat} - S_{res}) \left(1 + \left(\frac{s}{\alpha_{vG}}\right)^{n_{vG}}\right)^{-m_{vG}} \quad \text{with} \quad m_{vG} = 1 - \frac{1}{n_{vG}} \tag{2.14}$$

where n_{vG} is an adimensional model parameter linked to the rate of desaturation of the soil and m_{vG} is another adimensional model parameter associated to the curvature (slope) of

the water retention curve. The last model parameter, noted α_{vG}, is related to the air-entry pressure [Hubert, 2018]. One can finally see the maximum saturation S_{sat} and the residual saturation S_{res}, as well as the suction s.
This empirical relation is, initially, of asymptotic nature and is therefore only used to represent the water retention curve between the air-entry value and the residual value of the porous material [Fredlund et al., 2011]. This is where the terms S_{res} and S_{sat} come into play to allow the modelling of the whole curve.

2.4.3 Sorption Isotherms

For a given temperature, it is possible to link the equilibrium water content of the porous medium with the moisture content of its environment, with curves called sorption isotherms. Those sorption isotherms are analogous to the water retention curves explained before, the only difference being the x-axis which represents the relative humidity instead of the suction, those two notions being similar and linked through the Kelvin law (Equation 2.13). Nonetheless, the sorption isotherms are presented in this thesis as they offer another way of characterising the sorptivity.
Sorptivity is a material property describing the tendency of a porous hygroscopic media to absorb and transmit water to the ambient medium by capillarity [Hall, 1989][Kowalski, 2003], that is the many interactions taking place at the microscopic level between the solid skeleton and water molecules. They therefore make it possible to describe the hygroscopic behaviour of the solid [Léonard, 2002].
The sorption isotherm expresses the covering of the solid surface by one or more layers of gas molecules, in our case water vapour. These isotherms can be seen as an image of the affinity that exists between a solid surface (the adsorbent) and the vapour (the adsorbate) [Desaar, 2015].
Adsorption or desorption isotherms can be determined according to whether the sample is subjected to increasing (water intake) or decreasing (water loss) humidity.

Depending on the type of material, the isotherms of adsorption of gases on the surface of a solid can take different appearances among five types well described in the literature [Brunauer et al., 1940]. These isotherms represent the adsorbed volume as a function of partial pressure, as shown in the Figure 2.19.

Type I corresponds to a single-layer adsorption, also known as the Langmuir isotherm. Types II and III are encountered for macroporous solids while the Type IV and V correspond, respectively, to mesoporous and microporous solids, and often include hysteresis related to capillary condensation [Inglezakis et al., 2018][Léonard, 2002]. Type II is also obtained for non-porous material and represents unrestricted multi-layer adsorption [Inglezakis et al., 2018]. All the types except for Type I correspond to a multi-layer adsorption [Baroghel-Bouny, 1994].
However, classifying a product into a specific isotherm is often difficult as its sorption isotherm may belong to different classes simultaneously [Léonard, 2002].

The various types of isotherms therefore correspond to various porosities. Indeed, a microporous material contains pores smaller than 2 nm in diameter, while the pores of a macroporous material are larger than 50 nm in diameter and the ones of a mesoporous material are in between the two others, that is between 2 and 50 nm [Rouquerol et al., 1994].

Type II, IV and V are all S-shaped isotherms, with one or more inflection point. The middle section of the isotherms, almost linear, is often referred to as the stage at which the mono-layer coverage is complete, and multi-layer adsorption begins. Those S-shape isotherms have their origin in two opposite mechanisms: a cooperative adsorption due to solute-solute attractive forces at the surface, and the inhibition of the solute's sorption by a competing reaction within the solution [Inglezakis et al., 2018][Limousin et al., 2007].

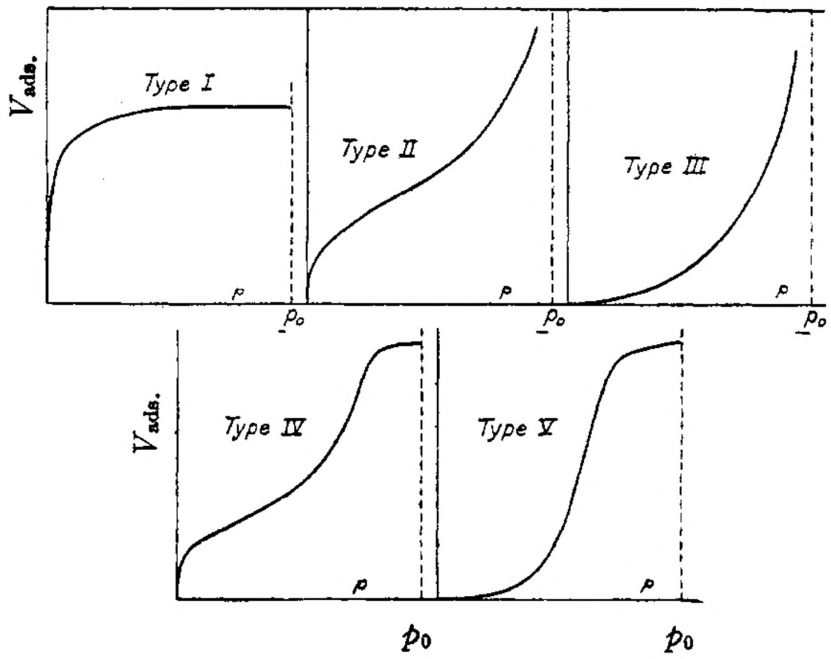

Figure 2.19: The five types of Van der Waals adsorption isotherms. [Brunauer et al., 1940]

When the adsorbed species is in equilibrium with the gas phase, its surface concentration on a solid depends on the nature of the gas and the solid as well as the gas pressure (or the partial pressure of the water vapour in the case of humid air) and the temperature [Ollivier & Torrenti, 2008]. Within the scope of this study, the adsorbed species is water and the gas phase is water vapour.

For water isotherms, the x-axis is often representing the relative humidity while the y-axis represents the equilibrium water content. Furthermore, the isotherms often encountered with water are classified as type II (Figure 2.20) [Léonard, 2002].

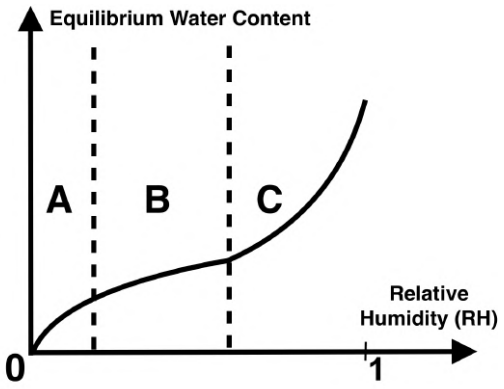

Figure 2.20: Isotherm of type II also called S-shape isotherm (adapted from [Léonard, 2002]

The type II sorption isotherm can be divided into three parts for a better understanding [Léonard, 2002]. At the beginning of the curve, that is for low relative humidity (section A), a first layer of water is fixed to the solid skeleton. As the theory of Langmuir depicts it, the binding energy is very strong and the water molecules are therefore not very mobile.
For intermediate relative humidity or pressure (section B), the slope of the curve starts to increase. Indeed, a second layer of water molecules is formed and the adsorption is therefore characterised as multi-layered, whose origin is adsorbate-adsorbate interactions [Giles & Smith, 1974]. However, the binding energy is lower than for the first layer, as it was proven by the BET (Brunauer-Emmet-Teller) model [Brunauer et al., 1938].
At pressures close to saturation (section C), the slope of the curve increases even more strongly, and the last water molecules attach themselves to the irregularities of the material surface: this phenomenon is called capillary condensation [Ollivier & Torrenti, 2008], and the binding energy is once more lower than for the previous layers.

To summarise, at a given temperature, the number of layers of water vapour molecules adsorbed on the surface of the sample is an increasing function of the partial pressure of water, and therefore the relative humidity. The binding energy of these various layers of water decreases with increasing distance from the solid, thus limiting the amount of water fixed [Ollivier & Torrenti, 2008].

The BET equation, while remaining the most widely used of all sorption equations, does not have a finite solid phase concentration limit and therefore no saturation, even if the liquid phase reaches its saturation [Inglezakis et al., 2018].

Hygroscopicity expresses the capacity of a material to adsorb (or desorb) and retain water, either by surface molecular adsorption or by capillary condensation, depending on the relative humidity of the ambient air [Desaar, 2015]. Hence the use of the (de)sorption isotherms to characterise the hygroscopicity of the material.
The maximum hygroscopicity is reached when the solid is in equilibrium with the surrounding saturated air: this water content defines the hygroscopic threshold, below which the humid material is in the so-called hygroscopic range [Léonard, 2002].

As for the water retention curve, sorption isotherms display a phenomenon called hysteresis: adsorption and desorption isotherms have different profiles depending on whether they were determined by rising or receding moisture content, which is inconsistent with the notion of equilibrium. Indeed, both curves have the same values only at their extremum RH, that is for 0% and 100% [Kowalski, 2003].

2.5 Conclusion

Throughout this chapter, one has learned the composition of concrete and the key properties of its constituents. Then, the porosity of concrete was thoroughly explained, from the various types of pores to the parameters influencing its porosity. And to conclude, the theory of the porous media was clarified with the explanation of the water retention curves and sorption isotherms.
The next step is to study the drying processes taking place in concrete. Indeed, drying experiments are required to better understand the porosity of a material and the exchange of air and water it has with its surrounding environment.

3 | Drying Processes

Contents

3.1 Introduction

In the previous chapter were presented the fundamentals of concrete as well as a thorough introduction to the porous medium and the various physical processes tied to it. We will now focus our attention on one of those processes which is the drying process happening in a porous medium.

Drying is a separation process in which the extraction of the solvent from a material is achieved by means of evaporation and removal of the gaseous phase newly formed [Léonard, 2002]. In most cases, the solvent extracted is water.
It is therefore the combination of two processes, vapour and heat transfers, both occurring simultaneously at the boundary of the material [Gerard et al., 2010].

Drying processes often involve the use of humid air at a controlled temperature and relative humidity (RH) which is defined as the ratio of the partial pressure of water vapour (p_v) to the equilibrium vapour pressure of water (p_v^0), at a given temperature [Hubert, 2018]:

$$RH = \frac{p_v}{p_v^0} \tag{3.1}$$

Another particular case of drying studied in this thesis is convective drying: a hot air stream provides both the energy needed to vaporise the solvent as well as the flow to transport the vapour produced [Léonard, 2002].

3.2 Drying processes

In this section, a summary of the different types of drying processes used in this thesis is showcased. However, some drying processes that might exist won't be presented here as

they are not relevant to this study.

As described in the introduction to this chapter, most drying techniques depend on the imposition of a controlled temperature and relative humidity at the boundary of the porous medium being dried. The variation of saturation (or water content) inside the medium is therefore driven by the boundary condition and the resulting change in capillary pressure [Hubert, 2018].

3.2.1 Vapour control technique

A hygroscopic body in contact with humid air soaks up vapour from the air or gives it back depending on its water content, until it reaches the equilibrium state. This equilibrium is reached when partial vapour pressure and temperature of the ambient medium and inside the pore space are equal [Kowalski, 2003].

The vapour control technique relies on the imposition of a constant relative humidity to a sample through the use of saline solutions, the nature and concentration of the saline solution dictating the relative humidity, in combination to the temperature which also influences the RH. The saline solution is placed in the same hermetically closed chamber than the sample studied [Pap et al., 2018][Hubert, 2018]. An example of an experimental setup is depicted in the Figure 3.1.

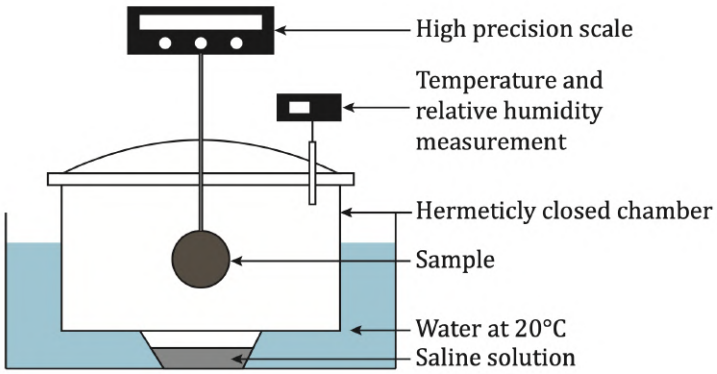

Figure 3.1: Suction (vapour) control using saline solutions [Hubert, 2018]

The relationship between the suction, the relative humidity and the temperature is given by the Kelvin law, as follows [Hubert, 2018]:

$$p_c = p_a - p_w = \frac{\rho_w \, R \, T}{M} \, \ln(RH) \tag{3.2}$$

where p_a and p_w are, respectively, the air and water pressures. R is the constant of perfect gases ($R = 8.3143$ J.mol/K), M is the molar mass of water ($M = 18.016$ g/mol) and ρ_w is the density of water. One also finds the temperature T [K] and relative humidity RH.

The water exchanges between the sample and the saline solution occur by vapour transfer, and a given suction is applied to the sample when vapour equilibrium is reached [Delage et al., 1998], hence this method is also presented as a suction control method. To achieve various relative humidity, one can simply use various saturated saline solutions, as it is done in this study, or various concentrations of the same product [Delage et al., 1998].

3.2.2 Convective drying methods

Convective drying is a particular case of drying, in which a warm humid air flow provides both the energy required to evaporate the water as well as the flow to transport the vapour subsequently produced out of the medium.

The convective dryer consists of an artificial wind tunnel in which a humid air flow is imposed, inside which the sample is placed on a tray. The air flow is perpendicular to the tray and therefore parallel to the weighing scale, which alleviates the problem of pressure losses.

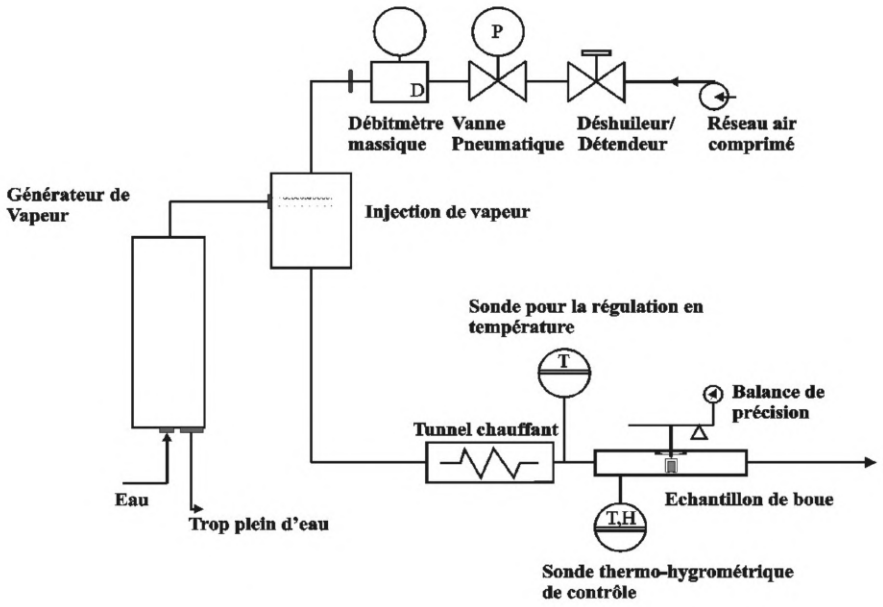

Figure 3.2: Schematic of the convective micro-dryer used [Léonard, 2002]

The temperature, velocity and relative humidity of the air flow are controlled. During the experiment, drying kinetics are obtained by regular weighing of the sample.

3.3 Drying Kinetics for convective drying

Convective drying is often supported by precise and regular weighing of the sample during the experiment, hence allowing the expression of the drying kinetics [Hubert, 2018].
Based on those measurements, a mass vs. time curve may be drawn. Moreover, two other curves may be used to analyse the drying kinetics: drying rate vs. time and drying rate vs. water content, also known as the Krischer curve. Finally, a last useful curve is the temperature vs. time curve, studied in parallel to the Krischer curve [Kemp et al., 2001]. Those four curves are depicted in the Figure 3.3.

The drying rate may be obtained, if the material is undeformable, through derivation of the mass loss with time. However, if the material is not considered as undeformable, the drying rate requires the variation of the external drying surface as shown in the following equation [Hubert, 2018]:

$$q = \frac{\partial m}{\partial t} \frac{1}{S(w)} \tag{3.3}$$

where one can see the derivation of the medium mass m with respect to time t, but also the external drying surface S which depends on the gravimetric water content w.

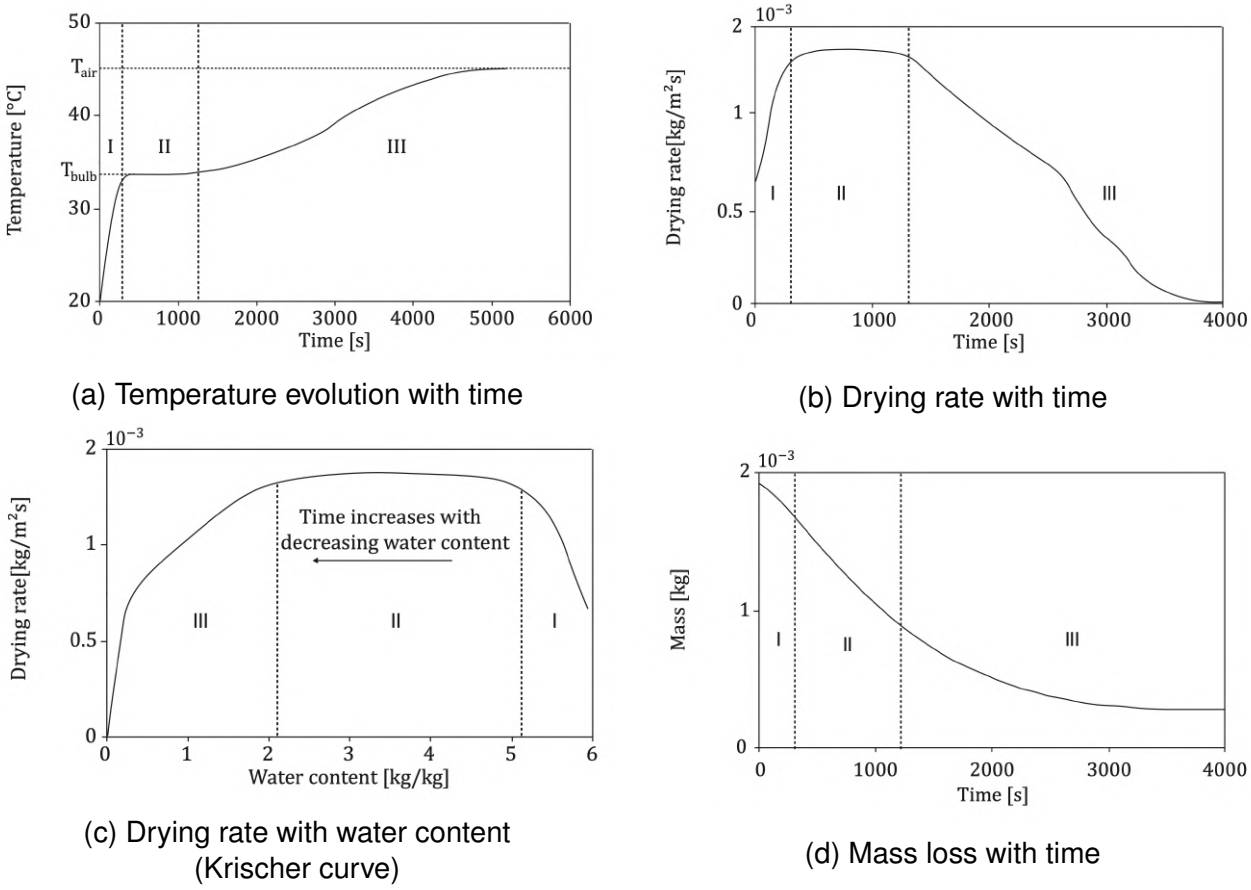

(a) Temperature evolution with time

(b) Drying rate with time

(c) Drying rate with water content (Krischer curve)

(d) Mass loss with time

Figure 3.3: Drying kinetics for convective drying [Hubert, 2018]

In those four curves, three distinct periods may be observed [Kowalski, 2003][Gerard et al., 2010]:

- I - Preheating period: the drying rate increases as the temperature at the boundary of the sample (T_0) rises to reach the wet-bulb temperature (T_{wb}), that is the lowest temperature a volume of air could reach under current ambient conditions if it was adiabatically brought to saturation by evaporation of water [Hubert, 2018]. Indeed, evaporation induces the cooling of the solid, which in turn leads to a lower rate of evaporation. This feedback process then equilibrates when the drying surface reaches T_{wb} [Scherer, 1990]. The wet bulb temperature is expressed as follows [Gerard, 2011]:

$$T_{wb} = \frac{1810.8 \left(p_v^0(T_{wb}) - p_v\right) - T_{db} \left(p_{atm} - p_v^0(T_{wb})\right)}{2\, p_v^0(T_{wb}) - p_v - p_{atm}} \tag{3.4}$$

  which is a nonlinear formulation. One can see the dry bulb temperature, noted T_{db}, often referred to as the ambient air temperature. The wet bulb temperature also relies on the vapour pressures p_v, p_v^0 and p_{atm} which are respectively the water vapour pressure, saturating water vapour pressure and finally the atmospheric pressure, the latter being equal to 101325 Pa. The vapour pressures are calculated by the following formulae [Gerard, 2011]:

$$p_v^0(T_{wb}) = 112659\ \exp\left(-\frac{5192.74}{T_{wb}}\right) \tag{3.5}$$

$$p_v = RH\ p_{v,sat} \quad \text{with} \quad p_{v,sat} = 112659\ \exp\left(-\frac{5192.74}{T_{air}}\right) \tag{3.6}$$

which are valid if the temperatures T_{wb} and T_{air} are within the range between 272 K and 373 K, and with the pressure given in [MPa].

- II - Constant Rate Period (CRP): heat supplied by the hot air flow to the drying sample is entirely used for the vaporisation of liquid water in a saturated boundary layer, the temperature of the surface remaining constant to the wet bulb temperature. This layer of saturated air, that is as if it appeared over a free water surface, is in thermodynamic equilibrium with the wet material [Scherer, 1990][Kowalski, 2003]. This second stage is marked by a plateau of the drying rate in the Krischer curve if the drying conditions are stable. A locally uniform distribution of vapour concentration at the surface is assumed, caused by the intensity of the internal water transfers which allows the evaporation at a rate limited by the capacity of the drying air [Hubert, 2018][Gerard et al., 2010]. The drying rate is mainly dependent on the external conditions such as the superficial speed, relative humidity and temperature of the drying air [Kowalski, 2003][Idso et al., 1974][Léonard, 2002].

- III - Falling Rate Period (FRP): the vapour in the boundary layer is not saturated anymore and the partial pressure of this vapour is therefore lower than that over a free water surface (saturated water vapour) [Kowalski, 2003]. Once the medium' saturation starts decreasing, its permeability also decreases as there is more resistance to the transport phenomena. Therefore, the drying rate decreases until equilibrium between the water content of the wet material and the environmental conditions (RH and temperature) [Hubert, 2018]. This decrease in the drying rate is due to a change of the mode of transfer shifting primarily from liquid movement to vapour movement [Idso et al., 1974], hence the drying rate depends strongly on the vapour transport conditions inside the sample [Kowalski, 2003] and relies less on external conditions [Scherer, 1990]. Simultaneously, the dried body temperature increases from the wet bulb temperature to the temperature of the drying medium (T_{air}) due to the excessive heat supply [Gerard et al., 2010].
  The falling rate period is also characterised by an evaporation rate from the disconnected isolated liquid clusters close to the surface which becomes comparable to (or lower than) the evaporation rate of the main liquid cluster [Lehmann et al., 2008]. Once this happens, the disconnected pores closer to the material surface are filled with gas at greater rates than the pores located deeper in the medium as their concentration gradient are steeper [Yiotis et al., 2006].

The mass and heat transfers occurring during those phases can be determined through the boundary layer model (more details are given in the Section 4.6) and these equations [Hubert, 2018]:

$$\bar{q} = \alpha\ (\rho_{v,surf} - \rho_{v,air}) \tag{3.7}$$

$$\bar{f} = L\ \bar{q} - \beta\ (T_{air} - T_{surf}) \tag{3.8}$$

where $\bar{q}$ and $\bar{f}$ are the mass and heat transfer, respectively.

The existence or absence of a constant rate drying period indicates whether the material goes through a heat-transfer-controlled phase when the external conditions are limiting the drying rate or if the drying rate is limited by internal moisture transport throughout the whole drying experiment [Kemp et al., 2001].

The difference in the drying rate of the constant rate period (CRP) between two porous materials is mainly due to the effective drying surface, that is the surface of water in contact with the atmosphere [Hubert, 2018]. Indeed, the effective drying surface of a rock sample (such as concrete) is bigger than its macroscopic section (and therefore bigger than its equivalent free water surface) because of adsorption and capillary effects [Tournier, 2001]. The effective drying surface depends on the saturation degree as well as on pore size and distribution, hence its bigger value for concrete which is rather porous.

A fourth period is also presented in the literature as the Receding Front Period (RFP) during which a completely dry zone develops from the drying surface through the sample body, the process being controlled by diffusion-induced transport phenomena instead of evaporation [Yiotis et al., 2006][Lehmann et al., 2008]. In our case, this period constitutes the end of the FRP (the part with the bigger slope) presented in the Figure 3.3c, where the slope of the Krischer curve increases continuously as the dry region increases with time. This model will be further addressed in the following section.

3.4 Transition between the CRP and FRP: Hydraulically connected transition zone

The transition between the Constant Rate Period and the Falling Rate Period is linked to a decrease in the drying rate. To explain this decrease, multiple approaches exist such as the "receding front model" or the "wetted surface model", which are more traditional, but the one used in this thesis is the concept of "hydraulic connection layer" [Hubert, 2018], hence the latter only will be explained hereafter.

The transition from the CRP to the FRP is said to be due to the disruption of the liquid water transfer from the sample to its drying surface, which is represented in the Figure 3.4. Those water fluxes are now assumed to result from micro-capillarity effects, as further studies have shown [Hubert, 2018].

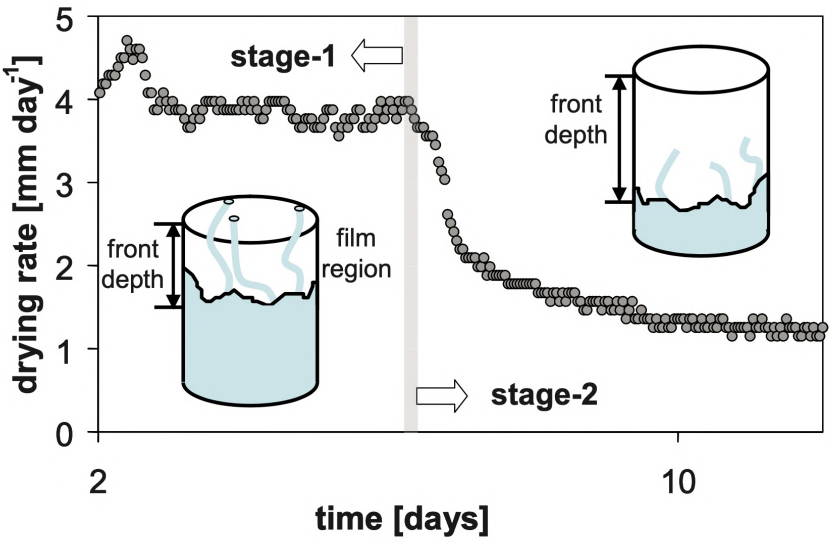

Figure 3.4: Conceptual diagram of the transition from the CRP to the FRP [Lehmann et al., 2008]

A constant drying rate is maintained as long as the liquid connections between the drying front and the evaporation surface are sustained and high enough to produce vapour at the evaporation surface faster than its withdrawal to the ambient environment by diffusion [Yiotis et al., 2006][Idso et al., 1974]. Therefore, the duration of the CRP is linked to the size of the spanning liquid clusters and the water retention properties of the porous medium. The drying front is located at the interface separating the liquid-saturated from the partially air-filled region of the porous material, and depends on the mean pore size and the width of the pore size distribution [Hubert, 2018][Lehmann et al., 2008]. The drying front and its characteristics such as the front depth and width are represented in the Figure 3.5, where the higher saturation area is darker, the white zone being partially to completely dried.

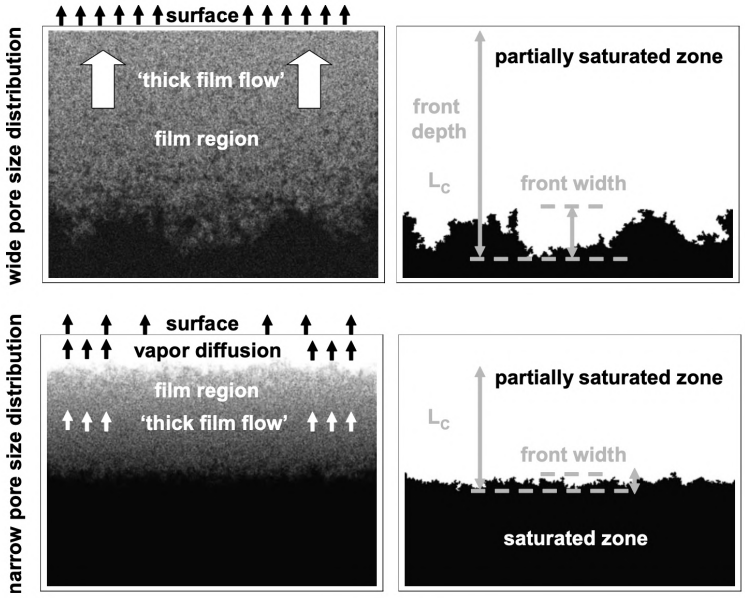

Figure 3.5: Representation of the drying front and its depth [Lehmann et al., 2008]

Once the drying front is not hydraulically connected to the evaporation surface anymore, the drying rate decreases rapidly. The hydraulic connection layer represents the maximum distance where water from the material can reach the evaporation surface. Therefore, if the drying front depth exceeds this length, the liquid connections between the drying front and the evaporation surface stop and the flow rate is reduced and imposed by controlled vapour transports.
The length of the hydraulic connection layer relies on capillary driven forces that are generated by the pressure gradient between the capillary pressure in large pores at the drying front, and the capillary pressure in small pores near the evaporation surface [Hubert, 2018].

3.4.1 Determination of the length of the hydraulic connection layer

Now that the physical explanations concerning the transition from the CRP to the FRP have been laid down, an expression of the length of the hydraulic connection layer will be determined.

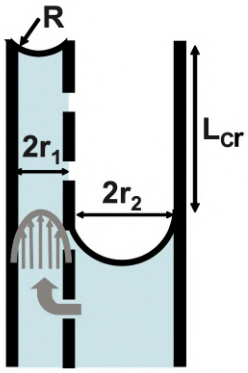

Figure 3.6: Representation of a pair of hydraulically connected capillaries [Lehmann et al., 2008]

Let us assume two hydraulically connected capillaries of different radii filled with liquid water (Figure 3.6). The larger the radius of the capillary and the faster it will empty due to the evaporation, resulting in a capillary pressure gradient between both capillaries, whose expression is obtained from the Jurin law (Equation 2.11):

$$\Delta p_c = 2\sigma \left(\frac{\cos\theta_1}{r_1} - \frac{\cos\theta_2}{r_2} \right) \tag{3.9}$$

with $r_1 < r_2$ the radii of the capillaries, σ the surface tension between the fluid and the capillary walls and θ the contact angle between the liquid and the capillary tube. The capillary pressure of the bigger capillary is maximised if the contact angle is null, and further evaporation will not change the curvature of this meniscus. The resulting water flow, expressed in terms of hydraulic head, is then:

$$\Delta h_c = \frac{\Delta p_c}{\rho_w\, g} = \frac{2\sigma}{\rho_w\, g} \left(\frac{\cos\theta_1}{r_1} - \frac{1}{r_2} \right) \tag{3.10}$$

As the evaporation proceeds, it creates a receding front in the bigger capillary that increases the distance to the evaporating surface, hence the necessity of an adjustment in the curvature of the meniscus in the smaller capillary until it reaches its intrinsic air-entry value, leading to the maximum capillary driving force [Lehmann et al., 2008]:

$$\Delta h_c = \frac{\Delta p_c}{\rho_w\, g} = \frac{2\sigma}{\rho_w\, g} \left(\frac{1}{r_1} - \frac{1}{r_2} \right) \tag{3.11}$$

However, the gravitational forces (noted Δh_g) are opposed to the capillary driving forces, and they become equal when the meniscus in both capillaries are maximum, that is for the expression shown in the Equation 3.11 above. Once the meniscus in the smaller capillary starts receding too, the hydraulic connection is lost and one can write:

$$\Delta h_c = \Delta h_g = L \tag{3.12}$$

where L is the distance between the menisci of both capillaries. This marks the end of the evaporation stage and the transition to a slower diffusion-limited stage [Lehmann et al., 2008].

Liquid flow toward the evaporation surface induces viscous dissipation in the capillaries, which creates a pressure drop proportional to the velocity of the flow in the capillary. This

pressure loss is equal to the following expression (see [Lehmann et al., 2008] for more details):

$$\Delta h_{visc} = \frac{\mu_w \; L \; e_0}{\rho_w \; g} \frac{8 \; (r_1^2 + r_2^2)}{r_1^4} \tag{3.13}$$

where e_0 [$\mathrm{m/s}$] is the drying rate (positive for inflow) supplied by the water flow q [$\mathrm{m/s}$] going through the small capillary. It is equal to the value of the drying rate during the constant rate period (CRP).
The gravitational and viscous effects can be combined to counteract the capillary driving force:

$$\Delta h_c = \Delta h_g + \Delta h_{visc} \tag{3.14}$$

and a new expression of the length of the hydraulic connection layer for two capillaries L is found:

$$L = \frac{\dfrac{2\sigma}{\rho_w \; g} \left(\dfrac{1}{r_1} - \dfrac{1}{r_2} \right)}{\dfrac{8 \; \mu_w \; e_0 \; (r_1^2 + r_2^2)}{\rho_w \; g \; r_1^4} + 1} = \frac{L_g}{\dfrac{L_g}{L_{visc}} + 1} \tag{3.15}$$

and as long as the gravitational length L_g is much shorter than the viscous dissipation L_{visc}, the combined length is said to be equal to the gravitational length [Lehmann et al., 2008].

The value of the capillary pressure, whose expression was given in the Equation 3.11, is not directly available. A new expression was therefore proposed based on the water retention curve and, in our case, the Van Genuchten model [Lehmann et al., 2008].
The capillary pressure required to drain the largest and smallest pores in the connection layer may be estimated using the slope of the tangent to the water retention curve at the inflection point, expressing the capillary hydraulic head, whose expression is then [Lehmann et al., 2008]:

$$\Delta h_c = \frac{\alpha_{vG}}{(n_{vG} - 1) \; \rho_w \; g} \left(\frac{2n_{vG} - 1}{n_{vG}} \right)^{(2n_{vG}-1)/n_{vG}} \left(\frac{n_{vG} - 1}{n_{vG}} \right)^{(1-n_{vG})/n_{vG}} \tag{3.16}$$

where one recognises the Van Genuchten model parameters α_{vG} [Pa] and n_{vG}.

In the same way, the expression of the viscous dissipation (Equation 3.13) contains a term with the ratio of radii of the capillaries, which corresponds to the unsaturated water permeability of the system composed of those capillaries. In our case, we study a porous medium whose unsaturated macroscopic water permeability for a Darcy flow is given by the following expression:

$$\frac{r_1^4}{8 \; (r_1^2 + r_2^2)} = k_{rel,w} \; k_{sat} \quad \text{with} \quad k_{rel,w} = f(S_{r,w}) \tag{3.17}$$

and the viscous head loss can be rewritten as:

$$\Delta h_{visc} = \frac{L_{cr} \; e_0 \; \mu_w}{\rho_w \; g} \frac{1}{k_{rel,w} \; k_{sat}} \tag{3.18}$$

where the length L becomes the length of the hydraulic connection layer, noted L_{cr}. The water content is assumed to decrease linearly between the drying front and the drying surface, the mean permeability between those two points being used to determine the viscous resistance [Lehmann et al., 2008].

The Equation 3.14 can therefore be rewritten with the two new expressions of Δh_c and Δh_{visc}. Furthermore, the gravitational head loss Δh_g is directly linked to the length L_{cr} such that [Lehmann et al., 2008]:

$$\Delta h_c = \Delta h_{visc} + \Delta h_g = L_{cr} \left(\frac{e_0 \ \mu_w}{\rho_w \ g} \frac{1}{k_{rel,w} \ k_{sat}} + 1 \right) \rightarrow L_{cr} = \frac{\Delta h_c}{1 + \frac{e_0 \ \mu_w}{\rho_w \ g} \frac{1}{k_{rel,w} \ k_{sat}}} \tag{3.19}$$

3.5 Conclusion

This chapter started with a summary of the different types of drying processes existing and used throughout this master thesis. Indeed, the vapour control technique and the convective drying were presented.
Moreover, convective drying is a particular case of drying which requires a larger theoretical basis as various pieces of information can be deduced from it. The drying kinetics of convective drying were then laid out, in particular the theory of the Krischer curve and its three periods. Finally, the model of the hydraulic connection layer was introduced to explain the transition from the constant rate period to the falling rate period, this transition being a key element in the understanding of multiple drying properties of a material.

It is now time to write the multiple equations governing those physical processes and to develop the model used in this thesis.

Part II

MODELLING AND EXPERIMENTATION

4 | Modelling of Water Transfer in Concrete

Contents

4.1 Introduction

One has learned through the last chapters the porous medium that is concrete and the physical processes involved in drying, and more particularly convective drying.

This chapter focuses on the model and equations governing those physical processes. To begin with, the state of the art about modelling of water transfer inside concrete is laid out, with a particular emphasis on concrete made from recycled aggregates.

Then, the referential used in the model is defined, followed by the numerous equations of equilibrium. Indeed, the mass and volume conservation equations will be introduced, followed by a theory of the multiphasic flows happening in an unsaturated porous media.

Once the thermal aspects of this thesis are covered, the thermo-hydraulic couplings are introduced. Then, the boundary layer model governing the exchange of mass and heat between the surface of the sample and the environment is clarified.

Finally, the finite element formulation is described, that is the discretisation in time and space and the type of finite elements used.

4.2 State of the Art

4.2.1 Introduction

Concrete is a well-known building material and numerous models have already been designed to study it in all its aspects. Drying of concrete is a complex process influenced by various effects such as concrete composition and age, environmental conditions but also temperature and humidity of the concrete element [Vinkler & Vitek, 2016].
Moreover, concrete with RCA is a relatively new material and therefore, not many models have been applied or designed for it. Hence, this chapter will cover the state of the art in terms of modelling of the drying of concrete.

When using a numerical model, the difficulty resides in the determination of the various parameters required, raising the question on the manner to determine those parameters from experimental data.
The distinction between NA and RCA may consequently be based solely on the value of those parameters.

The following sections will summarise the state of the art about convective drying models as well as a literature review of moisture models designed for concrete. Finally, we will display the work already done on the subject of concrete with recycled concrete aggregates and what still remains to be done.

4.2.2 History of convective drying models

One of the first studies on the drying of solids is Sherwood's (1929) whose research led to a model based on a diffusion equation following the principle that drying is primarily driven by diffusion [Sherwood, 1929]:

$$\frac{\partial w}{\partial t} = D_h \frac{\partial^2 w}{\partial x^2} \tag{4.1}$$

where w [-] is the moisture content and D_h [m^2/s] is the diffusion coefficient determined experimentally. By this formulation, Sherwood meant that the only driving force governing the mass transfer is a moisture content gradient.

Following this theory, a lot of research was done on drying using only diffusion as the predominant process, which led to the work of Gilliland and Sherwood (1933) who studied the Constant Rate Period and developed equations to obtain the length of this period as well as its critical moisture content [Gilliland & Sherwood, 1933].

In parallel to the development of theories regarding diffusion-driven drying, research was being conducted on the movement of moisture in porous medium resulting from capillary effects [Gardner & Widtsoe, 1921]. These studies demonstrated that the capillary effects should not be neglected when considering liquid motion in unsaturated porous medium. Hence the work of Comings and Sherwood (1934) which studied the moisture movement by capillarity in drying granular materials such as clay [Comings & Sherwood, 1934]. They concluded that the diffusion equation was working remarkably well for slow-drying materials such as wood but was insufficient to explain drying of granular materials such as clay or

sand, where the capillary effects play an important role in drying.
Few years later, Ceaglske and Hougen (1937) studied the drying of granular solids and concluded with the following postulate: "*In the drying of a granular solid, the rate of water flow is determined by capillary forces and not by moisture concentration gradients ; the flow may be in the direction of increasing concentration. These two facts are contrary to the requirements of the diffusion law*" [Ceaglske & Hougen, 1937]. Further investigations were conducted, notably through the work of Hougen et al. (1940) which compared the results of drying tests obtained by a diffusion only model and the ones from a capillary-based model with an experimental validation. This comparison further comforts the superiority of the capillary model to mimic theoretical and experimental curves [Hougen et al., 1940].

While the questions about capillary action and the diffusion of moisture were being addressed by the researchers named above, Krischer (1940) was also exploring drying phenomena in a series of papers. While the heat transfer had been put aside on the previous papers on drying, Krischer was the first to consider seriously the role that the transport of energy plays in a drying process [Whitaker, 1977].

Due to all the work of Ceaglske and Hougen (1937) and Hougen et al. (1940), the diffusion theory of drying has been criticised, although there was some definite evidence that this diffusion equation modelled accurately the latter stages of drying. Indeed, the liquid at this stage is in a pendular state and the motion of fluid due to capillary action is heavily reduced to the benefit of the convection and diffusion-induced motion.
Further investigations were then conducted to better model the latter stage of drying with diffusion among which Van Arsdel (1947) investigated the use of a variable diffusivity coefficient depending on the water content [Van Arsdel, 1947]:

$$\frac{\partial w}{\partial t} = \frac{\partial}{\partial x}\left(D_h(w)\frac{\partial w}{\partial x}\right) \tag{4.2}$$

Philip and De Vries (1957) extended the previous research on drying to associate the influence of capillary effects and vapour transport, incorporating the thermal energy equation into the governing set of equations describing the drying process [Philip & De Vries, 1957]. Whitaker (1977) took it a step further and suggested a multi-transfer and multi-physics model by incorporating the continuum physics governing equations for liquid, gas and energy transfers into the diffusion theory [Whitaker, 1977]. His formulation is still, nowadays, one of the most commonly referred models of the drying process.

4.2.3 Literature review of moisture models for concrete

In addition to the development of convective drying models, research was done in the field of moisture in concrete. Models were then established to better control and apprehend the various processes happening in concrete and related to moisture.

One of the most cited models in the literature is Bažant and Najjar's (1972) physical model, based on a nonlinear diffusion equation. In their model, they state that "*the equations governing drying and wetting of concrete are formulated assuming the diffusivity and other material parameters to be dependent on pore humidity, temperature and degree of hydration*" [Bažant & Najjar, 1972]. Drying of concrete is then described by the following second-order

equation, if a one-dimensional problem along the coordinate x is assumed and without variation of temperature [Vinkler & Vitek, 2016]:

$$\frac{\partial w}{\partial h}\frac{\partial h}{\partial t} - \frac{\partial}{\partial x}\left(D_h \frac{\partial h}{\partial x}\right) - \frac{\partial h_s}{\partial t} = 0 \tag{4.3}$$

where w [-] is the moisture content, h [-] is the pore relative humidity and h_s [-] a function describing self-desiccation. The ratio $\partial w/\partial h$ represents the slope of a sorption isotherm, while the coefficient D_h [m^2/s] is the moisture diffusivity.
Nevertheless, this model uses coefficients which are determined empirically, in addition to the sorption isotherm that is described by a linear function [Vinkler & Vitek, 2016], despite their obvious nonlinear character.

Parrott (1988) developed another empirical model of drying of concrete, where moisture content is described as a function of the water-to-cement ratio and the ambient relative humidity [Parrott, 1988].
In 1994, Xi et al. adapted the Bažant and Najjar model by introducing the BET model for sorption isotherms developed by Brunauer et al. in 1938 [Xi et al., 1994a][Brunauer et al., 1938], therefore resolving the issue of the linear function for sorption isotherms. They also defined the moisture diffusivity in dependence of the W/C ratio, and the sorption isotherms were linked to the W/C ratio, type of cement, temperature and age of concrete.
The moisture content is therefore described by the three-parameter BET model, which became the BSB model in 1969 after modification by Brunauer et al. [Brunauer et al., 1969][Vinkler & Vitek, 2016]:

$$w = \frac{C\ k\ w_m\ h}{(1 - k\ h)\big[1 + (C-1)\ k\ h\big]} \tag{4.4}$$

where the three parameters C, k and w_m are functions of the concrete composition, age and temperature, w_m representing the monolayer capacity [Xi et al., 1994a]. Xi et al. (1994) also derived an expression of the moisture diffusivity based on experimental data fitting [Xi et al., 1994b]:

$$D_h = \alpha_h + \beta_h \left[1 - \exp\left(-10^{\gamma_h^{(h-1)}}\ \ln(2)\right)\right] \tag{4.5}$$

where the three parameters α_h, β_h and γ_h are functions of the water-to-cement ratio.

More and more models, based on drying experiments and dependent on more and more properties relative to concrete (time and type of curing, influence of the ITZ, degree of hydration, pore water pressure, ...) were developed over time [Vinkler & Vitek, 2016]. One of the last models is the Baroghel-Bouny's one (2007) which is based on an extensive experimental work during which the influence of the water-to-cement ratio on the moisture properties, microstructural characteristics and transport properties was studied [Baroghel-Bouny, 2007].

4.2.4 Application to concrete made from RCA

To this day, a lot of research has been conducted to try to model the drying processes as the two previous sections showed. Nonetheless, the centre of interest of this thesis is concrete made with recycled concrete aggregates (RCA), theme that happens to be particularly recent in the material engineering community. This section therefore tries to summarise the

work already done and what this thesis might provide to further investigate this subject.

The mechanical properties of concrete are often the most popular research theme, and combined with drying processes, it results in a lot of paper about shrinkage of concrete. Nonetheless, even if shrinkage is indeed correlated to drying, our focus is on the drying phenomena and the accuracy with which models are able to predict the drying or wetting of concrete.
Once you enter the RCA into the frame, even fewer results concern the drying process, comforting the utility of this thesis.

Recent work has nonetheless been done on recycled concrete aggregates, trying to model various properties of concrete. Among others, Lovato et al. (2012) and Biglarijoo et al. (2017) used the response surface methodology (RSM) to model the results of various experimental tests: water absorption, carbonation depth, tensile and compressive strength, density among other properties of concrete [Lovato et al., 2012][Biglarijoo et al., 2017].

Drying shrinkage models were also adapted to account for the properties of RCA. Fathifazl et al. (2011) used experimental creep and drying shrinkage tests on concrete made with RCA and whose method of composition varied, trying to modify existing models to better fit their experimental results [Fathifazl et al., 2011].

Other studies have certainly treated a subject similar to this thesis, nevertheless none were focused on the drying processes happening in concrete with recycled concrete aggregates. Indeed, what seems to be the most studied field of concrete is linked to mechanical properties such as compressive resistance and, when focusing on drying, shrinkage of concrete.

4.3 Referential definition

Prior to defining the equations of equilibrium that will govern our model, it is required to define the reference configuration used. Two formulations are usually referred to:

- Lagrangian description: the problem is stated with regard to the reference (initial) configuration while we study the movement of all the particles of the body. The referential frame therefore moves with the material points.
- Eulerian description: the problem is stated with regard to the deformed configuration and the movement of a particle is described with respect to a fixed referential frame. It is assimilated to a control volume.

The Lagrangian description is the one used in mechanic problems while the Eulerian description is mostly found in hydraulic problems.

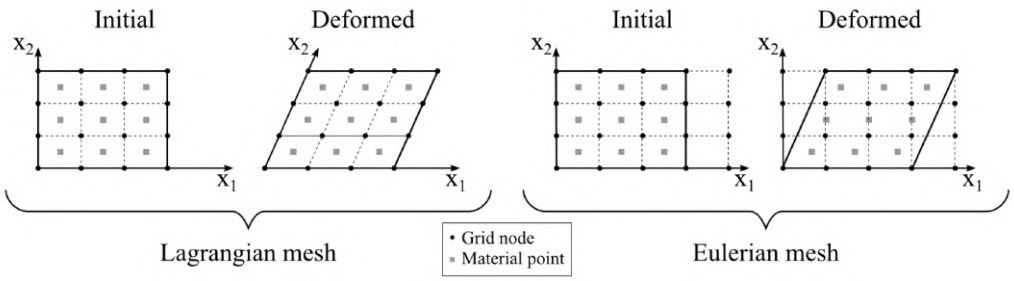

Figure 4.1: Lagrangian and Eulerian description [Collin & de Ville de Goyet, 2019]

In this thesis, as the mechanical aspects are neglected, the Lagrangian description is set aside as the deformations are small and negligible, and the equations shown hereafter will be derived in the Eulerian description. However, the Lagamine software is programmed using Lagrangian description which means that the equations presented in this section are, for the most part, written in a Lagrangian form.

4.4 Equations of equilibrium

4.4.1 Introduction

The reference fluid used in this thesis will be water, even though in practice, different fluids can occupy the pores (air, gas, oil, ...). In any case, the hypothesis of a sufficiently low Reynolds number will make it possible to restrict oneself to the case of laminar flows [Collin & de Ville de Goyet, 2019].

The fundamental variable used to formulate the water flows in a porous medium is, according to the authors, pressure or hydraulic potential. Each has advantages and disadvantages. However, the pressure variable, noted p, will be the one used hereafter. The dual variable of pressure is the fluid flow rate, noted Q. Associated with it is the fluid flow rate per unit area, denoted v. This is equivalent to an average velocity of the fluid particles, called Darcy velocity. Finally, the amount of fluid S stored in the pores must be taken into account [Collin & de Ville de Goyet, 2019].

The Lagamine program developed at the University of Liège is particularly used when coupled phenomena are studied: it is able to compute a thermal-hydro-mechanical coupling. However, the work achieved in this master thesis will focus primarily on the hydraulic and thermal study of the concrete medium, while the mechanical aspects will not be addressed.
The medium studied will therefore be considered as fixed and undeformable.

4.4.2 Mass and volume conservation equations

The mass of water contained in a fixed and undeformable system is equal to:

$$M_f = \int_{\Omega} (\rho_f \; n \; S_r) \; d\Omega \tag{4.6}$$

where Ω is the studied volume, ρ_f is the fluid density, n is the porosity of the medium and S_r is the saturation degree of the pores.

The mass conservation equation is therefore written, in an Eulerian configuration:

$$\frac{\partial M_f}{\partial t} = 0 \xrightarrow{\text{Reynolds transport theorem}} \frac{\partial(\rho_f \; n \; S_r)}{\partial t} + \frac{\partial(\rho_f \; n \; S_r) \; v_i}{\partial x_i} = 0 \tag{4.7}$$

where v_i is the fluid flow rate per unit area. Under the hypothesis of an incompressible fluid, it is possible to write the volume conservation equation: in an open system, the water content stored depends on the injected discharge and the difference between incoming and outgoing flows:

$$\int_\Omega \frac{\partial S}{\partial t} \; d\Omega = \int_\Omega Q \; d\Omega + \int_\Gamma q \; d\Gamma \tag{4.8}$$

where Γ is the border of the volume Ω.

The surface balance equation is expressed as:

$$n_i \; v_i + q = 0 \longrightarrow q = -n_i \; v_i \tag{4.9}$$

and therefore, the volume conservation equation just above writes:

$$\int_\Omega \frac{\partial S}{\partial t} \; d\Omega = \int_\Omega Q \; d\Omega - \int_\Gamma (n_i \; v_i) \; d\Gamma \tag{4.10}$$

where, by convention, the oncoming flows are positive and the outgoing ones are negative.

The Green's theorem is then applied to obtain:

$$\int_\Omega \frac{\partial S}{\partial t} \; d\Omega = \int_\Omega Q \; d\Omega - \int_\Omega \frac{\partial v_i}{\partial x_i} \; d\Omega \longrightarrow \frac{\partial S}{\partial t} + div \; \underline{v} - Q = 0 \tag{4.11}$$

which is the strong form of the conservation equation. It is, of course, possible to solve this problem of flow in porous media analytically by checking this equation at each point of the medium. However, there are other techniques such as the virtual power theorem: be a small virtual perturbation of the pressure field, noted δp, kinematically admissible, that is it respects the pressure conditions imposed on the border. Under this perturbation, the imposed solicitations (the volume flow Q and surface flow q) develop a virtual external power:

$$\delta W_E = \int_\Omega Q \; \delta p \; d\Omega + \int_\Gamma q \; \delta p \; d\Gamma \tag{4.12}$$

Assuming that the surface balance equation is verified, as well as the conservation equation, it is possible to express the external virtual power as a function of the internal quantities:

$$\delta W_I = \int_\Omega \left(\frac{\partial S}{\partial t} \; \delta p + div \; \underline{v} \; \delta p - div \; (\underline{v} \; \delta p) \right) d\Omega = \int_\Omega \left(\frac{\partial S}{\partial t} \; \delta p - \underline{v} \; \underline{\text{grad}} \; \delta p \right) d\Omega \tag{4.13}$$

where the Leibniz equation was used. This last equation corresponds to the internal virtual power.

The equality of the internal and external virtual powers for any virtual perturbation of the pressure leads to the respect of the local balance equations at any point of the domain, thus the global equilibrium. The equality verified for a limited number of disturbances leads to the respect on average of the global and local equilibrium, thus of the local balances. Since the equation in its strong form is verified on average, it is said to be in its weak form.

In order to use the principle of virtual powers, it is necessary to define the expression of water storage and flow, which constitute in a way the laws of behaviour of the fluid.

4.4.2.1 Darcy's law

Darcy's law is used to determine the specific flow, noted $\underline{v}$, going through a porous medium:

$$\underline{v} = -\frac{\underline{\underline{K}}}{\rho_f \; g} \left(\underline{\nabla} p + \underline{\nabla} \rho_f \; g \; z \right) = -\frac{\underline{\underline{k}}}{\mu} \left(\underline{\nabla} p + \underline{\nabla} \rho_f \; g \; z \right) \tag{4.14}$$

where $\underline{\underline{K}}$ [$\mathrm{m/s}$] is the hydraulic conductivity and depends on the fluid properties as well as the porous medium properties: k [$\mathrm{m^2}$] is the intrinsic permeability of the porous medium, ρ_f [$\mathrm{kg/m^3}$] is the fluid density and μ [$\mathrm{kg/m.s}$] is the dynamic viscosity of the fluid.

The formulation just presented links the hydraulic conductivity and the intrinsic permeability:

$$K_{ij} = \frac{k_{ij} \; \rho_w \; g}{\mu_w} \tag{4.15}$$

Another parameter worth introducing is the relative permeability that considers the change of saturation inside the porous material. Indeed, the less saturated the medium is and the lower the relative permeability, thus the overall permeability, is. It is theoretically equal to 0 in perfectly dry conditions and 1 in saturated conditions. An empirical formulation used to obtain it is the one by Van Genuchten, based on the degree of water saturation [Hubert, 2018]:

$$k_{rel,w} = \sqrt{S_{r,w}} \left(1 - \left(1 - S_{r,w}^{1/m_{vG}} \right)^{m_{vG}} \right)^2 \tag{4.16}$$

4.4.2.2 Storage

In a transitional regime flow, storage is variable and the amount of water in the pores depends on:

- deformations of the granular skeleton (which is neglected in this work);
- fluid density;
- saturation degree.

One may therefore write:

$$\dot{S} = \frac{\dot{p}}{\xi} \quad \text{with} \quad \xi = \frac{1}{c_p} \tag{4.17}$$

where S is the storage, ξ_i is the fluid compressibility and c_p is the storage coefficient.

The fluid density is also depicted as:

$$\rho_f = \rho_0 \left(1 + \frac{1}{\xi_f} \left(p - p_0 \right) - \alpha_T \left(T - T_0 \right) \right) \tag{4.18}$$

which is the linearisation of the behavioural law of the dilating and compressible fluid. Thermal aspects appear through the variation of temperature and the coefficient of thermal dilatation α_T.

4.4.3 Multiphasic flows in unsaturated porous media

Our focus will now be on multiphasic flows in unsaturated porous media. To begin with, an isothermal medium will be studied and then thermal equations will be introduced.

An unsaturated porous media presents two fluid phases:

- A liquid phase in which dissolved air is inside liquid water;
- A gas phase in which water vapour and dry air are mixed.

Properties of the liquid phase

Under the assumption that the presence of dissolved air doesn't modify the properties of the liquid phase, the density of dissolved air inside the liquid water is given by the Henry's law:

$$\rho_a^w = H_a(T)\ \rho_a^g \tag{4.19}$$

with ρ_a^w the density of dissolved air and H_a the Henry's constant for air which depends on the temperature.

Properties of the gas phase

The density of the gas mix is the sum of the density of the dry air and the water vapour:

$$\rho_g = \rho_a^g + \rho_w^g \tag{4.20}$$

where each gas respects the law of perfect gases:

$$p_{gas}^g = \frac{\rho_{gas}^g}{M_{gas}}\ R\,T \tag{4.21}$$

The density of water vapour is therefore:

$$\rho_w^g = \rho_{w,0}^g\ \exp\left(\frac{(p_w - p_g)M_w}{\rho_w\ R\,T}\right) \tag{4.22}$$

where $\rho_{w,0}^g$ is the density of saturating water vapour:

$$\rho_{w,0}^g = \left[194.4\ \exp\left(-0.06373(T-273) + (0.1634\ 10^{-3}(T-273)^2\right)\right]^{-1} \tag{4.23}$$

The viscosity of the gaseous mix is given by the following equation:

$$\mu_g = \left[\frac{X_a^g}{\mu_a^g} + \frac{X_w^g}{\mu_w^g}\right]^{-1} \quad \text{where} \quad X_a^g = \frac{\rho_a^g}{\rho_g} \tag{4.24}$$

with μ^g the gas dynamic viscosity and X^g its mass fraction.

Overall flow of the liquid phase

The flow of the liquid phase is governed by the Darcy's law:

$$\underline{q}_l = -\frac{k\ k_r^w\ (S_{r,w})}{\mu_w}\ (\underline{\nabla} p_w + \rho_w\ g\ \underline{\nabla} z) \tag{4.25}$$

with the intrinsic permeability (k) and the water relative permeability (k_r^w), the latter depending on the water saturation degree ($S_{r,w}$), and finally the dynamic viscosity of water (μ_w).

There are two possible flows in this solution: either the liquid moves and therefore the dissolved air as well, or only the dissolved air moves inside the liquid.

The advection flow of both the liquid water and dissolved air when the whole liquid moves are:

- Advection flow of the liquid water: $\rho_w\ \underline{q}_l$
- Advection flow of the dissolved air: $\rho_a^w\ \underline{q}_l = H_a\ \rho_a^g\ \underline{q}_l$

The diffusion of dissolved air inside the liquid water is expressed by the Fick's law:

$$\underline{i}_{a,d} = -\rho_w\ S_{r,w}\ n\ \tau\ D_a^w\ \underline{\nabla}\left(\frac{\rho_a^w}{\rho_w}\right) \tag{4.26}$$

where n is the porosity and τ the tortuosity, and with ρ_a^w the density of dissolved air and $D_a^w = 2\ 10^{-9}\ \mathrm{m}^2/\mathrm{s}$ the coefficient of diffusion of dissolved air inside liquid water.

Overall flow of the gaseous phase

The Darcy's law for the gaseous phase is:

$$\underline{q}_g = -\frac{k\ k_r^g\ (S_{r,g})}{\mu_g}\ (\underline{\nabla} p_g + \rho_g\ g\ \underline{\nabla} z) \tag{4.27}$$

with μ_g the viscosity of the gaseous mix air-water vapour and ρ_g its density.

In the same way as above, the displacement of the whole gas phase induces:

- Advection flow of the water vapour: $\rho_w^g\ \underline{q}_g$
- Advection flow of the air: $\rho_a^g\ \underline{q}_g$

The diffusion of the gaseous mix is expressed by the Fick's law:

$$\underline{i}_{a,g} = -\rho_g\ (1 - S_{r,w})\ n\ \tau\ D_a^v\ \underline{\nabla}\left(\frac{\rho_a^g}{\rho_g}\right) = -i_{w,g} \tag{4.28}$$

D_a^v is the diffusion coefficient of the dry air inside the water vapour:

$$D_a^v = D_0\left(\frac{p_0}{p_g}\right)\left(\frac{T}{T_0}\right)^{1,75} \tag{4.29}$$

where $D_0 = 2.42\ 10^{-5}\ \mathrm{m}^2/\mathrm{s}$, $p_0 = 101325\mathrm{Pa}$ and $T_0 = 303\mathrm{K}$.

Equations of mass conservation

The conservation of the water mass is:

$$\dot{S}_{w,l} + div(\underline{f}_{w,l}) + \dot{E}^{l\to g}_{H_2O} = Q_{w,l} \quad \text{where} \quad f_{w,l} = \rho_w \, \underline{q}_l \tag{4.30}$$

$$\dot{S}_{w,g} + div(\underline{f}_{w,g}) - \dot{E}^{l\to g}_{H_2O} = Q_{w,g} \quad \text{where} \quad f_{w,g} = \rho^g_w \, \underline{q}_g + \underline{i}_{w,g} \tag{4.31}$$

with S the storage term, $\underline{f}$ the mass flow, $\underline{q}$ the mean velocity of the phase, $\underline{i}_{w,g}$ the diffusion flow of vapour, Q the term of production/consumption, and finally $\dot{E}^{l\to g}_{H_2O}$ is the term of exchange from the liquid phase to the gaseous phase.

All in one, the equation of conservation of the mass of water is:

$$\frac{\partial}{\partial t}\left(\rho_w \, n \, S_{r,w} + \rho^g_w \, n \, S_{r,g}\right) + div(\rho_w \, \underline{q}_l) + div(\underline{i}_{w,g} + \rho^g_w \, \underline{q}_g) - Q_w = 0 \tag{4.32}$$

The same applies for the air mass:

$$\dot{S}_{a,g} + div(\underline{f}_{a,g}) + \dot{E}^{g\to d}_{air} = Q_{a,g} \quad \text{where} \quad f_{a,g} = \rho^g_a \, \underline{q}_g + \underline{i}_{a,g} \tag{4.33}$$

$$\dot{S}_{a,d} + div(\underline{f}_{a,d}) - \dot{E}^{g\to d}_{air} = Q_{a,d} \quad \text{where} \quad f_{a,d} = \rho^g_a \, H_a \, \underline{q}_l + \underline{i}_{a,d} \tag{4.34}$$

And finally, the equation of conservation of the mass of air is:

$$\frac{\partial}{\partial t}\left(\rho^g_a \, n \, S_{r,g} + \rho^g_a \, H_a \, n \, S_{r,w}\right) + div(\rho^g_a \, \underline{q}_g + i_{a,g}) + div(\rho^g_a \, H_a \, \underline{q}_l + \underline{i}_{a,d}) - Q_a = 0 \tag{4.35}$$

4.4.4 Thermal aspects

The unsaturated porous medium was, until now, considered isothermal. The thermal aspects will now be introduced, beginning with the energy balance equation.

All phases in the medium are supposed to be at the same temperature, which alleviates the need for multiple energy balance equations. The energy balance equation, expressed in its enthalpic form, only considers the energies linked to the heat transfer as well as the energy required for the vaporisation/condensation of water. Moreover, only convection and conduction are taken into account as radiation is neglected [Hubert, 2018]:

$$\dot{S}_T + \frac{\partial V_{T,i}}{\partial x_i} + \dot{E}^{l\to g}_{H_2O} \, L - Q_T = 0 \tag{4.36}$$

with S_T the enthalpy of the system, V_T the heat flux, Q_T the heat production term and finally L the water evaporation latent heat.

The enthalpy of the system is expressed by the sum of the enthalpy of each component [Collin, 2003]:

$$\begin{aligned} S_T = {} & n \, S_{r,w} \, \rho_w \, c_{p,w} \, (T - T_0) + n \, (1 - S_{r,w}) \, \rho_a \, c_{p,a} \, (T - T_0) \\ & + n \, (1 - S_{r,w}) \, \rho_v \, c_{p,v} \, (T - T_0) + (1 - n) \, \rho_s \, c_{p,s} \, (T - T_0) \end{aligned} \tag{4.37}$$

where $c_{p,i}$ is the specific heat of the constituent and ρ_i its density, while n is the porosity of the solid and $S_{r,w}$ the water saturation degree. The subscripts w, a, v and s are respectively

the water, air, vapour and solid.

The heat flux consists, as stated above, of a conduction term proportional to the thermal conductivity of the porous medium and a convection term proportional to the transport of heat by the fluid flows. The convection of the solid phase is taken into account in the Lagamine software through the Lagrangian description used and there is therefore no need to add it into the following equation [Hubert, 2018]:

$$V_{T,i} = -\Gamma \frac{\partial T}{\partial x_i} + \rho_w \; c_{p,w} \; q_{l,i} \; (T - T_0) + c_{p,a} \; (\rho_a \; q_{g,i} + i_{da,i}) \; (T - T_0) + c_{p,v} \; (\rho_v \; q_{g,i} + i_{v,i}) \; (T - T_0) \tag{4.38}$$

where Γ is the thermal conductivity of the porous medium. As a reminder, $q_{l,i}$ and $q_{g,i}$ are the flow of liquid and gaseous fluid, respectively, while $i_{da,i}$ and $i_{v,i}$ are the diffusive flow of dissolved air into the liquid water and of vapour, respectively.
It was chosen to define the thermal conductivity of the porous medium as an arithmetic average of the thermal conductivity of each phase present in the medium [Hubert, 2018]:

$$\Gamma = (1 - n)\Gamma_s + n \; S_{r,w} \; \Gamma_l + n \; (1 - S_{r,w}) \; \Gamma_g \tag{4.39}$$

One last term of the energy balance equation to be investigated is the energy required for the evaporation of water, which undoubtedly depends on the quantity of water changing phase [Hubert, 2018]:

$$\dot{E}^{l \to g}_{H_2O} = \frac{\partial m^w_g}{\partial t} + \frac{\partial f^w_{g,i}}{\partial x_i} = \frac{\partial}{\partial t}\big(n \; (1 - S_{r,w})\rho_v\big) + \frac{\partial}{\partial x_i}(\rho_v \; q_{g,i} + i_{v,i}) \tag{4.40}$$

Solid grain density variation

Another thermal aspect noteworthy is the variation of the solid grain density with respect to the temperature, the equivalent fluid formulation being presented at the Equation 4.18:

$$\rho_s = \rho_{s,0}\big(1 - \alpha_s \; (T - T_0)\big) \tag{4.41}$$

where $\rho_{s,0}$ is the solid grain density at the reference temperature (T_0) and α_s is the thermal expansion coefficient of the solid grains.

4.4.5 Equilibrium restrictions

As it was presented in the Section 2.4, the study of a porous media requires the study of three distinct incompressible phases that respect the theory of mixtures. Therefore, equilibrium restrictions are required to link all the different phases (solid, liquid or gas) of each species (water, air, concrete, and so on), and are obtained by assuming a thermodynamic equilibrium between the different phases of the species [Hubert, 2018]. Those restrictions will be presented hereafter.

4.4.5.1 Kelvin law

The Kelvin law is used to express a thermodynamic equilibrium between the two phases of water: liquid water and water vapour. It defines the pressure of water vapour, noted p_v, as a function of the suction, written s:

$$p_v = p^0_v \; \exp\left(\frac{-s \; M_w}{R \; T \; \rho_w}\right) \tag{4.42}$$

with p_v^0 the saturated pressure of water vapour, M_w the molar mass of water, R the constant of perfect gases and T the temperature.
It was also expressed in the Equation 3.2 by using the relative humidity RH instead of the pressures of water vapour.

4.4.5.2 Henry's law

The Henry's law has been used in the Section 4.4.3 and expresses the equilibrium between dry air in the gas phase and dissolved air in the liquid phase:

$$p_a = K_l^a \, x_l^a \tag{4.43}$$

which formulates that under constant temperature, the molar fraction of dissolved air, noted x_l^a, is proportional to the partial pressure of air through a constant K_l^a.

The formulation of the Henry's law used previously (Equation 4.19) was the one in terms of densities:

$$\rho_{da} = H_a \, \rho_a \tag{4.44}$$

where H_a is the Henry's constant for air, depending on the temperature, pressure and gas type.

4.5 Thermo-Hydraulic couplings

The scope of this thesis is to model the drying phenomena happening inside concrete. To reach our goals, a thermo-hydraulic coupling will be done, consisting of:

- T→H: the temperature affects the properties of the fluids, in particular their viscosity and density;
- H→T: the heat convection through the fluid phases results from the hydro-thermal coupling as the quantity of heat transferred depends on the fluid flows.

In addition to these, the water flow and heat flow are often in opposition during drying: the heat flux goes from the drying surface to the inside of the material while the water flows the other way, possibly interacting with each other.

4.6 Boundary layer model

The mass and heat transfers at the surface of the sample are modelled through the use of a boundary layer taking place all around the sample where those transfers take place [Hubert, 2018].

With the boundary layer model in mind, the water content at the drying surface of the sample is therefore supposed to be in equilibrium with the partial pressure of water vapour. The vapour flow from the sample to its surroundings, noted $\bar{q}$, is then assumed proportional to the difference between the vapour density of the drying air, written $\rho_{v,air}$, and the vapour density of the external surface of the sample, noted $\rho_{v,surf}$ [Gerard et al., 2010][Hubert,

2018].
The mass transfer, equal to the water flow just described, is then expressed as:

$$\bar{q} = \alpha \ (\rho_{v,surf} - \rho_{v,air}) \tag{4.45}$$

where the coefficient α is the mass transfer coefficient that characterises the surface's transfer properties and is dependent on the saturation degree of the boundary layer. It is assumed that the mass transfer coefficient is maximal when the boundary layer is saturated and decreases with desaturation [Gerard et al., 2010].

The same logic is followed with regard to the heat transfer which is expressed through the heat flux from the boundary of the sample to the drying air, noted $\bar{f}$ [Hubert, 2018][Gerard et al., 2010]:

$$\bar{f} = L \ \bar{q} - \beta \ (T_{air} - T_{surf}) \tag{4.46}$$

with T_{air} and T_{surf} the temperature of the drying air and at the surface of the sample, respectively. One can see the use of another coefficient β called the heat transfer coefficient, as well as the water evaporation latent heat L which is equal to 2500 $\mathrm{kJ/kg}$.
The heat flux is therefore the subtraction of two terms: the heat consumed to evaporate the water at the surface of the sample, $L \ \bar{q}$, and the heat transferred from the atmosphere to the porous medium by convection, $\beta(T_{air} - T_{surf})$.

The mass and heat transfer coefficients can be determined based on the drying kinetics, specifically the CRP [Hubert, 2018]. Indeed, the value of the drying rate during this period is directly linked to the capacity of the drying air to evaporate the water at the surface of the porous medium and the mass transfer coefficient is therefore:

$$\alpha = \frac{\bar{q}_{CRP}}{\rho_{v,surf} - \rho_{v,air}} \tag{4.47}$$

where the vapour density of the drying air is known since the drying is done by controlling its relative humidity and temperature. Moreover, the vapour density at the surface is also known as during the CRP, the sample is considered saturated at its surface ($RH = 100\%$) and the temperature is equal to the wet bulb temperature whose analytical expression is shown in the Equation 3.4 and can be developed to obtain:

$$\begin{aligned} 0 = &-225318 \ \exp\left(\frac{-5192.74}{T_{wb}}\right) \ T_{wb} + 112659 \ \exp\left(\frac{-5192.74}{T_{wb}}\right) \ (1810.8 + T_{air}) \\ &- 1810.8 \ p_v - p_{atm} \ T_{air} + (p_v + p_{atm}) \ T_{wb} \end{aligned} \tag{4.48}$$

The saturated vapour densities are determined by the following experimental formula, valid for temperatures (T) between 293K and 331K [Gerard, 2011]:

$$\rho_{v0} = \frac{1}{194.4 \ \exp\left(-0.06374 \ (T - 273.15) + 0.1634 \ 10^{-3} \ (T - 273.15)^2\right)} \tag{4.49}$$

and then the vapour density at a given relative humidity is obtained by using the definition of the relative humidity (Equation 3.1) and the law of perfect gas:

$$RH = \frac{p_v}{p_{v0}} = \frac{n_v \ R_v \ T_v}{n_{v0} \ R_{v0} \ T_{v0}} \frac{V_{v0}}{V_v} = \frac{\rho_v}{\rho_{v0}} \tag{4.50}$$

The heat flux from the environment to the sample ($\bar{f}$) is considered null during the CRP as all the heat provided is used to evaporate the water at the surface of the sample, which therefore leads to the following expression of the heat transfer coefficient:

$$\beta = \frac{L\ \bar{q}_{CRP}}{T_{air} - T_{wb}} \tag{4.51}$$

where, as mentioned for the determination of the mass transfer coefficient, the temperature of the drying air and the wet bulb temperature are known.

4.7 Finite element formulation

This section will briefly introduce the finite element formulation used in this thesis, as well as the way the variables are discretised spatially and temporally. For more information about the discretisation of the equilibrium equations, see the work of Collin (2003) [Collin, 2003].

The finite element used in this thesis is an isoparametric element of the Serendipity type, called MWAT 2D in the Lagamine software and visible at the Figure 4.2. The geometry and discretised fields (displacement, pressure and temperature) are defined according to their nodal values through N interpolation functions. These are expressed in the local coordinates plane (ξ,η) which facilitates the analytical expression of the element as well as the integrals over its volume [Collin, 2003].

In the MWAT 2D element, five equations of equilibrium must be verified and the element therefore has five degrees of freedom (DOF) for each node. Those five equations are divided as follows: two mechanical, two hydraulic and one thermal. However, the mechanical aspect being put aside in this thesis, the two mechanical DOF, corresponding to the geometric coordinates x and y, will be fixed for all nodes.
The hydraulic DOF are to be chosen between the following possibilities: fluid pressure, saturation or suction. The fluid pressures were chosen as it easily allows the determination of the suction, and because the saturation is not a continuous function in the whole domain. In the case of a gas phase composed of two gases (air and water vapour for example), the total pressure of the mix was chosen as a DOF [Collin, 2003].

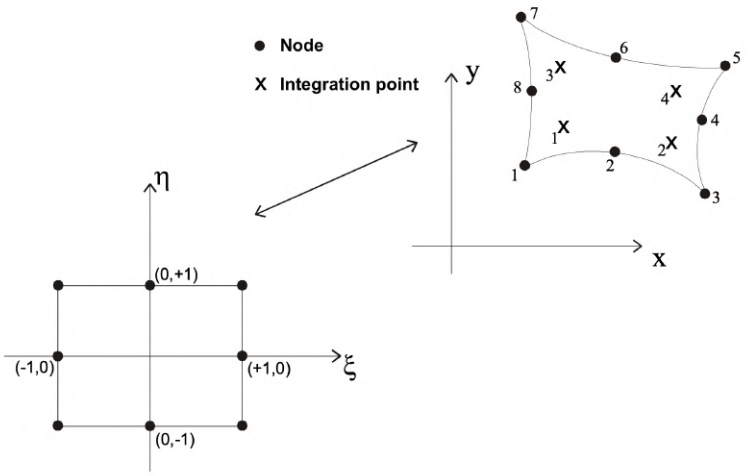

Figure 4.2: Isoparametric element with 8 nodes (translated from [Collin, 2003])

The choice of DOF influences the manner in which the boundary conditions are imposed. The two DOF of pressure allow a direct control of the fluid pressures at any point in the domain [Collin, 2003]. Moreover, it is difficult to impose a suction or saturation with variable fluid pressures, comforting us in our DOF choice.
Therefore, the MWAT 2D element's coordinates, displacements, velocities, pressures and temperature are expressed as a function of their nodal values using the same interpolation functions [Collin, 2003]:

$$x_i = N_L \, X_{L,i} \quad \text{and} \quad p = N_L \, P_L \tag{4.52}$$

for example, with L ranging from 1 to the number of nodes in the element (8 in our case).

We have just presented the spatial discretisation applied for our finite elements. However, there is still one aspect to be defined: time. Indeed, it intervenes directly in the fluid and heat balance equations presented before, and it is therefore necessary to discretise it. We thus introduce the notion of time steps (temporal finite elements) and time discretisation.

A time step is defined by two moments, which we note A and B. We assume that pressure and temperature vary linearly over the time step, whether at any point or at a node [Collin, 2003]:

$$\begin{aligned} t &= (1-\theta)t^A + \theta t^B \\ p &= (1-\theta)p^A + \theta p^B \\ T &= (1-\theta)T^A + \theta T^B \end{aligned} \tag{4.53}$$

where θ ranges from 0 to 1.

Henceforth, the derivative of the pressure with respect to time is reduced to a pattern similar to that of finite differences:

$$\frac{dp}{dt} = \frac{p^B - p^A}{t^B - t^A} = \frac{\Delta p}{\Delta t} \tag{4.54}$$

For the balance equations to be respected over the entire time step (as we only know the value of the nodal unknown at discretised times), we use the weighted residue method with a time-varying weighting function that was chosen to be reduced to a collocation. The choice of θ is therefore based on this collocation and on the precision and stability it can reach, the most commonly used schemes being the implicit ($\theta = 1$) and Galerkin ($\theta = 2/3$) schemes [Collin, 2003][Collin & de Ville de Goyet, 2019].

5 | Experimental Approach

Contents

5.1 Introduction

The modelling of any phenomenon requires an experimental investigation to support it. It is required to determine the value of the various model parameters or simply to validate the results obtained numerically.

To better understand the impact of the recycled concrete aggregates inside concrete on the water transfer properties of this material, multiple compositions are used. At first, the Dreux-Gorisse method, used to determine the composition of our reference concrete, is explained. Then, the composition methods of the other concretes/mortars used in this thesis are described and justified. The choice of a method or another was based on one simple principle: to be able to study as accurately as possible the influence of each parameter alone and therefore create compositions which are similar except for one parameter (the type of aggregate or cement, the quantity of sand used, and so on).
Once our concrete compositions are settled, we are able to establish an experimental plan which will explain the various tests done and their objectives.

The extensive experimental part of this study aims to understand and quantify the various parameters playing a role in the water transfer properties of a concrete. Those experiments consist of a water absorption by immersion test, static and dynamic sorption and desorption experiments, as well as convective drying and water permeability experiments. Moreover, a test of resistance to carbonation is carried out to try to evaluate a measurable indicator of the durability of a concrete.

5.2 Experimental concrete composition

The goal of this experimental campaign is to highlight the influence of the recycled concrete aggregates on a series of key model parameters. To achieve that goal, different compositions have been considered. We first considered a classical concrete made from natural aggregates which will serve as our reference concrete. We then produced a concrete of similar properties (same cement paste) in which the NA were substituted with RCA. We also developed two different mortars to single out the influence of the presence, or not, of aggregates in the mix. The first mortar was produced by replacing the aggregates by an equivalent amount of sand as to keep a constant water-to-cement ratio. The second one was developed using the Concrete Equivalent Mortar (C.E.M.) method to have a cement paste similar to the one of our reference concrete. Finally, the influence of the cement type was also studied by replacing the cement type in the reference concrete with CEM III.

Within this field, the following compositions were established:

1. C-NA: Micro-concrete made with natural aggregates and CEM I;
2. C-NA-CEMIII: Micro-concrete made with natural aggregates and CEM III;
3. C-RCA: Micro-concrete made with recycled concrete aggregates and CEM I;
4. M1-CEMI: Mortar made from CEM I and screed sand (constant water-to-cement ratio);
5. M2-CEMI: Mortar made from CEM I and screed sand (C.E.M. method);

where the term micro-concrete refers to a concrete whose biggest aggregates are inferior or equal to 8mm in diameter. The compositions used in this thesis are displayed in the Appendix A.

5.2.1 Reference Concrete (C-NA): Dreux-Gorisse method

The first concrete composition, i.e. the micro-concrete made with natural aggregates and CEM I cement, was done according to the Dreux-Gorisse method explained hereafter. It will be our reference concrete for the rest of the study. The same concrete with CEM III cement obviously has the same composition as the change of cement type doesn't affect it.

The Dreux-Gorisse method is a well-known method for the composition of concrete. An overview of this approach will be presented here, as it is the one we applied to establish our reference concrete's composition. All the information and Figures shown in this section come from [Courard, 2018].

It is based on two series of data, namely general experimental laws and information from old concrete formulations that have given satisfaction (strength, workability). This method applies for "normal" concrete, i.e. without additives nor additions.

The technique is divided into two parts:

- the water-to-cement ratio is defined to achieve a targeted resistance;
- the parameters are adjusted to have a consistency adapted to the conditions of execution chosen.

5.2.1.1 Determination of the water-to-cement ratio

As mentioned above, the water-to-cement ratio is linked to the resistance by various relations, but we'll use the Bolomey's one in this thesis:

$$R_c = G\ F_{CE}\ \left(\frac{C}{W} - 0.5\right) \tag{5.1}$$

with F_{CE} the real class of the chosen cement (at 28 days) which is often given by the cement's manufacturer. The mean targeted resistance in compression is $f_{c,cube}$, which is used through $R_c = 1.15\ f_{c,cube}$. Finally, G is a granular coefficient which depends on the quality and size of the chosen aggregates, as shown in the Table 5.1.

Qualité des granulats	Dimension D des granulats		
	Fins (D ≤ 16 mm)	Moyens (25 ≤ D ≤ 40 mm)	Gros (D ≥ 63 mm)
Excellente	0,55	0,60	0,65
Bonne, courante	0,45	0,50	0,55
Passable	0,35	0,40	0,45

Table 5.1: Values of the granular coefficient G depending on the aggregates' size and quality [Courard, 2018]

5.2.1.2 Determination of the cement and water concentration

Once the water-to-cement ratio is determined, we need to compute the cement concentration in order to obtain the water content required.
The quantity of cement is obtained approximately from an abacus (Figure 5.1), depending on the C/W ratio as well as the desired consistency expressed in terms of slump (Abrams' cone).

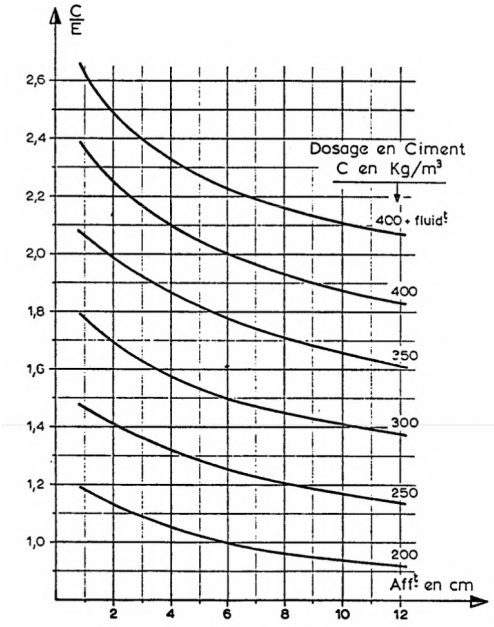

Figure 5.1: Abacus to determine approximately the cement concentration based on the C/W ratio and desired consistency [Courard, 2018]

Once the cement concentration is known, the water concentration is simply derived from the water-to-cement ratio. However, the Figure 5.1 is based on a particular value of the maximum diameter of the aggregates, that is $D_{max} = 25$mm and there is therefore a correction to achieve if the maximum diameter is different. This is done through the Figure 5.2.

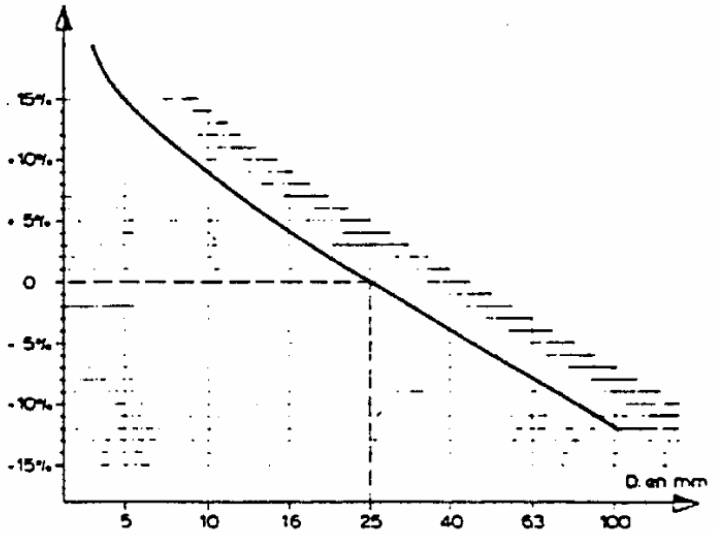

Figure 5.2: Correction to apply to the theoretical water dosage depending on the aggregate's maximum diameter [Courard, 2018]

The newly obtained water quantity is the total amount of water required. However, it also needs to be corrected due to the water content of the aggregates which may provide additional water. On the contrary, the aggregates may also absorb water and therefore diminish the amount available for the reaction of hydration.
The moisture content and amount of water absorbed by the aggregates are to be obtained prior to this calculation, as it was done in our experimentation. The moisture content is obtained by drying of the aggregates in their "storage state" and measurements of their mass loss which is linked to their water content. The water absorption of those aggregates is obtained by a water absorption test.

5.2.1.3 Optimisation of the granular skeleton

Once the water and cement concentrations are obtained, the following step is to determine the sand and various aggregates' content. That is done in terms of volume proportions p (aggregates) and s (sand) which give a granulometric curve as close as possible to a theoretical one.

The theoretical granulometric curve according to Dreux is representing the most compact granular skeleton depending on the D_{max}, aggregates' type, cement content, compaction method and other more specific considerations. The theoretical curve is composed of two line segments OA and AB on a granulometric diagram ($\log D$, passer-by):

$$\begin{cases} O = (0.08\text{mm} \ ; \ 0) \\ B = (D_{max} \ ; \ 100) \\ A = \left(D/2 \ ; \ 50 - \sqrt{D_{max}} + K + K_s + K_p\right) \end{cases} \tag{5.2}$$

The values of the K coefficients are found in the Table 5.2 and depend on the cement content, vibrational power of the compaction and aggregates angularity.

Vibration		faible		normale		puissante	
Forme des granulats (du sable en particulier)		roulé	concassé	roulé	concassé	roulé	concassé
Dosage en ciment	400 + Fluidifiant	- 2	0	- 4	- 2	- 6	- 4
	400	0	+ 2	- 2	0	- 4	- 2
	350	+ 2	+ 4	0	+ 2	- 2	0
	300	+ 4	+ 6	+ 2	+ 4	0	+ 2
	250	+ 6	+ 8	+ 4	+ 6	+ 2	+ 4
	200	+ 8	+ 10	+ 6	+ 8	+ 4	+ 6

Nota 1 : correction supplémentaire K_s *:* si le module de finesse du sable est fort (sable grossier), une correction supplémentaire sera apportée de façon à relever le point A, ce qui correspond à majorer le dosage en sable et vice versa. La correction supplémentaire (sur K) peut être effectuée en ajoutant la valeur $K_s = 6\,Mf - 15$

Nota 2 : correction supplémentaire K_p *:* si la qualité du béton est précisée "pompable", il conviendra de conférer au béton le maximum de plasticité et de l'enrichir en sable par rapport à un béton de qualité "courante". On pourra pour cela majorer le terme correcteur K de la valeur K_p = + 5 à + 10 environ, selon le degré de plasticité désiré.

Table 5.2: Values of the K coefficients used in the optimisation of the granular skeleton [Courard, 2018]

The Figure 5.3 shows the Dreux-Gorisse curve to optimise the granular skeleton of our concrete with natural aggregates. Once the OAB curve and the sand/aggregates granulometric curves are in place, it is required to connect the 95% of passer-by from the sand to the 5% of passer-by from the closest aggregate. If there is more than one size of aggregates, then the process is repeated taking the value of the two closest aggregates type. This connecting line will then make an intersection with the Dreux-Gorisse curve and that gives the value of the p/s ratio.

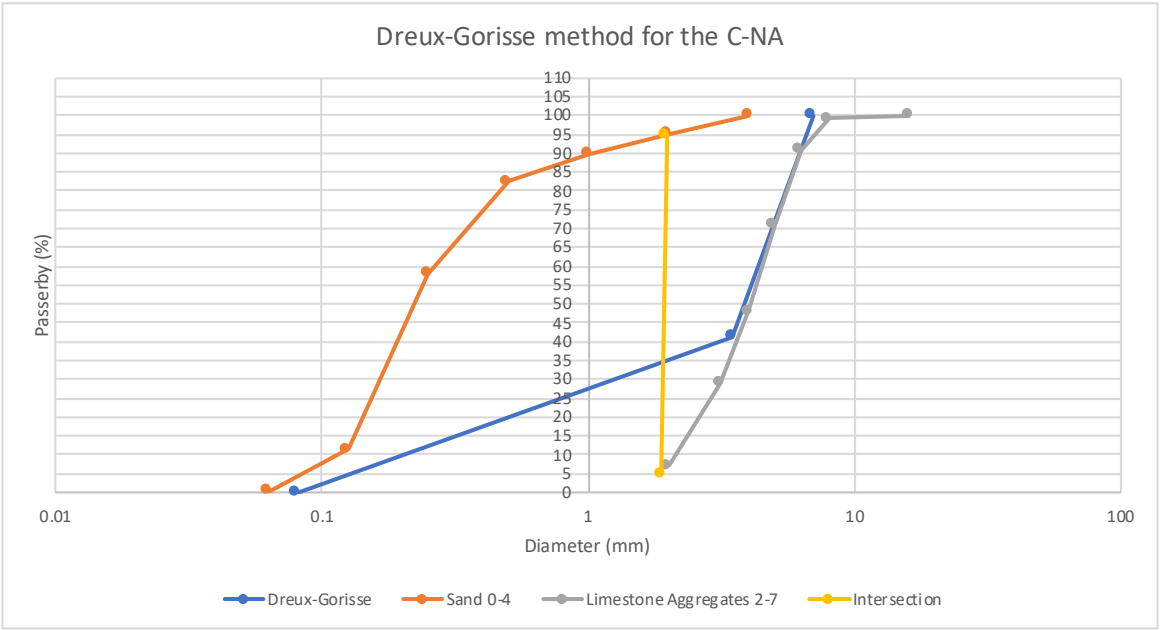

Figure 5.3: Dreux-Gorisse curve for determination of the composition of the C-NA

Once the p/s ratio is known, we may obtain the value of p and s through a compacity coefficient γ:

$$\gamma = p + s + c \tag{5.3}$$

which is obtained by the Table 5.3 for "normal concrete" and based on the value of D_{max}, the consistency and the compaction method.

Consistance	Serrage	γ coefficient de compacité						
		D=5	D=10	D=16	D=25	D=40	D=63	D=100
molle	piquage	0,750	0,780	0,795	0,805	0,810	0,815	0,820
	vibration faible	0,755	0,785	0,800	0,810	0,815	0,820	0,825
	vibration normale	0,760	0,790	0;805	0,815	0,820	0,825	0,830
plastique	piquage	0,760	0,790	0,805	0,815	0,820	0,825	0,830
	vibration faible	0,765	0,795	0,810	0,820	0,825	0,830	0,835
	vibration normale	0,770	0,800	0,815	0,825	0,830	0,835	0,840
	vibration puissante	0,775	0,805	0,820	0,830	0,835	0,840	0;845
ferme	vibration faible	0,775	0,805	0,820	0,830	0,835	0,840	0,845
	vibration normale	0,780	0,810	0,825	0,835	0,840	0,845	0,850
	vibration puissante	0,785	0,815	0,830	0,840	0,845	0,850	0,855

Nota :
- Ces valeurs sont convenables pour des *granulats roulés*, sinon il conviendra d'apporter les corrections suivantes :
  - sable roulé et gravier concassé = - 0,01
  - sable et gravier concassé = - 0,03
- Pour les granulats légers, on pourra diminuer de 0,03 les valeurs de γ qui correspondent ici à des granulats denses ordinaires.

Table 5.3: Values of the compacity coefficient γ [Courard, 2018]

5.2.2 Concrete with RCA (C-RCA): Constant aggregates' volume

The concrete made from RCA was produced to be equivalent to the reference concrete, the only difference being the type of aggregates used. To obtain a concrete of similar properties, the NA were substituted for RCA with a constant volume method, the other constituents being similar to the reference composition. That means that the volume is constant but the mass is proportional to the bulk density of the aggregates.

First of all, the granulometric curve of the RCA must be equal to the one of the NA, requiring a sieving of the various available size-cuts of RCA. The percentage of each fraction is given in the Table 5.4.

Diameter (mm)	Percentage of mass (%)
2/4.0	48
4/5.0	22.9
5/6.3	20
6.3/8	9.1

Table 5.4: Fractions used to mimic the granulometric curve of the natural aggregates

The mass of recycled concrete aggregates required was then obtained by the following formula:

$$M_{\text{RCA}} = V_{\text{aggregates,C-NA}}\ \rho_{\text{RCA}} = P_{\text{C-NA}}\ \frac{\rho_{\text{RCA}}}{\rho_{\text{NA}}}\ \text{[kg/m}^3\text{]} \tag{5.4}$$

where $P_{\text{C-NA}}$ is the required mass of aggregates found by the Dreux-Gorisse method for the reference concrete ([kg/m^3]). The bulk density of the recycled aggregates and natural aggregates used are respectively 2290kg/m^3 and 2590kg/m^3.

In addition to the mass of aggregates which is modified to consider the change from NA to RCA, the amount of water required is also updated in consideration of the absorption and water content related to the RCA.

5.2.3 Mortar with the same W:C ratio (M1-CEMI)

The first composition of mortar is done in order to keep the same water-to-cement ratio as the reference concrete. The Dreux-Gorisse method was also partially used in order to find the sand content required, by adaptation of the Equation 5.3.

This mortar is used in this thesis to separately analyse the influence of the paste and aggregates on the drying phenomena studied.

5.2.4 Concrete Equivalent Mortar (M2-CEMI)

The second composition of mortar is obtained by using the method of the Concrete Equivalent Mortar (C.E.M.), whose goal is to produce a mortar with the same rheological properties as a "reference" concrete.

The composition of the C.E.M. can be deduced from the composition of the concrete according to [Schwartzentruber & Catherine, 2000][Erdem et al., 2009]:

- same type and dosage of cement;
- same water-to-cement ratio;
- use of the sand which was used in the concrete;
- addition of a quantity of sand reproducing the same granular specific surface than the gravel removed.

First, the volume of each constituent (water, cement and sand) of the reference concrete composition is calculated. Then all those are added to have a final volume less than the one with the aggregates, noted $V_{\text{C-NA,equiv}}$. Finally, the required mass of each constituent is obtained by multiplying the ratio of the initial volume (in which there are aggregates) over the new one with the mass used in the reference composition, e.g. with the water:

$$m_{\text{water,M2-CEMI}} = m_{\text{water,C-NA}} \frac{V_{\text{casting}}}{V_{\text{C-NA,equiv}}} \tag{5.5}$$

where V_{casting} is the required volume to cast each sample, as explained in the Appendix A.

Once the constituents are found, the mass of sand to add to reproduce the same granular surface than the gravel removed may be computed by:

$$S_{tot} = \sum_i n_{\text{aggregates},i}\, S_i = \sum_i \frac{M_i}{\rho\, V_{\text{grain},i}}\, S_i = \sum_i \frac{M_i}{\rho} \frac{4\ \pi\ r_i^2}{\frac{4}{3}\ \pi\ r_i^3} = 6\frac{M_{tot}}{\rho}\ \sum_i \frac{p_i}{d_i} \tag{5.6}$$

5.3 Experimental plan

The following section is dedicated to the experimental plan of this thesis. The various experiments performed are explained as well as their goals.
This experimental plan is obviously oriented towards drying and wetting experiments but porosity and permeability measurements will also be conducted.

5.3.1 Water Absorption by Immersion (NBN B 15-215:2018)

The Water Absorption by Immersion (WAI) test gives an indication of the water absorption and porosity of the sample. The modus operandi is dictated by the Belgian standard NBN B 15-215:2018.

The sample is weighed when completely saturated, in our case when exiting the humid chamber where it was conserved during curing: a first time under water to obtain the saturated mass, noted m_{sat}, and a second time in the air to obtain the humid mass, written m_{humid}. Then, it is weighed once again after being dried in a heat chamber at 105 $^\circ$C until reaching a constant mass m_{dry}.
The samples used were the one intended for the static sorption explained below, that is square plates of 100×100mm sides and approximately 10mm of thickness.

The water absorption, noted WA [% mass], is obtained by the following relation between the humid and dry mass:

$$\text{WA} = \frac{m_{humid} - m_{dry}}{m_{dry}} \times 100 \tag{5.7}$$

Another indicator of durability available through the WAI test is the porosity accessible to water, noted n_w [% volume]:

$$n_w = \frac{m_{humid} - m_{dry}}{m_{humid} - m_{sat}} \times 100 \tag{5.8}$$

However, this measure of open porosity is not as precise as the measure one would get from a mercury intrusion porosimetry, for example.

The two final pieces of information available are the dry and humid bulk density, noted respectively ρ_d and ρ_h:

$$\rho_d = \frac{m_{dry}}{V_{sample}} = m_{dry} \times \frac{\rho_w}{m_{humid} - m_{sat}} \tag{5.9}$$

$$\rho_h = \frac{m_{humid}}{V_{sample}} = m_{humid} \times \frac{\rho_w}{m_{humid} - m_{sat}} \tag{5.10}$$

5.3.2 Static Sorption and Desorption

Sorption and desorption isotherms, as well as water retention curves, may be obtained from static sorption and desorption experiments applying the vapour control technique presented in the Section 3.2.1. Those consist of hermetically sealed chambers (Figure 5.4) containing saline solutions to control the relative humidity. The samples hence lose or gain mass to reach a water content at equilibrium with the RH imposed by the saline solution.

Figure 5.4: Left: Chambers used for the static sorption and desorption experiment, with the RH and temperature probe and the samples inside. Right: sensor housing displaying the measures for the four probes used.

Each chamber contains four square plates of 100×100mm sides and approximately 10mm of thickness per composition, for a total of 20 plates. Before the experiment, the samples used for the sorption are completely dried until constant mass (the one used for the WAI test). The desorption requires saturated samples, and those are therefore taken directly from the humid chamber where they were curing. Each plate is carefully weighed before being put in the chamber.

Approximately once a week (each opening of the chamber disturbs the RH equilibrium), all the samples are weighed and the relative humidity and temperature of their chamber are taken from hygrometric sensors. Those chambers being kept in a room with controlled environment (60% RH and temperature of 21°C), the temperature isn't supposed to vary meaningfully. The weighing stops once the mass of the samples is considered constant.

In order to better control and interpret the results, five chambers (each containing a different saline solution) are used for the sorption and desorption. The Table 5.5 summarises the saline solutions chosen and their target relative humidity. The choice was oriented to cover the whole range of possible relative humidity.
The Kelvin law (Equation 3.2) allows, based on the temperature (supposed equal to 21°C) and target relative humidity, to determine a target suction. In the case of a target RH of 0%, which could never be completely met, the targeted suction is infinite. However, for a value of 6%, which is conceivable, the suction is equal to -381MPa.

Chamber id.	Saline solution	Target RH [%]	Target suction [MPa]
1 and 1'	KCl	90	-14.3
2 and 2'	$NaCl$	75	-39.1
3 and 3'	$Ca(NO_3)_2$	56	-78.7
4 and 4'	$MgCl_2$	35	-142.5
5 and 5'	Silica salt	0	∞

Table 5.5: Saline solutions used for the static sorption and desorption experiments.

Once the relative humidity of each chamber is stabilised and the mass of each plate is constant, the experiment stops. The mean water content is then calculated for each composition and for each RH in order to obtain the water retention curves of each composition. The water content requires the dry mass of each plate, and those therefore need to be dried in a heat chamber at $105°C$ after the experiment (except for the one used in sorption as they started dry).
The water retention curve, as it was mentioned in the Section 2.4.2, represents the evolution of the degree of saturation with respect to the suction. This water retention curve is then used to fit the Van Genuchten model to be used in the modelling aspect of this thesis.

5.3.3 Dynamic Vapour Sorption (DVS)

The Dynamic Vapour Sorption is an experiment equivalent to the static sorption/desorption experiment but faster as the term dynamic indicates. It consists of a device called DVS Intrinsic (Figure 5.5) in which a sample is continuously weighed while the environment around it is carefully controlled.

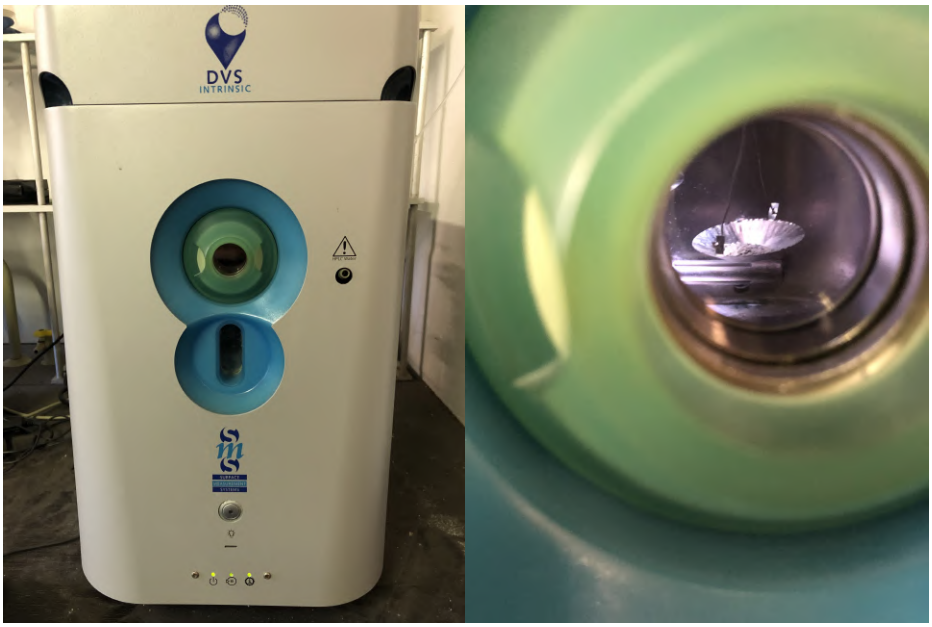

Figure 5.5: Device (DVS Intrinsic) used for the experiment, with the sample inside a little tray.

The experiment consists of a desorption and then sorption experiment under controlled constant temperature and controlled but variable relative humidity. The sample is initially saturated and in a targeted relative humidity of around 90% for a temperature of 21°C, chosen to better compare the results with the static ones. Then, each 450min., the relative humidity is reduced by 10% until 0% and then increased back to 90% following the same process.
The targeted relative humidity is obtained by means of a mix of dry gas (nitrogen) and water-saturated gas in the right proportions.

The samples used are required to be in powder form and their mass must be below 60mg. Therefore, only the mortars were tested as creating a homogeneous powder from concrete would be rather difficult due to the presence of aggregates. To create this powder, small samples of the mortar were crushed and then a small amount was sampled arbitrarily from the whole powder to keep the tested sample as representative as possible of the whole mortar.

The Figure 5.6 shows the process followed to crush the sample into a powder form, and then the results. The solid samples are taken from the filled water bucket and then crushed with a hammer onto a thick metal plate (below the towel). The sample is put inside the towel to decrease the losses and create the finest powder possible. Once the powder is sufficiently fine, it is scooped with a "flat spoon" and put inside a plastic container for a homogenisation process before being put on the DVS Intrinsic's tray.

Figure 5.6: Crushing process and final sample for the DVS Intrinsic.

The results obtained at the end of the experiment are similar to the one for the static sorption/desorption.

5.3.4 Convective micro-dryer

The convective drying is first done in what is called a "micro-dryer", constructed by A. Léonard during her PhD thesis [Léonard, 2002]. As its name indicates, it is built for the drying of small samples.

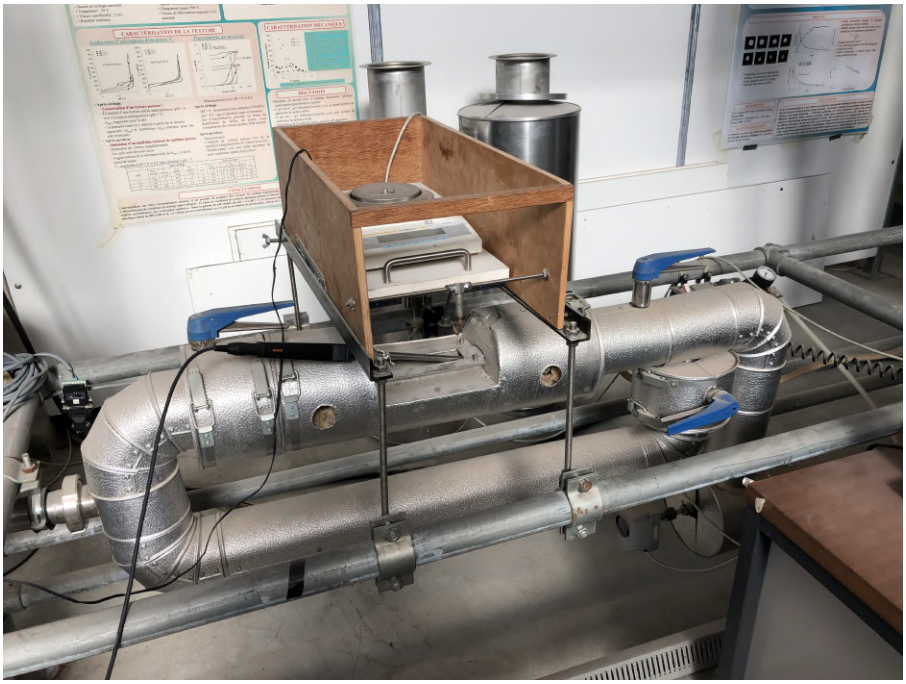

Figure 5.7: Convective dryer (called micro-dryer) built by A. Léonard during her PhD thesis [Léonard, 2002]

This instrument (Figure 5.7) allows the control of the relative humidity in addition to the temperature and velocity of the drying air. It is composed of two parts [Desaar, 2015]:

- an air conditioning and feeding system;
- the drying chamber;

the air being delivered thanks to the air compressor of the building. A pneumatic valve allows to regulate the air flow rate previously set and controlled by a mass flow metre.
The control of the relative humidity of the air is done with a steam generator. The drying air then passes through a heating body (resistance) to be brought to the desired temperature. In our case, as the goal is to completely dry the sample, the relative humidity targeted is null.

Once the drying air is at the desired velocity and temperature (which can be verified thanks to various sensors), it is sent to the drying cell where the sample is placed on a support allowing drying from all faces. This support is attached to a scale with an accuracy of a milligram (Figure 5.8).
Note that those various sensors are not linked to the software that saves the measures. Indeed, this experiment only yields the evolution of the mass with time. Therefore, the relative humidity of the drying air is not known precisely.

Figure 5.8: Platform and support containing the sample.

The environmental conditions chosen for this thesis are shown in the Table 5.6, as well as the chosen time interval between two measures.

Parameter	**Target value**
Temperature	40°C
Relative Humidity	0%
Air velocity	2.5 $\mathrm{m/s}$
Δt measure	120 s

Table 5.6: Conditions imposed to the drying air in the micro-dryer.

The samples used are cylinders of approximately 20mm of height for 15mm of diameter. Due to their small size, only the mortars were tested as the aggregates from the concrete would bias the results.
The drying takes place on all the faces of the sample, which would optimally require a spherical sample. However, this is obviously not possible and the closer we would get to a sphere is by using a sample whose height is equal to the diameter. In our case, the excessive height was chosen to decrease the risk of a predominant influence of a sand particle while keeping reasonable proportions with regard to the spherical form.

Initially, the samples are saturated as they were kept in the humid chamber. During the transport from one laboratory to another, they were kept in a bucket filled with water.
All samples are weighed on an analytical scale before and after the drying test to possibly correct the measurements if they were off (Figure 5.9). Then the samples are placed in an oven at 70°C to measure their dry weight and therefore obtain their water content.
It is also possible to measure the size of the sample before and after drying to observe any shrinkage, but previous similar studies have shown no measurable differences due to the high elastic modulus of the material [Desaar, 2015].

Figure 5.9: Weighing of the sample for the micro-dryer, before (saturated, left) then after the convective drying (partially dried, middle). The sample is also measured after drying (right).

The drying is considered finished when the mass is rather constant, which takes approximately one week. The samples are weighed every 120s. during the experiment and based on those measurements, we can determine the drying rate (Equation 3.3) and the water content at all time. However, the drying rate being a derivative, it amplifies the noise created by the experimental measures, which requires a filter or smoothing of the results.
The goal of this experiment is to obtain the Krischer curve for both mortar compositions, then determine, from the CRP, the mass and thermal transfer coefficients (α and β respectively) required for the modelling part.

5.3.5 Convective macro-dryer

The convective macro-dryer follows the same protocol as the micro-dryer except that it allows the use of bigger samples.

The samples used are cylinders of 40mm height for 80mm diameter. As they are bigger, it is possible to test all the compositions, the two mortars allowing a comparison of methods/results between the micro and macro-dryer.
It is important to use a sample of at least 80mm of diameter as this is equal to 10 times the maximum size of the aggregates used, which is important to remain representative and measure properties not related to the aggregates only.

The other important difference comes from the direction of the flow, which is perpendicular to the scale in this case while it was parallel to it in the micro-dryer. This induces load losses that are to be corrected in the final results. The Figure 5.10 shows the macro-dryer with its inside tray where the sample sits. The drying air comes from the top and is evacuated in the bottom. Once the sample is in place, the plastic ring is closed and sealed to the top with the help of the hangers visible on the top of the cell.

Figure 5.10: Macro-dryer used for the convective drying experiment, with the cell containing the sample.

5.3.6 Resistance to carbonation (NBN EN 13295:2004)

An important tool to measure the durability of concrete is the resistance to carbonation. This experiment is done in conditions dictated by the standard NBN EN 13295:2004 and summarised in the Table 5.7.

Parameter	Target value
CO_2 concentration	1%
Temperature	$21 \pm 2°C$
Relative Humidity	$60 \pm 10\%$

Table 5.7: Conditions imposed by the standard NBN EN 13295:2004.

The samples used are bars of square cross-section (100×100mm) and variable length (up to 400mm). The depth of carbonation is measured by breaking a sample and immediately applying a phenolphthalein solution used as an indicator. This solution will turn purple without carbonation and colourless if there is carbonation.
The same specimen may be used several times to measure the progression of the carbonation depth with time, by removing a small slice of the specimen at each measurement. A measurement is done each month to characterise the evolution.

Before being put in the controlled atmosphere, the samples must be dry-conditioned during at least 14 days until the mass is constant, with a loss of less than 0.2% in 24 hours.

The measurements of the carbonation depth are done as follows: divide the non-carbonated length (at least 30mm) of each flat surface (centred to remove the corners) into four equal parts, constituting five measuring points. The depth of carbonation is then measured with a calliper at each of the points determined, perpendicularly to the surface, with an accuracy within 0.1mm.
The average depth of carbonation of one side of the test piece is then obtained from the five individual values, rounded off to the nearest 0.5mm. This process is then repeated for the four sides of the sample.

5.3.7 Water permeability

Water permeability is an important property of concrete: it is defined as the ability of fluids to penetrate and migrate inside the porous medium.

The measurement of water permeability is done in a triaxial cell. The samples used are cylinders of approximately 100mm diameter and 100mm height, initially saturated as they are stored in the humid chamber and then in a filled water bucket before testing. The sample is then wrapped, along its height, inside a waterproof membrane to force the flow in one direction. Both its upper and lower sides are in contact with a porous disc to allow water movements. This sample is then put inside the triaxial cell and a water discharge is forced from the top to the bottom of the sample and controlled to obtain a constant internal pressure (P_{int}) of 2 bar: this method is called the constant-head method [Wikipedia, 2020b]. As concrete is poorly deformable, the macro-porosity on the side of the sample is filled with plaster in order to decrease the risk of microperforation of the waterproof membrane. The Figure 5.11 shows the triaxial cells used to measure the water permeability, as well as the device controlling the internal pressure. Upon closer look, the samples are visible, wrapped inside a thin latex sheet.

Figure 5.11: Triaxial cells (left) used for the water permeability measurement, with the pump (right) controlling the pressure.

Once the in-flow discharge is equal to the out-flow one, the saturated conductivity can be determined based on the Darcy's law under the hypothesis of a permanent flow in saturated

porous media [Dassargues, 2017]:

$$K_{sat} = \frac{Q}{i \times A} = \frac{Q}{A} \times \frac{H}{\Delta h} \tag{5.11}$$

with K_{sat} the water-saturated conductivity [$\mathrm{m/s}$], Q the discharge [$\mathrm{m^3/s}$], i the hydraulic gradient [-] and A the cross-sectional area of the member [$\mathrm{m^2}$]. The hydraulic gradient is calculated as the ratio of the hydraulic head (Δh [m]) over the height of the sample (H [m]).
The discharge is not measured directly, but a volume of water going through the sample is measured at certain times and then the discharge can be determined from the ratio of the volume over the elapsed time.

This value of water-saturated conductivity is highly dependent on the temperature and will therefore be transformed into a generic value at 10°C:

$$K(10^\circ\mathrm{C}) = \frac{Q \times H}{(P_{int} \times 10.19) \times A} \frac{1}{0.7 + 0.03 \times T} \tag{5.12}$$

where H [m] is the height of the sample, P_{int} [bar] is the internal pressure and is converted to pressure head [m] through the coefficient 10.19, and T [$^\circ$C] is the temperature of the environment (and therefore water). Finally, once this conductivity has been calculated, the intrinsic permeability [$\mathrm{m^2}$] can be obtained:

$$k_{int} = K(10^\circ\mathrm{C}) \times \frac{\mu_w}{\rho_w \, g} \tag{5.13}$$

Part III

Analysis of the Results

6 | Experimental Results

Contents

6.1 Introduction

This chapter summarises all the experimental results obtained during this thesis. Indeed, the experimental plan whose practical and theoretical aspects have been laid down in the previous chapter provided measurements and results requiring further investigation to gather the value of the various parameters used in the modelling part.

At first, some micro-photographs will be displayed to observe details such as the macro-porosity or the difference between a natural aggregate and a recycled concrete aggregate.
Then the Water Absorption by Immersion (WAI) experiment will be covered and used to confirm and validate the compositions and predictions used in this thesis.
Subsequently, the results of the static (de)sorption experiment and then the Dynamic Vapour Sorption (DVS) will be interpreted, allowing the determination of water retention curves and relative permeability curves. Continuing with drying experiments, the convective drying performed in the micro-dryer and macro-dryer will be studied.
Finally, the resistance to carbonation will be addressed in addition to the water permeability, the latter yielding results for the intrinsic permeability of our samples.

Note to the reader: due to the disease known as Covid-19 and the lockdown it resulted in, multiple experiments had to be stopped or couldn't occur, the access to the laboratories being restrained. Therefore, some complementary steps to the results laid down thereafter should have been conducted but simply couldn't. Overall, apart from the lack of results and reproducibility of the various experiments, the results obtained are valid. Nonetheless, some hypotheses have been necessary to the analysis of certain results.

6.2 Micro-Photography

Micro-photography is a good way to observe samples and to validate certain hypotheses or questions, hence its use in this thesis.

The first composition visible in the Figure 6.1 is the C-NA, where a pyrite inclusion is visible on the left. One can also see the ITZ around the aggregates which exhibits a whiter colour than its surroundings due to the less compact area and presence of cement in a greater quantity than the sand and/or aggregates.

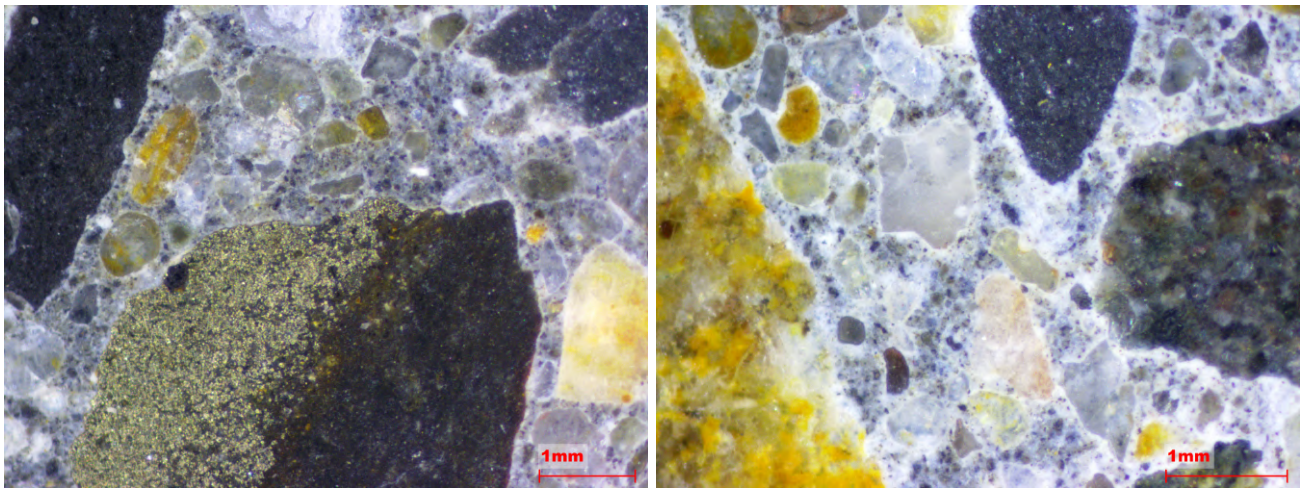

Figure 6.1: Micro-photographs of the C-NA sample

The Figures 6.1 and 6.2 show that there are no significant differences between the C-NA and C-NA-CEMIII except the colour of the cement.

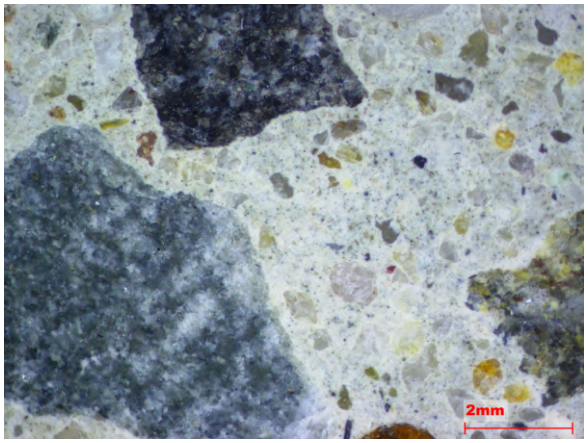

Figure 6.2: Micro-photography of the C-NA-CEMIII sample

If we now focus on the C-RCA in the Figure 6.3, it is possible to observe recycled concrete aggregates by their whiter colour due to the old mortar paste from the old concrete. Therefore, it looks like (to the naked eye) this composition possesses less aggregates than the C-NA but they both contain the same amount of aggregates in reality (due to our composition), the RCA being only less visible due to their old mortar paste. Indeed, the difference between a fully released RCA and a RCA with old mortar is visible in the last picture of the figure, explaining the difficulty to see every recycled concrete aggregate with a naked eye.

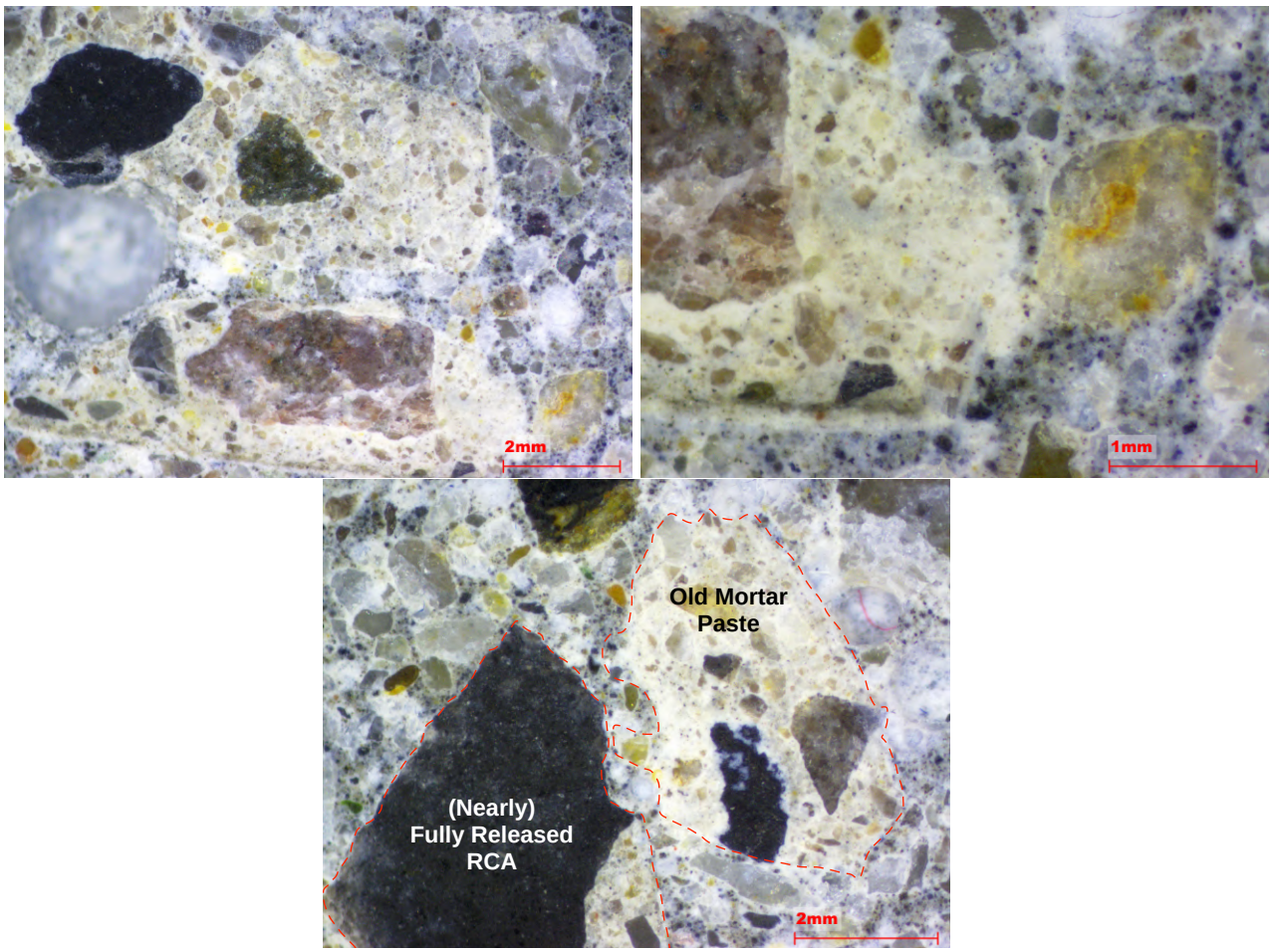

Figure 6.3: Micro-photographs of the C-RCA sample

The Figure 6.4 easily highlights the macro-porosity of the M1-CEMI composition, with macro-pores easily visible even to the naked eye. Moreover, it testifies the huge amount of sand used in the composition as it seems to be composed of only sand linked by a little cement paste. Indeed, if we compare those pictures with the ones of the Figure 6.5 relative to the M2-CEMI mix, the difference in the amount of sand used is eye-catching. The M2-CEMI also exhibits less visible pores.

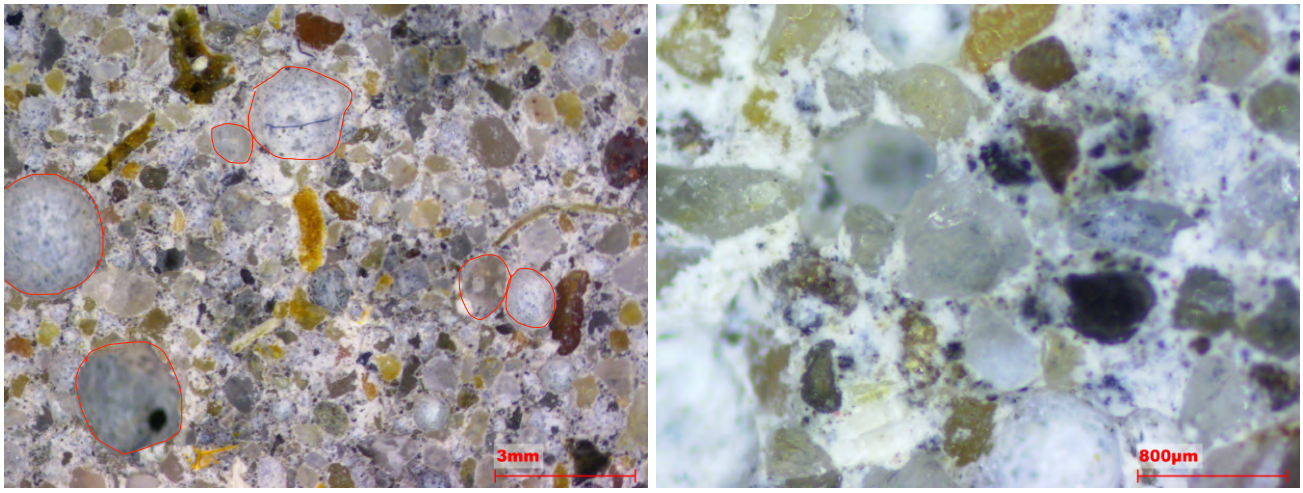

Figure 6.4: Micro-photographs of the M1-CEMI sample (with macro pores circled in red)

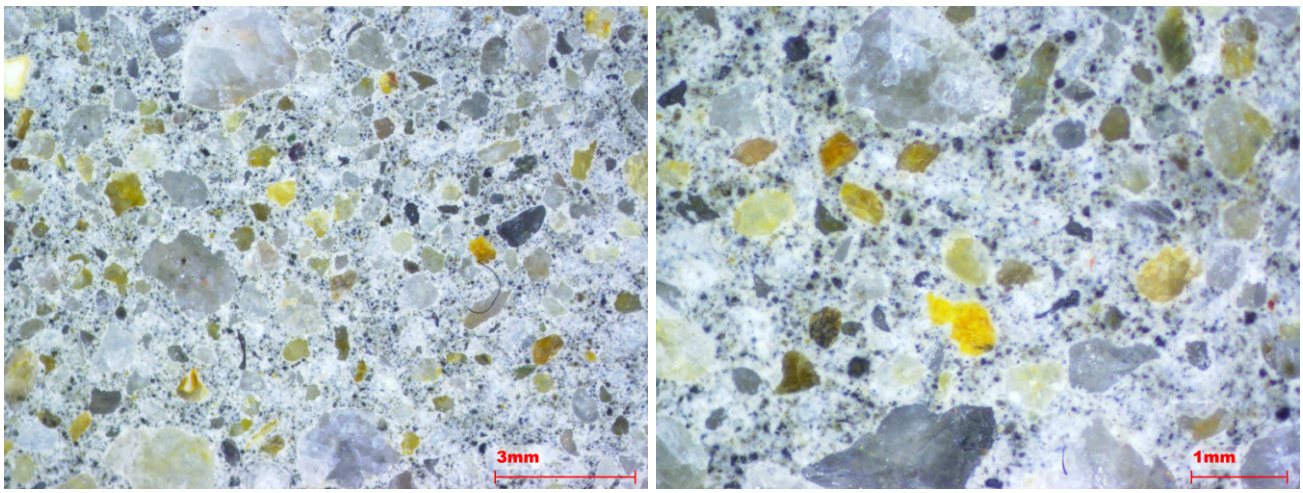

Figure 6.5: Micro-photographs of the M2-CEMI sample

6.3 Water Absorption by Immersion

The first experiment whose results are analysed is the water absorption by immersion test. This experiment yields values of the dry and humid densities of our five compositions as well as the water absorption and porosity, as it was introduced in the theoretical Section 5.3.1.

The density of each composition is exposed at the Figure 6.6 with their standard deviations. One can see both the dry and humid densities obtained from the WAI experiment but also the theoretical density and the density measured after unmoulding. The theoretical density is equal to the sum of the mass of each constituent (water, sand, cement and aggregates) for one cubic metre of composition, while the density after unmoulding is the density measured after the samples have been removed from the mould in the laboratory.

In the best of all worlds, the humid density, theoretical density and density after unmoulding are all equal. Indeed, the theoretical density and density after unmoulding are relatively similar except for the composition M1-CEMI, the difference being supposedly due to an insufficient workability which led to air bubbles being trapped inside the mould and therefore creating macro-porosity and decreasing the density of the mix.
The humid density from the WAI is also relatively similar to the density after unmoulding while remaining higher, mainly due to the saturation of the sample during their stay in the humid chamber.
Finally, the dry density cannot be compared to any other densities of the same Figure except that it is lower due to the moisture loss of the samples, the difference between both being, in theory, equal to the water absorption of each composition multiplied by the density of water. However, as the water absorption obtained during this experiment is solely based on this assumption, it is useless to calculate this density difference as we're sure it would correspond.

The two final properties obtained from the WAI experiment are the water absorption [% mass] and the porosity [% volume], both exhibiting similar trends (Figure 6.7). However, the measure of the porosity is not as accurate as one could expect as it only represents the porosity accessible to water.

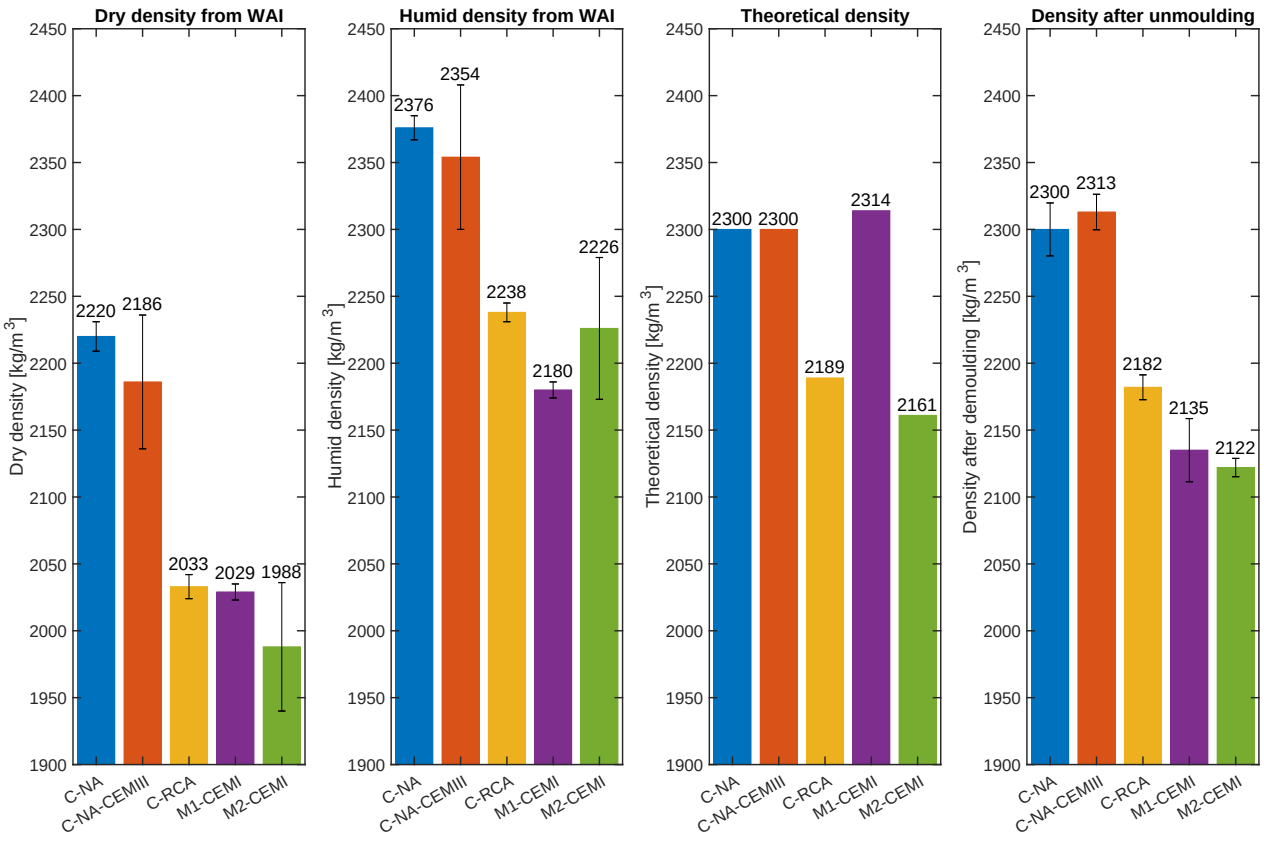

Figure 6.6: Results from the Water Absorption by Immersion experiment: densities. From the left to the right: dry density, humid density, theoretical density and density after unmoulding.

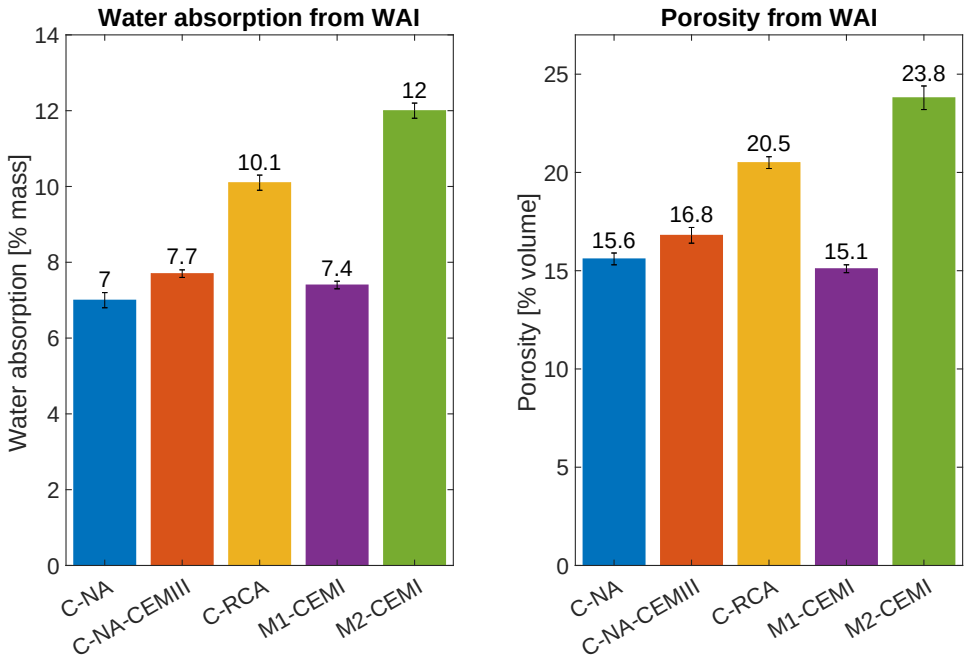

Figure 6.7: Results from the Water Absorption by Immersion experiment: water absorption and porosity.

It is known that the recycled concrete aggregates have a higher water absorption than the natural aggregates. The water absorption of both aggregates has been measured before mixing the compositions and it is therefore possible to correlate the difference in water absorption between the C-NA and C-RCA with the difference in water absorption of their respective aggregates:

$$\begin{cases} \Delta \text{WA}_{\text{C-NA and C-RCA}} = \text{WA}_{\text{C-RCA}} - \text{WA}_{\text{C-NA}} = 10.1 - 7 = 3.1\% \\ \Delta \text{WA}_{\text{NA and RCA}} = \text{WA}_{\text{RCA}} - \text{WA}_{\text{NA}} = 3.41 - 0.57 = 2.84\% \end{cases} \tag{6.1}$$

which are close enough to validate that the two compositions will exhibit differences in properties due to the differences in aggregates mainly, and not because of an inappropriate composition.

Another possible validation of the compositions consists in the study of the water absorption of the mortar of the C-NA and the M2-CEMI as both are supposed to have the same rheological properties due to the Concrete Equivalent Mortar formulation. Indeed, the first step is to find the amount of water absorbed by the natural aggregates in the C-NA mix:

$$m_{NA} \times \text{WA}_{\text{NA}} = 1065 \times 0.57\% = 6.07\text{kg} \tag{6.2}$$

Then this quantity of water is divided by the theoretical density of the C-NA to obtain a water absorption due to the NA, which is withdrawn from the water absorption of the C-NA to obtain the water absorption of the mortar paste only:

$$\text{WA}_{\text{mortar of C-NA}} = \text{WA}_{\text{C-NA}} - \text{WA}_{\text{NA inside C-NA}} = 7 - \frac{6.07}{2300} = 6.73\% \tag{6.3}$$

Finally, we can calculate the percentage of mass occupied by the mortar paste inside the C-NA composition and then, by a simple "rule of three", the water absorption can be obtained as if there was 100% of mortar only:

$$\text{WA} = 6.73\% \text{ for } \frac{2300 - 1065}{2300} \times 100 = 53.69\% \longrightarrow \text{WA} = 12.54\% \text{ for } 100\% \text{ of mortar} \tag{6.4}$$

which is close enough to the 12% of water absorption of the M2-CEMI mix.

A remark worth doing is that the M1-CEMI contains a lot of macro-pores due to air bubbles being trapped during the casting of the samples, while the M2-CEMI exhibits a less visible porosity (as it was mentioned based on the Figures 6.4 and 6.5). It is therefore hard to believe that the M1-CEMI has a lower porosity and WA than the M2-CEMI and this could be verified by a water absorption test under vacuum.

6.4 Static Sorption and Desorption

The next experiment whose results will be analysed is the static sorption and desorption experiment. After stabilisation of the relative humidity inside each chamber, the mass was obtained and the water retention curves were drawn and fitted with the Van Genuchten model. The equilibrium RH obtained and its corresponding suction (through the Kelvin law, Equation 3.2) have been added to the Table 6.1.

Chamber id.	Saline solution	Target		Equilibrium	
		RH [%]	**Suction** [MPa]	**RH** [%]	**Suction** [MPa]
Static Sorption					
1	KCl	90	-14.3	83.79	-24.07
2	$NaCl$	75	-39.1	77.69	-34.38
3	$Ca(NO_3)_2$	56	-78.7	56.12	-78.72
4	$MgCl_2$	35	-142.5	39.99	-124.94
5	Silica salt	0	∞	8.21	-340.13
Static Desorption					
1'	KCl	90	-14.3	84.66	-24.04
2'	$NaCl$	75	-39.1	78.44	-34.35
3' and 3'bis	$Ca(NO_3)_2$	56	-78.7	76.87 and 66.9	-35.82 and -54.67
4' and 4'bis	$MgCl_2$	35	-142.5	40.22 and 57.22	-123.93 and -76.06
5' and 5'bis	Silica salt	0	∞	39.66 and 33.19	-125.8 and -149.9

Table 6.1: Saline solutions used for the static sorption and desorption experiments: equilibrium RH and suction.

The evolution of the relative humidity inside each chamber with respect to time can be seen in the Figure 6.8. One can observe in dash-dot line the RH targeted inside each chamber and then, in simple line, the actual value of the RH inside each chamber. Moreover, for the static desorption, the chambers 3'-4'-5' have been doubled in order to speed up the process: the dash line represents each new chamber (starting from day 10).
The values of the RH at equilibrium are not always equal to the values predicted, especially for low RH. Moreover, the chambers used for the static sorption have been stabilised long before the ones for the static desorption as the conditions are easier to work with (saturation of the sample and not desaturation).

As one can also see, the measurements were initially done once a week but were then spaced out to minimise disruption of the chambers and give more time to the samples to reach a constant mass.

The Figure 6.9 represents the cumulative mass gain (sorption) and loss (desorption) for each composition inside the chambers 1 and 1'. The same graphics may be seen in the Appendix B for the other chambers. On the title of each graph, one can read the final value of the RH (or two values for the desorptions of the chambers 3'-4'-5': the first one for the plain line and the second one for the dash line). Moreover, at each weighing, the standard deviation is also shown to measure the confidence in our results.

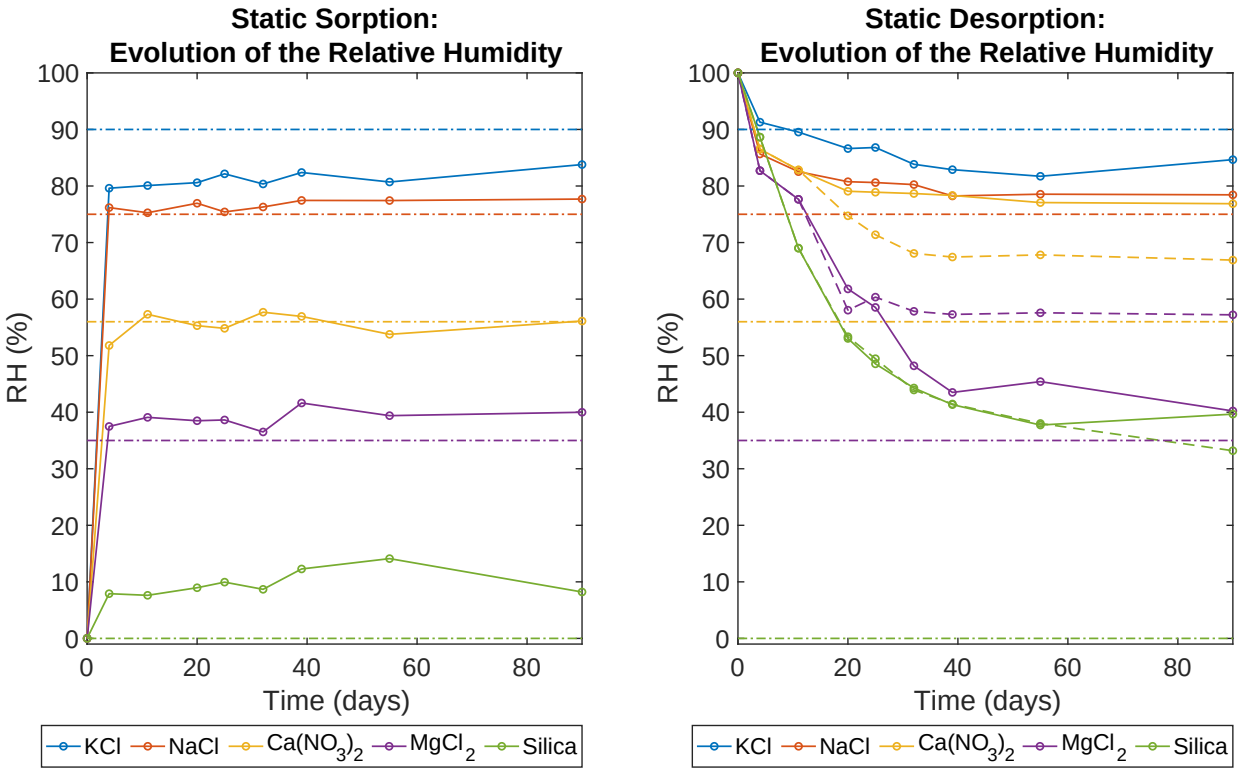

Figure 6.8: Evolution of the Relative Humidity inside each chamber towards a target RH.

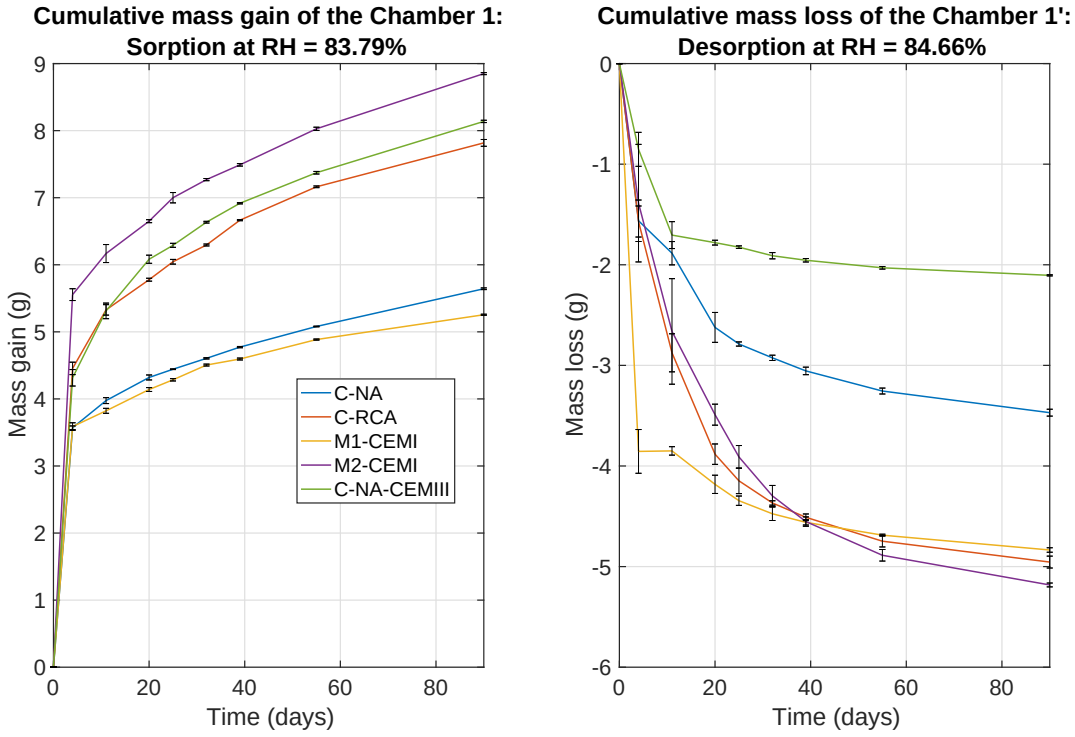

Figure 6.9: Cumulative mass gain (sorption) or loss (desorption) for the Chambers 1 and 1'.

Based on the value of the RH and the final mass of each sample, it is possible to determine the saturation corresponding to each suction in order to draw the Water Retention Curve for each composition. Then, the Van Genuchten model can be applied to those curves (Equation 2.14) and the relative permeability can also be deduced from this model (Equation

4.16). The water retention curve and relative permeability curve corresponding to the C-NA composition are shown in the Figures 6.10 and 6.11 for the desorption and sorption respectively, while the same results for the other compositions can be found in the Appendix B.

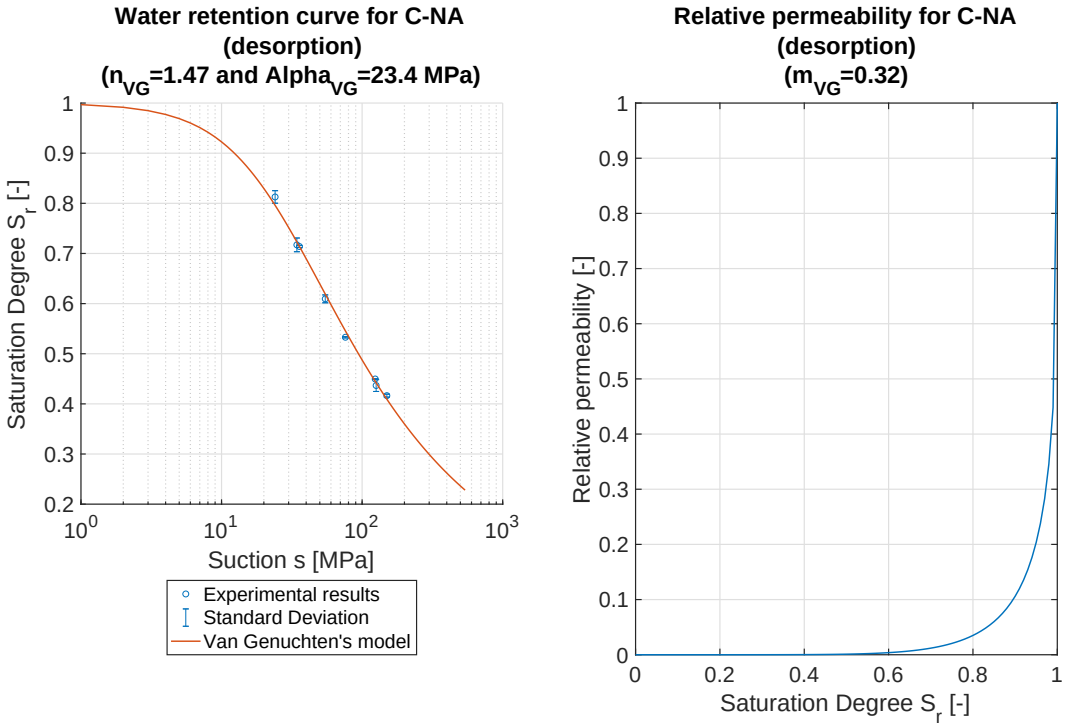

Figure 6.10: Water retention curve fitted with the Van Genuchten model and its corresponding relative permeability curve for C-NA in desorption.

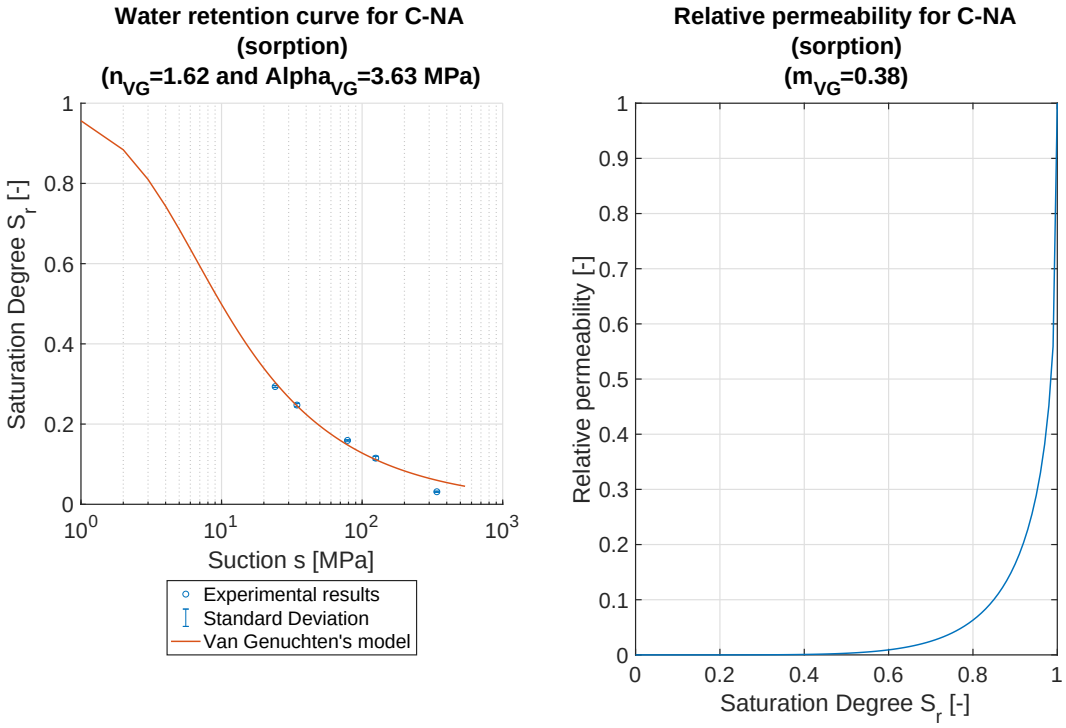

Figure 6.11: Water retention curve fitted with the Van Genuchten model and its corresponding relative permeability curve for C-NA in sorption.

The Table 6.2 summarises the value of all the parameters obtained for each composition, for both the sorption and desorption experiments. In addition to the Table 6.2, one can compare the results in terms of water retention curve through the Figure 6.12.

Parameter	C-NA	C-RCA	M1-CEMI	M2-CEMI	C-NA-CEMIII
Static Desorption					
α_{vG} [MPa]	23.4	19.88	9.93	26.69	35.75
n_{vG} [-]	1.47	1.44	1.33	1.66	1.93
m_{vG} [-]	0.32	0.31	0.25	0.4	0.48
Static Sorption					
α_{vG} [MPa]	3.63	4.65	3.48	3.26	6.58
n_{vG} [-]	1.62	1.67	1.59	1.58	1.71
m_{vG} [-]	0.38	0.4	0.37	0.37	0.42

Table 6.2: Values of the Van Genuchten model's parameters to be used in the modelling and obtained through the static sorption and desorption experiments.

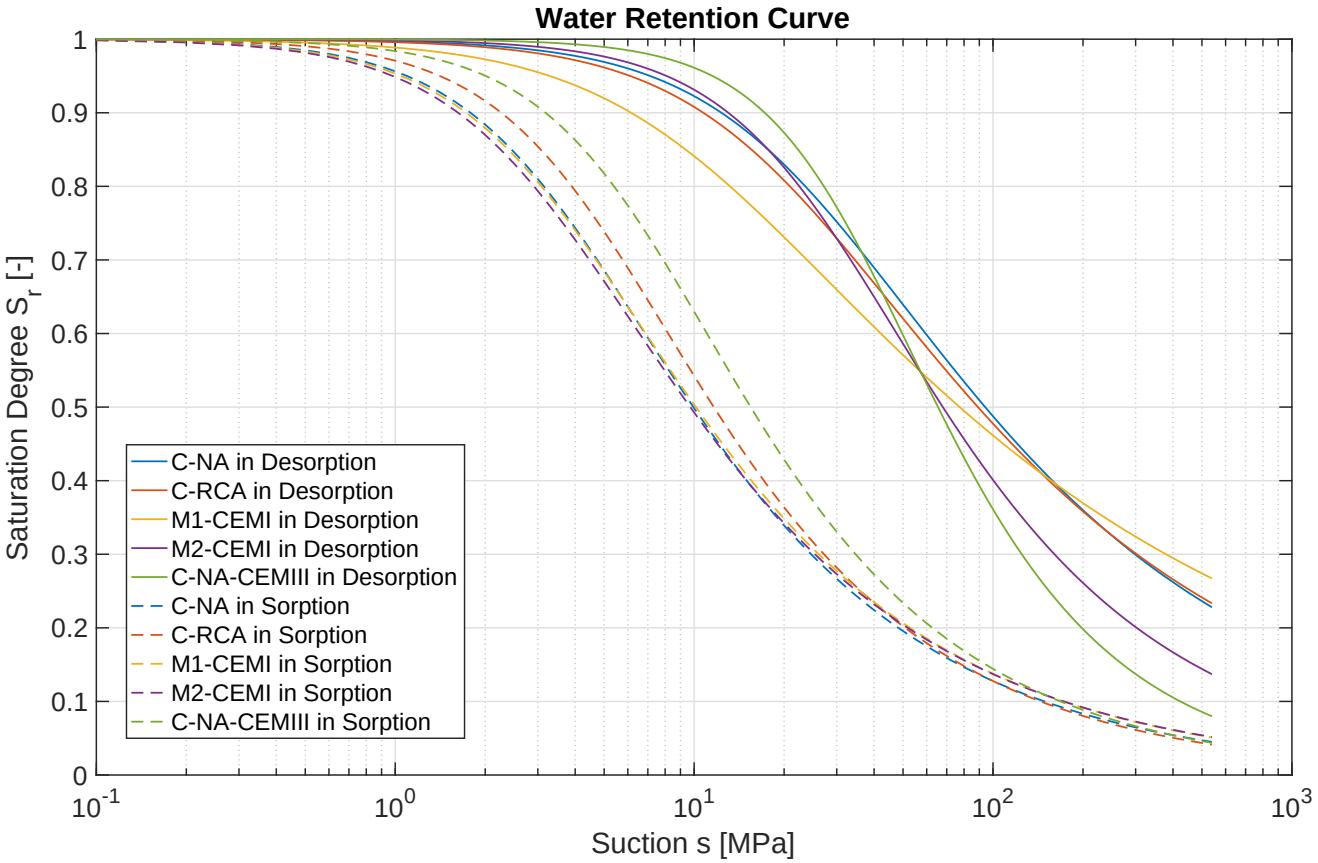

Figure 6.12: Water retention curves from the Van Genuchten model for all compositions.

The results show that the use of RCA in concrete reduces the air-entry pressure α_{vG} (for desorption) while having no significant effect on the parameter n_{vG}. It means that, for any

value of the suction and more particularly for low suction, the saturation degree will be lower in the C-RCA than in the C-NA. The C-NA-CEMIII, on the other hand, has a greater air-entry pressure and exhibits a steeper curve, meaning that the material will start to desaturate for bigger suction value, but this desaturation will happen faster. However, one should not forget that the faster a sample desaturates and the lower the relative permeability gets. Therefore, a low-permeability zone is created and the water content inside the sample has more difficulty to reach the surface.
For the mortars, the M1-CEMI has an air-entry pressure far lower than the M2-CEMI, which could come from a greater porosity, which is in opposition with the results from the Water Absorption by Immersion. However, the static desorption experiment seems to be of a greater precision than the WAI, and further experiments in terms of porosity measurement should be conducted.

For static sorption results, the curves should be analysed the other way around. Indeed, sorption happens when the relative humidity increases, which in turn decreases the suction. By looking at the curves, one can see that the C-RCA has an increase of its saturation greater than the C-NA, for a same increase of the suction, which is similar to the results of the desorption. Furthermore, results from the C-NA-CEMIII, M1-CEMI and M2-CEMI are identical to the ones for the desorption too, which is to be expected.

A final remark is that there is clearly a hysteresis in the water retention curve for all compositions, as it was outlined in the theoretical study of water retention curves.

6.5 Dynamic Vapour Sorption (DVS)

As it has been explained in the theoretical approach of our experimental plan, the dynamic vapour sorption experiment is relatively similar to the static sorption/desorption experiment. The main and important difference between both is the sample. Indeed, the samples consisted of plates for the static sorption while it is in form of a crushed powder for the dynamic sorption. Crushing the sample into a powder reduces the porosity of the paste as most of the pores just vanish, therefore reducing the differences between compositions.

The only two compositions tested are the mortar ones: M1-CEMI and M2-CEMI, as the crushing process is forbidden for concrete due to the higher aggregates' size. Indeed, the mass of the sample used is quite limited (60mg) and the risk of only characterising an aggregate would be too high, while the greater homogeneity of a mortar is better suited for this experiment.

However, please take note that two hypotheses were made in this experiment:

- The sample is initially saturated: indeed, the sample is initially saturated as it was stored in the humid chamber since casting and was then transported in a filled water bucket to the laboratory. However, the crushing process decreases the saturation of the sample, and it would therefore be required to saturate it once again after the experiment, which was not done here;
- The residual saturation of the sample is equal to zero: once again, this would need to be confirmed by drying the sample at the end of the experiment in order to compare

the dry mass of the sample to its mass at the end of the 0% RH cycle, which couldn't be done in this thesis.

6.5.1 M1-CEMI composition

The first composition studied is the M1-CEMI. The Figure 6.13 represents the evolution of the mass with time (on the left) as well as the hysteresis of the mass as a function of the relative humidity (on the right). On the left graph, one can clearly see the different cycles of RH done, with the blue line representing each measure of the mass and the orange one only the last measure of each cycle.
As it was mentioned in the theoretical presentation of this experiment, the shift from one value of the RH to the following is done automatically after a fixed period of time (600 or 450 minutes depending on the experiment) and not once the sample mass was stabilised, in the pursue of time saving. However, one can see that the last points are nearly all on a plateau or at the beginning of one, ensuring the accuracy of the results.

On the right curve, one can see that the hysteresis is not fully closed which is due to the lack of nitrogen at the last step (RH=90%) which made it impossible to stabilise the RH at the desired value.
Furthermore, the two parts of the hysteresis (the upper one being the desorption and the lower one the sorption) are relatively close to each other, the differences possibly resulting from the non-stabilisation of the mass before a RH change. However, this hysteresis effect is also mainly due to the increased resistance a porous system offers to saturation compared to desaturation. Indeed, the air in the pores needs to be pushed outside of the sample for the pores to be filled with water (see Section 2.4.2 for more details).

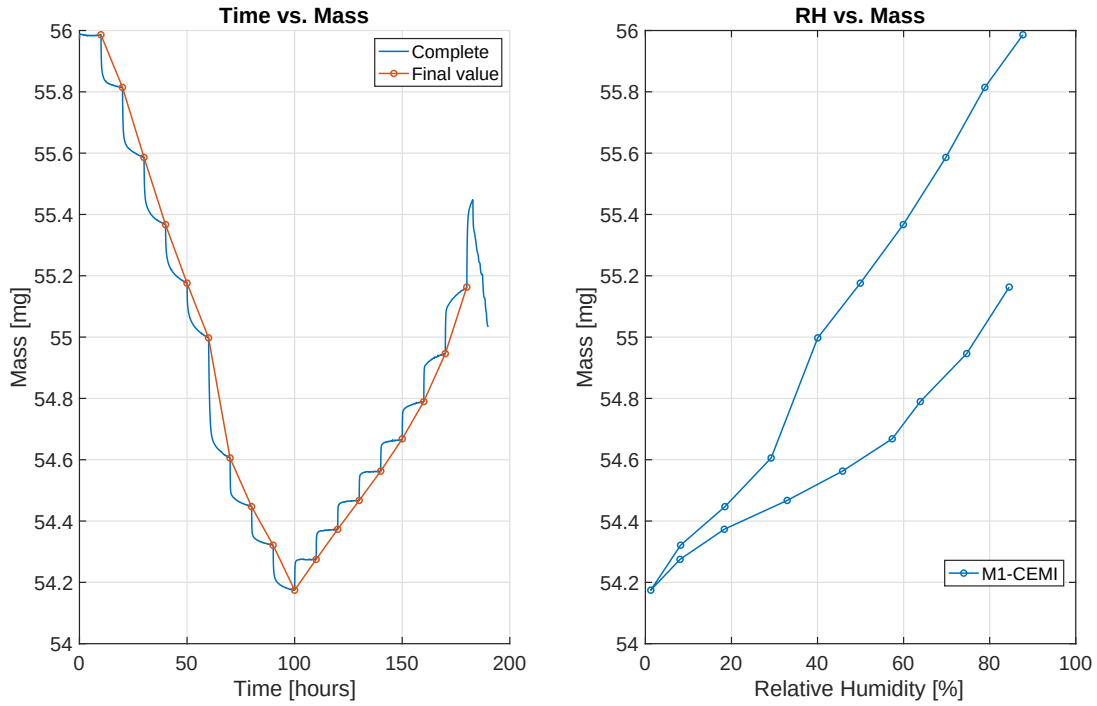

Figure 6.13: Evolution of the mass with respect to time and hysteresis RH vs. Mass for the M1-CEMI composition.

The Figure 6.14 shows the water retention curve and relative permeability curve fitted with the Van Genuchten model. The values of the three model parameters are written in the title of each graph. The two hypotheses stated before (for S_{max} and S_{res}) are also visible and the value of the parameters may have changed a little bit if those were not confirmed.

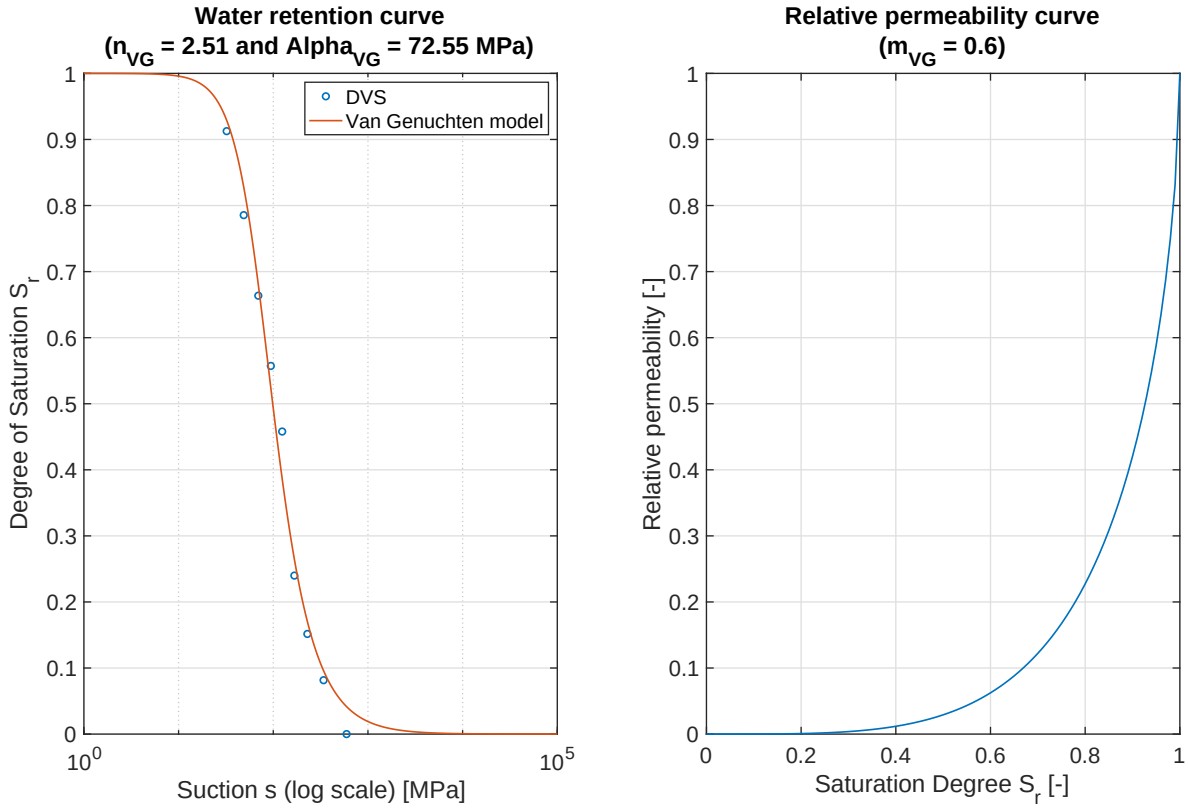

Figure 6.14: Water retention curve fitted with the Van Genuchten model and its corresponding relative permeability curve for M1-CEMI.

6.5.2 M2-CEMI composition

The composition M2-CEMI was tested two times, the only difference between both being the amount of time between each change of relative humidity. The Figure 6.15 exhibits the evolution of mass with time (left) as well as the final mass value for each RH (right). The same conclusions as for the M1-CEMI can be stated.

Finally, the Figure 6.16 also represents the water retention curve and relative permeability curve fitted with the Van Genuchten model. The values of the model parameters are nearly identical to the one of the M1-CEMI, which confirms the hypothesis that the crushing process deteriorates the porosity and that only the material itself, without porosity, is tested. Moreover, as the quantity of material sampled for the two compositions is relatively similar, the main difference may only come from the amount of sand in the sample, one composition having more sand than the other. Indeed, the absorption is dependent on the specific surface of the sample mainly as the porosity has been hugely decreased and therefore the capillary effects happening are due to an agglomeration of particles with the humidity. All in one, the small difference between the two compositions is mainly due to the crushing and sampling process.

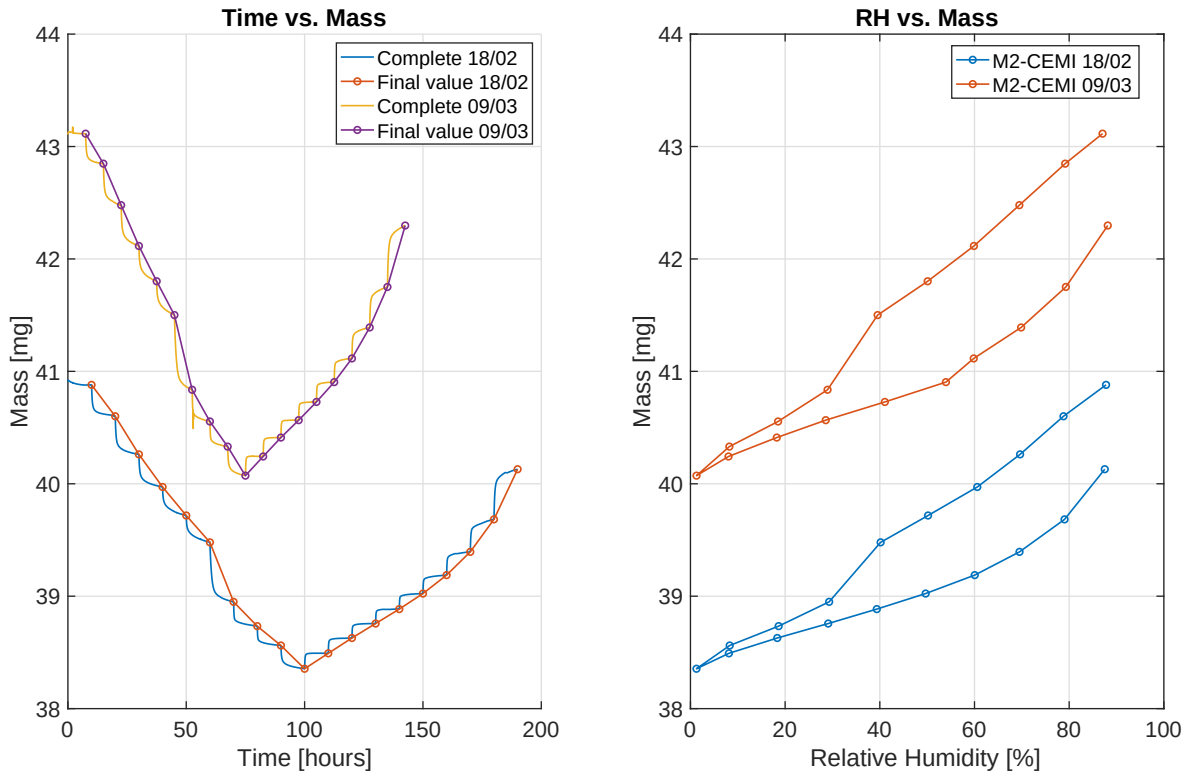

Figure 6.15: Evolution of the mass with respect to time and hysteresis RH vs. Mass for the M2-CEMI composition.

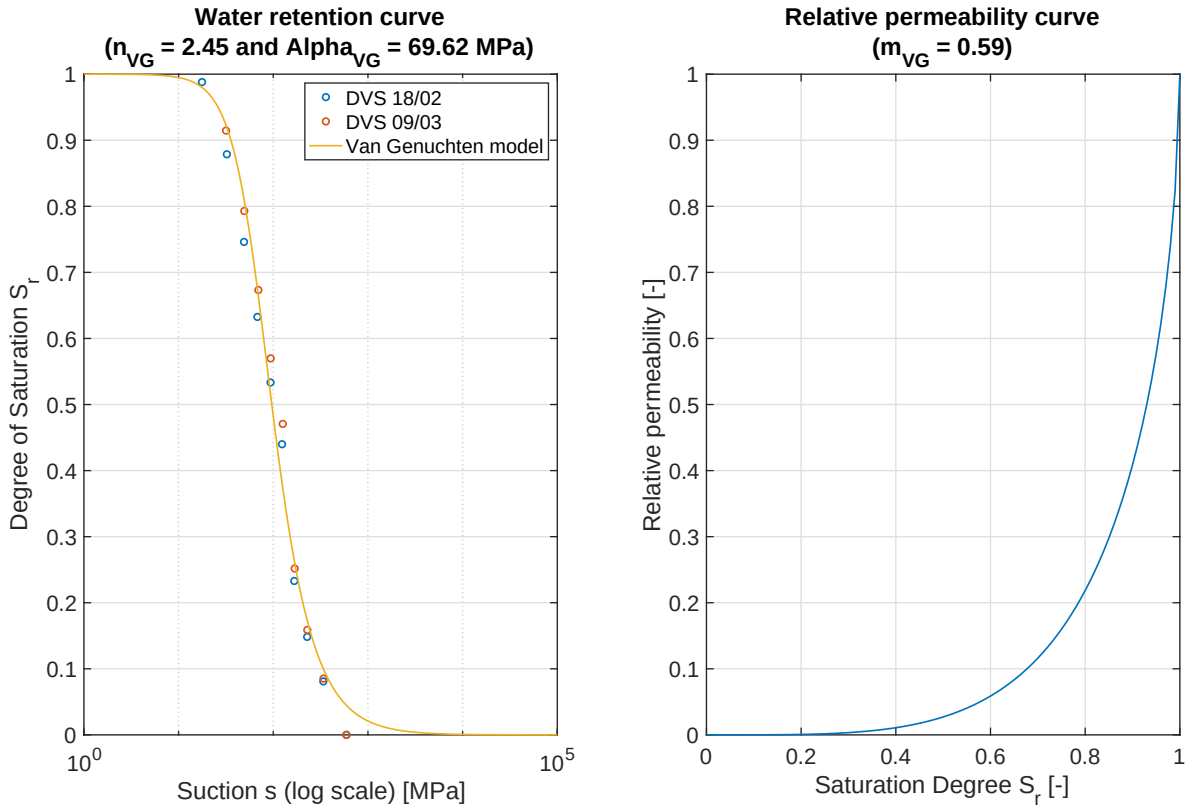

Figure 6.16: Water retention curve fitted with the Van Genuchten model and its corresponding relative permeability curve for M2-CEMI.

6.6 Convective drying

We will now focus our attention on the convective drying experiments conducted. At first, the results of the micro-dryer are investigated and then the one of the macro-dryer will be analysed. Both drying experiments were conducted for the same composition M1-CEMI and with the same conditions regarding the drying air. All the theoretical bases have been laid out before and are therefore not addressed here.

6.6.1 Micro-dryer

The Figure 6.17 shows the mass loss with time on the left and the Krischer curve on the right, that is the drying rate as a function of the normalised moisture content. All results are shown unrefined and then smoothed with a moving median filter. The smoothing is done to better apprehend the various phases of the Krischer curve by reducing the noise of the initial measures. However, smoothing the curves induces a high dependency of the results on the filter, particularly for the value of the drying rate during the CRP.

As one can see, two experiments were conducted with results slightly different. Indeed, the second one (in yellow and purple) was far smoother from the beginning than the first one, which results in a smoother Krischer curve. However, both exhibit a relatively similar mass loss, the drying rate being a little bigger for the second one than for the first one as it is also visible in the Krischer curve. An explanation for this phenomenon may be that the first experiment took place once the drying air was at the desired temperature, but the whole system was certainly not, while for the second experiment, the whole system had been heated to the desired temperature during 6 days, possibly increasing the drying rate.

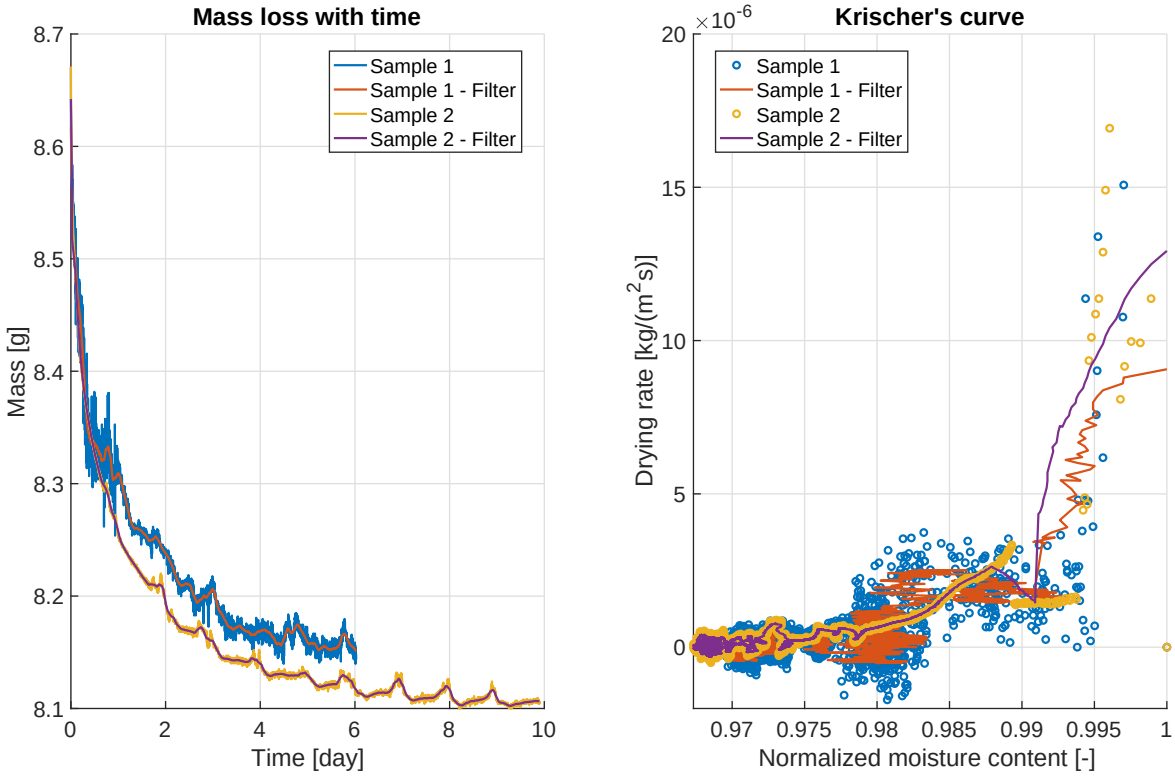

Figure 6.17: Mass loss and Krischer curve for the micro-dryer for the M1-CEMI.

The Table 6.3 contains the initial and final mass measured on an analytical scale for both samples tested. The final mass was measured just after the sample has been removed from the micro-dryer. However, to determine the residual saturation of the sample, it was then dried in a heat chamber at 70°C until reaching a constant mass. This has only been done for the first sample as access to the lab has been removed during the second experiment.

Initial Mass [g]	Final Mass [g]	Mass loss [g]	Dried mass [g]	Duration [hours]
8.6707	8.103	0.5677	8.02	144.6
8.6711	8.003	0.6681	-	237.53

Table 6.3: Measured mass and duration of each drying experiment.

The Table 6.4 shows the value of the drying rate during the CRP determined from the Krischer curve of the Figure 6.17, for each experiment. Then, based on those and the theoretical formulations explained in the Chapter 4, the value of the transfer coefficients α and β were determined. To obtain these, the value of the temperature and relative humidity of the drying air are also required. As explained in the theoretical approach for convective drying, the temperature is set to 40°C and the goal is to reach a relative humidity of 0%. However, this value is not measured during the test as only the mass is measured. The only value of RH known is the RH of the air exiting the compressor, which is at 17%. However, the value of the RH could also be determined by fitting the experimental curve with the model and a value of around 3% was found, which is the one used for the calculation of the transfer parameters.

q_{CRP} [kg/(m^2.s)]	α [m/s]	β [W/(m^2.K)]
8.8E-6	7.25E-4	0.915
13E-6	11E-4	1.352

Table 6.4: Parameters determined from the convective micro-drying experiment for M1-CEMI.

6.6.2 Macro-dryer

The same convective drying experiment was done in the macro-dryer. The main difference between the micro and macro-dryer is the size of the sample as well as the direction of the drying air flow, which in the case of the macro-dryer is perpendicular to the scale and therefore induces perturbations in the measures of the mass. However, the sample has been weighed before and after the experiment to correct the measures.

As one can see on the Figure 6.18, the macro-dryer has experienced greater disruptions than the micro-dryer, the mass loss and Krischer curves being less smooth. A moving median filter was also applied to reduce the noise of the measurements and to better grasp the various phases of the Krischer curve.

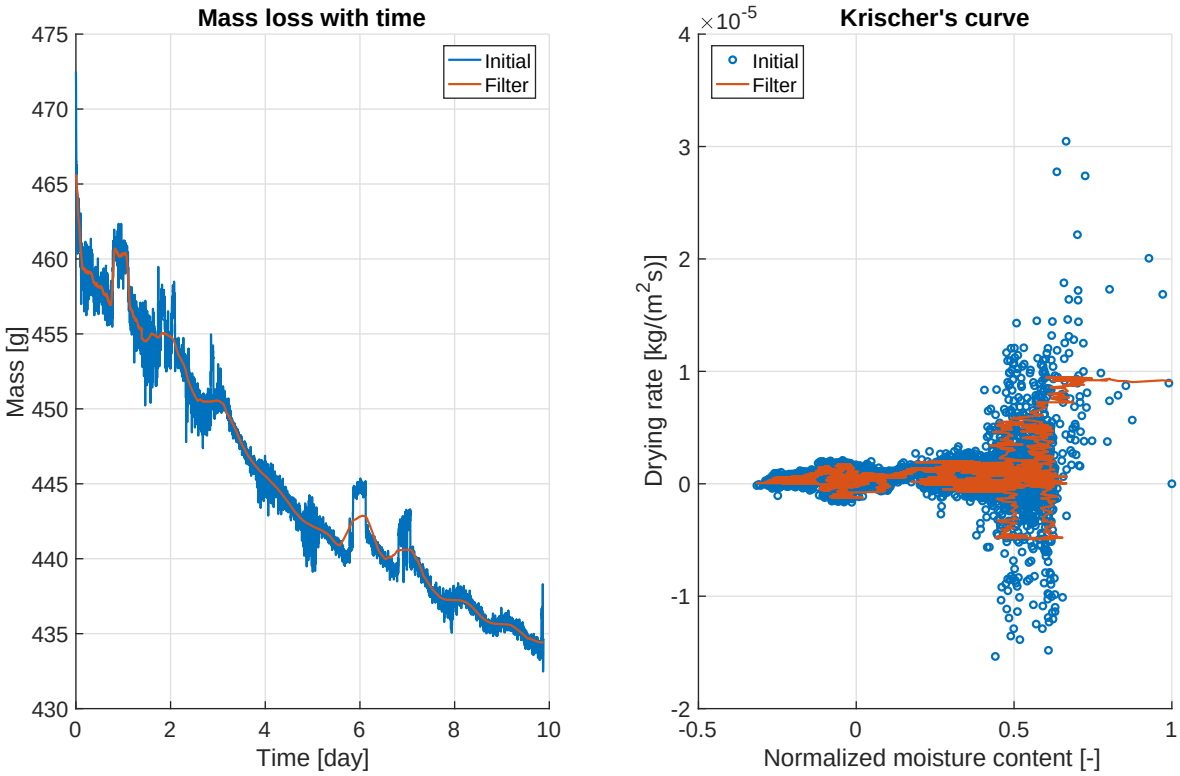

Figure 6.18: Mass loss and Krischer curve for the macro-dryer for the M1-CEMI.

As for the micro-dryer, the initial and final mass were obtained through weighing on an analytical scale just before and after the experiment, respectively. The dried mass after drying in a heat chamber was not obtained due to the restrained access to the lab. All this information is displayed in the Table 6.5.

Initial Mass [g]	Final Mass [g]	Mass loss [g]	Dried mass [g]	Duration [hours]
472.5	452	20.5	-	237.1

Table 6.5: Measured mass and duration of the convective macro-drying for M1-CEMI.

The Table 6.6 also shows the value of the drying rate during the CRP determined based on the Krischer curve, as well as the value of the transfer coefficients α and β through the same hypotheses as stated for the micro-dryer.

q_{CRP} [kg/(m^2.s)]	α [m/s]	β [W/(m^2.K)]
9E-6	7.42E-4	0.936

Table 6.6: Parameters determined from the convective macro-drying experiment for M1-CEMI.

6.7 Resistance to carbonation

The experiment measuring the resistance to carbonation provides results in terms of carbonation depth. The evolution of the carbonation depth for all four sides of the C-NA composition is represented in the Figure 6.19 as well as in the Appendix B for the other compositions. In addition, pictures showing the samples coloured with phenolphthalein are displayed in the Appendix C. The first side is the upper one, exposed when the sample is still inside the mould, while the others are counted in the trigonometric way, as displayed in the Figure 6.20. The x-axis is the evolution of the time in $\sqrt{t}$ as the carbonation depth is calculated as:

$$s = k\sqrt{t} \tag{6.5}$$

where s is the carbonation depth, t is the time and k is a coefficient depending on the amount of product that can be carbonated, concentration of CO_2 in the surroundings as well as a diffusion coefficient.

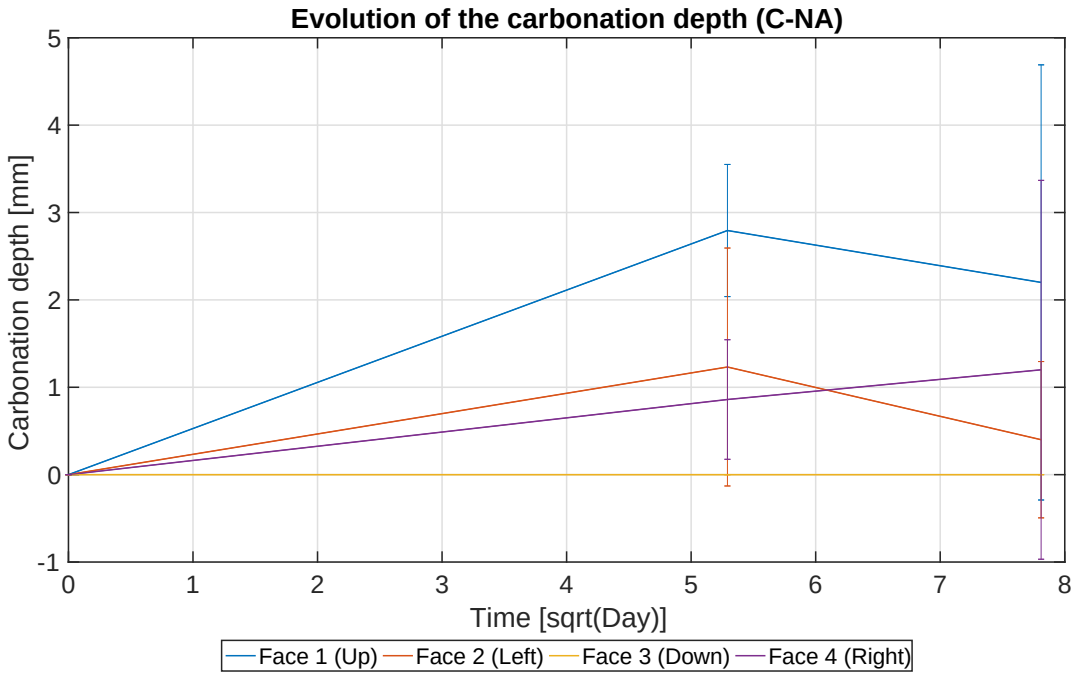

Figure 6.19: Evolution of the carbonation depth [mm] for the C-NA composition.

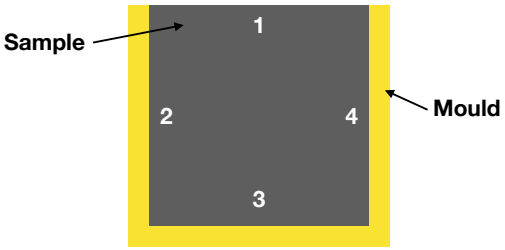

Figure 6.20: Example of the numbering of each side of the sample for the measures of the resistance to carbonation.

The final value of the carbonation depth for all compositions is then represented at the Figure 6.21 as well as in the Table 6.7. Various remarks can be made:

- The bottom face (Face 3) seems to be, in general, the less impacted one by carbonation, mainly because this is the face where the compaction is the greatest during the moulding of concrete.
- Except for the upper face (Face 1), the C-NA-CEMIII displays the higher carbonation depth among all the compositions. It is due to the cement type which contains fewer products prone to carbonation (lime $\mathrm{CaOH_2}$) and therefore allows a greater speed of carbonation.
- The M1-CEM1 always displays a higher carbonation depth than the M2-CEMI, which may be due to a higher porosity or more accessible porosity, once again proving the insufficient accuracy of the porosity obtained by the WAI experiment.
- The C-RCA always displays a greater carbonation depth than the C-NA, possibly due to the higher value of porosity. However, one could also think that the greater cement content due to the recycled concrete aggregates would slow the reaction of carbonation. Nonetheless, those RCA are probably already pre-carbonated due to their storage in contact with the ambient air. The greater value for the Face 1 may be due to a higher local porosity created during compaction.

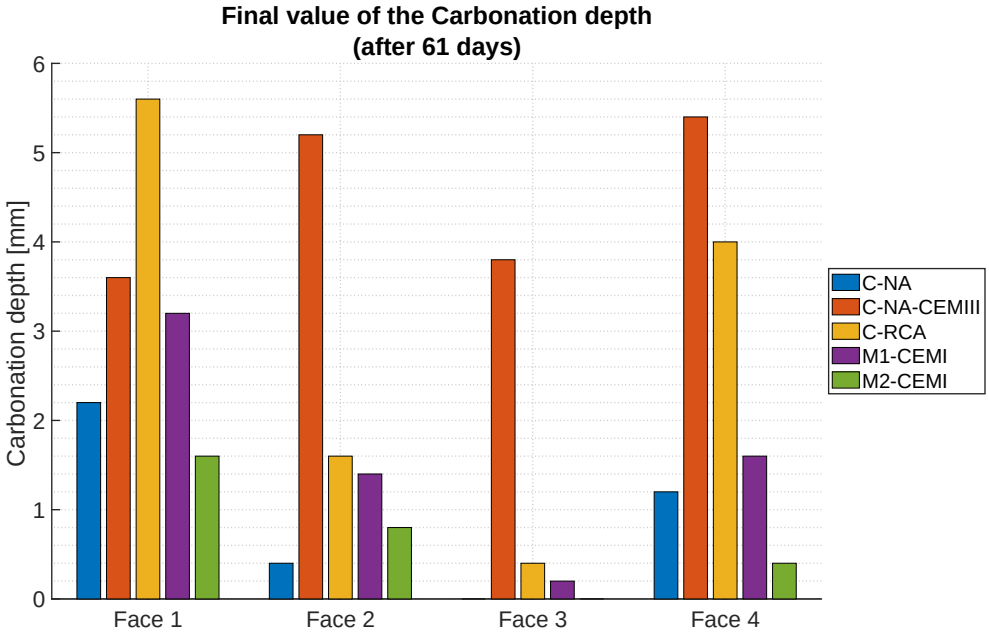

Figure 6.21: Carbonation depth after two months for all the compositions.

Face	C-NA	C-RCA	M1-CEMI	M2-CEMI	C-NA-CEMIII
1	2.2	5.6	3.2	1.6	3.6
2	0.4	1.6	1.4	0.8	5.2
3	0	0.4	0.2	0	3.8
4	1.2	4	1.6	0.4	5.4

Table 6.7: Final values of the carbonation depth [mm] for all sides of each composition.

6.8 Water permeability

The final experiment whose results are displayed is the water permeability experiment. Two samples were tested for each composition, and the results obtained can be found in the Table 6.8, where one can see the intrinsic permeability for each sample and then the mean value, for each composition studied. In addition to this table, the Figure 6.22 allows a better comparison of the results. Furthermore, if one compares this graph with the one of the water absorption and porosity (Figure 6.7), there seems to be an error with the measurement of the porosity for the M1-CEMI, which was implied by the visible macro-porosity of this composition.

Composition	Intrinsic Permeability [m^2]		
	Sample 1	Sample 2	Mean value
C-NA	2.76E-20	1.26E-19	7.68E-20
C-RCA	8.28E-20	1.26E-19	1.04E-19
M1-CEMI	3.88E-19	4.27E-19	4.08E-19
M2-CEMI	9.96E-21	8.05E-21	9.01E-21
C-NA-CEMIII	1.06E-20	1.37E-20	1.22E-20

Table 6.8: Water permeability results for all compositions

One can see that the C-RCA is a bit more permeable than the C-NA (by 35%), which is a remarkable difference without being excessive. Moreover, the C-NA-CEMIII is even less permeable than the C-NA, possibly because of its lower production of heat during curing which restricts the creation of capillaries.
For the mortars, the M2-CEMI is less permeable than the M1-CEMI which was to be expected when looking at the micro-photographs. In addition, the lower permeability of the M2-CEMI with respect to the C-NA proves that the presence of aggregates in concrete increases the porosity and therefore water permeability.

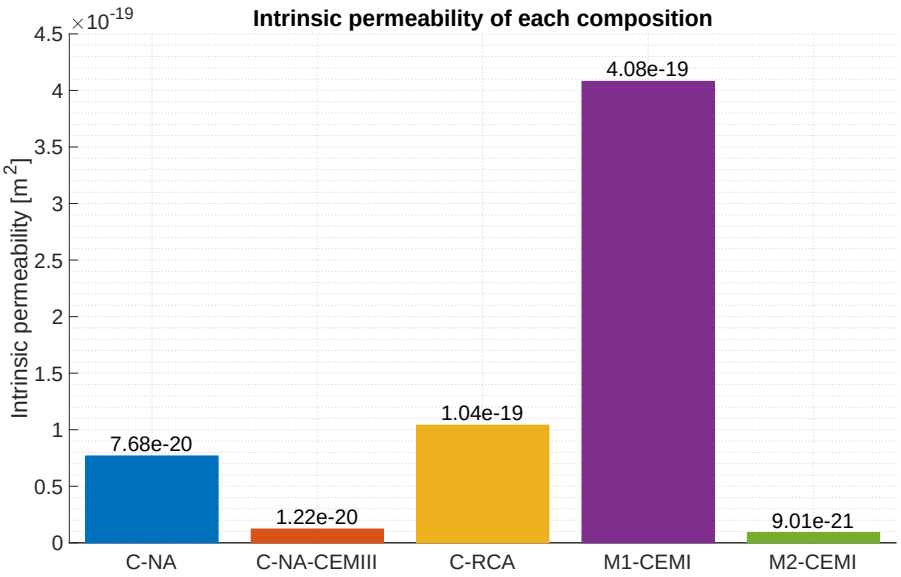

Figure 6.22: Intrinsic permeability for each composition.

The results of the experiments are also found in the Figures 6.23 and 6.24 as well as in the Appendix B for the three last compositions. Most of the samples responded well, however, some samples such as the two of C-NA and second of C-RCA displayed a too low water permeability and since concrete is poorly deformable, it degraded the waterproof sleeve around the sample, inducing possible micro-perforations and false measurements.

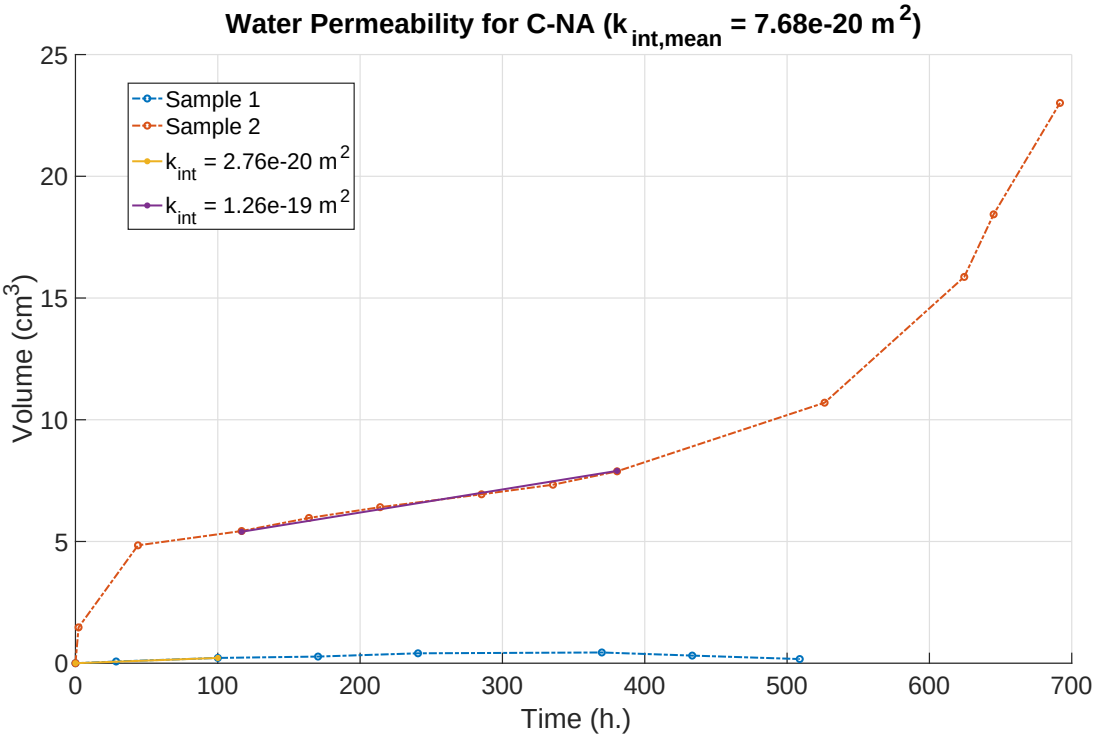

Figure 6.23: Water permeability measured for the C-NA.

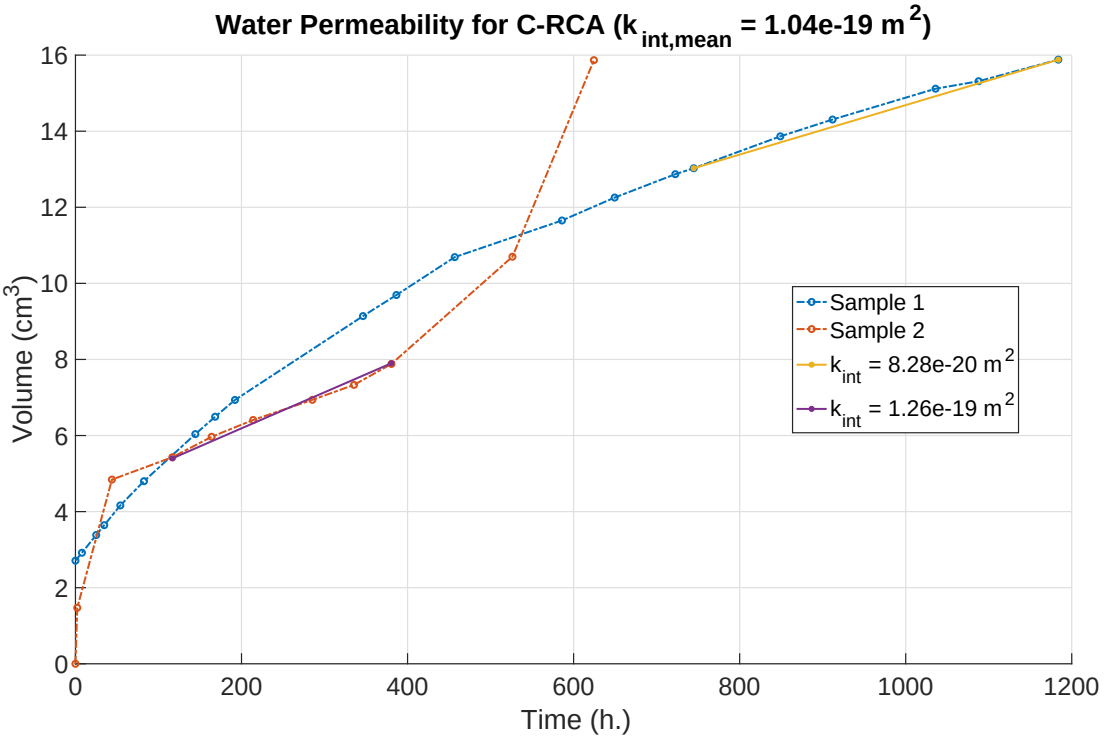

Figure 6.24: Water permeability measured for the C-RCA.

6.9 Conclusion

Throughout this chapter, one has observed the results obtained in our experimental programme. As the main goal of this study is to characterise the use of RCA inside concrete, this conclusion will serve as a summary of the differences between the C-NA and C-RCA.

The micro-photography has highlighted the differences between a natural aggregate and a recycled concrete aggregate, the latter being partially or totally freed from adherent cement paste.
The Water Absorption by Immersion test showed an increase of the water absorption and porosity when substituting NA for RCA. Indeed, the RCA being more porous and displaying a greater water absorption, it was certain that the C-RCA would present the same characteristics.
The static sorption and desorption exhibited the same results: the C-RCA has a smaller air-entry pressure which is characteristic of greater pores and leads to a saturation loss/gain starting before the C-NA. Therefore, if two beams, one of each composition, were subjected to the same external conditions, the C-RCA would display greater changes of saturation than the C-NA.
For water permeability, the C-RCA is 35% more permeable than the C-NA, which increases the ability with which fluids can move inside the porous structure and therefore facilitates the water exchanges between the concrete and its surroundings.

To end this conclusion, the resistance to carbonation showed that the greater the porosity and the greater the carbonation depth. Moreover, the more product prone to carbonation there is and the less quickly the carbonation front increases, which is in respect with the Equation 6.5. If we compare the C-NA and C-RCA, the C-RCA has a greater speed of carbonation than the C-NA due to its increased open porosity.
However, the small number of tests achieved and the too small period studied (two months) prevent us from drawing conclusions on the effect of the RCA on the resistance to carbonation. Nonetheless, the literature also confirms that the use of RCA inside concrete may promote carbonation [Arredondo-Rea et al., 2012], but the carbonation depth depends on the chemical composition of the RCA (and overall concrete) [Levy & Helene, 2004] as well as the size of RCA used [Zhao et al., 2018].

7 | Modelling of transport phenomena in concrete

Contents

7.1 Introduction

This chapter exposes the results of the modelling carried out during this thesis and whose theoretical basis has already been laid out.
To begin the modelling aspect of this thesis, a sensibility analysis is conducted in order to better grasp the physical processes and effects behind the various parameters of the model. The modelling of the many transport phenomena cited before will then be used for an experimental case done in the past as a part of an expertise[1] as well as for the convective drying done on the M1-CEMI. This will validate the model and ensure that the equations it solves are representative of the real physical processes happening.
Then, once the validation of the model is completed, it will be applied to a more realistic case: the modelling of humidity cycles happening in an exterior parking lot's column. This application will be carried out with only two compositions: the C-NA and the C-RCA, allowing an extrapolation of the results and a conclusion on the effects of those RCA in regards to the drying phenomena.

7.2 Sensibility Analysis

As it was introduced, the modelling part of this thesis starts with a sensibility analysis. Indeed, the value of multiple model parameters was changed in order to better apprehend

[1] The concrete compositions of this thesis were not used as no convective drying has been done due to the Covid-19's lockdown.

their effect on the results of a drying experiment and modelling. In addition to those "internal" parameters, the applied constraints (temperature and capillary pressure, i.e. relative humidity RH) were also modified, as well as their order of application. Finally, the effect of the mesh was also studied to obtain a convergence of the results.
The various parameters that played a role in the sensibility analysis are exposed in the Table 7.1.

Parameter	Parameter's name
Model parameters	
α_{vG} [Pa]	Air-entry pressure
n_{vG} [-]	Van Genuchten model parameter
m_{vG} [-]	Van Genuchten model parameter
Internal parameters	
k_{int} [m^2]	Intrinsic permeability
Applied environmental parameters	
T [K]	Applied temperature
p_c [Pa]	Capillary pressure
Mesh parameters	
N_{elem} [-]	Number of elements

Table 7.1: Parameters used during the sensibility analysis

For each parameter, four different figures will be studied: the evolution of the saturation degree within the sample, the evolution of the temperature at the surface of the sample and with respect to time, and finally the mass loss with time and the Krischer curve.
The sample studied is a cylinder of 40mm width for a height of 40mm. Due to its shape, it is possible to study it in an axisymmetric state. Moreover, the drying occurs at both the top and bottom faces of the sample, allowing the modelling of only half of its height. The sample and its mesh are represented at the Figure 7.1. One can see that the mesh has been refined into three distinct parts, the closer to the surface it is and the more refined the mesh is to compensate for the bigger gradients near the drying surface.
One will be able to remark that the evolution of the saturation degree with time will be displayed along the height of the sample. More precisely, what is called the height of the sample is the position in the mesh, and therefore the results on the real sample would be the ones shown and their symmetric below.

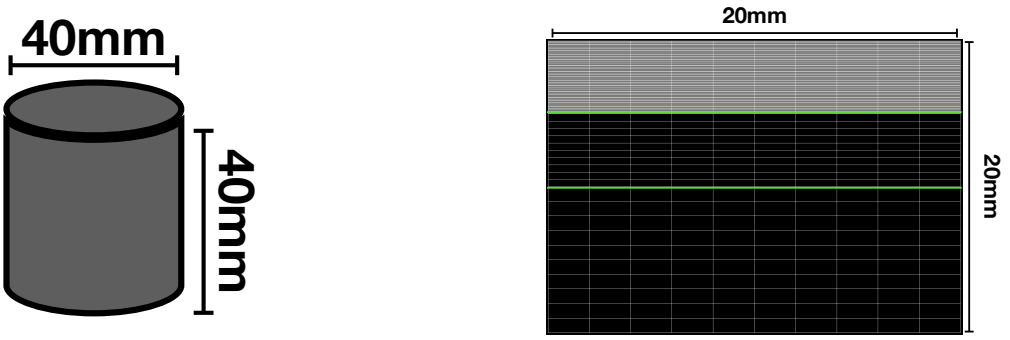

Figure 7.1: Sample modelled for the sensibility analysis and its mesh.

7.2.1 Intrinsic permeability

The first parameter studied is the intrinsic permeability. The lower it is and the greater resistance the flow will encounter. Therefore, for a constant relative humidity and temperature of the drying air, the saturation will decrease faster for a bigger intrinsic permeability. It is easily confirmed by the first graph of the Figure 7.2, where one can see the value of the saturation degree along the height of the sample and at a given time (one hour in this case).

Moreover, the biggest permeability exhibits a more uniform saturation front while the lower permeabilities present a steep gradient near the drying surface due to the difficulty the flow encounters to pump the fluid from deep inside the sample. This phenomenon is easily confirmed by the length of the hydraulic connection layer whose value for each intrinsic permeability is shown in the Table 7.2. Indeed, if the length of the hydraulic connection layer is greater than the length of the sample, it means that the saturation front will be uniform and the smaller it is, the harder it will be for the drying air to extract water from the sample and therefore a steeper gradient will appear (see Section 3.4.1 for more details).

k_{int} [m^2]	α_{vG} [MPa]	n_{vG} [-]	m_{vG} [-]	q_{CRP} [$\mathrm{kg}/(\mathrm{m}^2.\mathrm{s})$]	L_{cr} [m]
1E-18	5	1.25	0.2	1.8E-4	0.03258
1E-17	5	1.25	0.2	2.2E-4	0.2668
1E-16	5	1.25	0.2	2.4E-4	2.444

Table 7.2: Length of hydraulic connection for the sensibility analysis on the intrinsic permeability.

The sample reaches its equilibrium between the temperature of the sample at its surface and the temperature of the drying air at various times for the different values of intrinsic permeability. Indeed, the bigger it is and the more time it will take to reach an equilibrium as water from the sample will be supplied more quickly, water whose temperature is in equilibrium with the temperature inside the sample and is therefore lower than at its drying surface.

Finally, the two characteristic curves of drying, namely the evolution of the mass with respect to time and the Krischer curve, were studied. They display that, as it was suspected, the bigger the permeability and the bigger mass loss the sample exhibits for a given period.

Indeed, if given enough time, every value of intrinsic permeability should still converge towards the same dried mass as all other parameters are equal, and the permeability is just an expression of the speed at which water movements occur.
Moreover, the bigger permeability sample presents a longer CRP (Constant Rate Period) as the length of the hydraulic connection layer is bigger, increasing the easiness the water has to flow through the porous system.

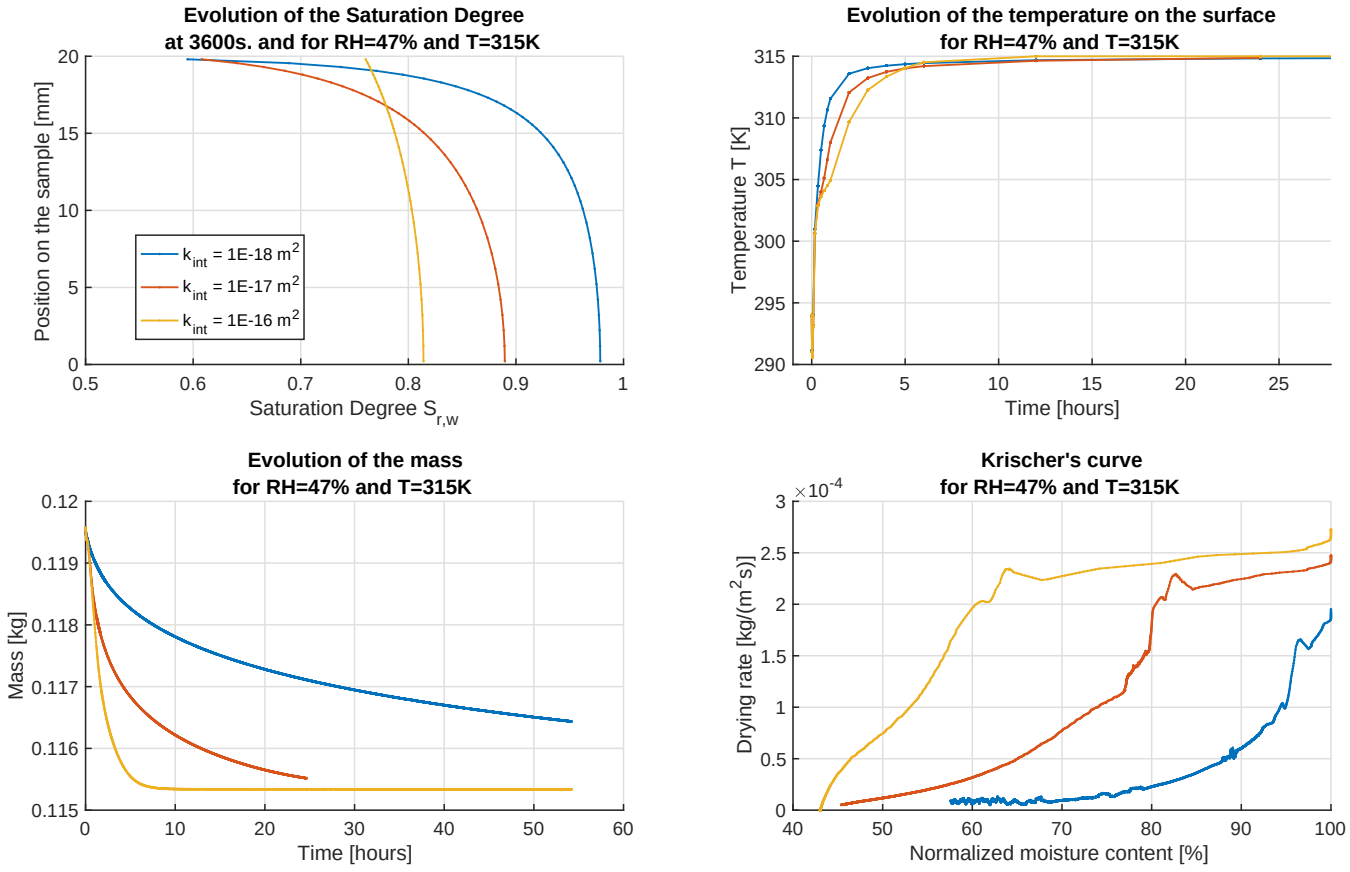

Figure 7.2: Sensibility analysis on the intrinsic permeability of the sample.

7.2.2 Van Genuchten model parameters

The parameters studied in this section will be the Van Genuchten model parameters. Indeed, those influence the water retention curve and relative permeability through the formulae 2.14 and 4.16 respectively.

The influence of the three model parameters on the water retention curve (for α_{vG} and n_{vG}) and on the relative permeability curve (m_{vG}) is represented in the Figure 7.3, where the two parameters n_{vG} and m_{vG} are linked by the following formula:

$$m_{vG} = 1 - \frac{1}{n_{vG}} = \frac{n_{vG} - 1}{n_{vG}} \tag{7.1}$$

In those three graphs, the blue line is always the same: that is our reference. The bigger the air-entry pressure and the more the curve is shifted to the right, because the medium requires a greater suction to let air enter its porous system and flush water out, drying the

sample. The model parameter n_{vG}, on the other hand, changes the slope of the water retention curve, the bigger value of n_{vG} introducing steeper slopes and therefore more brutal changes of saturation during the drying. Finally, the last model parameter m_{vG} only influences the relative permeability curve, also increasing its slope for lower values.

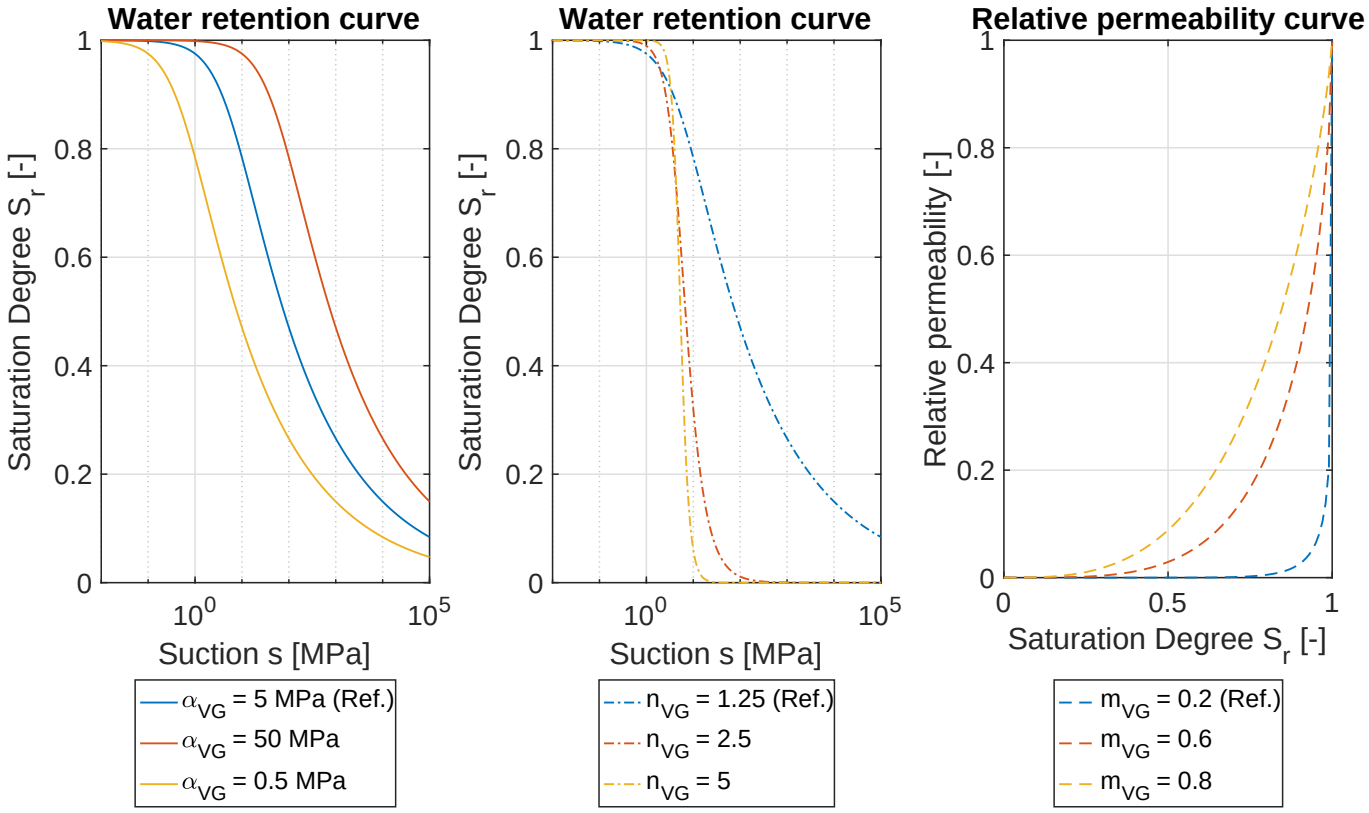

Figure 7.3: Influence of the Van Genuchten model's parameters on the water retention curve and relative permeability curve.

The first of the three parameters to catch our attention is the air-entry pressure α_{vG} [Pa], whose results are shown in the Figure 7.4. Theoretically, the lower the air-entry pressure and the sooner water will be extracted out of the porous media, therefore requiring a lower value of the suction to start. In other words, for a given suction, the "equilibrium" saturation is lower and fluid is extracted more rapidly near the drying front. However, as it is shown in the first graph of the Figure 7.4, the lower the air-entry pressure and the bigger the saturation degree is, for the same external applied conditions and at the same time, inside the sample. This is because a lower air-entry pressure means, for the same value of suction, that the drying surface will desaturate faster, therefore decreasing the relative permeability and creating a zone where no water can flow through. Indeed, one can see the apparition of a steeper gradient which, if correlated with the intrinsic permeability, means that it is harder to extract fluid out of the medium.

The same conclusions as for the intrinsic permeability can be extracted from the graph representing the evolution of the temperature on the surface of the sample: the easier it is to extract water from the sample and the slower the surface reaches the drying air's temperature.

For the mass loss and Krischer curves, one can see that the bigger the air-entry pressure is, the faster the sample loses mass and the longer its CRP is. It is simply due to the greater

relative permeability a bigger air-entry pressure exhibits. Indeed, once the low relative permeability zone is installed, the drying rate decreases sharply to nearly 0.
Another remark worth doing is that the smaller the air-entry pressure is, the bigger total mass loss the sample exhibits (after convergence to the final dried mass). It may be because a smaller air-entry pressure is linked to a greater open porosity and therefore higher possible mass loss.

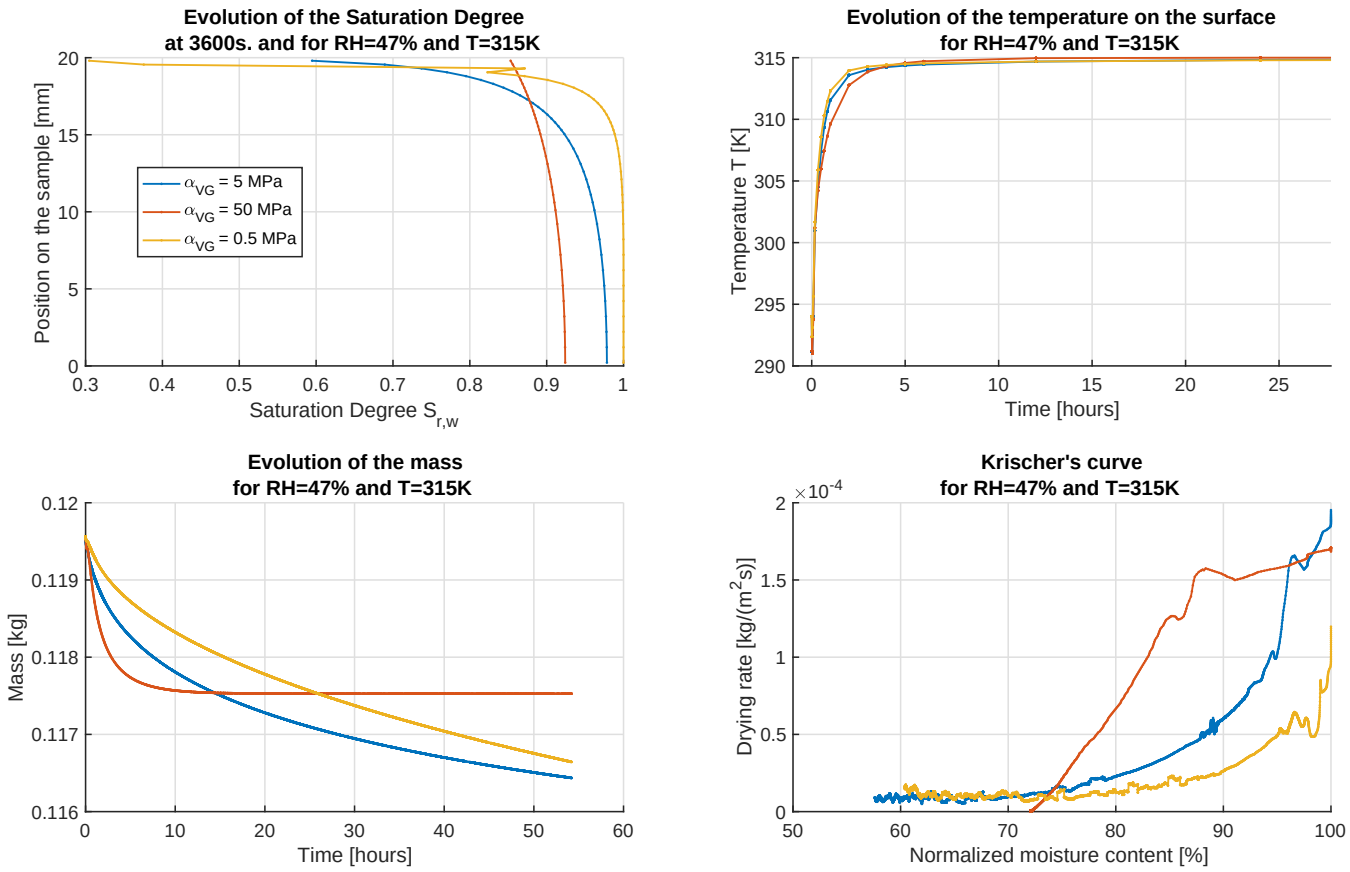

Figure 7.4: Sensibility analysis on the Van Genuchten model parameter α_{vG}.

In terms of length of the hydraulic connection layer (Table 7.3), the same conclusions can be deduced. The greater air-entry pressure leads to a greater length, therefore promoting a bigger relative permeability during the drying.

k_{int} [m^2]	α_{vG} [MPa]	n_{vG} [-]	m_{vG} [-]	q_{CRP} [$kg/(m^2.s)$]	L_{cr} [m]
1E-18	5	1.25	0.2	1.8E-4	0.0326
1E-18	50	1.25	0.2	1.6E-4	0.3668
1E-18	0.5	1.25	0.2	0.8E-4	0.00734

Table 7.3: Length of hydraulic connection for the sensibility analysis on the air-entry pressure.

The next parameter to be studied is the one controlling the slope of the water retention curve, n_{vG}. The bigger it is and the steeper the slope is, resulting in a faster saturation drop once

the capillary pressure reaches and exceeds the air-entry pressure. If n_{vG} is small, then m_{vG} is small too due to the relation between both. However, both were studied here separately as the equations representing the Van Genuchten model use them separately in the Lagamine software: indeed, the parameter n_{vG} is used in the equation for the saturation degree (Equation 2.14) while m_{vG} is used for the relative permeability (Equation 4.16).

One can see in the Figure 7.5 that the higher the parameter n_{vG} is and the bigger the saturation is inside the sample. However, the presence of a steeper gradient near the drying surface induces a lower saturation degree at the surface, which is due to the faster loss of saturation due to the steeper water retention curve. As the graph representing the saturation in the sample is only taken at 3600s., this is not well marked, but this phenomenon will continue to increase with time. However, the temperature at the surface is nearly not influenced by this parameter as the three values exhibits a similar mass loss, which means that water is extracted at a similar rate and therefore the temperature increases at a similar rate.

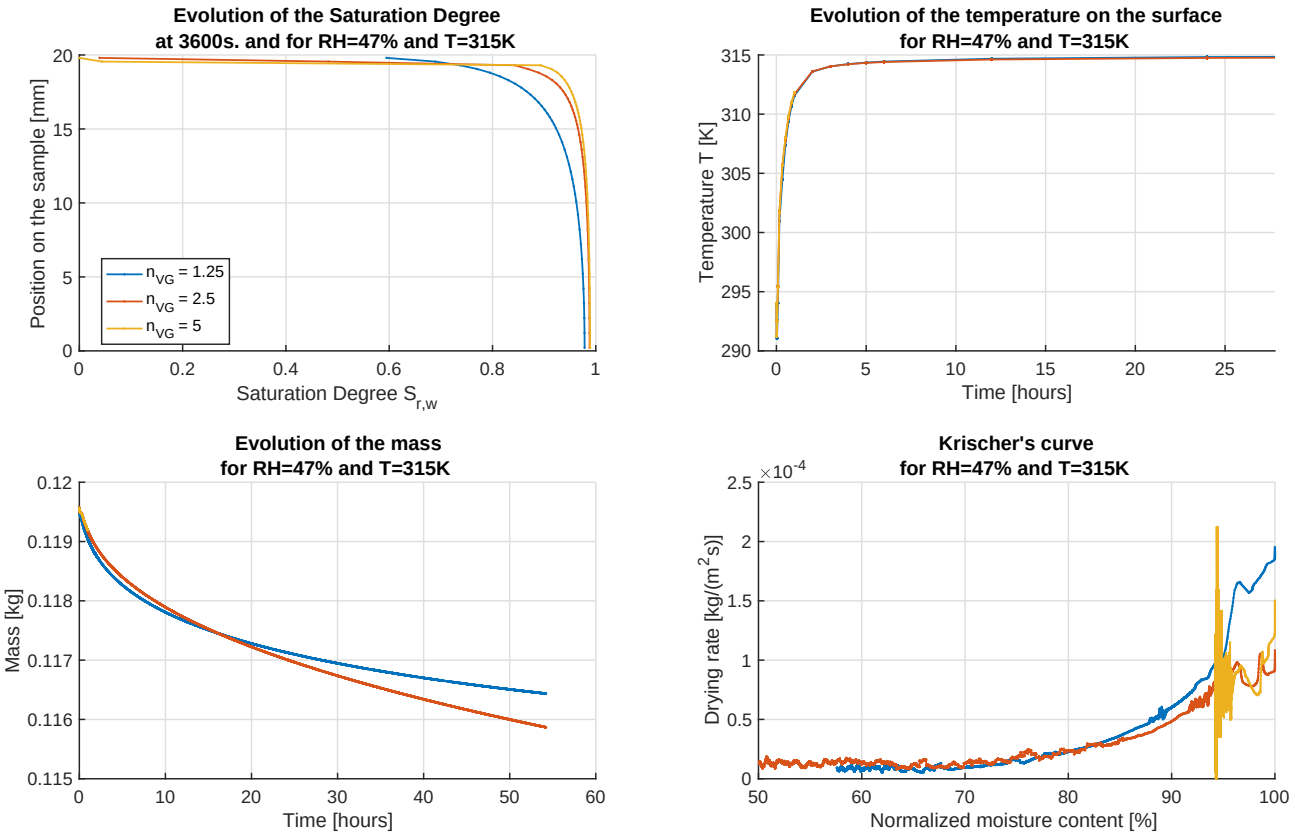

Figure 7.5: Sensibility analysis on the Van Genuchten model parameter n_{vG}.

For the mass loss during the drying experiment, one can see that the bigger the parameter n_{vG} and the faster the sample loses mass. However, this is not the case during the whole experiment because at first, the lower value of n_{vG} loses more mass and then the results switch. If we look closely at the beginning of the graph related to n_{vG} in the Figure 7.3, we can see that for lower values of the suction, the saturation degree begins to decrease sooner for lower values of n_{vG}. As the capillary pressure is set progressively in the model, this may explain the quicker mass loss at the beginning for lower values of n_{vG} and then, as the suction increases, the saturation degree decreases more and more for the higher values of n_{vG} until the tendencies switch.
The Krischer curve exhibits the same results: the lower values of n_{vG} possess a CRP with a

bigger drying rate but once this drying rate drops, it becomes smaller than for higher values of n_{vG}.

The Table 7.4 displays the length of the hydraulic connection layer for the three values of n_{vG} studied. The lower it is and the deeper the hydraulic connection layer is, due to the low relative permeability zone that once again appears for the bigger values of n_{vG}.

k_{int} [m^2]	α_{vG} [MPa]	n_{vG} [-]	m_{vG} [-]	q_{CRP} [$kg/(m^2.s)$]	L_{cr} [m]
1E-18	5	1.25	0.2	1.8E-4	0.03261
1E-18	5	2.5	0.2	0.8E-4	1.06E-8
1E-18	5	5	0.2	0.85E-4	1.6E-16

Table 7.4: Length of hydraulic connection for the sensibility analysis on the model parameter n_{vG}.

In the Figure 7.6, the coefficients were chosen accordingly to the three values of n_{vG}. The smaller the coefficient m_{vG} is and the faster the relative permeability will drop, creating a zone near the drying surface whose permeability is lower than the rest of the sample. The temperature is obviously impacted by the parameter m_{vG} as it plays a role in the relative permeability, therefore a bigger value of this model parameter increases the easiness with which the fluid flows through the porous media, therefore resulting in a faster heating of said media.

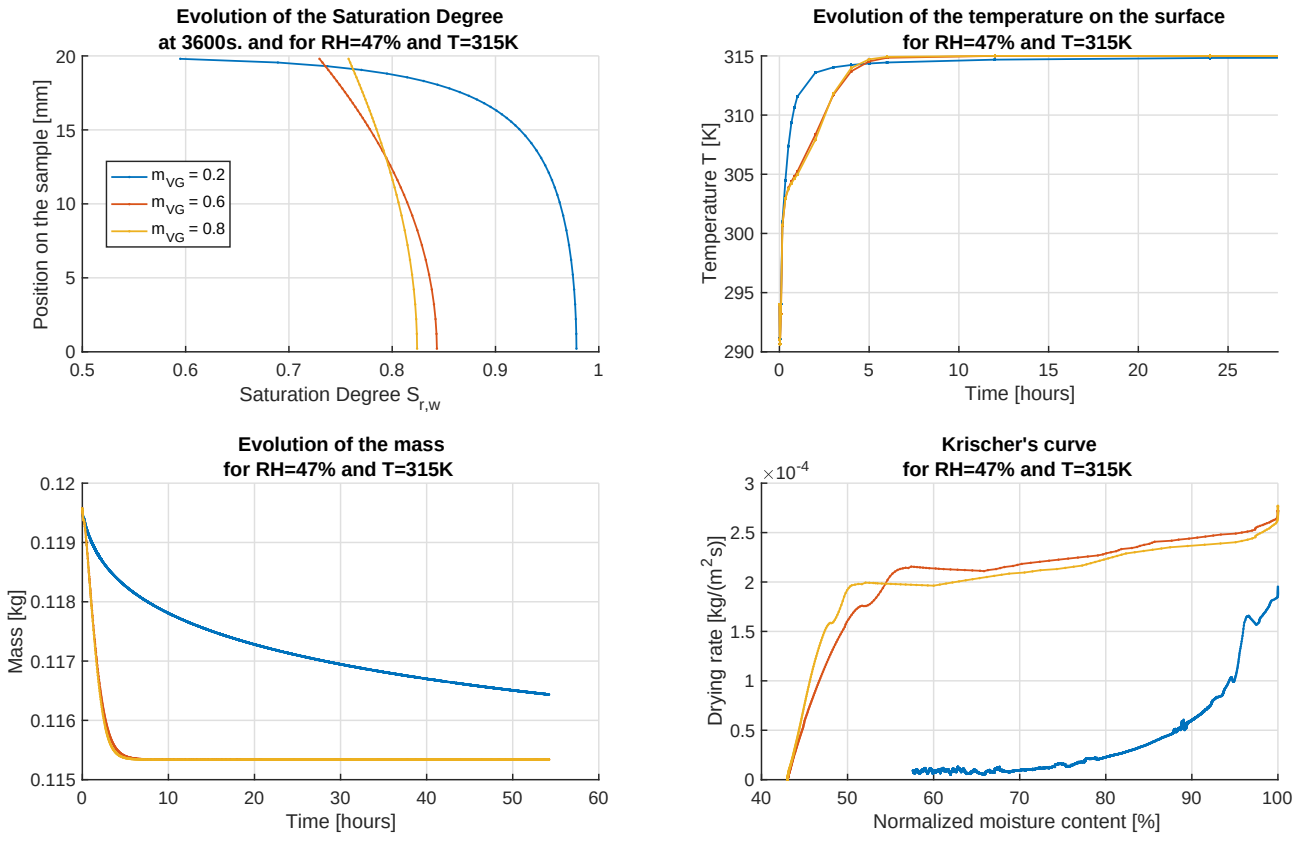

Figure 7.6: Sensibility analysis on the Van Genuchten model parameter m_{vG}.

In terms of the mass loss and Krischer curves, they indeed exhibit a bigger difference between the lower and higher values of the parameter m_{vG}. The lower value of m_{vG} creates the low relative permeability zone, therefore reducing the drying rate and the speed at which the sample loses mass. However, once again, the sample will stabilise to the same mass regardless of the value of m_{vG} if given enough time.

In the study of the sensibility of this parameter, the length of the hydraulic connection layer can't be used as the two parameters m_{vG} and n_{vG} are uncoupled in the Lagamine software, therefore the value we would obtain won't be representative of the simulations done and exposed at the Figure 7.6.

7.2.3 Drying air's parameters

Once the parameters related to properties specific to the sample have been studied, the focus is on the drying air's parameters, namely the temperature and the capillary pressure which are linked to the relative humidity through the Kelvin law (Equation 3.2).

Two values of temperature were used (with $294\mathrm{K}$ being the initial temperature of the sample), as well as a constant drying air temperature (the degree of freedom linked to the temperature is then blocked). One can see in the legend of the Figure 7.7 that the relative humidity of those three cases are similar, which is why there is little difference in the saturation degree for those three temperatures.

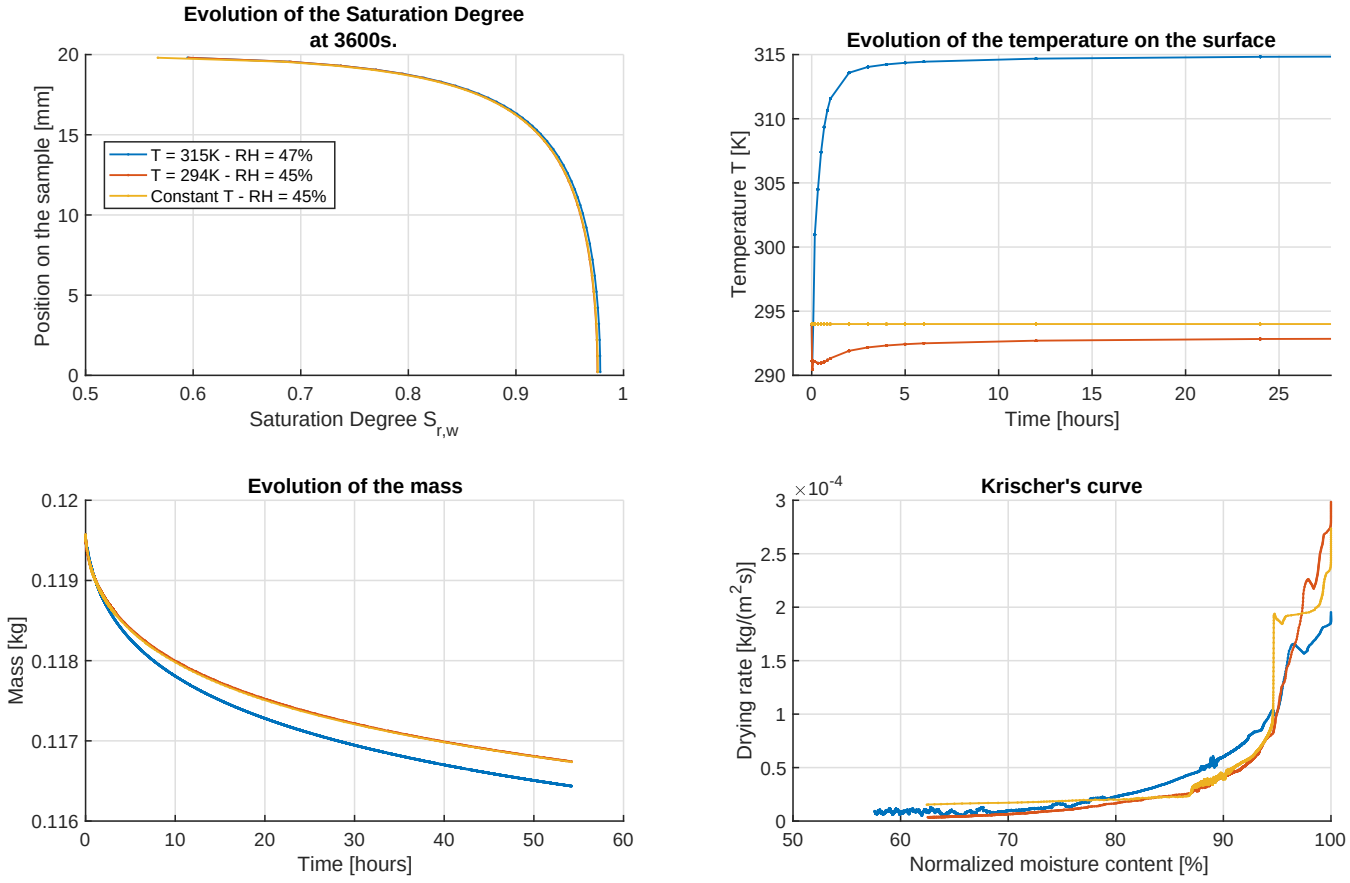

Figure 7.7: Sensibility analysis on the temperature of the drying air.

The evolution of the temperature at the surface of the sample is not really useful in this case as this is directly controlled by the parameter studied, except for the case with the temperature equal to 294K (orange curve). Indeed, as the temperature of the environment is equal to the temperature of the medium, the drying requires the use of energy to create vapour, which therefore decreases the temperature of the drying surface below its initial value. However, as the ambient temperature is fixed to 294K, the drying surface will slowly increase its temperature to reach equilibrium once the drying is finished, which is not the case during this simulation as one can observe the absence of a plateau in the evolution of the mass.

However, the mass loss and Krischer curves are useful and show that the bigger the temperature and the faster mass loss the sample exhibits, as it is easily predicted. Moreover, the use of the DOF related to temperature doesn't really change the mass loss and it could therefore be useful to accelerate the simulation's time as fewer equations would be required. Besides, the Krischer curve doesn't exhibit a huge difference between both cases at 294K but shows the following: the smaller the temperature and the higher the value of the drying rate during the CRP. This is mainly due to the lower value of the RH resulting from the lower value of the temperature for a constant suction. The lower the RH and the bigger the drying rate, which is the result obtained in this analysis.

The results of the sensibility analysis on the capillary pressure are shown in the Figure 7.8. One can see that the smaller the pressure is (i.e. the more negative it is) and the smaller the saturation degree is, even more near the drying surface where a steep gradient appears. However, the capillary pressure has little to no effect on the evolution of the temperature on the surface.

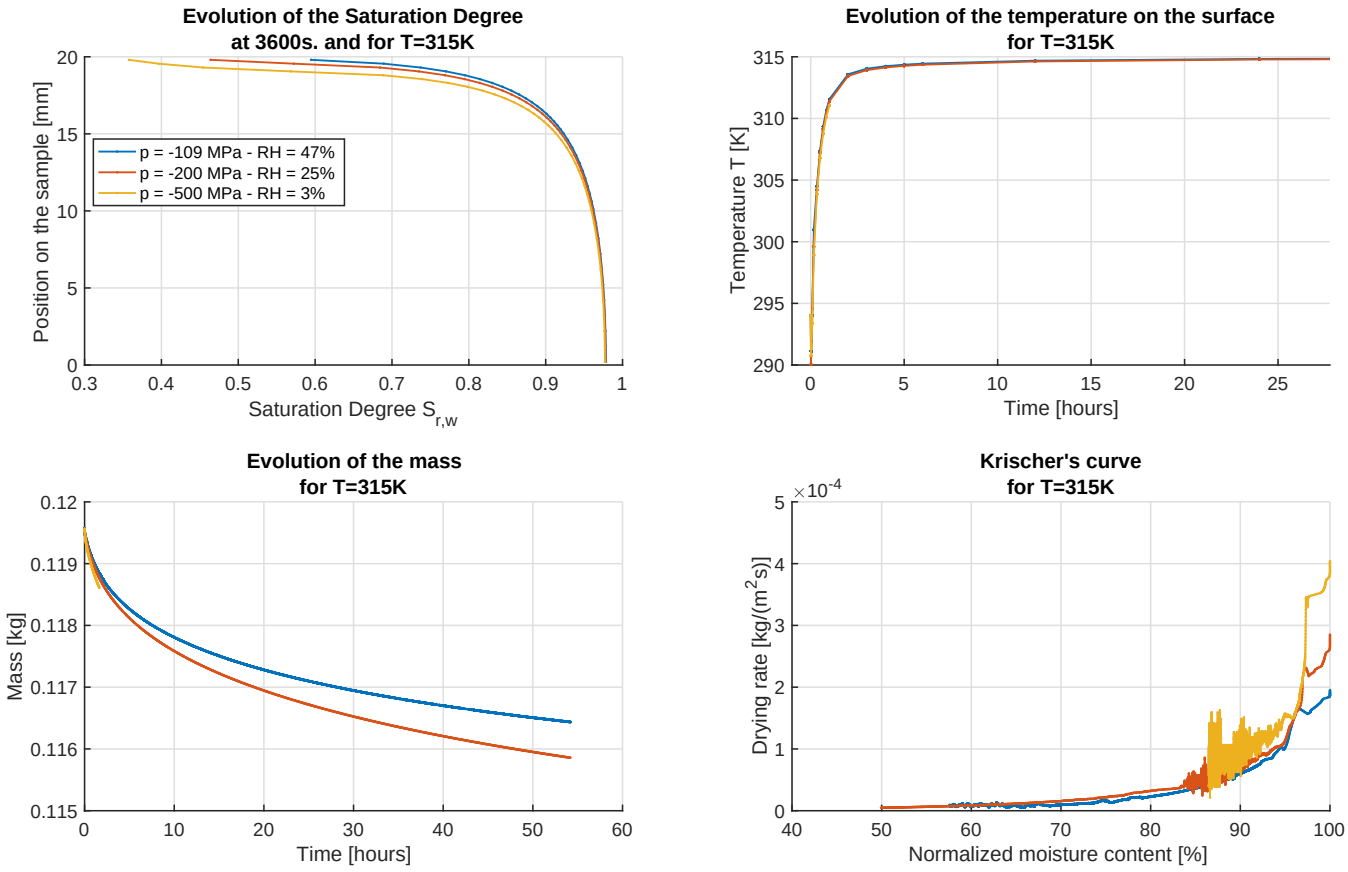

Figure 7.8: Sensibility analysis on the capillary pressure applied to the sample.

Focusing on the drying curves, one can see that the smaller the pressure is and the bigger mass loss the sample experiences. Moreover, the drying rate during the CRP (and possibly during the whole drying experiment) is higher for lower capillary pressures.

7.2.4 Mesh parameter

The final parameter studied in this sensibility analysis is the density of the mesh. Indeed, four different meshes were studied:

- First, two meshes with the same distribution of elements than for the one shown in the Figure 7.1, with the number of all the vertical elements multiplied or divided by 4;
- Then it was decided to focus on the mesh in the zone closer to the drying surface as it is where the biggest gradient appears. To do so, two meshes with only the upper zone varying were studied.

The results are represented in the Figure 7.9.

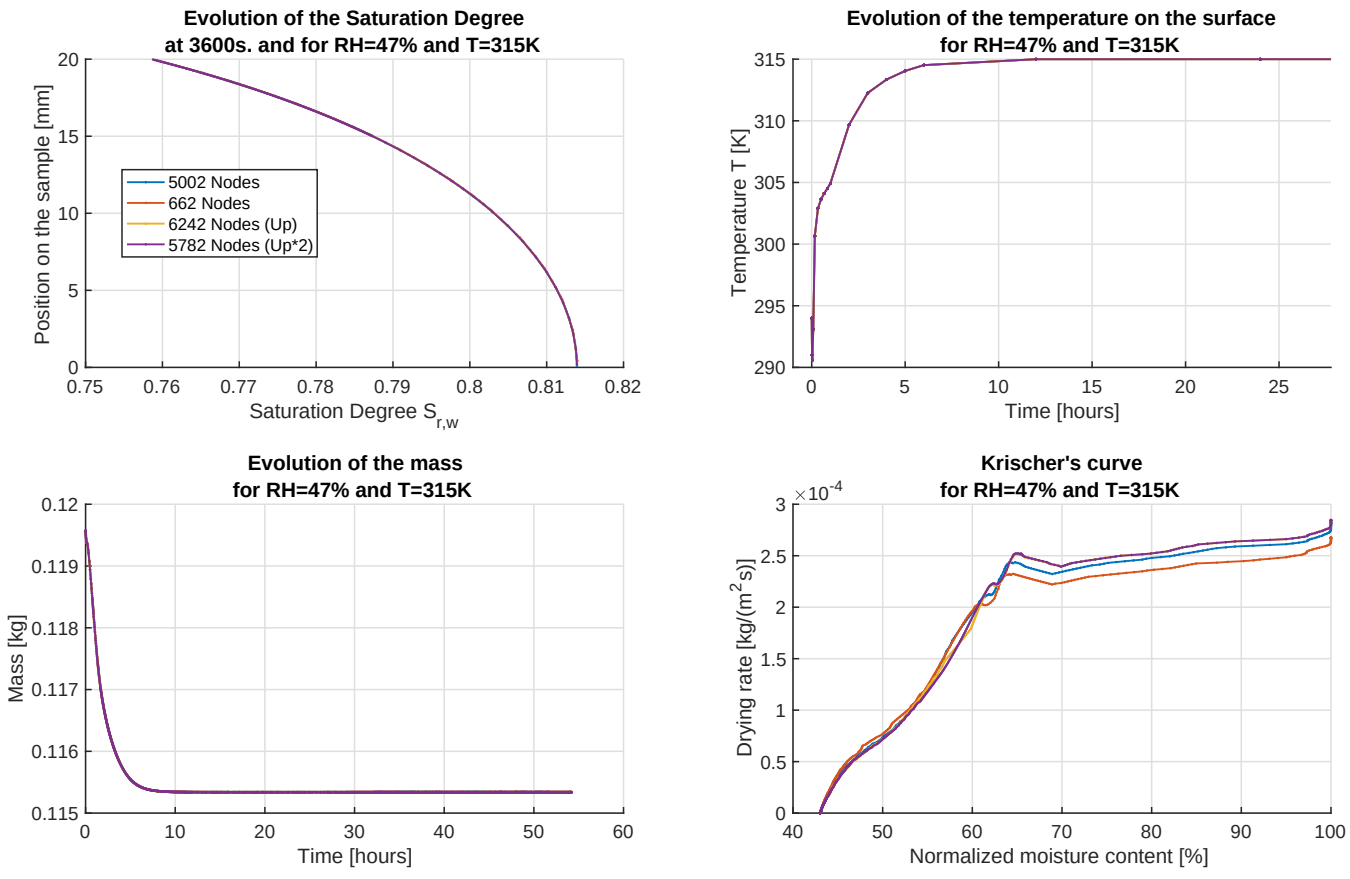

Figure 7.9: Sensibility analysis on the density of the mesh.

No difference is visible between all except in the Krischer curve which enhances the differences between the meshes. One can therefore see that the meshes all have different values of the drying rate during the CRP except the two where we refined the zone closer to the drying surface, which shows that those two really converge towards an identical solution and

we must therefore use the more refined mesh to make sure our solution is the best possible. However, the differences are of a small order and mainly due to the derivative nature of the drying flux. Indeed, as we use the derivative of the mass on each node, the more there is and the higher the drying rate tends to be, which is purely numeric and due to the derivative. Therefore, a good equilibrium has to be chosen between time of simulation (which is greater for a more refined mesh) and the precision we want to reach.

As this sensibility analysis on the mesh didn't exhibit visible differences, it was also decided to vary the mesh for harder environmental conditions, in order to observe the influence a more refined mesh has on the convergence of the numerical simulation. The capillary pressure was then reduced to -500MPa while the intrinsic permeability was also divided by 100 to reach 1E-18 m^2. Due to those harsh conditions, one can see on the Figure 7.10 that not all meshes finished the simulation. Indeed, only the coarser one finished the simulation due to its increased speed, while all the others took more time and then reached the limit of iterations.

However, all meshes except the less refined one seem to converge towards the same mass loss with respect to time, the two refined upper meshes more particularly. Furthermore, and as it has been explained above, the differences in the Krischer curve are mainly numerical and due to the number of integration points, and therefore the number of nodes used during the modelling.

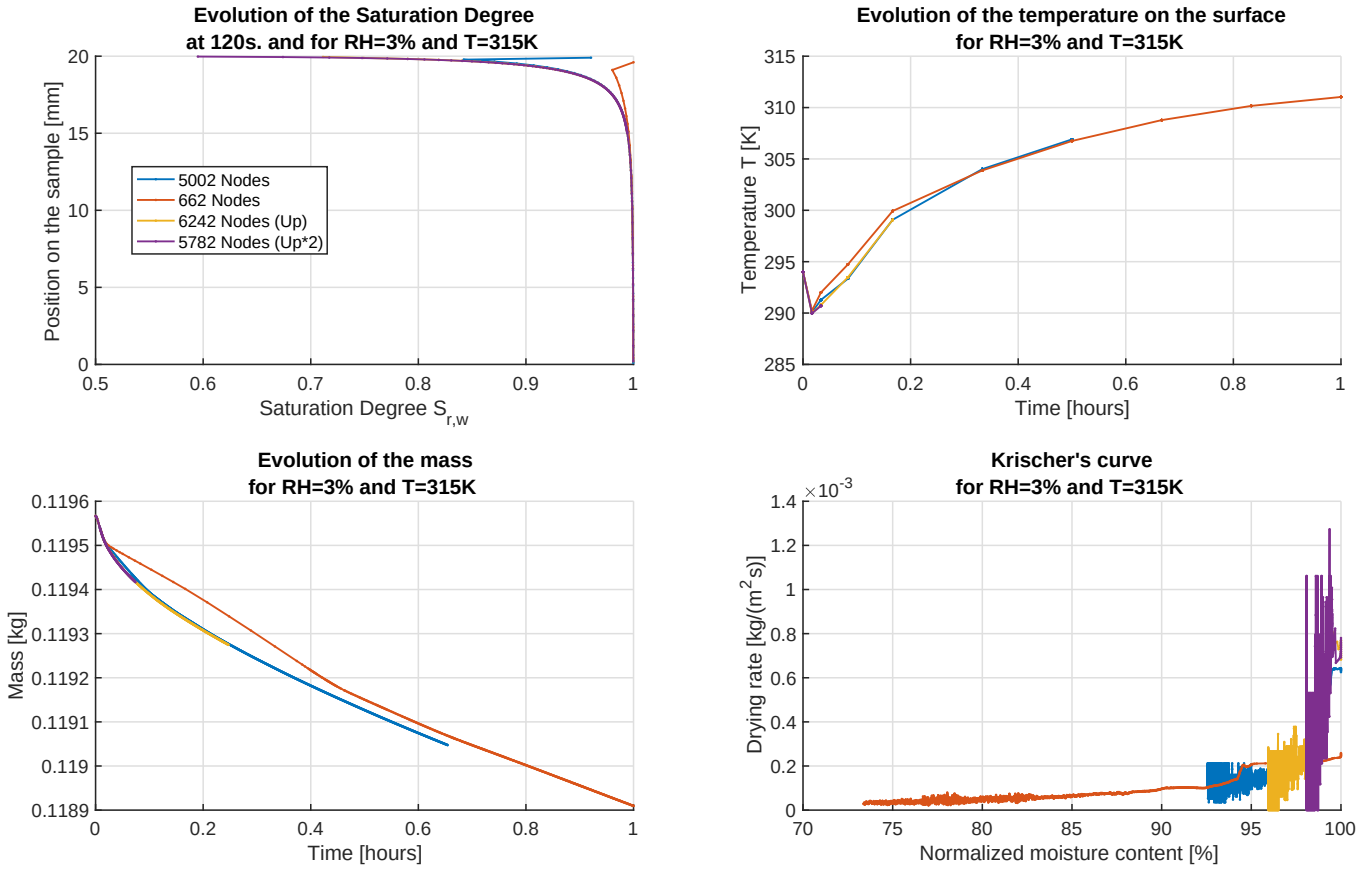

Figure 7.10: Sensibility analysis on the density of the mesh for harder drying conditions.

7.3 Validation of the model

The model will now be validated with the help of our M1-CEM1 composition as well as a concrete that had been tested for an expertise previously. The goal here is to input the experimental parameters obtained for both compositions into the model and verify that the latter provides the same results as the experimental drying. In addition to that, as some parameters were not accurately measured during the experimentations, a fitting of the convective drying's results is performed to demonstrate the capabilities of the model.

Various parameters are shared between all the compositions as they are constant relatives to water or air, initial temperature or pressure, among many others. Those parameters can be found in the Appendix D.

7.3.1 M1-CEMI composition

The first step to modelling is the creation of the mesh. As it has been mentioned for the sensibility analysis, the sample and conditions allow the modelling of only the upper half of the sample, and we can work in an axisymmetric state which allows to only model a slice as wide as half the sample. As the convective drying experiment was achieved on a cylinder with drying occurring on all faces, the mesh had to be refined along the two x and y directions. The mesh used, with the limit conditions, is represented in the Figure 7.11.

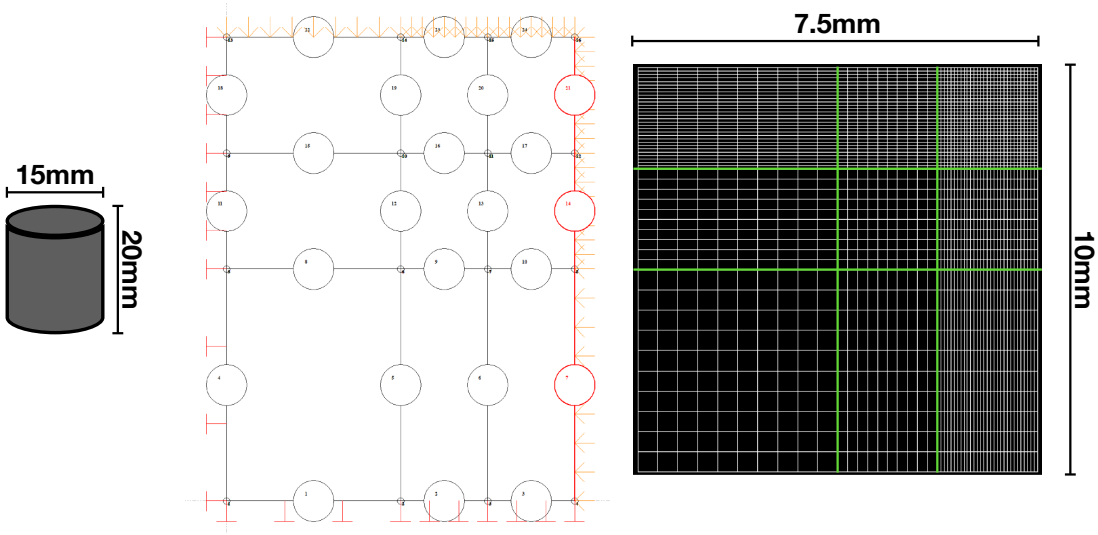

Figure 7.11: Mesh used for the modelling of the M1-CEMI.

The Table 7.5 summarises the value of each parameter fixed in this model. Those have been initially determined through the various experimentations achieved and they were then tweaked to obtain the same curve as the experimental one. Indeed, the Figure 7.12 shows two experimental curves as well as a curve obtained after fitting of the convective drying results. As a matter of fact, three parameters were not directly or at least accurately measured during our experimental campaign: the porosity n, the model parameter m_{vG} linked to the relative permeability and finally, the relative humidity inside the convective dryer. Indeed, it has been explained in the Section 5.3.1 that the porosity measured during the WAI experiment is the open porosity and that a more accurate measure of the porosity could have been

obtained through a mercury intrusion porosimetry experiment. For the RH inside the convective dryer, it was also explained in the Section 5.3.4 that the sensors used didn't measure the RH at all time nor did they save the data inside the software used.

Parameter	Value Exp.	Value Fit.	Units	Experimental source
Density of the solid grains (ρ_s)	2194	2194	$[\mathrm{kg/m^3}]$	WAI
Concrete's intrinsic permeability (k_{int})	4.08E-19	4.08E-19	$[\mathrm{m^2}]$	Water Permeability
Concrete porosity (n)	15.1 or 23.5	15.1	[%]	WAI
Van Genuchten model parameter (m_{vG})	0.25 or 0.18	0.25	[-]	Static Desorption
Van Genuchten model parameter (n_{vG})	1.33	1.5	[-]	Static Desorption
Air-entry pressure (α_{vG})	9.93	15	[MPa]	Static Desorption
Minimal concrete's relative permeability	1E-4 or 1E-5	3E-5	[-]	Static Desorption
Seepage penalty coefficient (K)	1E-13	1E-13	$[\mathrm{m/s.Pa}]$	-
Mass transfer coefficient (α)	1.5E-3	1.5E-3	$[\mathrm{m/s}]$	Convective Drying
Heat transfer coefficient (β)	1.5	1.5	$[\mathrm{W/m^2.K}]$	Convective Drying
Relative Humidity (RH)	3 or 17	3	[%]	Convective Drying

Table 7.5: Parameters used in the modelling of the M1-CEMI composition.

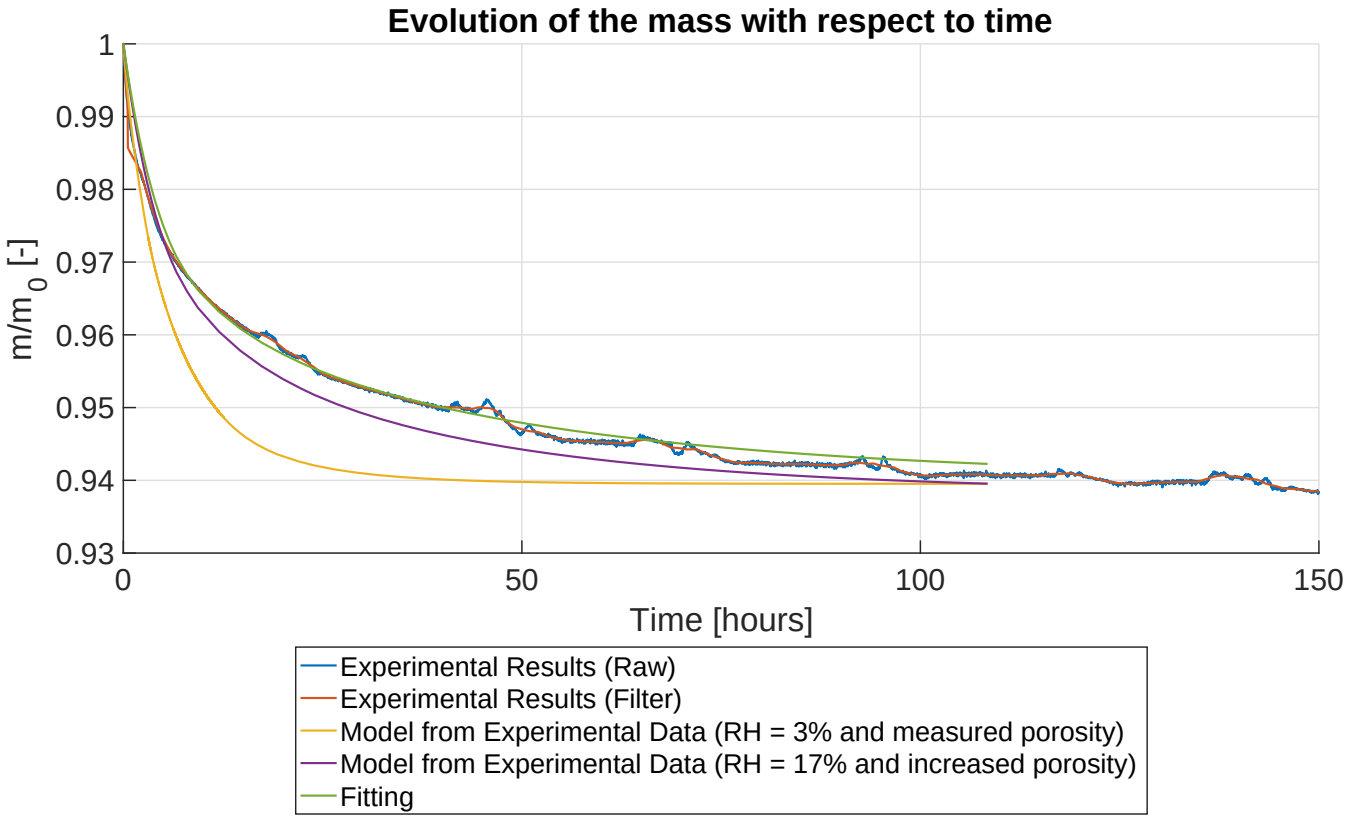

Figure 7.12: Mass loss comparison between the results from the convective drying experiment and the modelling performed for the M1-CEMI composition.

Based on those unknowns, it was therefore chosen to, on one hand, try to obtain a good fit by adapting the RH and, on the other hand, do the same keeping the relative humidity at 17% and adapting the porosity as well as m_{vG}. Finally, a fitting was also performed by changing the value of other parameters and with the goal to increase the accuracy with which the model replicates the results obtained with the convective dryer.

One can see from the results that, as it was mentioned during the analysis of the results of multiple experiments, the M1-CEMI seems to have a higher porosity than measured, as the curve with increased porosity and 17% of RH seems to better fit the drying results than the other curve with 3% RH. Moreover, this (purple) curve doesn't fit perfectly the experimental results but one could see that the difference between both doesn't exceed 0.5%, which is good enough.
However, the curve obtained by fitting shows that by tweaking a bit the parameters, it is possible to obtain a model that reproduces accurately the drying experiment, and the model is then validated.

7.3.2 Expertise's concrete

The Figure 7.13 represents the sample and the mesh used for the modelling of the expertise's concrete. In this case, as drying only occurs from the top face, the sample isn't as refined horizontally than vertically and was modelled along its whole height as no symmetry applies.

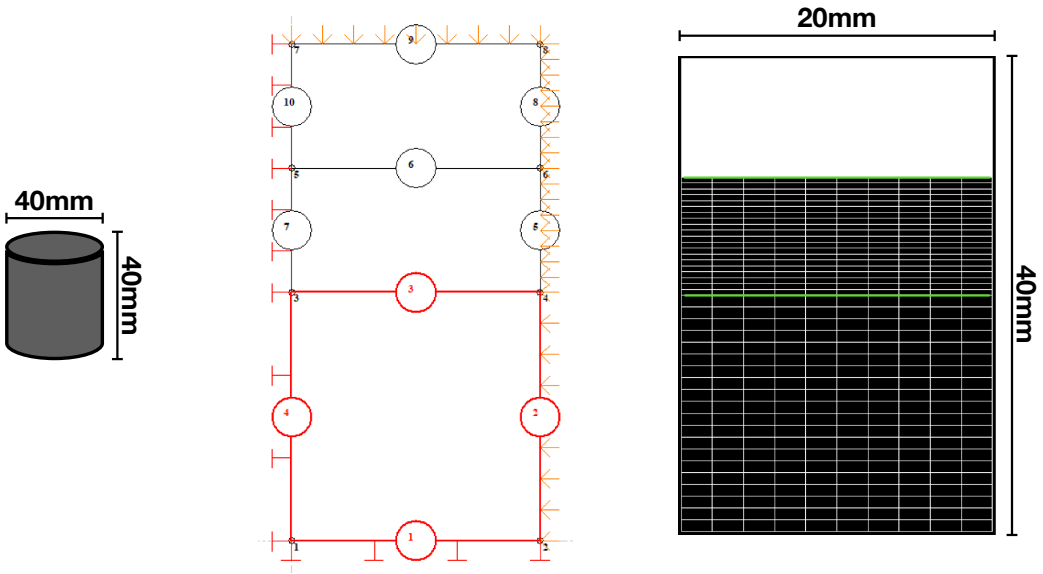

Figure 7.13: Mesh used for the modelling of the expertise's concrete

The Table 7.6 also summarises the value of each parameter used in the model, once again for both the experimental and fitting curve.

The Figure 7.14 displays the results obtained. At first, the modelling was performed with the results from experimentations conducted as part of this expertise. Then, a fitting was also performed, with a maximum difference between the convective drying results and the fitting of 0.2%. However, one can see that both the drying results and all the modelling results are not at a constant mass, meaning that the difference between both may increase, in particular

if we look at the $m_{vG} \times 2$ curve which, by definition, increases the relative permeability and therefore reaches a constant mass faster.

Parameter	Value Exp.	Value Fit.	Units	Experimental source
Density of the solid grains (ρ_s)	2602	2602	$[\mathrm{kg/m^3}]$	WAI
Concrete's intrinsic permeability (k_{int})	1E-19	1E-19	$[\mathrm{m^2}]$	Water Permeability
Concrete porosity (n)	13.9	13.9	[%]	WAI
Van Genuchten model parameter (m_{vG})	0.25	0.25	[-]	Static Desorption
Van Genuchten model parameter (n_{vG})	1.25	1.25	[-]	Static Desorption
Air-entry pressure (α_{vG})	5	3	[MPa]	Static Desorption
Minimal concrete's relative permeability	1E-4	1E-4	[-]	Static Desorption
Seepage penalty coefficient (K)	0	0	$[\mathrm{m/s.Pa}]$	-
Mass transfer coefficient (α)	0.0236	0.0236	$[\mathrm{m/s}]$	Convective Drying
Heat transfer coefficient (β)	31.42	31.42	$[\mathrm{W/m^2.K}]$	Convective Drying
Relative Humidity (RH)	47	47	[%]	Convective Drying

Table 7.6: Parameters used in the modelling of the concrete from the expertise

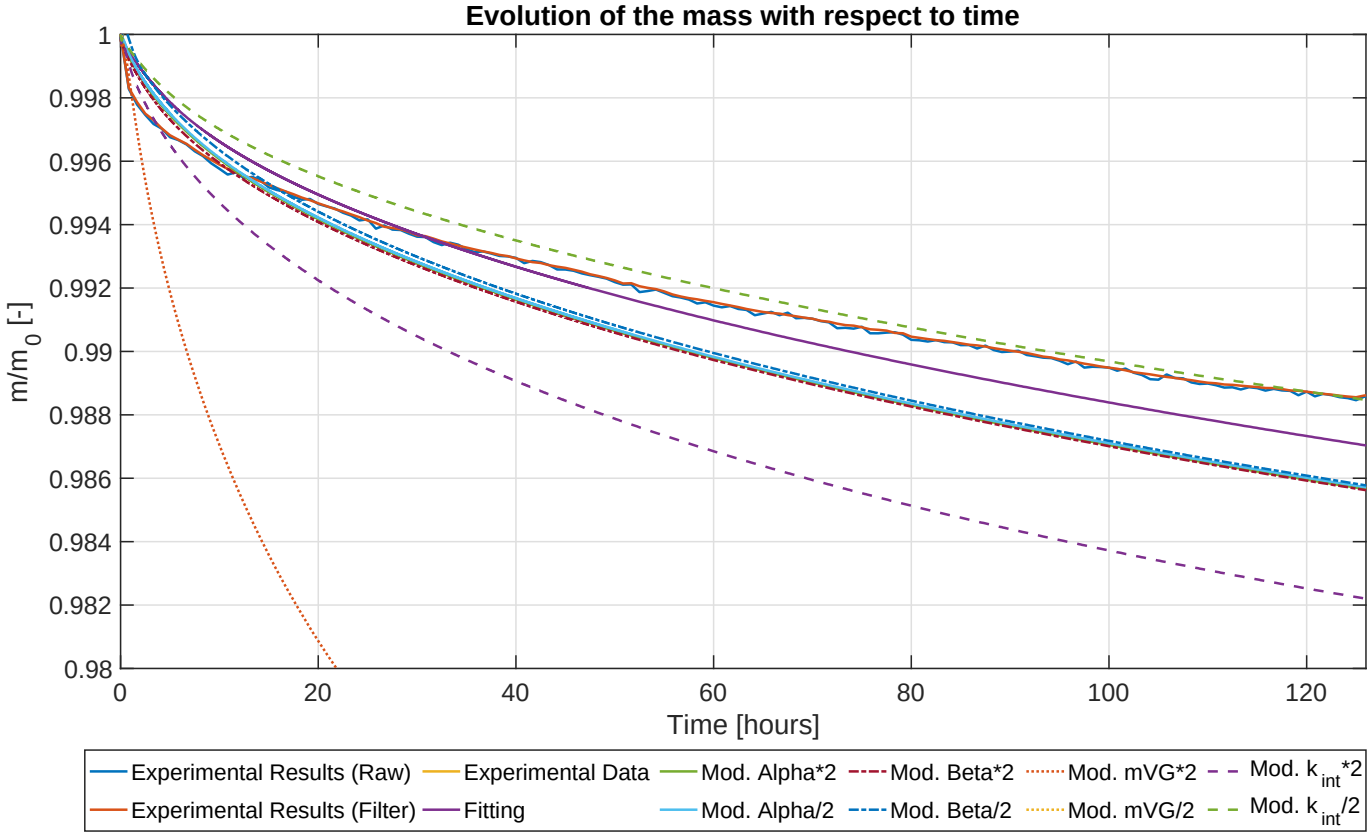

Figure 7.14: Mass loss comparison between the results from the convective drying experiment and the modelling performed for the expertise's concrete.

Within the frame of this expertise, various parameters were not accurately measured: the mass and heat transfer parameters (α and β), the parameter m_{vG} for the relative permeability and the intrinsic permeability k_{int}. It was therefore decided to perform a small sensibility analysis to confirm that the modification of those parameters doesn't really change the accuracy of the modelling, except for the parameter m_{vG} as the relative permeability has a great influence on the drying rate. Indeed, one can see that the experimental data and model with varying α and β are all equal, the differences being more pronounced at the very beginning of the drying experiment as their effect is limited to the Constant Rate Period. The variation of the intrinsic permeability can either increase the accuracy at the beginning of the drying experiment or at the end, which is why our fitting was chosen in between to try to keep a good accuracy all along the modelling. Finally, as mentioned, the parameter m_{vG} has a huge influence but it is mainly due to the non-stabilised character of our curves, as the graph doesn't display the stabilised relative mass of the sample after a complete drying.

7.4 Application

Once the model is sure to be valid, it can be applied to a more realistic case. Indeed, we will now model a rectangular column of 40cm height for 20cm width which would be submitted to the external environment on both its upper and lower sides. This column could be part of a multi-storey parking lot at the Brussels-Airport. Only the north and south side of the column are submitted to the environment because we study the base of this column as this is the zone the most impacted by environmental threats (de-icing salts, ...) and, to avoid accidents, walls link each external column (see Figure 7.15). The two compositions studied are the C-NA and C-RCA whose parameters were determined through the results of the experimentations.

Figure 7.15: Multi-storey parking lot with columns linked by walls. [Wikipedia, 2020c]

The mesh used for the modelling of the application is displayed at the Figure 7.16. As drying occurs symmetrically, only the upper half of the section is represented. However, the study can't be performed in an axisymmetric state as the sample isn't a cylinder. The modelling is then conducted in a plane strain state.

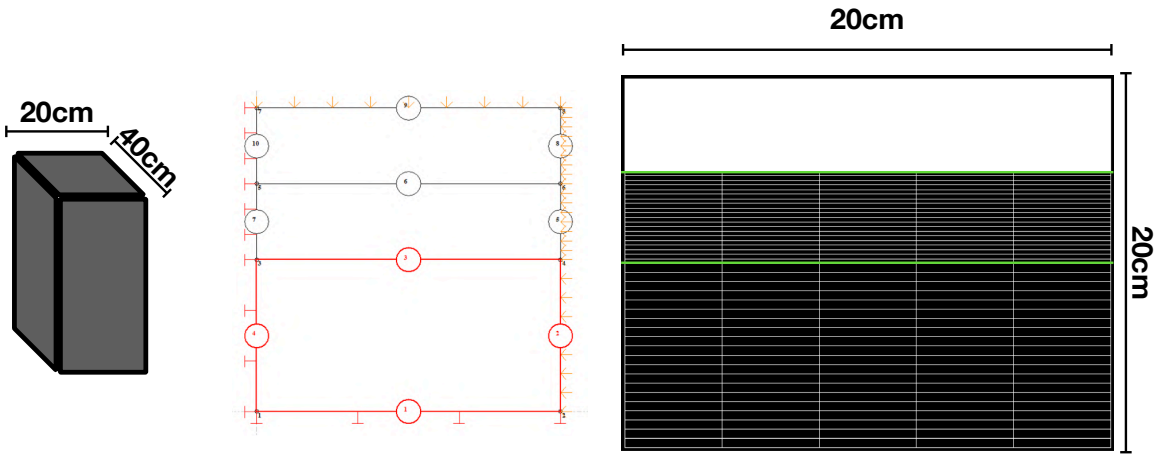

Figure 7.16: Mesh used for the modelling of the application's column

To begin with, the temperature is fixed to 21°C and the relative humidity is based on past measurements done at the Brussels-Airport (Figure 7.17). Based on this graph, one can see a semi-sinusoidal pattern with a period of one year, varying from 40% to 95% approximately. Then, according to the data concerning temperature from Brussels-Airport (Figure 7.18), the temperature will also vary from -5°C to 25°C in the same period as the relative humidity, the warmer the environment and the lower the relative humidity. The loading applied for both the constant and variable temperature is summarised in the Table 7.7.
The loading applied varies linearly with time and is therefore not exactly representative of the reality. Nonetheless, it still gives an indication on the evolution of the saturation degree of an exterior parking lot's column submitted to quasi-real environmental conditions.

The modelling is achieved for a period of five years in order to reach a transitional (due to the varying external conditions) yet kind of permanent regime. Indeed, as the solicitations are changing in the same exact manner every year, the saturation inside the beam should change accordingly between single upper and lower values, identical along the years.

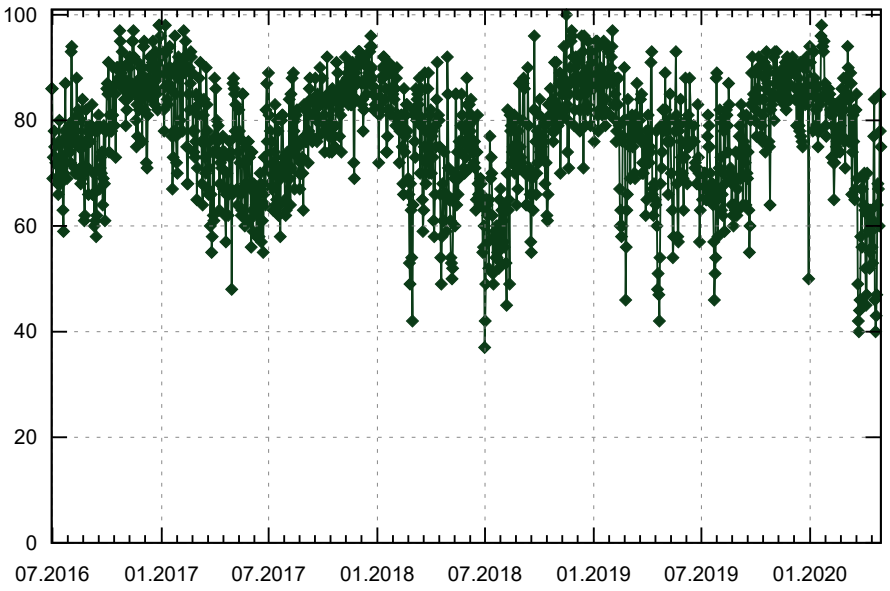

Figure 7.17: Relative humidity [%] at Brussel-Airport from 07/2016 to 05/2020 [WeatherOnline, 2020]

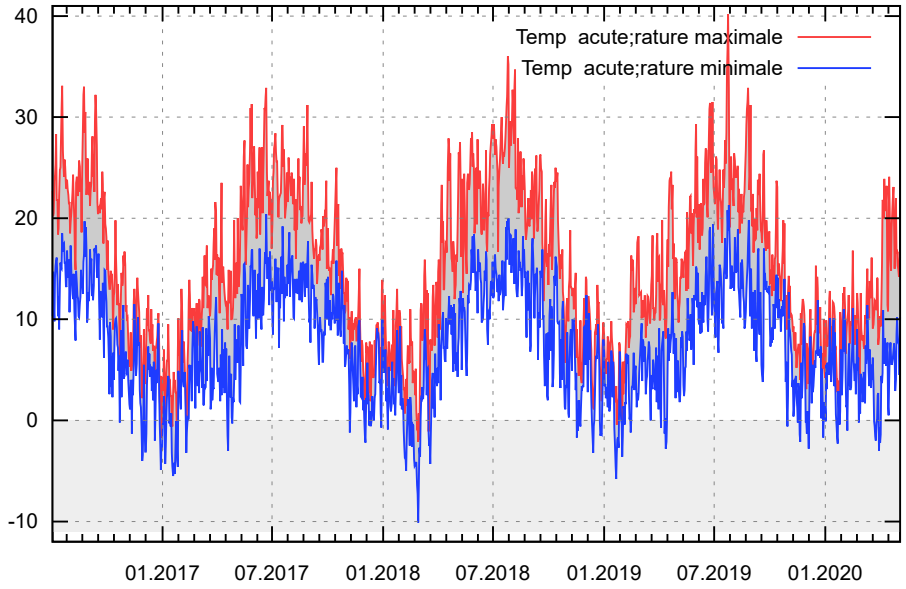

Figure 7.18: Temperature [$^{\circ}\mathrm{C}$] at Brussel-Airport from 07/2016 to 05/2020 [WeatherOnline, 2020]

Time	**RH** [%]	**Constant Temp.**		**Variable Temp.**	
		Temp. [K]	**Suction** [MPa]	**Temp.** [K]	**Suction** [MPa]
0 months $\approx$ 60 s.	40%		-124.39	298.15	-126.07
6 months = 15768E3 s.	95%		-6.963	268.15	-6.35
12 months = 31536E3 s.	40%		-124.39	298.15	-126.07
18 months = 47304E3 s.	95%		-6.963	268.15	-6.35
24 months = 63072E3 s.	40%		-124.39	298.15	-126.07
30 months = 78840E3 s.	95%	294.15	-6.963	268.15	-6.35
36 months = 94608E3 s.	40%		-124.39	298.15	-126.07
42 months = 110376E3 s.	95%		-6.963	268.15	-6.35
48 months = 126144E3 s.	40%		-124.39	298.15	-126.07
54 months = 141912E3 s.	95%		-6.963	268.15	-6.35
60 months = 157680E3 s.	40%		-124.39	298.15	-126.07

Table 7.7: External loading (temperature and suction) applied to the beam for both the constant and variable temperature.

The Table 7.8 displays the value of the parameters used for the modelling of the application for both compositions studied. As no convective drying experiments have been achieved on those concretes, it is not possible to determine experimentally the mass and heat transfer coefficients, α and β respectively, and it was thus decided to use the same coefficients as for the expertise. Those coefficients assume a wind speed of $3\mathrm{m/s}$, which is not unbelievable but maybe high for a parking lot's column. However, those are the most important in

the beginning of the drying, during the CRP, and their value is therefore not critical for our application. As for the seepage penalty coefficient, it was fixed to zero as seepage isn't required while working with such environmental conditions.

An important remark is that the environmental conditions applied introduce desorption as well as sorption inside the concrete elements. However, it is not possible to introduce two sets of parameters inside the modelling software. It was thus decided to use the parameters related to the desorption all along the modelling, therefore suppressing the hysteresis between the sorption and desorption.

Parameter	C-NA	C-RCA	Experimental source
Density of the solid grains (ρ_s) [$\mathrm{kg/m^3}$]	2630	2557	Water Absorption by Immersion
Concrete's intrinsic permeability (k_{int}) [$\mathrm{m^2}$]	7.68E-20	1.04E-19	Water Permeability
Concrete porosity (n) [-]	0.156	0.205	Water Absorption by Immersion
Van Genuchten model parameter (m_{vG}) [-]	0.32	0.31	Static Desorption
Van Genuchten model parameter (n_{vG}) [-]	1.47	1.44	Static Desorption
Air entry pressure (α_{vG}) [MPa]	23.4	19.88	Static Desorption
Minimal concrete's relative permeability [-]	1E-4	1E-4	-
Seepage penalty coefficient (K) [$\mathrm{m/s.Pa}$]	0	0	-
Mass transfer coefficient (α) [$\mathrm{m/s}$]	0.0236	0.0236	(from expertise)
Heat transfer coefficient (β) [$\mathrm{W/m^2.K}$]	31.42	31.42	(from expertise)

Table 7.8: Parameters used in the modelling of the column under variable relative humidity and temperature for both compositions C-NA and C-RCA.

As a reminder, the Figure 7.19 shows the water retention curve and relative permeability curve for the C-NA and C-RCA. One can see a small difference between both compositions. This difference seems negligible but still induces differences in saturation in the results obtained.

Indeed, the Figure 7.20 represents the evolution of the relative mass (m/m_0) as well as the water content loss ($w - w_0$), for both compositions and with constant and variable applied temperature. It was chosen to work in relative mass and water content loss as both compositions have a different bulk density and porosity, the results being easier to study if all curves start from the same point.

The first observation that can be made is that the C-RCA loses more mass than the C-NA due to its higher porosity (and therefore higher initial water content) as well as higher water permeability. Another remark is that, initially, the variable temperature results in a lower mass loss (and thus higher relative mass), but as the simulation reaches 18 months, the variable temperature induces a higher mass loss than the constant temperature, mainly due to the transient effects of this stage.

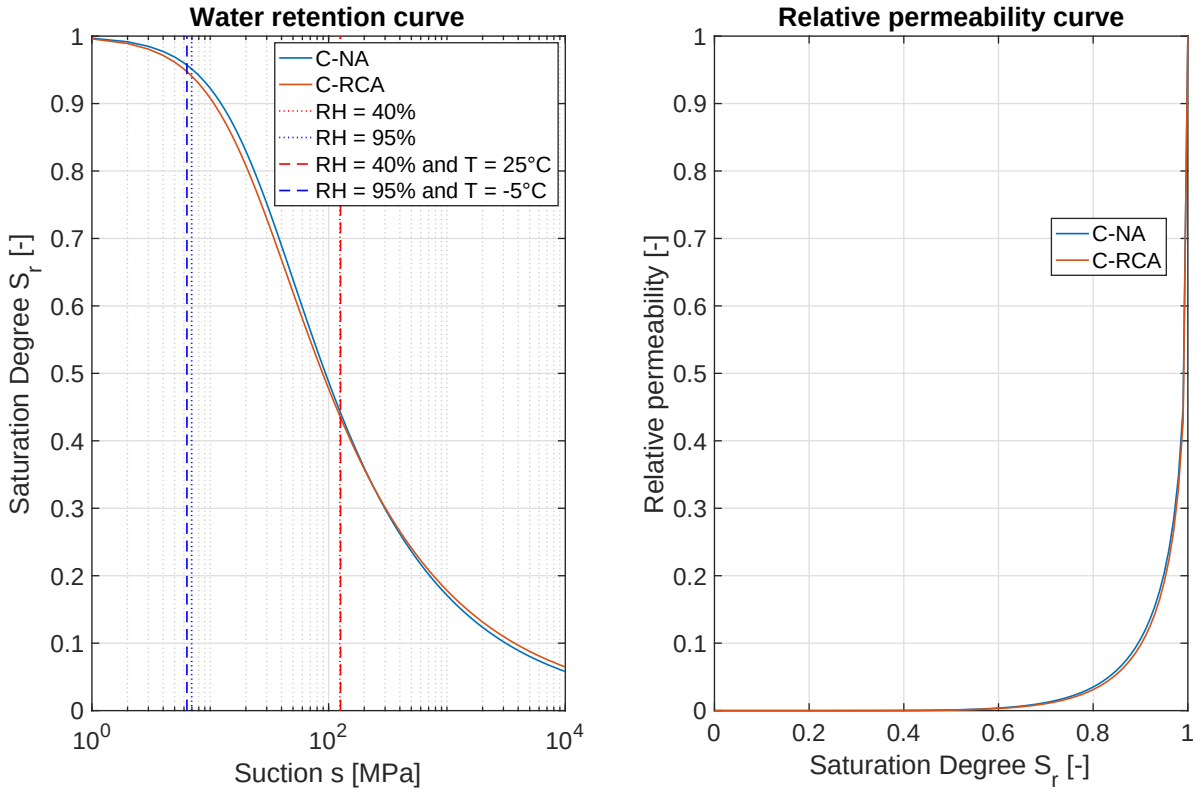

Figure 7.19: Water retention curve and relative permeability curve for C-NA and C-RCA.

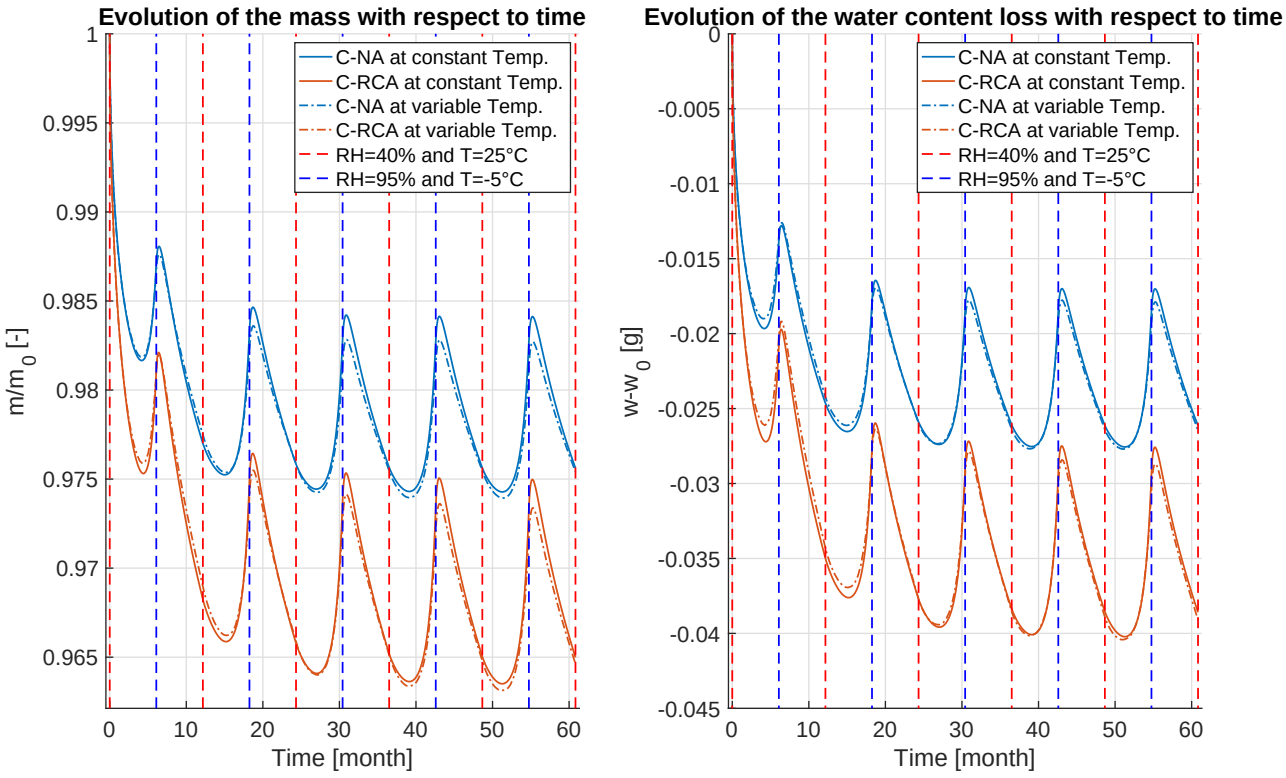

Figure 7.20: Evolution of the mass and water content with time, for both C-NA and C-RCA, with and without temperature change.

In addition to the graph representing the evolution of the mass, the Figure 7.20 displays the evolution of the water content loss. Once again, the C-NA loses less water content all along the simulation compared to the C-RCA, mainly due to its lower permeability. Concerning the variable or constant temperature, the same observations than on the graph of the evolution of the mass can be made.

The Figure 7.21 displays the evolution of the saturation degree inside the sample (along its discretised height), for several specific times, and for a constant (left) and variable (right) applied temperature. Until 18 months and during the desorption, the C-RCA has a lower saturation degree than the C-NA in the first 120mm from the drying surface, and then the C-NA has a lower saturation degree for the last 80mm. The opposite is observed during the sorption obviously. This is due to the C-RCA which is more permeable, thus losing more water than the C-NA initially and therefore creating a zone of lower relative permeability, decreasing the water transfer from deep inside the column's section.
After that time, the C-RCA always displays a lower saturation degree than the C-NA, as the curves for 24 months show. It was decided to only display the first two years of the simulation for clarity purposes.

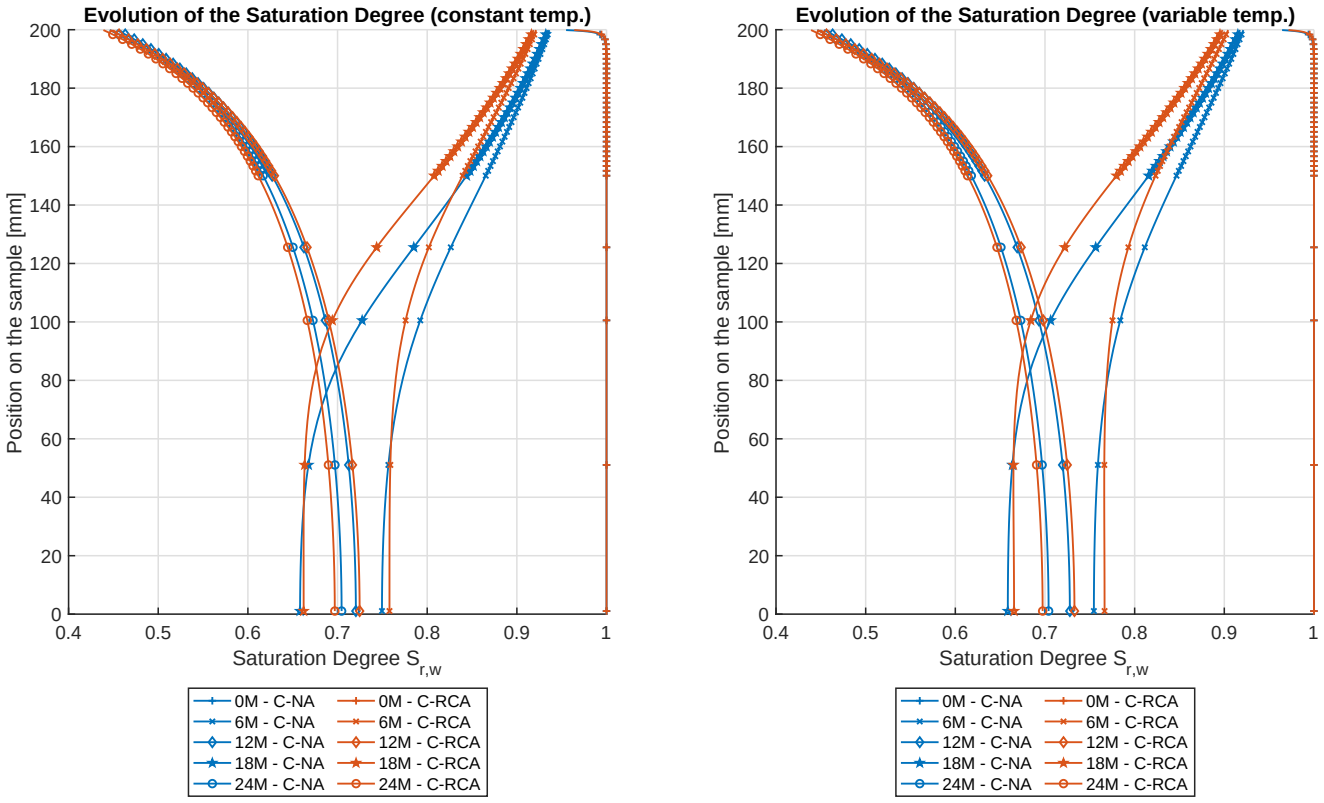

Figure 7.21: Evolution of the saturation along the height of the sample with time (0 to 2 years), for constant and variable external temperature.

The Figure 7.22 also represents the evolution of the saturation degree along the height of the sample for a period of four months and starting at 36 months of simulation. The goal of this graph is to better observe the delayed effects of the applied conditions changes. Indeed, one can see that the saturation increases at the surface while it still decreases at the middle of the sample (or bottom of the mesh in the figure shown). This is mainly due to the water and vapour flows which still go from the more saturated zone to the less saturated one in order to reach an equilibrium in the sample. Indeed, even if the surface's saturation increases

quickly and therefore the flows at the top of the sample go from the surface to the bottom, the middle section of the mesh is still less saturated than the bottom and therefore the flows in the bottom go from the inside of the sample to the drying surface.

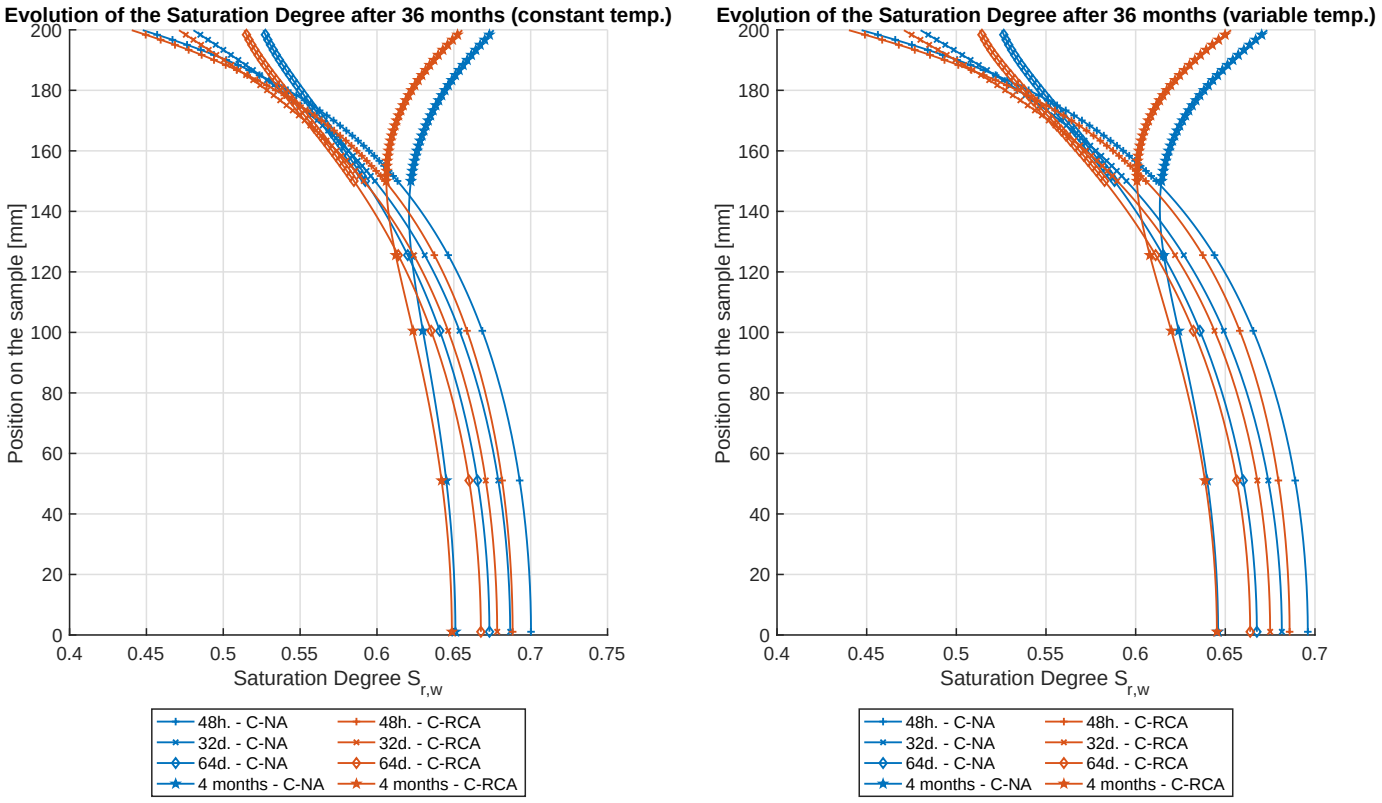

Figure 7.22: Evolution of the saturation along the height of the sample with time, for constant and variable external temperature and during the sorption (from 40% to 95% RH).

The same conclusions can be easily made from the Figure 7.23 which shows the evolution, with respect to time, of the saturation degree at various positions inside the column's section. The first position studied is at the drying surface of the section: the amplitudes of variation are indeed higher than at all the other positions as the drying surface is in direct contact with the environmental conditions applied. Moreover, the sorption/desorption changes happen directly as the applied conditions change. In terms of compositions, the C-RCA is less saturated than the C-NA all along the simulation.
The next position is at a 100mm from the drying surface: the amplitudes of the variations are obviously smaller than at the drying surface, and the C-RCA shows a lower saturation degree than the C-NA in the long term. However, at the beginning of the simulation, the opposite is once again observed: the C-NA loses and gains saturation faster than the C-RCA, resulting in a lower/higher saturation degree depending on the applied conditions (desorption or sorption respectively).
Finally, the middle section of the column was also studied. The amplitudes are once again smaller and the saturation is once again in between the maxima and minima of the last section studied. The same observations than for the previous cross-section studied can be made.
One important aspect to mention is that the deeper we go and the more delays there is between the section studied and the drying surface in terms of sorption/desorption, which was the conclusion obtained from the Figure 7.22.

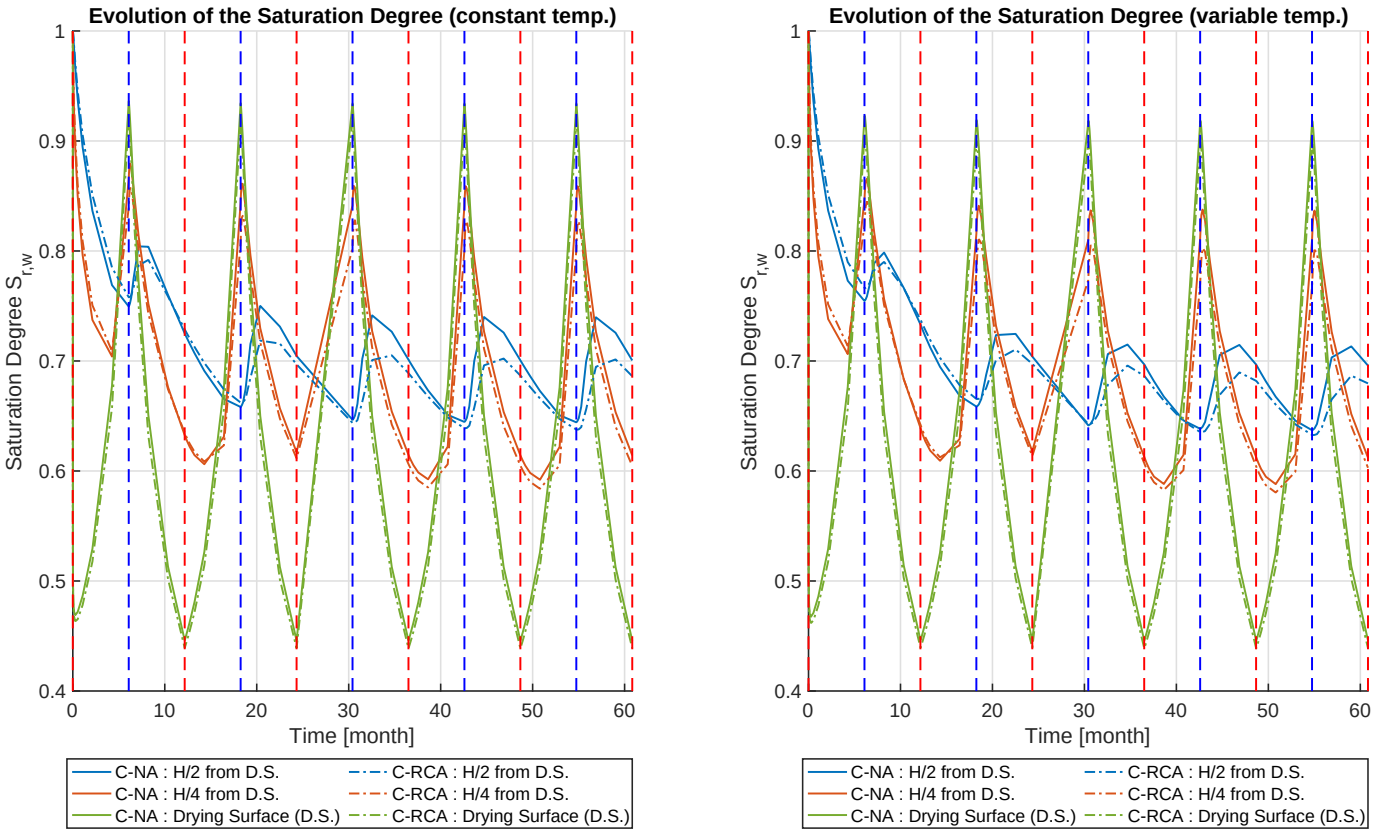

Figure 7.23: Evolution of the saturation with time, at 3 different depths in the sample.

The Figure 7.24 represents the evolution of the temperature at the drying surface of the columns, with and without variable external temperature.
With a constant applied temperature, one can see that the temperature at the drying surface is relatively stable and approximately in equilibrium with the temperature applied (that is 294.15 K). Indeed, the temperature decreases during the desorption because the change of phase of water, from liquid to vapour, consumes energy and therefore decreases the sample's temperature. The opposite is observed during the sorption as the change of phase is the opposite and excess heat is then transmitted from the water to the sample.
The spikes observed during the sorption are more pronounced than the temperature loss during the desorption mainly because the liquid water flows are always predominant on the water vapour flow, even during desorption. Therefore, there is less heat required for the vaporisation of the liquid water than there is heat generated during the condensation.

For a variable applied temperature, the temperature at the surface of the sample changes accordingly to the applied conditions, without any delay or variations due to the consumption (or production) of heat by the vaporisation (or condensation) of water. Small fluctuations could be seen if we analysed the temperature changes deeper in the section of the column.

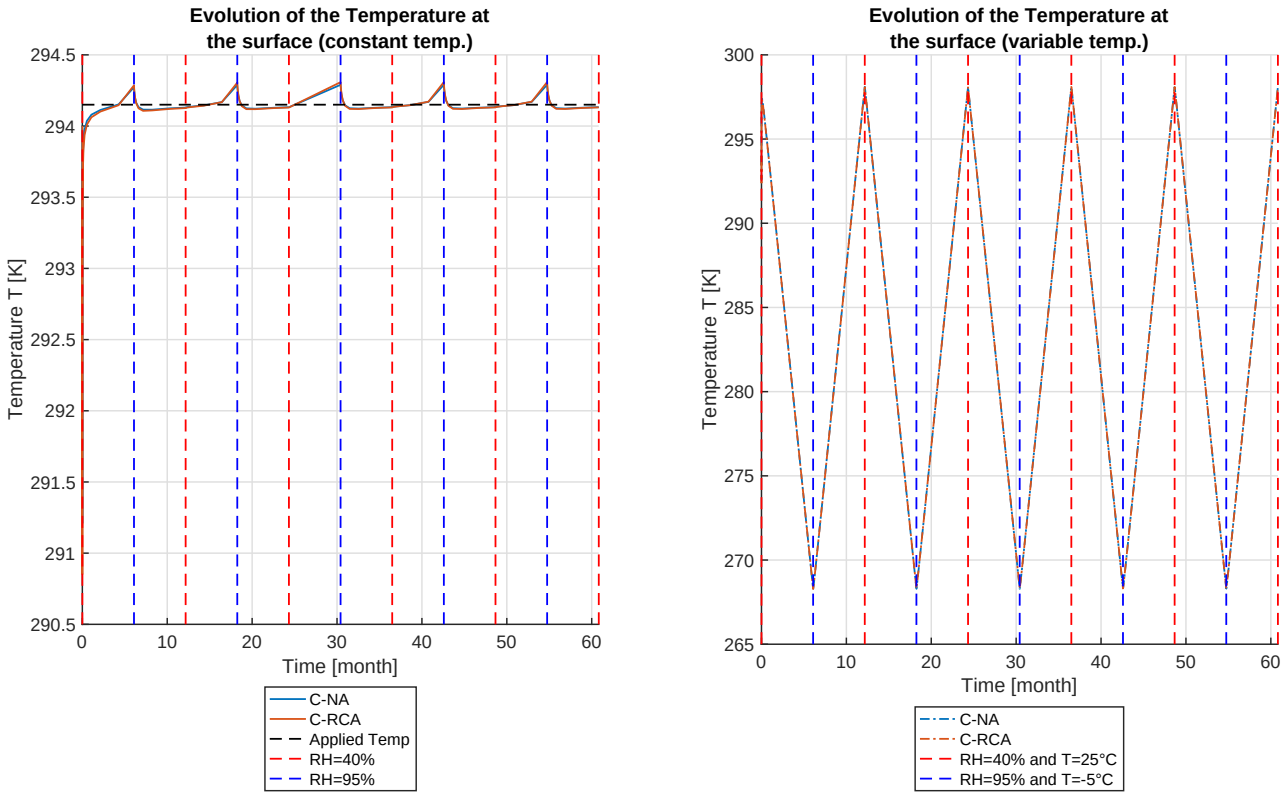

Figure 7.24: Evolution of the temperature at the drying surface of the columns, with and without variable external temperature.

The Figure 7.26 displays the evolution of the saturation degree, with time and along the discretised height of the column, under variable temperature only. This graph is helpful to predict the durability of a concrete member. Indeed, the Figure 7.25 shows that the carbonation rate is maximum around 70% of relative humidity in the environment, under the assumption that the concrete member is in equilibrium with its surroundings.
For the interval of temperature studied, that is in between -5°C and 25°C, the suction for a RH of 70% is in between 44.13MPa and 49.1MPa. If we use the water retention curve, it results that the carbonation rate is maximum if the saturation inside the concrete is approximately equal to 65% for the C-NA and 63% for the C-RCA.

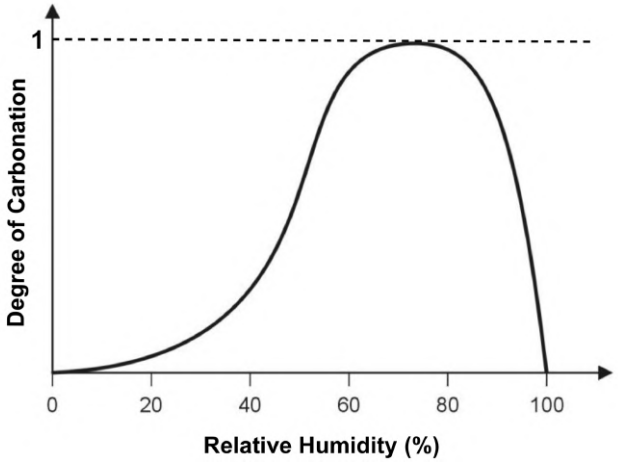

Figure 7.25: Carbonation rate with respect to the relative humidity of the environment (under equilibrium between the concrete and the environment) (adapted from [Bertolini et al., 2004])

The first observation is that at first, the C-RCA and C-NA are submitted to similar saturation variations. However, in the case of the variable temperature (which is more realistic than a constant temperature), the saturation of the C-RCA decreases sharply from approximately 24 months of simulation, creating a zone of saturation below 70% in the middle of the column. This can be confirmed by looking at the saturation of the C-RCA at the middle of the sample (or bottom of the mesh) in the Figure 7.23, which is always below 70%. However, the saturation at the drying surface of the sample still varies from approximately 45% in desorption to 92% in sorption, and therefore the carbonation rate is still reduced during the sorption as less CO_2 can enter the porous system of the concrete member.

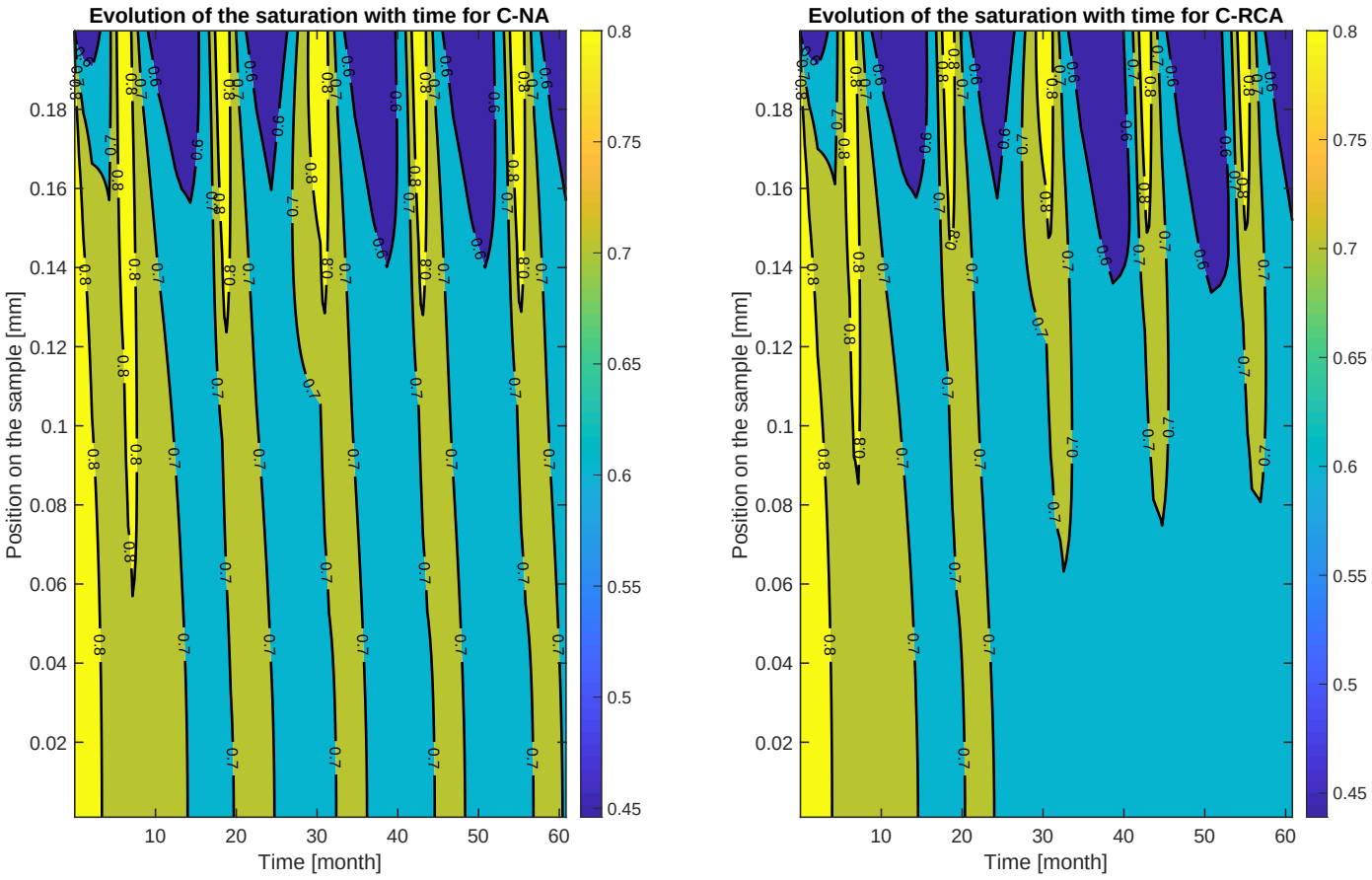

Figure 7.26: Evolution of the saturation degree with time on the whole section, for variable temperature only.

7.5 Conclusion

The final task in order to try predicting the durability of concrete made from recycled concrete aggregates was modelling the drying phenomena.

This chapter started with a sensibility analysis of the several parameters influencing the drying phenomena of concrete. Then, a validation of the model was performed through fitting and comparison of the modelling and experimental results, and it was shown that the numerical model is sufficiently accurate for convective drying experiments.

Finally, an application was conducted and consisted of an exterior parking lot's column submitted to variations of relative humidity and temperature in the environment. This simulation occurs over a period of five years in order to reach a quasi "steady state" where the column is always in equilibrium with its surroundings.
The application was performed with the C-NA and C-RCA compositions to compare the durability of a concrete made from natural aggregates with a concrete made from recycled concrete aggregates. The conclusion of this application is that the C-RCA is more prone to carbonation or other degradation processes. Indeed, the saturation inside the column is, in its stabilised state, always below the saturation of the C-NA which promotes CO_2 and other ions' transfers from the environment to the inside of the concrete.

8 | Conclusion

Throughout the work achieved in this thesis, concrete made with recycled concrete aggregates has been characterised in terms of drying phenomena for purposes of assessing and trying to predict the durability of this construction material. Indeed, the scientific question this thesis tried to answer was: "Is the use of recycled concrete aggregates inside concrete affecting its durability?"

Through the multiple experiments conducted, a comparison of our two main concrete compositions can be done: the C-NA and C-RCA. Indeed, the goal of this thesis is to highlight the influence of the substitution of NA by RCA. The main results obtained are:

- Water Absorption by Immersion: the addition of recycled concrete aggregates inside concrete increases its porosity (by 31.5%) and water absorption (by 30.5%). Indeed, and as it was proven in the literature, the Recycled Concrete Aggregates (RCA) alone have a greater water absorption than the Natural Aggregates (NA); therefore, the porosity and water absorption of concrete with RCA increase proportionally to the percentage of RCA used. As for porosity, the addition of aggregates with old cement paste decreases the quality of the Interfacial Transition Zone and increases its porosity.
- Water permeability: the intrinsic permeability of the C-RCA is 35% greater than the C-NA. This increased intrinsic permeability will allow easier water movements inside the porous system of concrete.
- Static sorption and desorption: the C-RCA has a smaller air-entry pressure than the C-NA, which means that it will start to desaturate for smaller values of suction than the C-NA. The same logic applies to the sorption. Nonetheless, both water retention curves are relatively close to each other and the properties of the C-RCA with regard to the water retention curves are therefore not as different as one could have imagined.
- Resistance to carbonation: the C-RCA is more prone to carbonation than the C-NA, mainly due to its greater porosity. Indeed, the added cement from the recycled concrete aggregates is already pre-carbonated and therefore doesn't slow the carbonation rate or at least not enough to equilibrate the increased rate due to the porosity.

In addition to the experimental results mentioned above, the modelling part of this thesis also helped to predict the durability of concrete made from RCA. Indeed, the application conducted numerically consisted of the study of a multi-storey exterior parking lot's column. We used properties (determined experimentally) of the C-NA and C-RCA to model five years of real environmental conditions based on meteorological data available at the Brussels Airport. This application showed that the column made from C-RCA has a saturation degree constantly below the one of the C-NA. This may induce a higher carbonation rate or decrease some degradation processes where water is required.

As a conclusion, one could state that **the use of Recycled Concrete Aggregates (RCA) inside concrete reduces the durability of concrete due to its composition and physical properties**. Indeed, the application showed that the substitution of the natural aggregates

by recycled concrete aggregates leads to a concrete whose saturation is below the saturation of the C-NA, in a range promoting carbonation or other degradation processes.

Nonetheless, characterising and consolidating this decrease in durability requires more time and means, which were not available within the frame of this master thesis.
It is indeed difficult to conclude anything without further testing and replication of the experiments achieved. Convective drying tests should be performed on concrete made from NA and RCA to confirm the model used, mercury porosimetry could increase the confidence in the value of the porosity as well as give indications on the pores' distribution, and as durability rhymes with carbonation, it is also linked to the resistance to chloride attacks, which should be assessed to better conclude on the durability of concrete made from RCA.
In terms of modelling, the hysteresis effect between the sorption and desorption observed in the water retention curves should be implemented into the Lagamine software. All in one, further experiments and modelling should be performed to confirm the trend exposed all along this thesis.

In addition to further experiments and modelling, recycled concrete aggregates coming from real construction and demolition waste could be used. Indeed, the RCA used in this thesis were obtained after crushing of concrete samples that were designed and cast in the laboratory for another research. Therefore, those RCA are of good quality and it influences the results of our study. The use of RCA coming from real C&DW could broaden the results obtained and help to better characterise the durability loss while substituting NA by RCA, further comforting the industrial use or not of RCA inside concrete.

Bibliography

[Apers & de Schutter, 2018] Apers, J. & de Schutter, G. (2018). *Technologie du béton - Chapitre 5 : V Durabilité*, volume 5. Bruxelles: Groupement Belge du Béton (GBB).

[Arredondo-Rea et al., 2012] Arredondo-Rea, S. P., Corral-Higuera, R., Gómez-Soberón, J. M., Castorena-González, J. H., Orozco-Carmona, V., & Almaral-Sánchez, J. L. (2012). Carbonation Rate and Reinforcing Steel Corrosion of Concretes with Recycled Concrete Aggregates and Supplementary Cementing Materials. *International Journal of Electrochemical Science*, 7, 1602–1610.

[Baroghel-Bouny, 1994] Baroghel-Bouny, V. (1994). *Caractérisation microstructurale et hydrique des pâtes de ciment et des bétons ordinaires et à très hautes performances*. PhD thesis, École Nationale des Ponts et Chaussées.

[Baroghel-Bouny, 2007] Baroghel-Bouny, V. (2007). Water vapour sorption experiments on hardened cementitious materials - Part I : Essential tool for analysis of hygral behaviour and its relation to pore structure. *Cement and Concrete Research*, 37, 414–437.

[Bažant & Najjar, 1972] Bažant, Z. P. & Najjar, L. J. (1972). Nonlinear water diffusion in nonsaturated concrete. *Matériaux et constructions*, 5(25).

[Bear & Verruijt, 1987] Bear, J. & Verruijt, A. (1987). *Modeling Groundwater Flow and Pollution*. D. Reidel Publishing Company.

[Belin et al., 2014] Belin, P., Habert, G., Thiery, M., & Roussel, N. (2014). Cement paste content and water absorption of recycled concrete coarse aggregates. *Materials and Structures*, 47(9), 1451–1465.

[Bentur & Odler, 1996] Bentur, A. & Odler, I. (1996). Development and nature of interfacial microstructure. In J. Maso (Ed.), *Interfacial Transition Zone in Concrete, RILEM REPORT*, volume 11 chapter 2, (pp. 21–50). E & FN Spon.

[Bertolini et al., 2004] Bertolini, L., Elsener, B., Pedeferri, P., & Polder, R. P. (2004). *Corrosion of Steel in Concrete*. WILEY-VCH Verlag GmbH and Co. KGaA, Weinheim.

[Biglarijoo et al., 2017] Biglarijoo, N., Nili, M., Hosseinian, S. M., Razmara, M., Ahmadi, S., & Razmara, P. (2017). Modelling and optimisation of concrete containing recycled concrete aggregate and waste glass. *Magazine of Concrete Research*, 69(6), 306–316.

[Bowen, 1980] Bowen, R. M. (1980). Incompressible porous media models by use of the theory of mixtures. *International Journal of Engineering Science*, 18, 1129–1148.

[Brunauer et al., 1940] Brunauer, S., Deming, L. S., Deming, W. E., & Teller, E. (1940). On a theory of the van de Waals Adsorption of Gases. *Journal of the American Chemical Society*, 62(7), 1723:1732.

[Brunauer et al., 1938] Brunauer, S., Emmet, P. H., & Teller, E. (1938). Adsorption of Gases in Multimolecular Layers. *Journal of the American Chemical Society*, 60, 309–319.

[Brunauer et al., 1969] Brunauer, S., Skalny, J., & Bodor, E. E. (1969). Adsorption on Nonporous Solids. *Journal of Colloid and Interface Science*, 30(4), 546–552.

[Ceaglske & Hougen, 1937] Ceaglske, N. H. & Hougen, O. A. (1937). Drying granular solids. *Industrial and Engineering Chemistry*, 29(7), 805–813.

[Collin, 2003] Collin, F. (2003). *Couplages thermo-hydro-mécaniques dans les sols et les roches tendres partiellement saturés*. PhD thesis, Uliège University.

[Collin & de Ville de Goyet, 2019] Collin, F. & de Ville de Goyet, V. (2019). *Non linear finite elements*. ULiège University.

[Comings & Sherwood, 1934] Comings, E. W. & Sherwood, T. K. (1934). The Drying of Solids - VII : Moisture Movement by Capillarity in Drying Granular Materials. *Industrial and Engineering Chemistry*, 26(10), 1096–1098.

[Concha, 2014] Concha, F. A. (2014). *Solid-Liquid Separation in the Mining Industry*, volume Fluid Mechanics and Its Applications (Book 105). Springer International Publishing Switzerland.

[Courard, 2017] Courard, L. (2017). *Matériaux de construction*. ULiège University.

[Courard, 2018] Courard, L. (2018). *Technologie des bétons et matériaux nouveaux*. ULiège University.

[Courard & Michel, 2014] Courard, L. & Michel, F. (2014). *Aspects phénoménologiques relatifs aux processus de dégradation chimique des barrières ouvragées à base de liant hydraulique - Évaluation de la phase d'initiation de la corrosion des armatures des structures en béton armé*. Analyse du rapport ONDRAF/NIRAS - NIROND-TR 2011-58 F 31 - August 2012, ULiege University.

[Courard et al., 2011] Courard, L., Michel, F., & Martin, M. (2011). The evaluation of the surface free energy of liquids and solids in concrete technology. *Construction and Building Materials*, 25, 260–266.

[Dassargues, 2017] Dassargues, A. (2017). *Hydrogéologie*. ULiège University.

[de Juan & Gutiérrez, 2009] de Juan, M. S. & Gutiérrez, P. A. (2009). Study on the influence of attached mortar content on the properties of recycled concrete aggregate. *Construction and Building Materials*, 23, 872–877.

[Delage, 1987] Delage, P. (1987). Aspects du comportement des sols non saturés. *Revue française de géotechnique*, 40, 33–43.

[Delage et al., 1998] Delage, P., Howat, M., & Cui, Y. (1998). The relationship between suction and swelling properties in a heavily compacted unsaturated clay. *Engineering Geology*, 50, 31–48.

[Deodonne, 2015] Deodonne, K. (2015). *Études des caractéristiques physico-chimiques de bétons de granulats recyclés et de leur impact environnemental*. PhD thesis, Université de Strasbourg.

[Desaar, 2015] Desaar, F. (2015). Effet des additions de type 2 sur les écoulements multiphasiques dans les pâtes de ciment. Master's thesis, ULiège University.

[Dhir et al., 1989] Dhir, R. K., Hewlett, P. C., & Chan, Y. N. (1989). Near surface characteristics of concrete: intrinsic permeability. *Magazine of Concrete Research*, 41(147), 87–97.

[Dieudonné, 2016] Dieudonné, A.-C. (2016). *Hydromechanical behaviour of compacted bentonite: from micro-scale analysis to macro-scale modelling*. PhD thesis, Uliège University.

[Dupré & Dupré, 1869] Dupré, A. & Dupré, P. (1869). *Théorie mécanique de la chaleur*. Gauthier-Villars.

[Erdem et al., 2009] Erdem, T. K., Khayat, K. H., & Yahia, A. (2009). Correlating Rheology of Self-Consolidating Concrete to Corresponding Concrete-Equivalent Mortar. *ACI Materials Journal*, 106(2), 154–160.

[European Commission, 2019] European Commission (2019). Construction and Demolition Waste (CDW). https://ec.europa.eu/environment/waste/construction_demolition.htm. Accessed: 8/11/2019.

[European Environment Agency, 2020] European Environment Agency (2020). *Construction and demolition waste : challenges and opportunities in a circular economy*. Technical report, European Environment Agency.

[Eurostat, 2014] Eurostat (2014). Archive: Cement and concrete production statistics - NACE Rev. 1.1. https://ec.europa.eu/eurostat/statistics-explained/index.php/Archive:Cement_and_concrete_production_statistics_-_NACE_Rev._1.1. Accessed: 8/11/2019.

[Fathifazl et al., 2011] Fathifazl, G., Razaqpur, A. G., Isgor, O. B., Abbas, A., Fournier, B., & Foo, S. (2011). Creep and drying shrinkage characteristics of concrete produced with coarse recycled concrete aggregate. *Cement and Concrete Composites*, 33, 1026–1037.

[Fredlund et al., 2011] Fredlund, D. G., Sheng, D., & Zhao, J. (2011). Estimation of soil suction from the soil-water characteristic curve. *Canadian Geotechnical Journal*, 48, 186–198.

[Gardner & Widtsoe, 1921] Gardner, W. & Widtsoe, J. A. (1921). The movement of soil moisture. *Soil Science*, 11(3), 215–232.

[Gerard, 2011] Gerard, P. (2011). *Impact des transfers de gaz sur le comportement poro-mécanique des matériaux argileux*. PhD thesis, ULiège University.

[Gerard et al., 2010] Gerard, P., Léonard, A., Masekanya, J.-P., Charlier, R., & Collin, F. (2010). Study of the soil-atmosphere moisture exchanges through convective drying tests in non-isothermal conditions. *International Journal for Numerical and Analytical Methods in Geomechanics*, 34, 1297–1320.

[Giles & Smith, 1974] Giles, C. H. & Smith, D. (1974). A General Treatment and Classification of the Solute Adsorption Isotherm - 1. Theoretical. *Journal of Colloid and Interface Science*, 47(3), 755–765.

[Gilliland & Sherwood, 1933] Gilliland, E. R. & Sherwood, T. K. (1933). The Drying of Solids - VI : Diffusion Equations for the Period of Constant Drying Rate. *Industrial and Engineering Chemistry*, 25(10), 1134–1136.

[Gómez-Soberón, 2002] Gómez-Soberón, J. M. (2002). Porosity of recycled concrete with substitution of recycled concrete aggregate - An experimental study. *Cement and Concrete Research*, 32, 1301–1311.

[Guo et al., 2018] Guo, H., Shi, C., Guan, X., Zhu, J., Ding, Y., Ling, T.-C., Zhang, H., & Wang, Y. (2018). Durability of Recycled Aggregate Concrete - A Review. *Cement and Concrete Composites*, 89, 251–259.

[Hall, 1989] Hall, C. (1989). Water sorptivity of mortars and concretes: a review. *Magazine of Concrete Research*, 41(147), 51–61.

[Hougen et al., 1940] Hougen, O. A., McCauley, H. J., & Marshall, W. R. (1940). Limitations of diffusion equations in drying. *Transactions of the American Institute of Chemical Engineering*, 36, 183–210.

[Hubert, 2018] Hubert, J. (2018). *Experimental and numerical study of cracking during the drying of porous materials : application to the fields of chemical engineering and geomechanics*. PhD thesis, ULiège University.

[Hussain et al., 2000] Hussain, H., Levacher, D., Quenec'h, J.-L., Bennabi, A., & Bouvet, F. (2000). Valorisation des aggrégats issus de bétons de démolition dans la fabrication de nouveaux bétons. *Sciences et techniques*, 19, 17–22.

[Idso et al., 1974] Idso, S. B., Reginato, R. J., Jackson, R. D., Kimball, B. A., & Nakayama, F. S. (1974). The Three Stages of Drying of a Field Soil. *Soil Science Society of America Journal*, 38, 831–837.

[Inglezakis et al., 2018] Inglezakis, V. J., Poulopoulos, S. G., & Kazemian, H. (2018). Insights into the S-shaped sorption isotherms and their dimensionless forms. *Microporous and Mesoporous Materials*, 272, 166–176.

[Kemp et al., 2001] Kemp, I. C., Fyhr, B. C., Laurent, S., Roques, M. A., Groenewold, C. E., Tsotsas, E., Sereno, A. A., Bonazzi, C. B., Bimbenet, J.-J., & Kind, M. (2001). Methods for processing experimental drying kinetics data. *Drying technology*, 19, 15–34.

[Kowalski, 2003] Kowalski, S. J. (2003). *Thermomechanics of Drying Processes*. Springer-Verlag Berlin Heidelberg GmbH.

[Kumar & Bhattacharjee, 2003] Kumar, R. & Bhattacharjee, B. (2003). Porosity, pore size distribution and in situ strength of concrete. *Cement and Concrete Research*, 33, 155–164.

[Lehmann et al., 2008] Lehmann, P., Assouline, S., & Or, D. (2008). Characteristic lengths affecting evaporative drying of porous media. *Physical Review*, 77.

[Léonard, 2002] Léonard, A. (2002). *Étude du séchage convectif de boues de stations d'épuration*. PhD thesis, ULiège University.

[Levy & Helene, 2004] Levy, S. M. & Helene, P. (2004). Durability of recycled aggregates concrete: a safe way to sustainable development. *Cement and Concrete Research*, 34, 1975–1980.

[Limousin et al., 2007] Limousin, G., Gaudet, J.-P., Charlet, L., Szenknect, S., Barthès, V., & Krimissa, M. (2007). Sorption isotherms: A review on physical bases, modeling and measurement. *Applied Geochemistry*, 22, 249–275.

[Lovato et al., 2012] Lovato, P. S., Possan, E., Molin, D. C. C. D., Masuero, Â. B., & Ribeiro, J. L. D. (2012). Modeling of mechanical properties and durability of recycled aggregate concretes. *Construction and Building Materials*, 26, 437–447.

[Mehta & Monteiro, 1988] Mehta, P. K. & Monteiro, P. J. M. (1988). Effect of aggregate, cement, and mineral admixtures on the microstructure of the transition zone. *Materials Research Society Symp. Proc.*, 114, 65–75.

[Ollivier & Massat, 1996] Ollivier, J.-P. & Massat, M. (1996). The effect of the transition zone on transfer properties of concrete. In J. Maso (Ed.), *Interfacial Transition Zone in Concrete, RILEM REPORT*, volume 11 chapter 7, (pp. 130–145). E & FN Spon.

[Ollivier & Torrenti, 2008] Ollivier, J.-P. & Torrenti, J.-M. (2008). *La structure poreuse des bétons et les propriétés de transfert*, chapter 3, (pp. 51–134). Presses de l'école nationale des ponts et chaussées.

[Pap et al., 2018] Pap, M., Mahler, A., & Nehme, S. (2018). Measurement of water retention curve for different concrete mixtures.

[Parrott, 1988] Parrott, L. J. (1988). Moisture profiles in drying concrete. *Advances in Cement Research*, 1(3), 164–170.

[Philip & De Vries, 1957] Philip, J. R. & De Vries, D. A. (1957). Moisture Movement in Porous Materials under Temperature Gradients. *Transactions, American Geophysical Union*, 38(2), 222–232.

[Powers, 1958] Powers, T. C. (1958). Structure and Physical Properties of Hardened Portland Cement Paste. *Journal of the American Ceramic Society*, 41(1), 1–6.

[Rouquerol et al., 1994] Rouquerol, J., Avnir, D., Fairbridge, C. W., Everett, D. H., Haynes, J. H., Pernicone, N., Ramsay, J. D. F., Sing, K. S. W., & Unger, K. K. (1994). Recommendations for the characterization of porous solids. *Pure and Applied Chemistry*, 66(8), 1739–1758.

[Salomao, 2019] Salomao, D. P. (2019). Effets des méthodes de fragmentation sur la qualité des granulats de béton recyclé. Master's thesis, ULiège University.

[Scherer, 1990] Scherer, G. W. (1990). Theory of Drying. *Journal of the American Ceramic Society*, 73(1), 3–14.

[Schwartzentruber & Catherine, 2000] Schwartzentruber, A. & Catherine, C. (2000). La méthode du mortier de béton équivalent (MBE) - Un nouvel outil d'aide à la formulation des bétons adjuvantés. *Matériaux et Constructions*, 33, 475–482.

[Sherwood, 1929] Sherwood, T. K. (1929). The Drying of Solids - I. *Industrial and Engineering Chemistry*, 21(1), 12–16.

[Tournier, 2001] Tournier, B. R. (2001). *Transferts par capillarité et évaporation dans des roches - Rôle des structures de porosité*. PhD thesis, Strasbourg I - Université Louis Pasteur.

[UEPG, 2018] UEPG (2018). Union Européenne des Producteurs de Granulats - Estimates of Aggregates Production data 2017. http://www.uepg.eu/statistics/estimates-of-production-data/data-2017. Accessed: 8/11/2019.

[Van Arsdel, 1947] Van Arsdel, W. B. (1947). Approximate diffusion calculations for the falling-rate phase of drying. *Chemical Engineering Progress*, 43(1), 13–24.

[Van Genuchten, 1980] Van Genuchten, M. T. (1980). A Closed-form Equation for Predicting the Hydraulic Conductivity of Unsaturated Soils. *Soil Science Society of America Journal*, 44, 892:898.

[Verruijt & Baars, 2007] Verruijt, A. & Baars, S. V. (2007). *Soil mechanics*. VSSD Delft.

[Vinkler & Vitek, 2016] Vinkler, M. & Vitek, J. L. (2016). Drying Concrete : Experimental and Numerical Modeling. *Journal of Materials in Civil Engineering*.

[WeatherOnline, 2020] WeatherOnline (2020). Bruxelles Aéroport - Humidité Relative. https://www.wofrance.fr/weather/maps/city?LANG=fr&WMO=06451&ART=RLF&CONT=euro&R=0&LEVEL=150&REGION=0003&LAND=BX&NOREGION=1&MOD=&TMX=&TMN=&SON=&PRE=&MONAT=&OFFS=&SORT=. Accessed: 1 May 2020.

[Whitaker, 1977] Whitaker, S. (1977). Simultaneous Heat, Mass, and Momentum Transfer in Porous Media: A Theory of Drying. *Advances in Heat Transfer*, 13, 119–203.

[Wikipedia, 2020a] Wikipedia (2020a). Circular economy. https://en.wikipedia.org/wiki/Circular_economy. Accessed: 27 March 2020.

[Wikipedia, 2020b] Wikipedia (2020b). Hydraulic conductivity. https://en.wikipedia.org/wiki/Hydraulic_conductivity. Accessed: 29 April 2020.

[Wikipedia, 2020c] Wikipedia (2020c). Multistorey car park. https://en.wikipedia.org/wiki/Multistorey_car_park. Accessed: 1 May 2020.

[Winslow et al., 1994] Winslow, D. N., Cohen, M. D., Bentz, D. P., Snyder, K. A., & Garboczi, E. J. (1994). Percolation and pore structure in mortars and concrete. *Cement and Concrete Research*, 24(1), 25–37.

[Xi et al., 1994a] Xi, Y., Bažant, Z. P., & Jennings, H. M. (1994a). Moisture Diffusion in Cementitious Materials - Adsorption Isotherms. *Advanced Cement-Based Materials*, 1, 248–257.

[Xi et al., 1994b] Xi, Y., Bažant, Z. P., Molina, L., & Jennings, H. M. (1994b). Moisture Diffusion in Cementitious Materials - Moisture Capacity and Diffusivity. *Advanced Cement-Based Materials*, 1, 258–266.

[Yiotis et al., 2006] Yiotis, A. G., Tsimpanogiannis, I. N., Stubos, A. K., & Yortsos, Y. C. (2006). Pore-network study of the characteristic periods in the drying of porous materials. *Journal of Colloid and Interface Science*, 297, 738–748.

[Zhao et al., 2018] Zhao, Z., Courard, L., Michel, F., Delvoie, S., Bouarroudj, M. E., & Colman, C. (2018). Properties of concrete with recycled construction and demolition wastes: a research experience in Belgium. Industry-Academia Forum on Advances in Structural Engineering, Tongji University, Shangai (7-9 September 2018).

[Zingg, 2013] Zingg, L. (2013). *Influence de la porosité et du degré d'humidité interne sur le comportement triaxial du béton*. PhD thesis, Université de Grenoble.

Part IV

APPENDICES

A | Experimental concrete composition

A.1 Introduction

The following appendix is used to define the composition of our various concrete samples, which are cited in the SECTION 5.2, mainly for purpose of study's reproducibility but also in order to better comprehend the possible differences between each concrete or mortar sample during the experimentation phase.

The material used were:

- Water: tap water respecting the standards;
- Cement: CEM I 42.5 N or CEM III/A 42.5 N LA depending on the composition;
- Sand: 0/4 Screed sand from the hardware store;
- Aggregates:
  - NA: Crushed limestone aggregates 2/7;
  - RCA: Recycled concrete aggregates 0/4, 4/6.3 and 6.3/8 mixed together to obtain the same granulometric curve as the NA.

The mixing method used is called the double mixing method [Guo et al., 2018] and consists of the following steps: the fine and coarse aggregates are mixed during 30s, followed by half the required water for 30s, cement for 60s and then the last half of water for another 120s.

The concrete was cast into various samples:

- 3 prisms of dimensions 10x10x40cm;
- 3 cubes of dimensions 15x15x15cm;

and an additional 15% of the initial volume was also provided to account for any possible loss during the mix of the concrete. This additional volume was therefore cast in another cube but only to be partially filled.

A.2 Concrete compositions

The various compositions used are listed in the Tables A.1 to A.4. Are also given the water-to-cement ratio obtained as well as the results of the slump test.
The same compositions are represented in the pie charts of the Figure A.1 to allow a better visual representation of the quantity of constituents used.

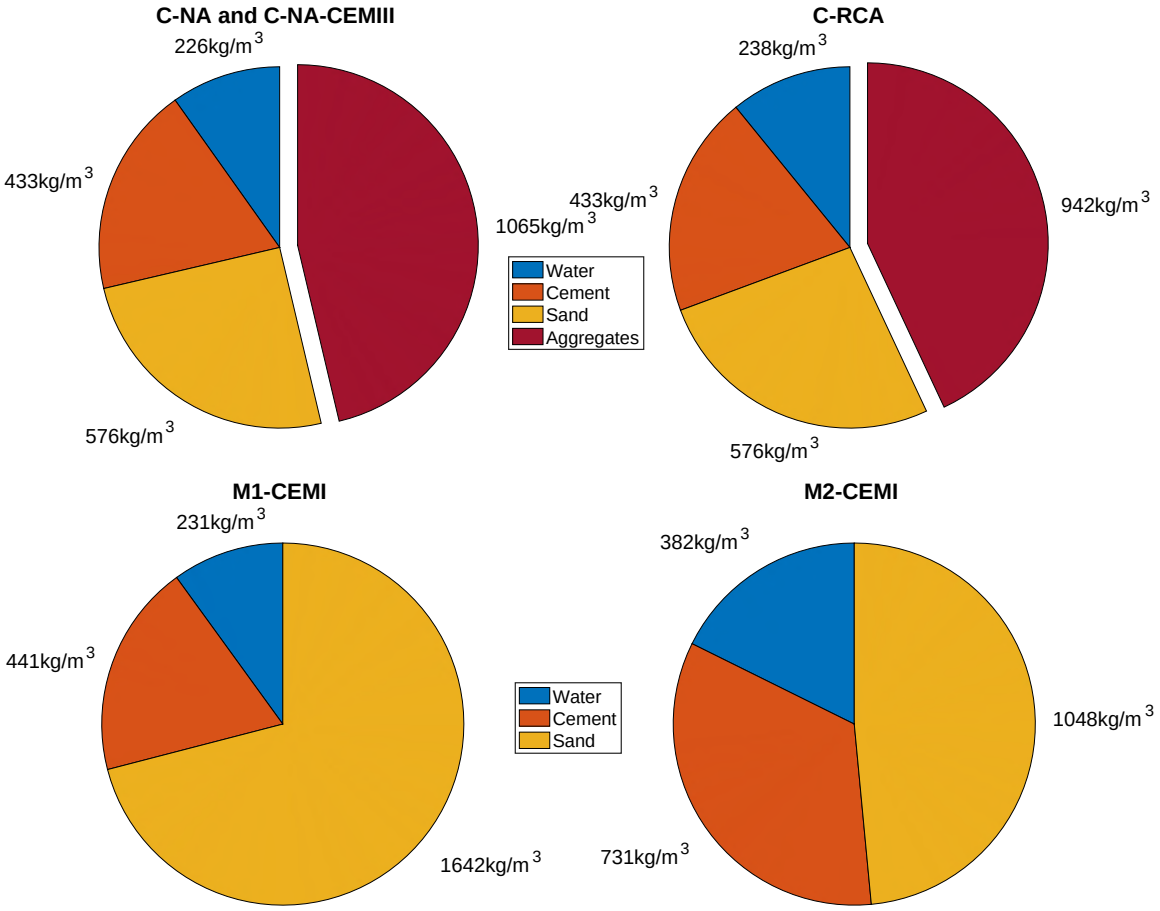

Figure A.1: Pie chart of the composition of the three concretes and two mortars used.

Micro-concrete made with NA and CEM I or CEM III (cast the 10/12/2019 or 21/12/2019)	
Water	226.2 kg/m^3
Cement	432.5 kg/m^3
Sand	575.9 kg/m^3
Aggregates	1065.4 kg/m^3
W/C ratio	0.523
Slump test	180mm (S4) or 80mm (S2)

Table A.1: C-NA and C-NA-CEMIII Composition

Micro-concrete made with RCA and CEM I (cast the 12/12/2019)	
Water	237.9 kg/m^3
Cement	432.5 kg/m^3
Sand	575.9 kg/m^3
Aggregates	941.9 kg/m^3
W/C ratio	0.502
Slump test	175mm (S4)

Table A.2: C-RCA Composition

Mortar made from CEM I and screed sand (cast the 19/12/2019)	
Water	230.7 kg/m^3
Cement	441.3 kg/m^3
Sand	1641.5 kg/m^3
W/C ratio	0.5228
Slump test	0mm (S1)

Table A.3: M1-CEMI Composition

C.E.M. Mortar made from CEM I and screed sand (cast the 20/12/2019)	
Water	382.2 kg/m^3
Cement	730.7 kg/m^3
Sand	1048.3 kg/m^3
W/C ratio	0.5231
Slump test	Liquid (S5)

Table A.4: M2-CEMI Composition

B | Additional results and Figures

This appendix is used to display additional results or results for some compositions that, if placed inside the body of the report, would reduce readability unnecessarily. The figures have all been introduced in the Chapter 6 but a short introduction will still remain to ease their comprehension.

B.1 Static Sorption and Desorption experiments

The Figures B.1 to B.4 represent the cumulative mass gain (sorption) and loss (desorption) for each composition inside all the chambers except for the 1 and 1'.
On the title of each graph, one can read the final value of the RH (or two values for the desorptions of the chambers 3'-4'-5': the first one for the plain line and the second one for the dash line). Moreover, at each weighing, the standard deviation is also shown to measure the confidence in our results.

A general statement is that the standard deviation is quite high for the first measurements but as the samples start to be in equilibrium with their environment, the deviations converge towards zero.

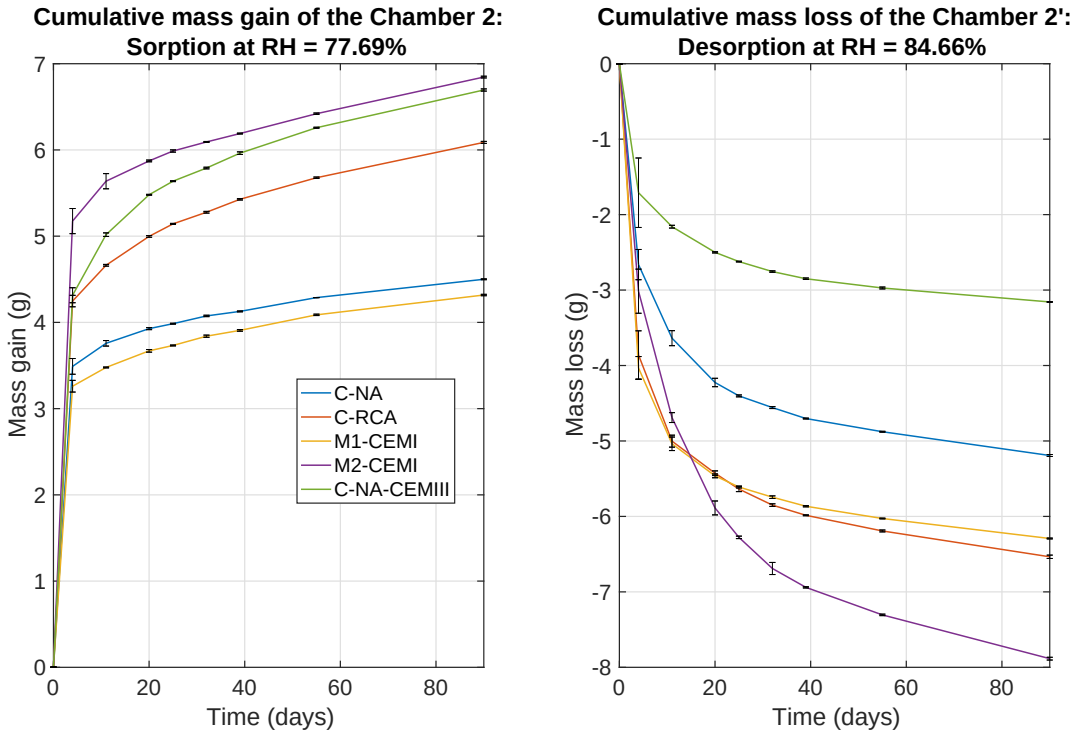

Figure B.1: Cumulative mass gain (sorption) or loss (desorption) for the Chambers 2 and 2'.

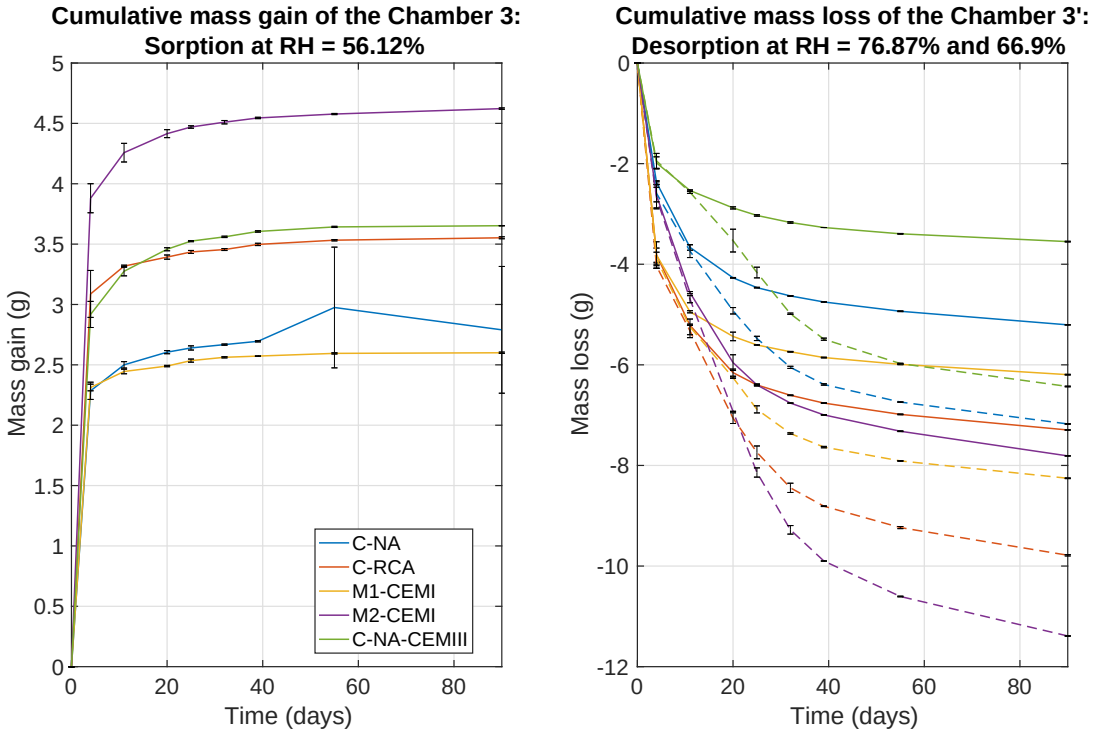

Figure B.2: Cumulative mass gain (sorption) or loss (desorption) for the Chambers 3 and 3'.

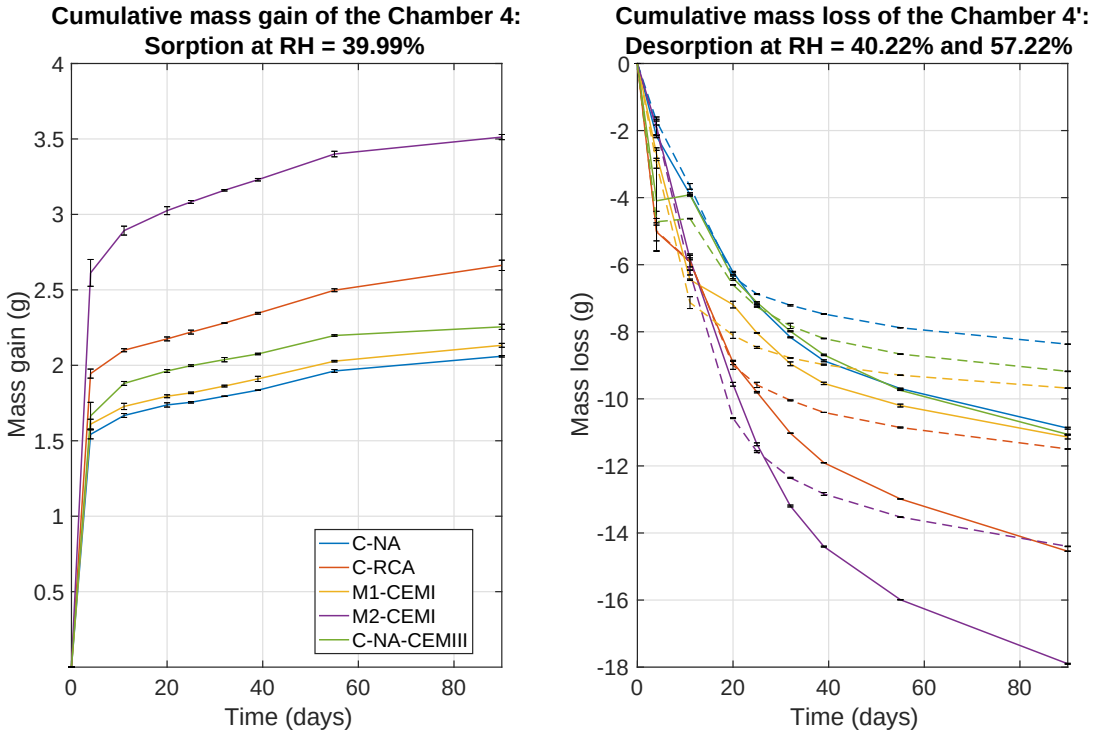

Figure B.3: Cumulative mass gain (sorption) or loss (desorption) for the Chambers 4 and 4'.

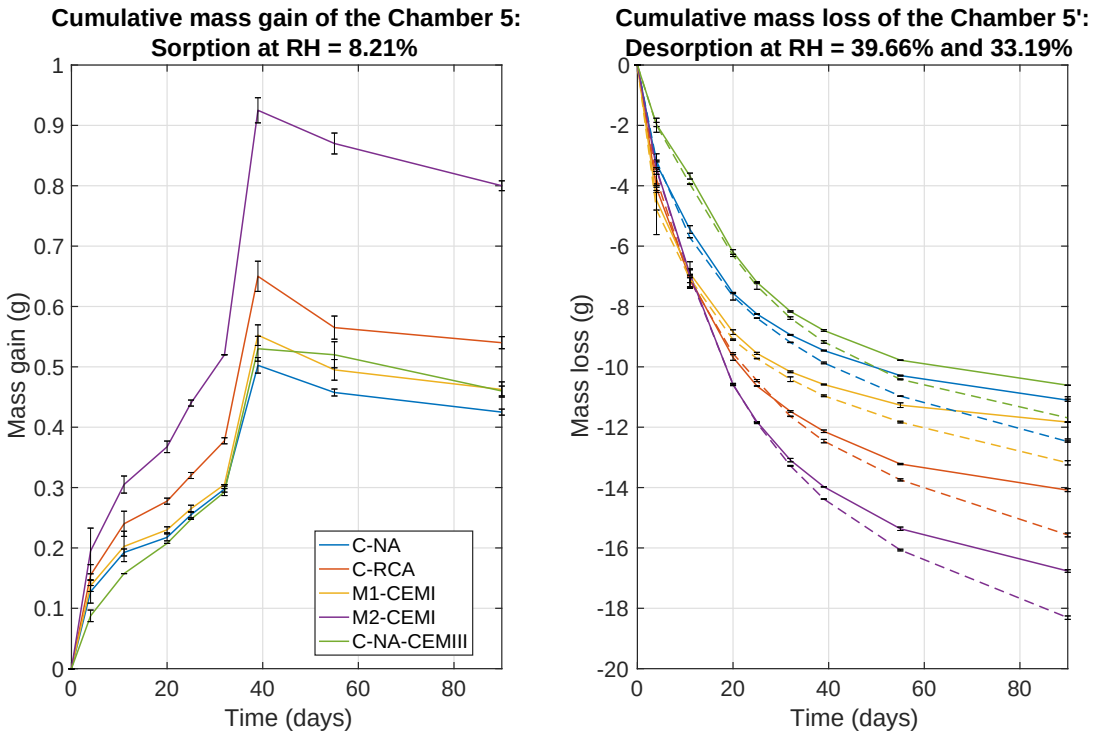

Figure B.4: Cumulative mass gain (sorption) or loss (desorption) for the Chambers 5 and 5'.

The Figures B.5 to B.12 represent the water retention curve and relative permeability curve based on the static sorption/desorption experiment and with the Van Genuchten model fitted, for the rest of the composition (C-RCA, M1-CEMI, M2-CEMI and C-NA-CEMIII). Both the desorption and then sorption experiments are displayed.

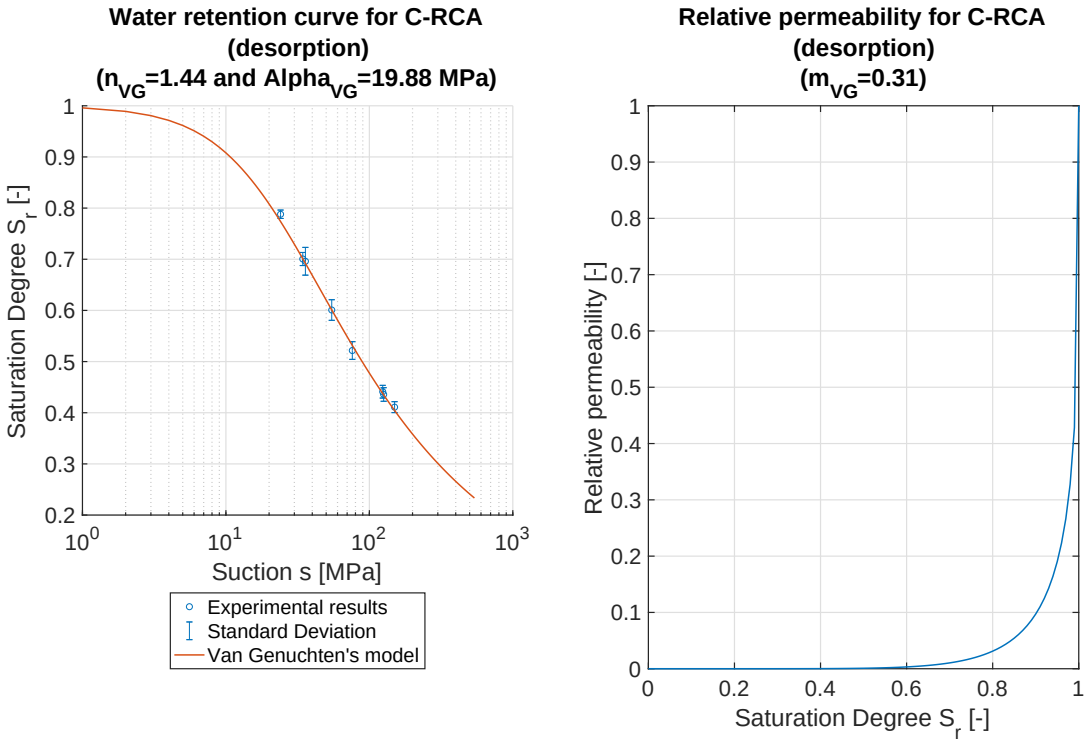

Figure B.5: Water Retention Curve fitted with the Van Genuchten model and its corresponding Relative Permeability Curve for C-RCA in desorption.

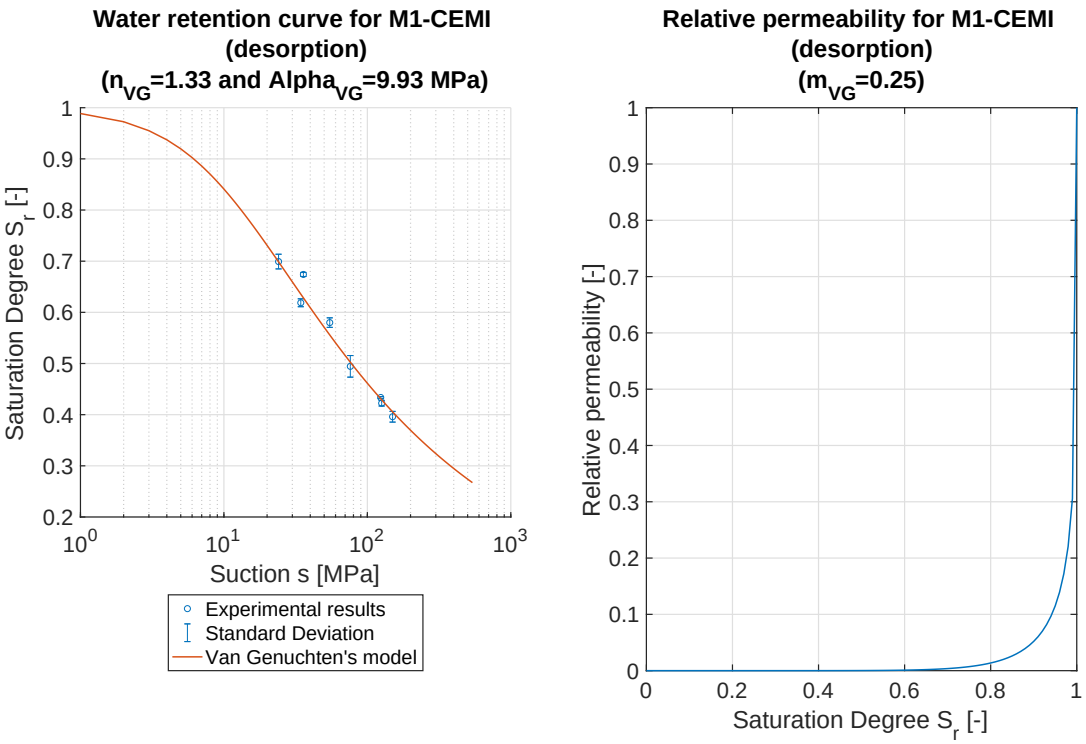

Figure B.6: Water Retention Curve fitted with the Van Genuchten model and its corresponding Relative Permeability Curve for M1-CEMI in desorption.

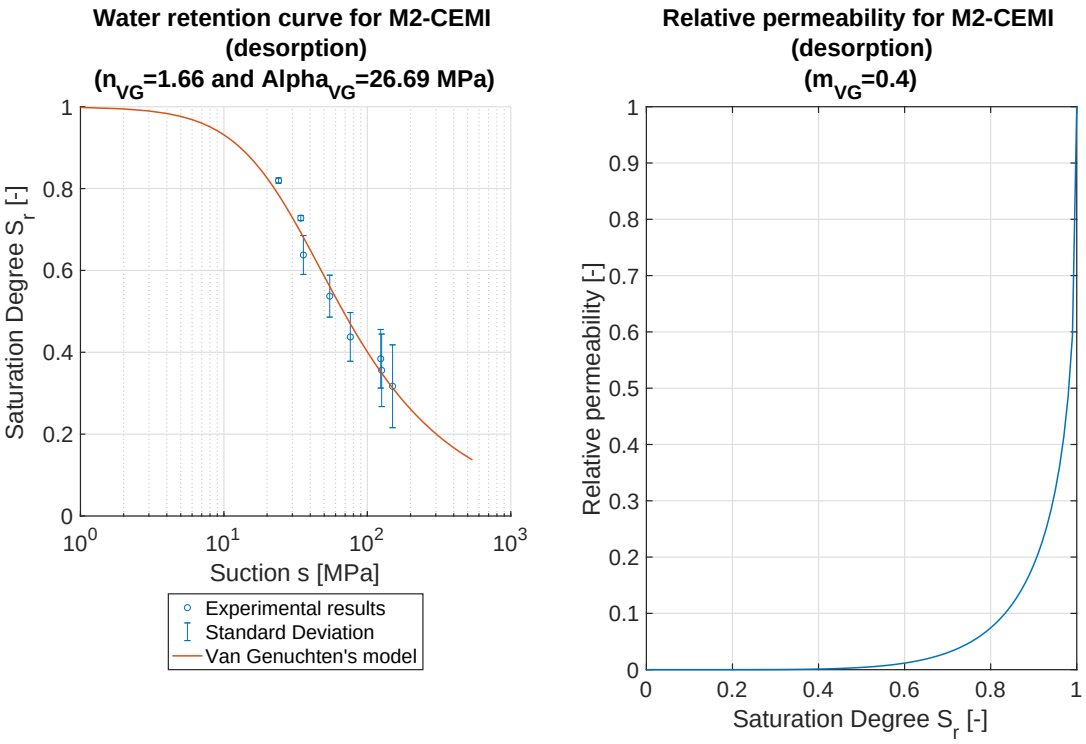

Figure B.7: Water Retention Curve fitted with the Van Genuchten model and its corresponding Relative Permeability Curve for M2-CEMI in desorption.

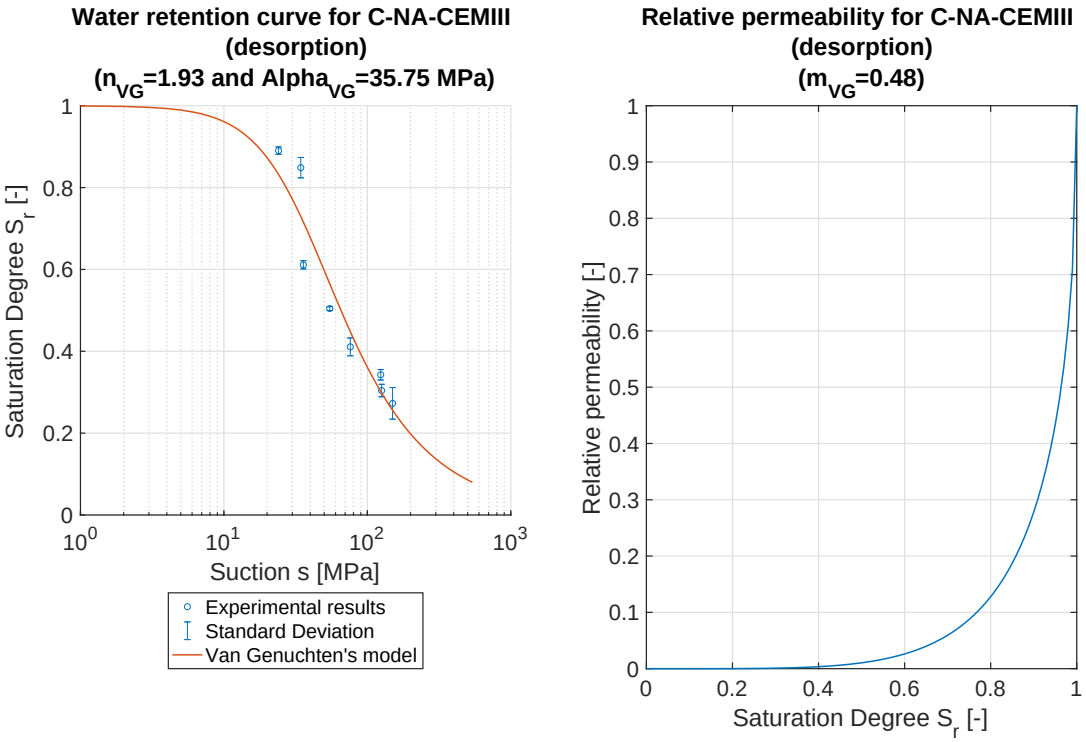

Figure B.8: Water Retention Curve fitted with the Van Genuchten model and its corresponding Relative Permeability Curve for C-NA-CEMIII in desorption.

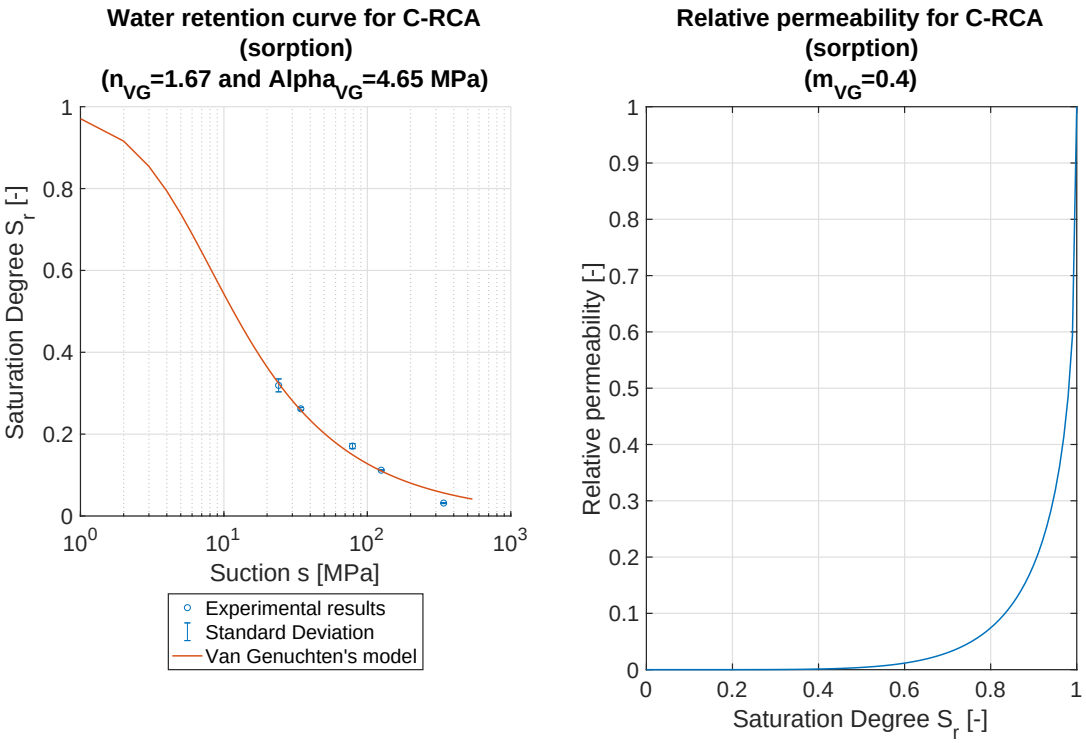

Figure B.9: Water Retention Curve fitted with the Van Genuchten model and its corresponding Relative Permeability Curve for C-RCA in sorption.

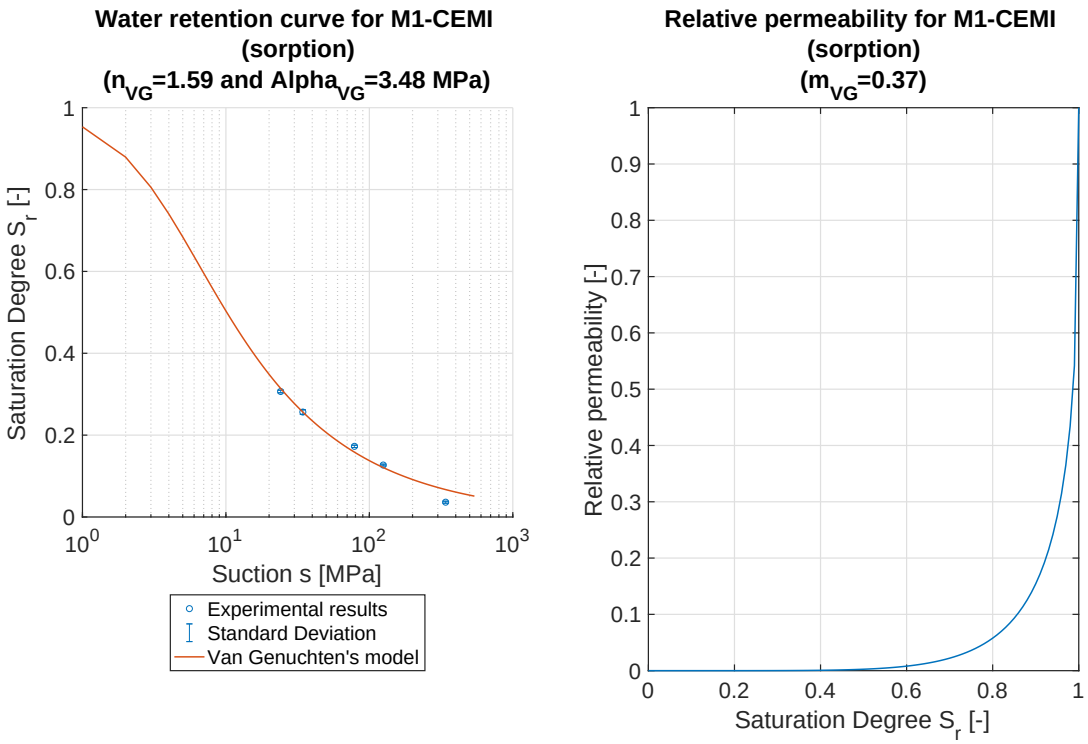

Figure B.10: Water Retention Curve fitted with the Van Genuchten model and its corresponding Relative Permeability Curve for M1-CEMI in sorption.

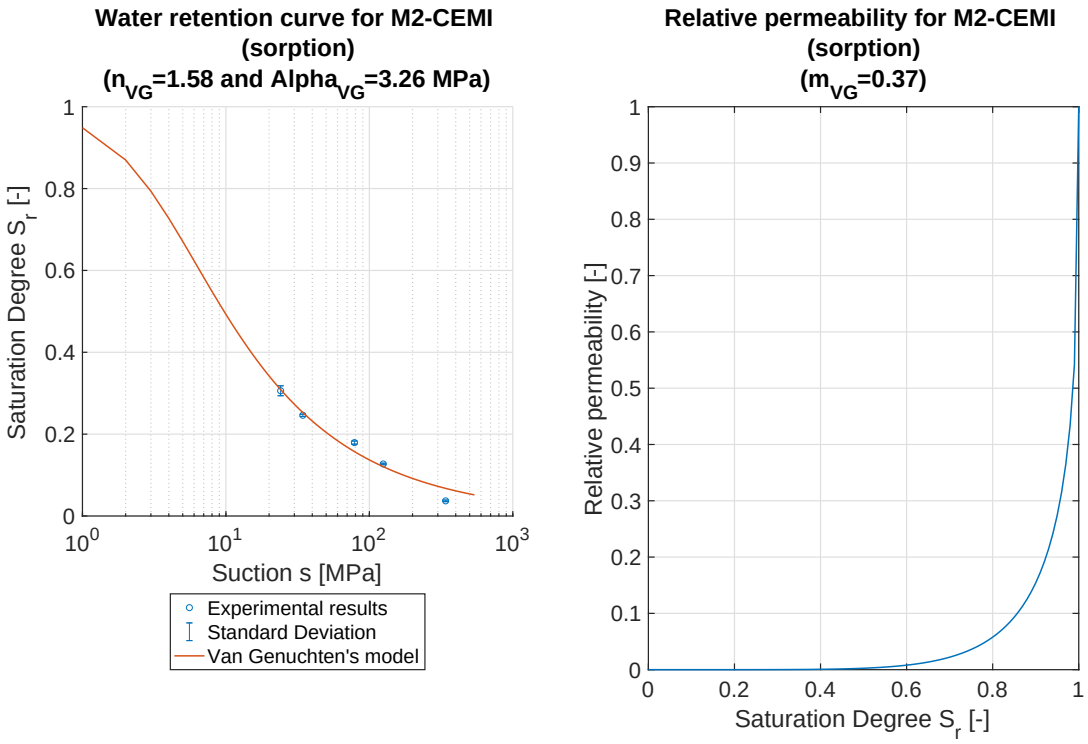

Figure B.11: Water Retention Curve fitted with the Van Genuchten model and its corresponding Relative Permeability Curve for M2-CEMI in sorption.

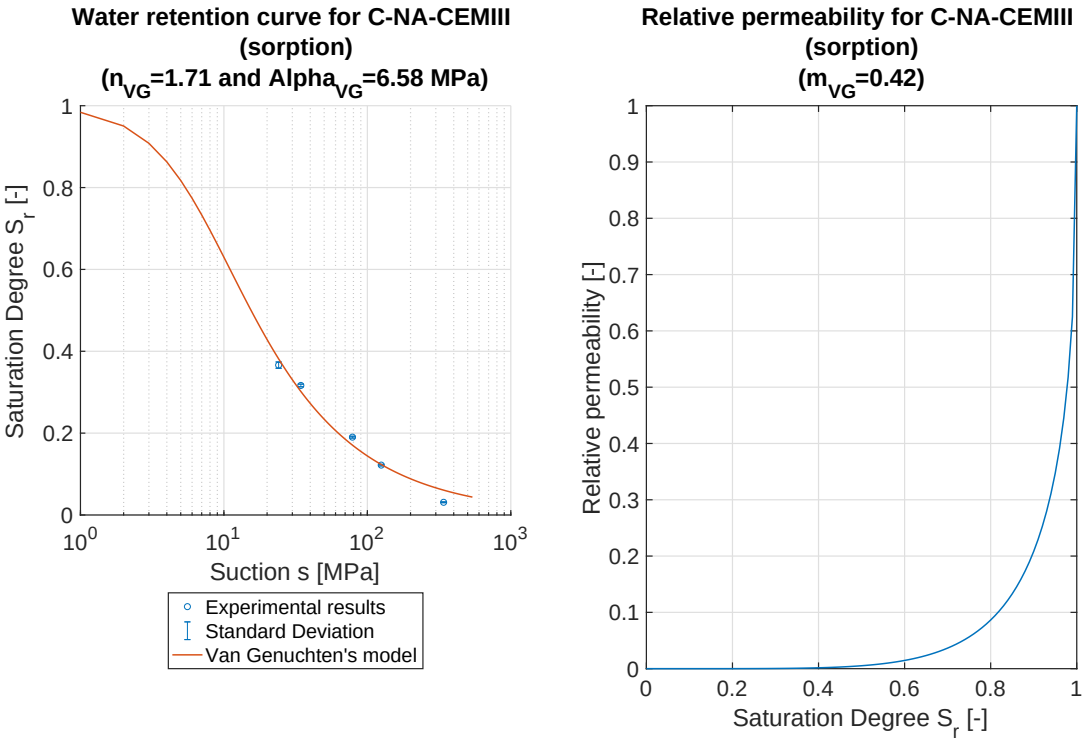

Figure B.12: Water Retention Curve fitted with the Van Genuchten model and its corresponding Relative Permeability Curve for C-NA-CEMIII in sorption.

B.2 Carbonation depth

The Figures B.13 to B.16 display the evolution of the carbonation depth with respect to time, on all four faces of the compositions C-RCA, M1-CEMI, M2-CEMI and C-NA-CEMIII.

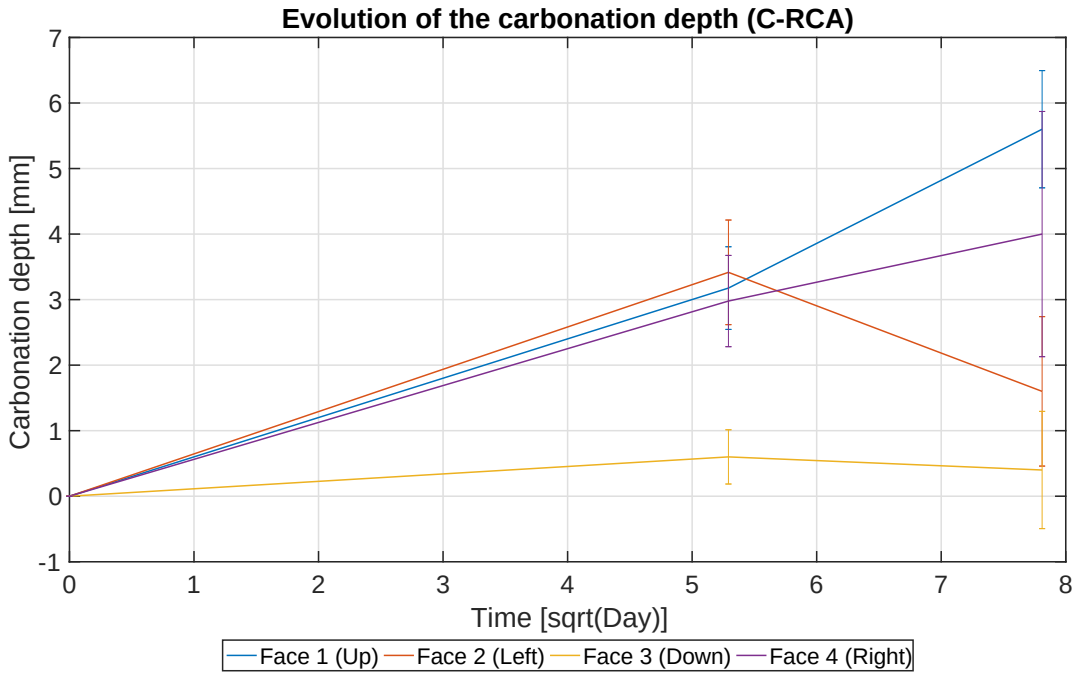

Figure B.13: Evolution of the carbonation depth [mm] for the C-RCA composition.

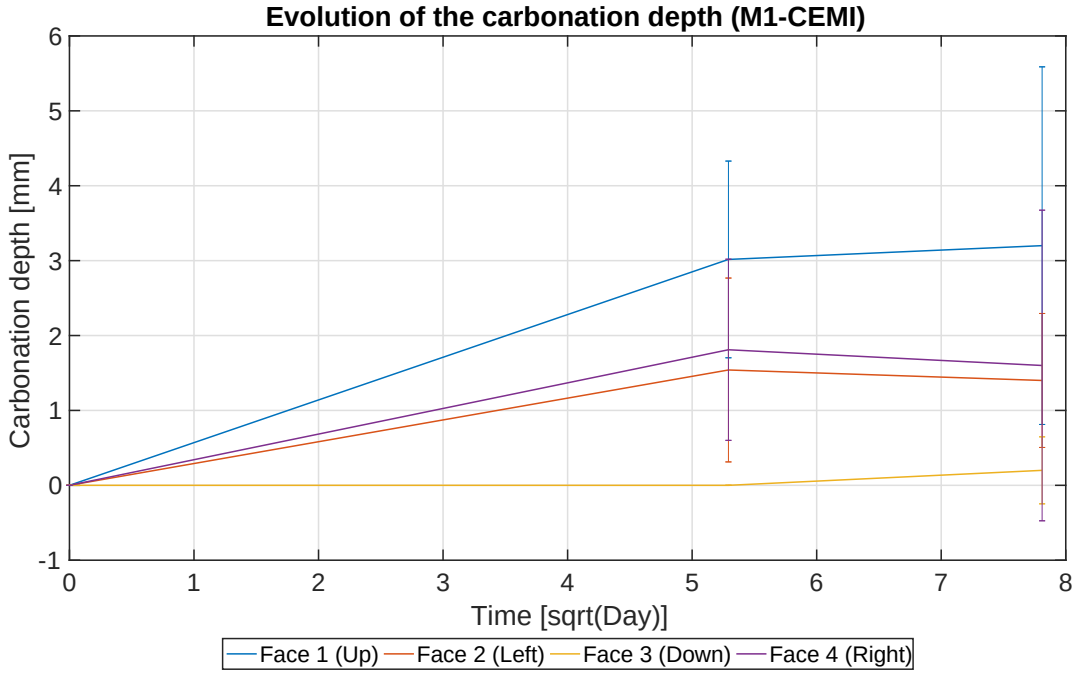

Figure B.14: Evolution of the carbonation depth [mm] for the M1-CEMI composition.

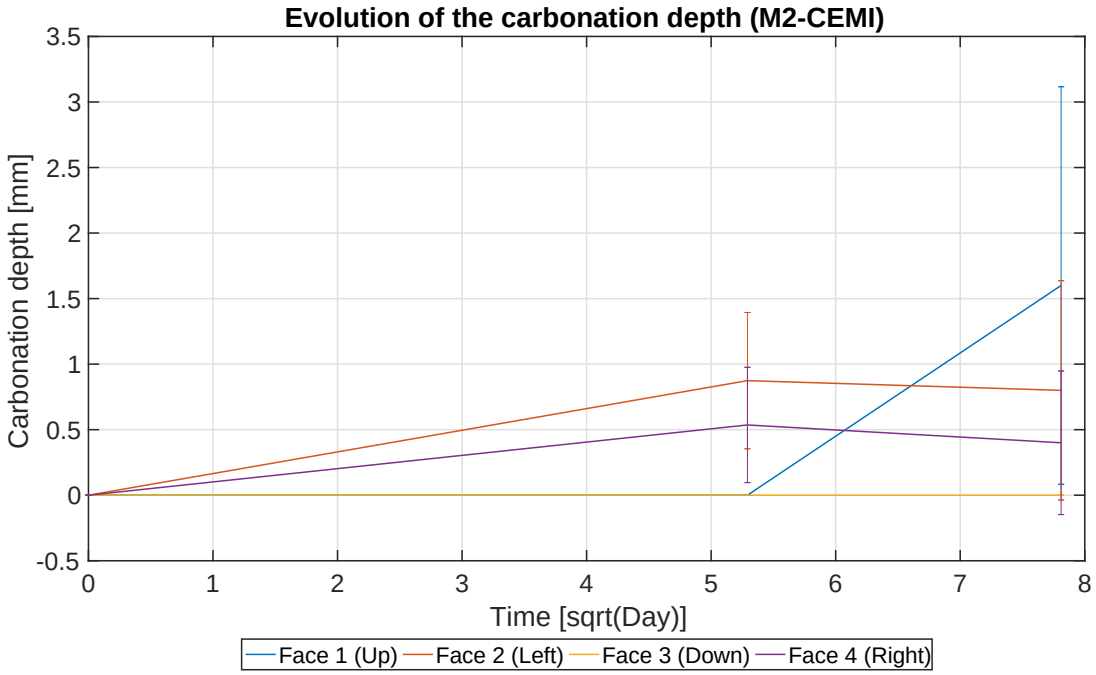

Figure B.15: Evolution of the carbonation depth [mm] for the M2-CEMI composition.

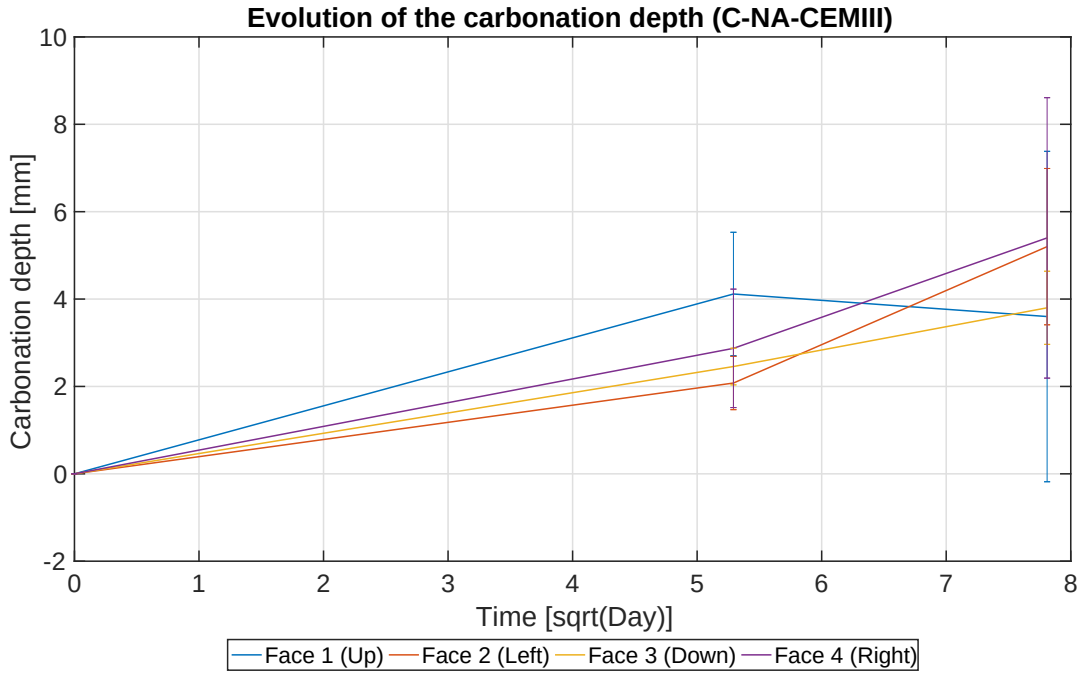

Figure B.16: Evolution of the carbonation depth [mm] for the C-NA-CEMIII composition.

B.3 Water Permeability

The Figures B.17 to B.19 show the results of the water permeability measurements for the M1-CEMI, M2-CEMI and C-NA-CEMIII.

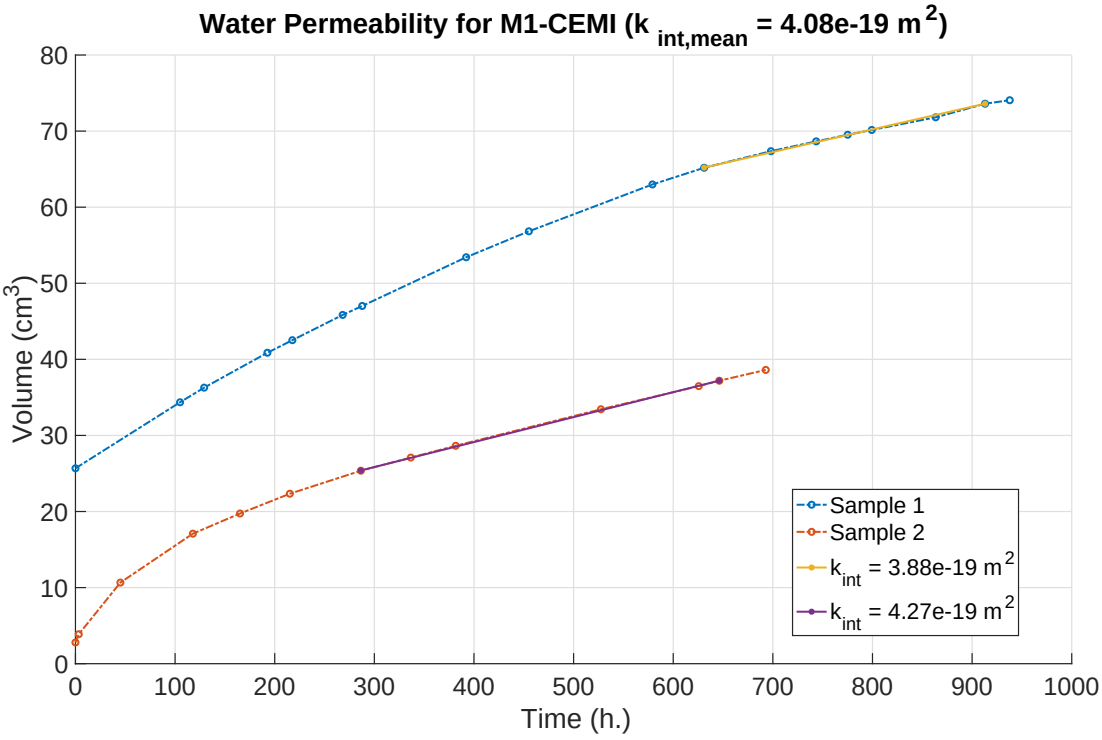

Figure B.17: Water permeability measured for the M1-CEMI.

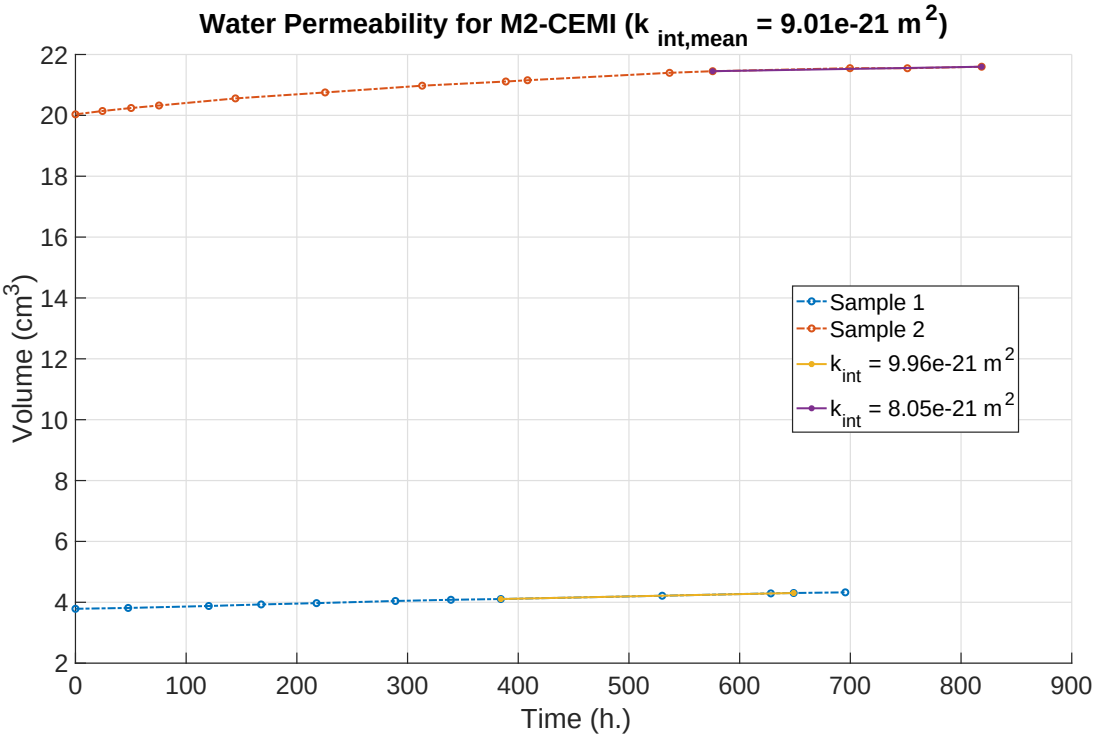

Figure B.18: Water permeability measured for the M2-CEMI.

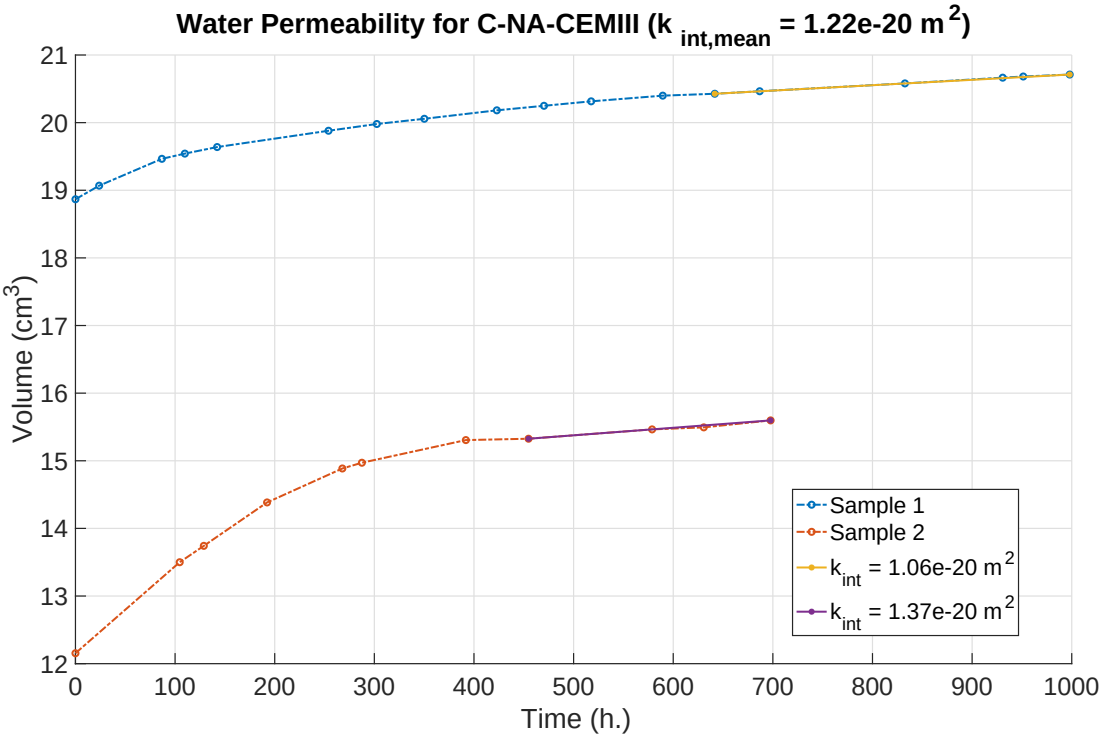

Figure B.19: Water permeability measured for the C-NA-CEMIII.

C | Resistance to Carbonation

C.1 Carbonation depth - 0 months

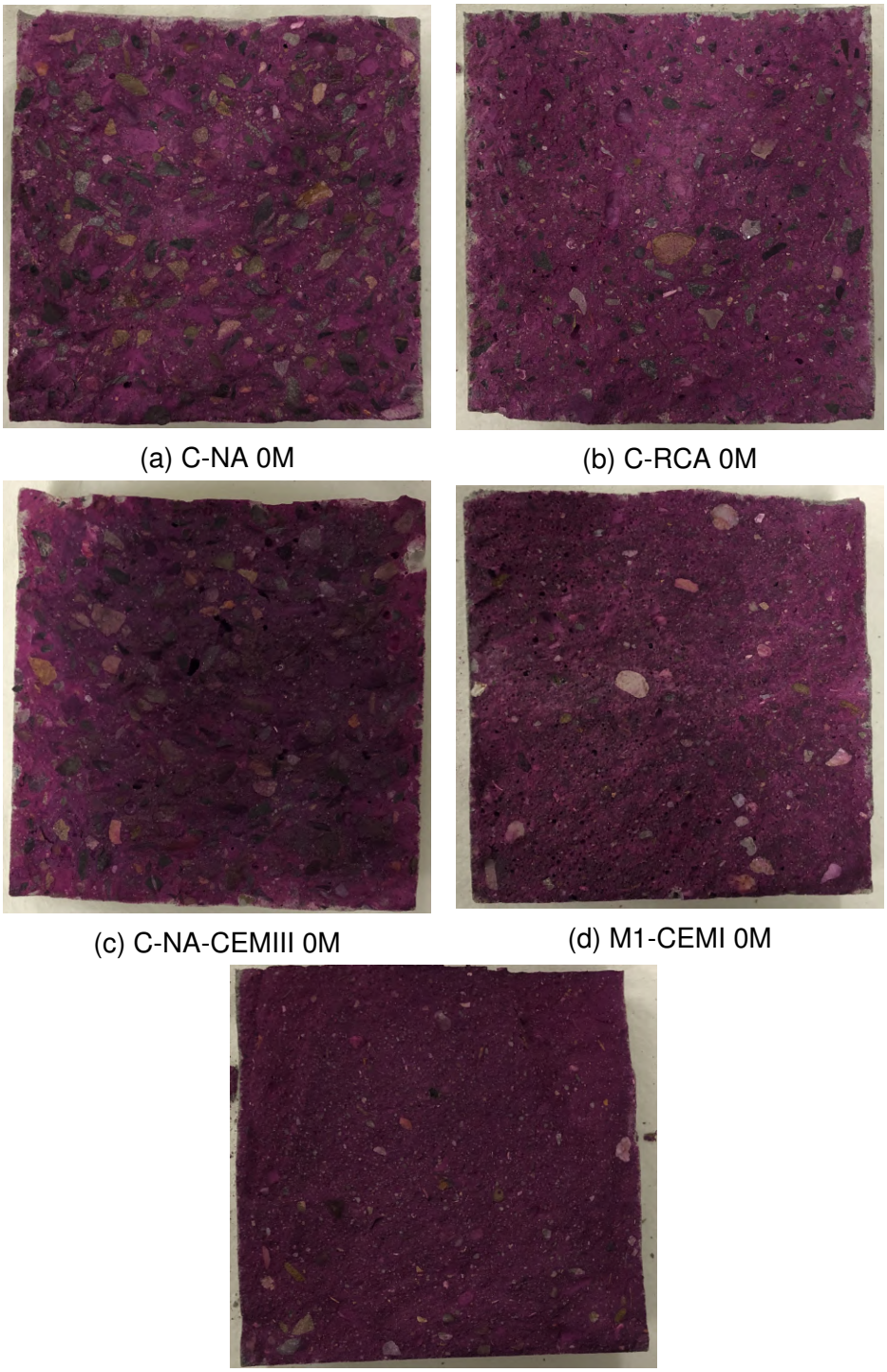

(a) C-NA 0M

(b) C-RCA 0M

(c) C-NA-CEMIII 0M

(d) M1-CEMI 0M

(e) M2-CEMI 0M

Figure C.1: Resistance to carbonation for each sample at the beginning of the experiment: C-NA, C-RCA, C-NA-CEMIII, M1-CEMI and finally M2-CEMI.

C.2 Carbonation depth - 1 month

(a) C-NA 1M

(b) C-RCA 1M

(c) C-NA-CEMIII 1M

(d) M1-CEMI 1M

(e) M2-CEMI 1M

Figure C.2: Resistance to carbonation for each sample after 1 month of carbonation: C-NA, C-RCA, C-NA-CEMIII, M1-CEMI and finally M2-CEMI.

C.3 Carbonation depth - 2 months

(a) C-NA 2M

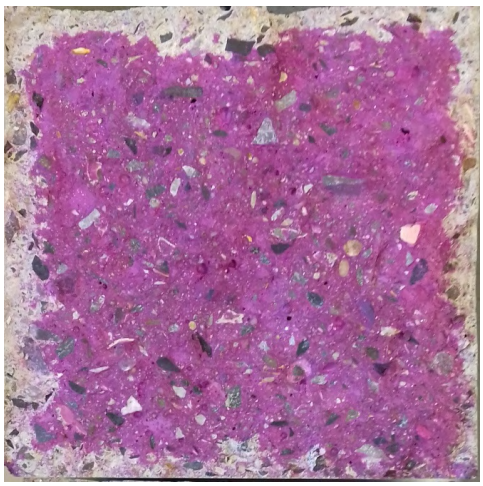

(b) C-RCA 2M

(c) C-NA-CEMIII 2M

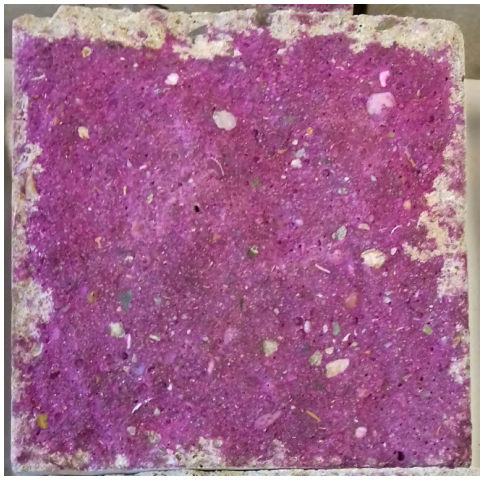

(d) M1-CEMI 2M

(e) M2-CEMI 2M

Figure C.3: Resistance to carbonation for each sample after 2 months of carbonation: C-NA, C-RCA, C-NA-CEMIII, M1-CEMI and finally M2-CEMI.

D | Model Parameters

As it has been introduced before, various parameters are common to all the simulations done in this thesis. Those parameters will be displayed hereafter.
The notations used in the Lagamine software may differ from the one presented before in this thesis. However, it seemed useful to explicit the value of the parameters used in the simulation for reproducibility purposes and to better understand the results.

The parameters presented in the ELA law are not used in our model as the mechanical aspects are blocked. Therefore, those values might be incorrect but without any influence on the results.

Parameter	Value	Units
ELA - ELAstic constitutive law		
Young's elastic modulus (E)	5000	[MPa]
Poisson's ratio (ν)	0.3	[-]
WAVAT - Water-Air seepage, VApour diffusion, Thermal coupled		
Medium tortuosity (τ)	0.1	[-]
Initial temperature (T_0)	294	[K]
Initial water pressure ($p_{w,0}$)	1E5	[Pa]
Initial air pressure ($p_{a,0}$)	1E5	[Pa]
Water dynamic viscosity ($\mu_{w,0}$)	1E-3	[Pa.s]
Water dynamic viscosity thermal coefficient (α_w^T)	0.01	[K^{-1}]
Water density ($\rho_{w,0}$)	1000	[kg/m^3]
Water compressibility coefficient ($1/\chi_w$)	5E-10	[Pa^{-1}]
Water thermal expansion coefficient (β_w^T)	3E-4	[K^{-1}]
Water thermal conductivity ($\Gamma_{w,0}$)	0.58	[W/m.K]
Water thermal conductivity coefficient (γ_w^T)	0	[K^{-1}]
Water specific heat ($c_{p,w0}$)	4180	[J/kg.K]
Water specific heat coefficient (H_w^T)	0	[K^{-1}]
Storage coefficient (E_s)	0	[Pa^{-1}]
Air dynamic viscosity ($\mu_{a,0}$)	1.8E-5	[Pa.s]
Air dynamic viscosity thermal coefficient (α_a^T)	0	[K^{-1}]
Air density ($\rho_{a,0}$)	1.205	[kg/m^3]

Table D.1: Common model parameters for all simulations

Parameter	Value	Units
Air thermal conductivity ($\Gamma_{a,0}$)	0.025	$[\mathrm{W/m.K}]$
Air thermal conductivity coefficient (γ_a^T)	0	$[\mathrm{K^{-1}}]$
Air specific heat ($c_{p,a0}$)	1000	$[\mathrm{J/kg.K}]$
Air specific heat coefficient (H_a^T)	0	$[\mathrm{K^{-1}}]$
Solid thermal expansion coefficient (β_s^T)	1.3E-5	$[\mathrm{K^{-1}}$
Solid thermal conduction ($\Gamma_{s,0}$)	1.68	$[\mathrm{W/m.K}]$
Solid conduction coefficient (I_s^T)	0	$[\mathrm{K^{-1}}]$
Solid specific heat ($c_{p,s0}$)	880	$[\mathrm{J/kg.K}]$
Solid specific heat coefficient (H_s^T)	0	$[\mathrm{K^{-1}}]$
Residual saturation degree (S_{res})	0	[-]
Field saturation degree ($S_{r,field}$)	1	[-]
Air entry value	0	$[\mathrm{Pa}]$
Henry coefficient	0	[-]
LICHA - constitutive law defining distributed loads on a line		
Initial environmental pressure (p_0)	101325	$[\mathrm{Pa}]$
FMIVP - constitutive law for mixed limit condition (seepage and evaporation)		
Latent heat of water (L)	2500E3	$[\mathrm{J/kg}]$

Table D.2: Common model parameters for all simulations - remaining parameters